VIBRATION-BASED ELECTROMAGNETIC ENERGY HARVESTER: ENERGY PERFORMANCE, VIBRATION CONTROL, AND FREQUENCY TUNING

CAI QINLIN

PhD

The Hong Kong Polytechnic University

2021

The Hong Kong Polytechnic University
Department of Civil and Environmental Engineering

Vibration-based Electromagnetic Energy Harvester: Energy Performance, Vibration Control, and Frequency Tuning

CAI Qinlin

A thesis submitted in partial fulfillment of the requirements for the Degree of **Doctor of Philosophy**

May 2021

CERTIFICATE OF ORIGINALITY

I hereby declare that this thesis is my own work and that, to the best of my knowledge and belief, it reproduces no material previously published or written, nor material that has been accepted for the award of any other degree or diploma, except where due acknowledgement has been made in the text.

(Signed)

CAI Qinlin (Name of student)

To my family

for their love and support

ABSTRACT

Vibration-based energy harvesting is an emerging technique that can convert vibration energy into electrical energy. Energy harvesters adopting various types of energy transducers have been developed to extract energy from different vibration sources, wherein the extracted energy can be applied to different objectives, such as structural health monitoring and semi-active/active control. However, the typical power levels in most micro-scale vibration-based harvesters are too low to meet the power demands of the aforementioned applications. This thesis investigates two important topics on vibration-based energy harvesters: the leveraging of the dynamic coupling effect between energy harvesters and vibration sources to realize both vibration control and energy harvesting functions, and the introduction of the frequency tuning functions into an energy harvester in the electrical and mechanical domains to realize broader energy harvesting bandwidth, whereby frequency tuning can enhance the energy harvesting performance of typical vibration-based energy harvesters.

Developed vibration-based harvesters fall into two categories and comprise two key components: an electromagnetic (EM) transducer and an energy harvesting circuit (EHC). An *ad hoc* resistance-emulation EHC was designed. Its equivalent resistance characteristic and the vibration damping performance when it was connected to an electromagnetic damper (EMD) were verified through experiments.

An energy-harvesting EMD (EHEMD), a simple type of dual-function damper, was fabricated and employed in an experiment on a full-scale bridge stay cable as an energy-harvesting passive vibration control device. Subsequently, similar EHEMDs were numerically applied to the secondary suspension of a high-speed train to realize an

energy-harvesting adaptive control strategy. These numerical and experimental cases illustrate the effectiveness of the proposed EHEMD device for providing the optimal vibration damping and energy harvesting function in the meantime.

Furthermore, a coupled analysis of structural vibrations and EM energy harvesters was performed, wherein broadband random excitations were applied, and the structures were assumed to respond within the elastic range. The optimization objectives were set as the minimization of the structural kinetic energy and the maximization of the power transferred into a dual-function device. Different systems with a single-degree-of-freedom structure coupled with an EHEMD, an energy-harvesting tuned mass damper (EHTMD), and an energy-harvesting tuned inerter damper (EHTID) were investigated analytically and numerically. The general consistency between vibration control and energy harvesting was demonstrated.

The second category of EM energy harvester typically contains an oscillating structure without a significant coupling effect on the vibration source; that is, the device operates as a pure energy harvester. An equivalent circuit model for such a case was developed based on the dynamic electromechanical analogy. Moreover, an overall impedance optimization theory is proposed for the first time by considering different excitation types, coupling effect strengths, and oscillator complexities. A potential electrical frequency tuning method was validated through numerical case studies.

Subsequently, a novel design of an energy harvester with tunable low frequency, termed double-mass-pendulum (DMP) oscillator, is proposed. The mathematical model of the DMP oscillator was established in terms of different base motions. The nonlinear characteristic, frequency tuning function, and energy harvesting performance of the DMP oscillator were evaluated through free vibration tests and shake table tests. In addition, the oscillator was enclosed in a floating-point absorber and then tested in a wave flume to evaluate its potential applications in wave energy converters.

Through the combination of theoretical, numerical, and experimental studies, this work demonstrates the promising prospects of the developed two categories of vibration-based energy harvesters for functionality and performance enhancement. Some challenges are also discussed based on the outcome of the work.

PUBLICATIONS ARISING FROM THE THESIS

Journal Papers

Cai, Q. L., and Zhu, S. (2019) "Enhancing the performance of electromagnetic damper cum energy harvester using microcontroller: concept and experimental validation." *Mechanical Systems and Signal Processing*. 134: 106339.

Cai, Q. L., and Zhu, S. (2020) "Unified strategy for overall impedance optimization in vibration-based electromagnetic energy harvesters." *International Journal of Mechanical Sciences*. 165: 105198.

Cai, Q. L., Zhu. S., and Ke, S. (2020) "Can we unify vibration control and energy harvesting objectives in energy regenerative tuned mass dampers?" *Smart Materials and Structures*. 29: 087002.

Cai, Q. L., Hua, Y. Y., and Zhu, S. (2021). "Energy-harvesting adaptive vibration damping in high-speed train suspension using electromagnetic damper." *International Journal of Structural Stability and Dynamics*. 2140002.

Cai, Q. L., and Zhu, S. (2021) "Applying double-mass pendulum oscillator with tunable ultra-low frequency in wave energy converter." *Applied Energy.* 298: 117228.

Cai, Q.L., and Zhu, S. (2021) "The nexus between vibration-based energy harvesting and structural vibration control: A comprehensive review." *Renewable and Sustainable Energy Reviews*. Submitted.

Conference Papers

Cai, Q. L., and Zhu, S. (2019, March). "Vibration-based energy harvesting circuit using feed-forward control". In *Sensors and Smart Structures Technologies for Civil, Mechanical, and Aerospace Systems 2019, International Society for Optics and Photonics*, Denver, Colorado, USA. Vol. 10970, p. 109700X.

Patents

Zhu, S., and **Cai, Q. L.** "A floating wave energy converter with tunable low frequency." China Model Utility Patent No.: CN212583871U, Grant Date: February 23, 2021.

ACKNOWLEDGEMENTS

First, I express my deepest gratitude to my supervisor, Prof. Songye Zhu, for providing me the opportunity to be a Ph.D. student in his group and for his patient guidance and continuous support. Since my master's study, I have benefited a lot from his knowledgeable and insightful advice. Prof. Zhu was incredibly patient and tolerant with my missteps. He spent many hours proofreading my papers and discussing new problems and topics with me, which are all the expectations of a Ph.D. student for a supervisor. I appreciate that he helped me to broaden my academic views and interests. In comparison to the completed work in this thesis, the passion, vision, and insight in the research process he has shared with me is more important, which I do believe will enlighten me in my future career. I appreciate his cultivation and encouragement and all his contributions of time and funding to make my Ph.D. experience fruitful and meaningful.

I also express my sincere gratitude to my advisor during my master's program at Xiamen University, Prof. Zhiwei Chen, for recommending me to pursue my Ph.D. degree at PolyU and for providing me with much helpful advice. My sincere appreciation goes to Prof. Zhizhao Liu from LSGI for financial support during my last year's study. I also thank Prof. Yiqing Ni and Dr. Siu Kai Lai for giving valuable suggestions to my confirmation report.

I am also grateful to Mr. Y. M. Lai, Mr. F. H. Wong, Mr. K. H. Leung, and Mr. W. K. Ho for their professional and valuable support during the laboratory experiment. Gratitude is also extended to the following students for their generous assistance during their final year projects: Mr. Kwok Wai Lau, Mr. Ho Man Kwok, Mr. Ka Yin Sha, Ms. Haoyuan Bai, and Mr. Lok Hin Yeung.

I additionally thank many of the past and current members of Prof. Zhu's and Prof. Chen's research groups who offered tremendous help in several ways, which made my Ph.D. study easier. Special thanks go to Dr. Wen-ai Shen, from Huazhong University of Science and Technology, who helped me greatly and shared with me useful information on dual-function dampers at the beginning of my study. I also thank Dr. Xiang Shi, Dr. Canxing Qiu, Dr. Bin Wang, Dr. Yingyu Hua, Dr. Qian Geng, Dr. Haoran Zuo, Mr. Xiong Sha, and Mr. Shiguang Wang for their constructive discussions. I also appreciate my friends at and beyond PolyU: Dr. Youwu Wang, Dr. Rongrong Hou, Dr. Chen Wang, Dr. Ran Chen, Dr. Jianfu Lin, Dr. Junbo Chen, Mr. Shen Zhan, Mr. Rui Li, Ms. Yaohan Li, Mr. Hao Jin, Mr. Yingxu Huo, and many others. We had fruitful and enjoyable discussions on numerous research topics, which made my past five years memorable.

Lastly, I sincerely appreciate my family members for their love and countless sacrifices over these years. To my grandmother, who accompanied me through my whole childhood but passed away just when I started my Ph.D. study, thank you for your unconditional love and support.

TABLE OF CONTENTS

LIST OF FIGURES

LIST OF TABLES

LIST OF ACRONYMS

AC	alternating current
A/D	analog/digital
CCM	continuous conduction mode
DC	direct current
D/A	digital/analog
DCM	discontinuous conduction mode
DMP	double-mass pendulum
DOF	degree-of-freedom
EHAC	energy-harvesting adaptive control
EHC	energy harvesting circuit
EHEMD	energy-harvesting electromagnetic damper
EHID	energy-harvesting inerter damper
EHPC	energy-harvesting passive control
EHTID	energy-harvesting tuned inerter damper
EHTMD	energy-harvesting tuned mass damper
EM	electromagnetic
EMD	electromagnetic damper
EMF	electromotive force
ESR	equivalent series resistance
FRF	frequency response function
HDPE	high-density polyethylene
HT	Hilbert transform
HST	high-speed train

ID	inerter damper
IM	impedance matching
MCU	microcontroller unit
MTS	material test system
MDOF	multi-degree-of-freedom
MMR	mechanical motion rectifier
MOSFET	metal-oxide-semiconductor field-effect transistor
MR	magnetorheological
PCB	printed circuit board
PSD	power spectral density
PWM	pulse-width modulation
RC	resistor-capacitor
RL	resistor-inductor
RMS	root-mean-square
SDOF	single-degree-of-freedom
TID	tuned inerter damper
TMD	tuned mass damper
WEC	wave energy converter

CHAPTER 1

INTRODUCTION

1.1 Motivations

Energy harvesting, which refers to the process of extracting energy from surrounding environments or systems and converting it to usable electrical energy (Park et al., 2008), is an emerging and promising technology to support the explosive growth of global power demands. Potential energy sources include, but are not limited to, sunlight, vibrations, heat, and radio waves. Among them, vibration sources are widespread in various surroundings; thus, vibration-based energy harvesting techniques have elicited increased interest.

In structural health monitoring, wireless sensors have been developed to monitor and assess the health conditions of structures and facilitate their optimal maintenance and safe operation (Spencer et al., 2004; Hu et al., 2013; Abdulkarem et al., 2020). However, the practical deployment of wireless sensors still faces many technical challenges, such as long-term reliability and power supply issues (Park et al., 2008; Shen et al., 2012). The frequent replacement of the batteries powering wireless sensors is tedious, which hinders their wide applications, especially in remote regions. Hence, researchers have been seeking sustainable alternative power supplies for wireless sensors (Chalasani and Conrad, 2008; Jung et al., 2011a; Shen et al., 2012; Shaikh and Zeadally, 2016; Newell and Duffy, 2019), and vibration-based energy harvesting is certainly one of the promising options.

In structural vibration control, semi-active and active control techniques usually

achieve better control performance than passive control. However, to some extent, the reliability of semi-active and active techniques depends on the external power supply and the sensing and feedback system. The utilization of vibration energy from controlled structures is an attractive strategy for realizing self-powered semi-active or active control, thus improving the robustness and practicability (Suda et al., 1998a; Chen and Liao, 2012; Chen et al., 2015; Jamshidi et al., 2017; Li and Zhu, 2021).

The power consumption of wireless sensors typically ranges from tens to hundreds of milliwatts (Mitcheson, 2005; Priya, 2005; Miller et al., 2010; Newell and Duffy, 2019), whereas semi-active or active control systems consume power amounts ranging from several watts to kilowatts (Symans and Constantinou, 1999; Ballo, 2007; Chen et al., 2015). The typical output power level of nano- or micro-scale vibration-based energy harvesters cannot meet these demands.

Large-scale vibration energy harvesters are a potential solution to address the relatively large demand for power. Zuo and Tang (2013) indicated that power generation by large-scale vibration energy harvesters can range from 1 W to 100 kW. When a large energy harvester extracts a large amount of vibration energy from a source (e.g., a vibrating structure), the coupling effect may be strong enough to affect the dynamics of the vibration source. Consequently, the energy harvester may suppress the source vibration through the energy harvesting mechanism and thus work as an energy-harvesting vibration control device. The energy-regenerative damper concept dates back to the 1970s when Arsem (1971) first explored its application in vehicle suspension systems, and in the 2010s, the concept was extended to civil structures and known as dual-function dampers that can realize simultaneous vibration control and energy harvesting functions (Zhu et al 2012; Tang, 2013; Shen, 2014; Loong, 2020).

It is believed that the power harvested by these dual-function devices from large-

scale structures is sufficient for wireless sensors and semi-active/active control systems. However, thus far, the application of these dual-function devices in civil engineering has received limited attention. In particular, most of the studies focused on the feasibility validation of passive dual-function devices. The investigation of adaptive energy-harvesting dampers represents an important step toward realizing self-powered semi-active and active controls. In addition, optimization of the dual functions is a fundamental issue that needs to be addressed. Shen (2014) revealed the conditional consistency between the objectives of energy harvesting and vibration control for a structure coupled with energy-harvesting electromagnetic dampers (EHEMDs) when subjected to white noise excitation. However, the answers for two other coupled systems with a structure and an energy-harvesting tuned mass damper (EHTMD) or a structure and an energy-harvesting tuned inerter damper (EHTID), which represent more complicated problems involving more optimization parameters, remain unclear.

Another question is how to realize broader energy harvesting bandwidth to improve the output power through appropriate approaches, including the development of energy harvesters with frequency tuning capabilities, multi-mode response, and nonlinearity (Tang et al., 2010; Maamer et al., 2019). The introduction of multi-mode response and nonlinearity will generally result in more complex design configurations compared with frequency tuning techniques. Energy harvesters with frequency tuning capabilities can usually maintain resonance over varying excitation frequencies, improving the energy harvesting performance. The coupling effect among the energy harvesting circuit (EHC), electromagnetic (EM) transducer, and mechanical part of the energy harvester makes classical impedance matching (IM) unsuitable. To optimize the output power, a unified impedance optimization theory is required. Furthermore, with this coupling effect, the energy harvester frequency can be effectively tuned through the electrical load of the EHC, known as electrical frequency tuning. For comparison, frequency tuning via mechanical approaches has also been explored. However, even considering the tuning approach, few

energy harvesters can cover the low-frequency range (<1 Hz). A vibration-based energy harvester with tunable low frequency is highly desirable, particularly for extracting energy from civil structural vibrations or ocean waves.

The aforementioned problems form the primary motivation for this thesis. This thesis proposes two strategies to address the aforementioned knowledge gaps: (i) leveraging of the strong coupling effects between the dual-function devices and controlled structures to achieve simultaneous vibration control and energy harvesting, and (ii) the use of frequency tuning techniques to realize broadband performance in pure (i.e., single-function) energy harvesters. Both strategies require a specific impedance-controllable EHC to provide the target resistance (equivalent damping) characteristics. To achieve functionality and performance enhancement using these two strategies, this thesis presents systematical studies, including modeling, optimization, design, numerical investigations, and practical applications.

1.2 Objectives

The major objectives of this thesis are twofold, aiming to enhance the functionality and performance of vibration-based energy harvesters. The first objective is to investigate the optimization of the dual-function devices, that is, vibration-based energy harvesters with structural vibration suppression functions. The specific tasks related to this objective are summarized as follows:

1. To model and design an EHC that provides controllable impedance characteristics according to the damping/harvesting requirement. This EHC and electromagnetic damper (EMD) jointly constitute a simple version of EHEMD.
2. To investigate the vibration control and energy harvesting performance of the EHEMD in two application cases, namely EHEMD as a passive energy-harvesting damper for a full-scale bridge stay cable, and EHEMD with an adaptive control strategy for high-

speed train (HST) secondary suspensions.

3. To analyze the structure–EHTMD or structure–EHTID coupled systems subjected to white noise excitation. The consistency between the objectives of vibration control and energy harvesting is analytically validated through a damped single-degree-of-freedom (SDOF) structure.

The second objective is to develop and investigate broadband vibration-based energy harvesters through frequency tuning approaches, including electrical and mechanical tuning. The specific tasks are as follows:

4. To develop a unified impedance optimization strategy for maximum output power and power efficiency. Such a strategy can be applied to several cases with different structural complexities, excitation types, and levels of electromechanical coupling effects. An energy harvester with broader bandwidth using electrical frequency tuning is numerically investigated.
5. To model and design a double-mass pendulum (DMP)–based EM energy harvester with tunable ultra-low frequency (<1 Hz) and to experimentally validate the impedance optimization theory by using the DMP-based harvester through shake table tests.
6. To examine the frequency tuning performance of a DMP-based point absorber in the wave flume tests. This DMP-based energy harvester is adopted as the vibration oscillator in the floating-point absorber.

1.3 Outlines

This thesis is divided into 10 chapters, and the thesis framework is given in Figure 1.1.

Chapter 1 introduces the motivations and main objectives of the thesis.

Chapter 2 reviews the literature on vibration-based energy harvesting. A general

picture is first painted in terms of energy transducer mechanisms and vibration sources. Then, comprehensive reviews on the dual-function devices and frequency-tuning broadband energy harvesters are provided.

Chapter 3 introduces the design principle and main characteristics of EMD and EHC. The designed EHC with a microcontroller unit (MCU) is introduced to realize controllable resistance (achieve the required damping characteristic). The impedance characteristic of the proposed EHC is verified through numerical simulations and circuit tests, and the corresponding damping feature of the EMD-EHC is presented through a cyclic test.

Chapter 4 presents a prototype of the EHEMD, and the corresponding lab test of this prototype applied to a 135 m full-scale bridge stay cable. The EHEMD is equivalent to a passive damper with an additional energy harvesting function. The vibration control and energy harvesting performance under different levels of harmonic excitation are evaluated.

Chapter 5 presents the numerical simulation of an HST with the EHEMDs installed in the secondary suspension. The feasibility of train speed–dependent adaptive control is investigated, and the corresponding performance is compared with the passive suspension.

Chapter 6 analyzes the structure–EHTMD coupled system with respect to damping and output powers by considering a linear SDOF structure. The consistency between energy harvesting and vibration control is illustrated analytically under white noise excitation, and the corresponding closed-form optimal parameters of the EHTMD are provided. The analysis is extended to the SDOF structure–EHTID coupled system considering different inerter-based networks. The effect of the inerter on the excitation power and output power is evaluated numerically.

Chapter 7 presents a unified overall impedance optimization strategy for the EHC to achieve the maximum output power and power efficiency, whereby the structural and electrical dynamics in vibration-based EM energy harvesters are considered. The proposed impedance optimization theory is verified through numerical simulation, and

the potential of frequency tuning for broader energy harvesting bandwidth using electrical load is also studied.

Chapter 8 introduces a specially designed DMP-based EM energy harvester with tunable ultra-low frequency. The mechanical frequency tuning of this device is realized by relocating the relative positions of the two masses. This chapter describes the shake table tests for the experimental validation of the unified overall impedance optimization in Chapter 7.

Chapter 9 presents the development of a floating-point absorber, realized by integrating the DMP-based energy harvester as an inside oscillating body. The energy harvesting performance considering the mechanical frequency tuning approach is evaluated under different wave periods and amplitudes in the wave flume tests.

Chapter 10 summarizes the main conclusions of this thesis. It discusses the limitations and challenges of the current study and provides suggestions for future work.

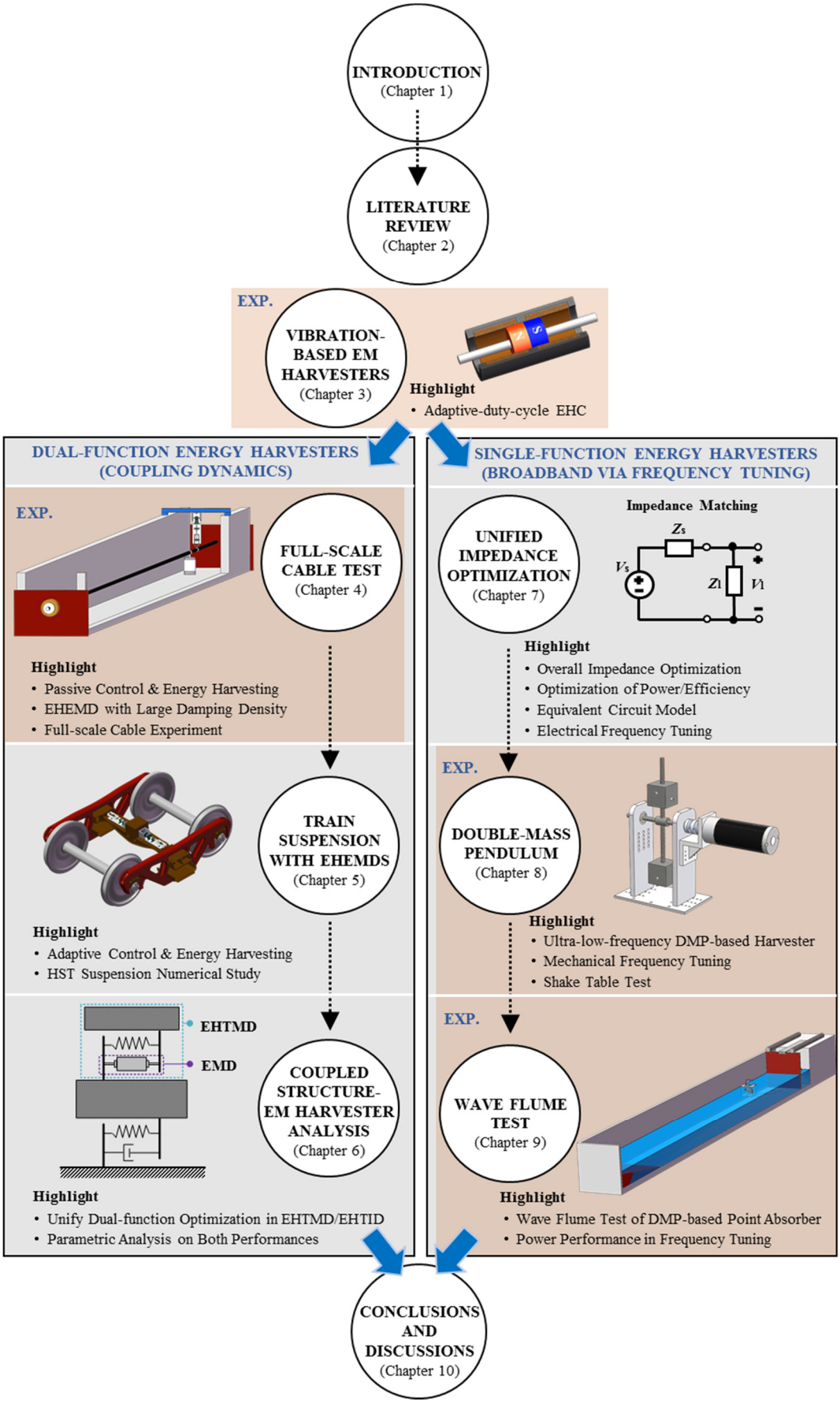

Figure 1.1 Framework of the thesis

CHAPTER 2

LITERATURE REVIEW

2.1 Vibration-based Energy Harvesting

Vibration-based energy harvesting, a technique for converting vibration energy into electrical energy, has attracted immerse research attention because of its wide application potential. Figure 2.1 shows the increasing trend of published studies related to vibration-based energy harvesters, and Figure 2.2 shows the corresponding distribution of these studies by country. Nearly 5,000 studies on this emerging topic have been published in over 10 countries. The following section provides a basic overview of vibration-based harvesting in terms of energy transduction mechanisms, vibration sources, energy harvesters integrated with vibration control function, and broadband harvesting designs.

A series of reviews on this topic from different perspectives has been published. Sodano et al. (2004) reviewed studies on piezoelectric energy harvesting from ambient vibrations. Anton and Sodano (2007) reviewed studies on piezoelectric vibration-based energy harvesting conducted between 2003 and 2006, including energy harvester geometry design and energy efficiency improvement. Safaei et al. (2018) summarized the development of these techniques from 2008 to 2018. Beeby et al. (2006) presented another early representative review on vibration-based energy harvesters from the perspective of microsystems using three different transduction mechanisms. Szarka et al. (2012) summarized the published techniques for power conditioning used in energy harvesting systems, focusing on power electronics and control concepts in the EHCs. Wei and Jing (2017) reviewed the design theory, modeling methods, and realization of

different transducers in vibration-based energy harvesting techniques. Siddique et al. (2015) and Iqbal et al. (2021) summarized the studies on vibration-based micro power generators and vibration-based applications in microsystems, respectively.

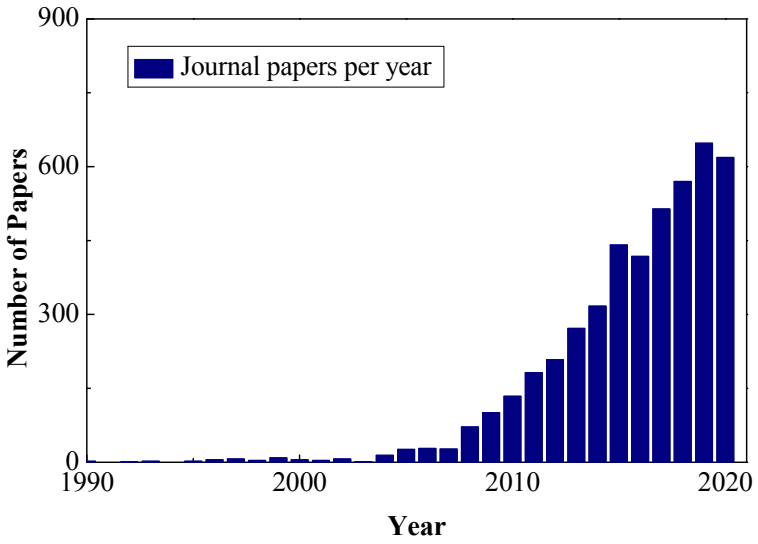

Figure 2.1 Number of papers published per year in the field of vibration-based energy harvesting (Scopus search keywords: "vibration" and "energy harvesting" or "energy regenerative")

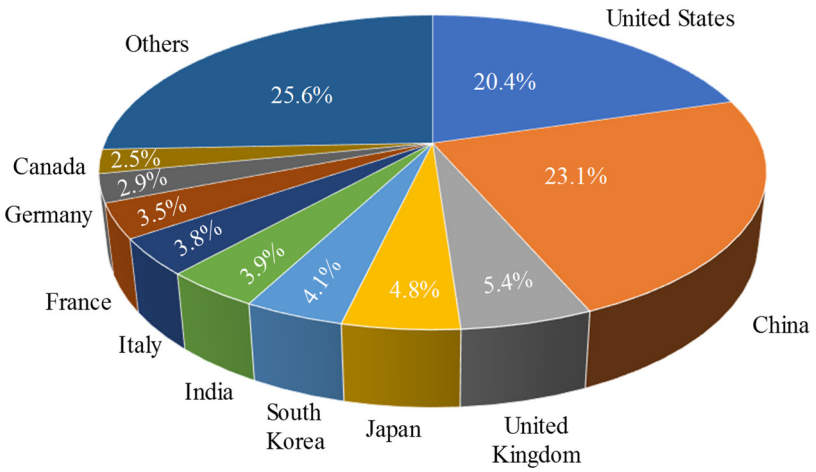

Figure 2.2 Distribution by country of papers on vibration-based energy harvesting

Regarding power improvement under variable-frequency or broadband excitations, Tang et al. (2010) reported the broadband techniques for vibration-based energy

harvesters before 2010. Harne and Wang (2013) summarized the development of bistable systems for vibration energy harvesting. Recently, Maamer et al. (2019) provided an updated review on the design improvements and techniques for vibration-based energy harvesters using piezoelectric or EM transducers.

Various sources of vibration energy have also been explored. Cai et al. (2020) illustrated the development of human motion–based wearable energy harvesters. Abdelkareem et al. (2018) reviewed the development of energy-regenerative suspension systems, summarizing the studies on the simulation, laboratory experimental, and field tests of such suspension systems. Chen et al. (2019) reviewed the application of piezoelectric materials in energy harvesters, sensors, and actuators for building structures. Regarding ocean wave–induced motions, Ahamed et al. (2020) conducted a review of wave energy converters (WECs) from the perspective of power take-off (PTO) mechanisms.

2.1.1 Energy Transduction Mechanisms

A typical configuration of vibration-based energy harvesters is a linear or nonlinear oscillator, in which the damping power can partially be converted into electrical energy through appropriate energy transducers, such as piezoelectric, EM, and electrostatic transducers (Figure 2.3). In some scenarios, an energy transducer with an EHC can directly form a vibration-based energy harvester, such as the EHEMD proposed by Zhu et al. (2012). These two configurations are differentiated in Chapter 3.

2.1.1.1 Piezoelectric Transducer

Piezoelectric transducers can transform mechanical strain into electrical charge, which is known as the piezoelectric effect (Sodano et al., 2004). A common setup is to mount piezoelectric transducers onto a cantilever beam with a proof mass attached at the free end to take advantage of the high strain characteristic of this beam structure (Park et

al., 2008). Figure 2.4 presents a typical cantilever beam with a bimorph-form piezoelectric material, as suggested by Roundy and Wright (2004). Arms et al. (2005) investigated the feasibility of powering a wireless sensor by using this beam-type piezoelectric energy harvester and obtained ~2 mW of power at a strain level of ~200 με. Peigney and Siegert (2013) performed an in-situ test on an in-service bridge subjected to traffic-induced excitation and harvested approximately 0.03 mW of power. Furthermore, Xie et al. (2014a) used such a beam-type piezoelectric energy harvester as a WEC and reported up to 0.55 W of power in numerical simulations of sea wave excitations.

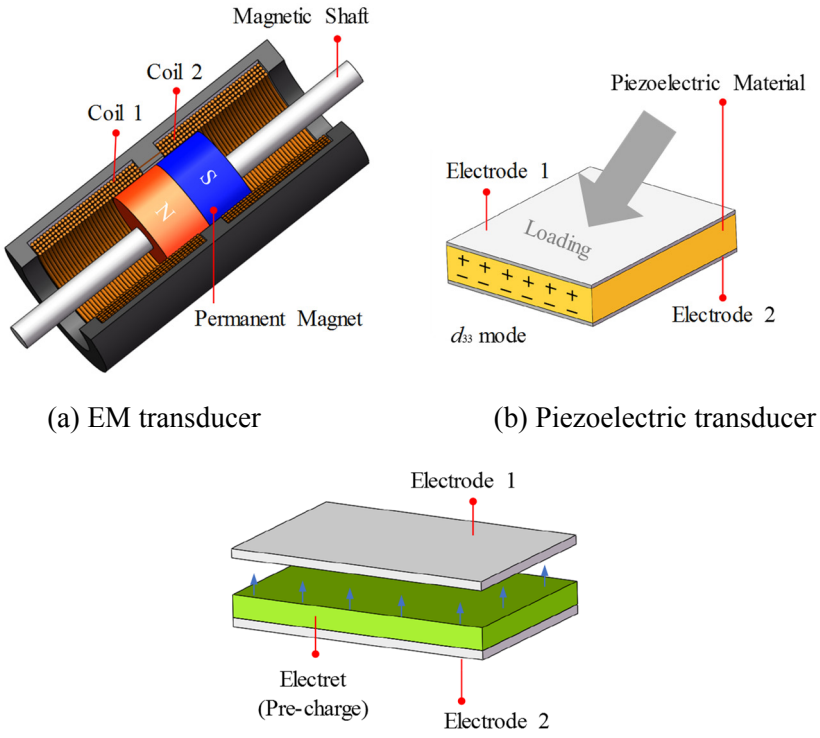

(a) EM transducer (b) Piezoelectric transducer

(c) Electrostatic transducer

Figure 2.3 Three main types of energy transducers

However, the high operational frequency and high output impedance characteristics of piezoelectric materials result in unexpectedly low output power, particularly when applied to civil structures that typically vibrate at low frequencies. Moreover, the characteristic that piezoelectric materials accept large stress but have a small strain limits their large-scale implementations (Lefeuvre et al., 2007).

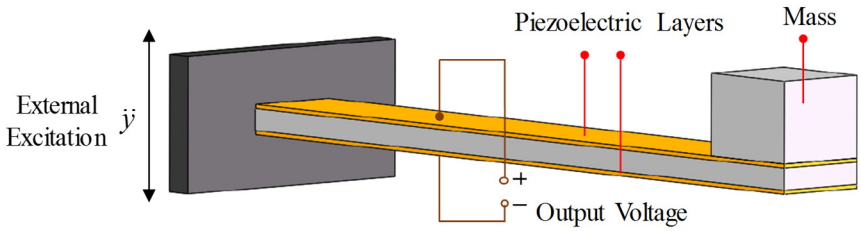

Figure 2.4 Beam-type piezoelectric energy harvester

2.1.1.2 EM Transducer

Electromagnetic induction can also convert mechanical vibration energy to electrical energy. The relative motion between the magnets and coils in an EM transducer results in voltage generation following Faraday's law. A common design of EM transducer–based energy harvesters is a linear SDOF oscillator inside a housing (Williams and Yates, 1996) that is essentially an inertial device (Figure 2.5). Rome et al. (2005) developed a suspended-load backpack using an EM transducer; the backpack could generate up to 7.4 W of power from the normal walking motion of humans, approximately 300 times the power generated by the energy-harvesting shoes presented by Shenck and Paradiso (2001). Zuo and Tang (2013) summarized a series of large-scale applications of EM transducers for generating energy from tall buildings, vehicle systems, long bridges, railroads, and ocean waves. Shen (2014) highlighted the potential of using EM transducers to realize energy harvesting and vibration control in civil structures and tested their feasibility in high-rise buildings and bridge stay cables.

Compared with piezoelectric transducers, EM transducers have better applicability in high-power, large-scale, and low-frequency conditions. Moreover, during the conversion from vibration energy to electrical energy, an accompanying controllable damping effect is provided to the vibration source/oscillator, which is an appealing point from the perspective of vibration control (Shen, 2014; Loong, 2020). One notable problem of small EM energy harvesters is their low output voltage (Yildiz, 2009). To

some extent, the machine constant (also known as the EM coupling effect) and the power performance depend on the EM transducer size (Beeby et al., 2007). Thus, EM transducers might not be an appropriate solution for scenarios with space or weight limitations.

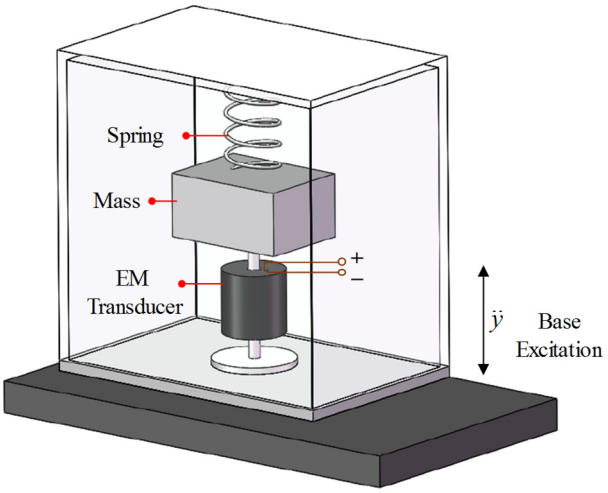

Figure 2.5 Example of an EM energy harvester

2.1.1.3 Electrostatic Transducer

A representative configuration of electrostatic energy harvesters is a linear mass-beam system in which a pre-charged electret layer or a bias voltage is employed (Guo et al., 2020), as shown in Figure 2.6. When the mass vibrates along with the vibration source, the change in either the overlapping area or the distance between the two plates results in capacitance variation, and electrical current is generated. Electrostatic energy harvesters are typically intended for high-frequency vibrations, and their output power is extremely low (only at the microwatt level). Their small size is a vital feature, given their compatibility with microelectromechanical technology. The following results have been reported: output power of 1.0 μW at an acceleration of 2 g with 63 Hz (Suzuki et al., 2010), output power of 0.15 μW at an acceleration of 1 g with 93 Hz (Wang and Hansen, 2014), and output power of 20.7 μW at an acceleration of 2 g with 110 Hz (Chiu and Lee, 2013).

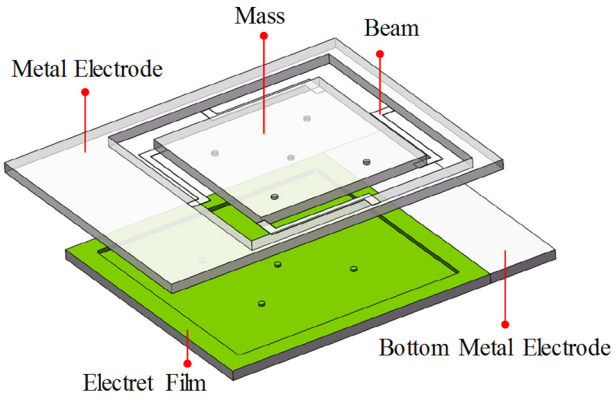

Figure 2.6 Example of an electrostatic energy harvester

2.1.1.4 Comparisons

Different types of transducers have their own merits and practical limitations. Table 2.1 compares the pros and cons of the three aforementioned transduction mechanisms from the perspective of energy harvesting.

Piezoelectric and electrostatic transducers are preferable in microscale energy harvesters and can be integrated into diminutive electronic devices due to their compatibility with microelectromechanical technology. Meanwhile, piezoelectric and electrostatic energy harvesters typically require high vibration frequencies for effective output performance. Compared with piezoelectric and electrostatic energy harvesters, EM transducers can be more easily scaled up and are more suitable for large-scale low-frequency vibration applications, such as harvesting energy from the vibration of civil structures (from 0.1 to 10 Hz) and ocean WECs (from 0.1 to 1 Hz).

Piezoelectric and EM transducers have large energy densities (Zuo and Tang, 2013). In particular, they have the potential to serve as vibration control units in applications where vibration mitigation is another main concern (Zhu et al., 2012; Tang, 2013; Loong, 2020; Xie et al., 2013). As shown in Section 2.2, most of the previous studies on dual-function devices enabling simultaneous vibration control and energy harvesting were based on the utilization of EM or piezoelectric transducers.

Table 2.1 Comparison of different energy transducers in vibration-based energy harvesting

Transducer type	Electromagnetic	Piezoelectric	Electrostatic
Harvesting principle	EM induction	Piezoelectric effect and electrostatic induction	Electrostatic induction
Impedance type	Resistive	Capacitive	Capacitive
Practical maximum energy storage density (mJ/cm^3)	24.8	35.4	4
Pros	• High output current, power, and efficiency • Easy to scale up • High durability • Low output impedance • Tuning is possible at low, medium, and high vibration levels	• Easy to scale down to nanoscale • Simple structure on a small scale • High coupling coefficient • High output voltage	• Lightweight • Very high output voltage • Easy for frequency tuning • Competitive in its compact size • Compatibility with microelectromechanical technology
Cons	• Heavy magnet required • Low voltage for small-scale devices	• Low output current and efficiency • Pulsed output • High matched impedance • Brittle • Low strain limit	• Pre-charge required • Low output current • High matched impedance • High resonant frequency required

Note: The information and data are from the reports by Wang (2017), Park et al. (2019), and Siddique et al. (2015).

The electromechanical coupling coefficient of a transducer governs the energy harvesting efficiency and vibration control performance. According to Elliott and Zilletti (2014), the coupling coefficients of EM transducers are larger than those of piezoelectric transducers in large-size actuators (>10 kg). Thus, EM transducers might be a more suitable candidate than piezoelectric transducers for large-size dual-function devices in large-scale structures, although previous studies have also demonstrated the feasibility of integrating piezoelectric transducers into conventional damper systems to harvest vibration energy.

2.1.2 Vibration Energy Sources

Various vibrations, including the vibration of vehicle suspensions; railway tracks excited by passing vehicles; civil structures excited by wind, waves, earthquakes, and other dynamic loads; human motions; and ocean waves, are considered potential sources for energy harvesting (Figure 2.7).

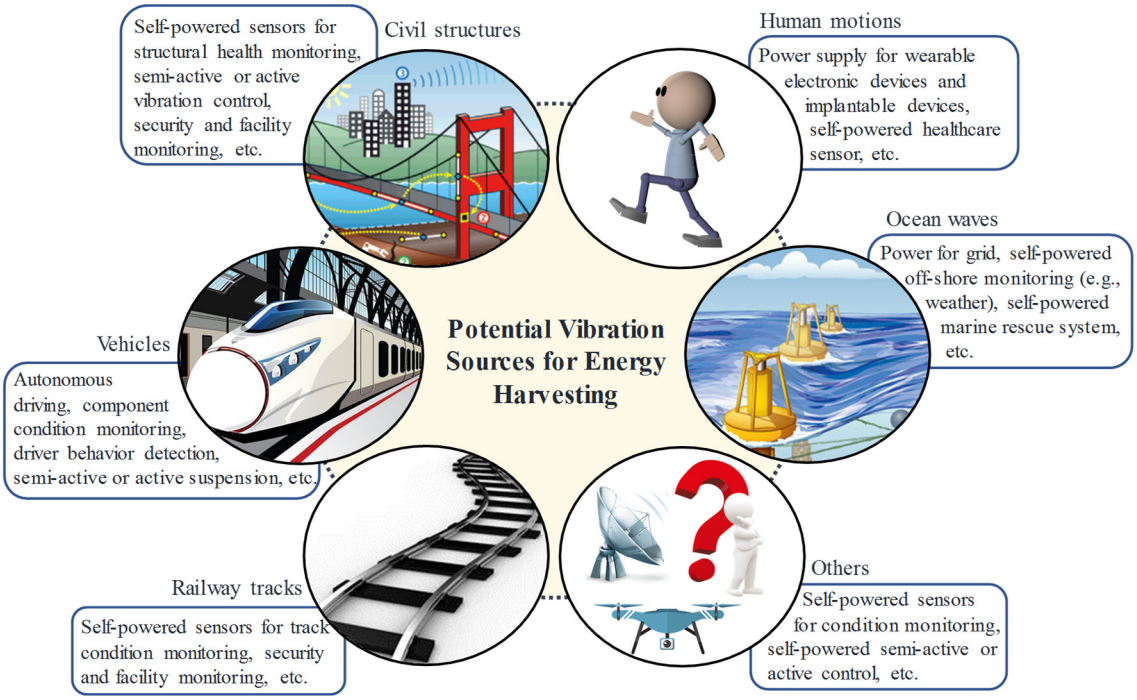

Figure 2.7 Potential vibration sources for energy harvesting

2.1.2.1 Railway Tracks

The vibration of railway tracks excited by passing trains is a promising energy source with a typical frequency of 0.6–1.8 Hz and a deflection amplitude range of 3.2–6.6 mm (Zuo and Tang, 2013). Nelson et al. (2008) were the first to explore the feasibility of harvesting energy from passing train–induced railway track vibrations by using EM and piezoelectric transducers, and their field tests showed that average output powers of 4 and 0.053 mW could be obtained through the two approaches, respectively. Later, aiming to enhance the energy harvesting performance, they successively prototyped three different EM energy harvesters to be mounted between two rail ties in consideration of different

transmission mechanisms or integration with a hydraulic motor (Nelson et al., 2009; Hansen et al., 2010; Pourghodrat, 2011). Wang et al. (2013) designed a single-shaft mechanical motion rectifier (MMR) that can transform train-induced pulse-like bidirectional linear vibration into unidirectional rotational motion and reported that the MMR could improve the efficiency of an EM track harvester. Their designed prototype could power two 50 W–rated power light bulbs in the cyclic test with an excitation amplitude of 3 mm at 1 Hz. Zhang et al. (2016, 2017) reported a portable track energy harvester based on an MMR mechanism similar to that described above (Figure 2.8) and achieved an efficiency of 55% and peak voltage of 58 V in the harmonic input. Recently, Lin et al. (2018) conducted a field test by using an MMR track harvester and reported an average power of 7 W when a train traveled at 64 km/h. Different from the above strategies that directly utilized track deflection response, Gatti et al. (2016) explored the potential of using an SDOF EM oscillator to harvest energy from the passing train–induced vibrations of a railway sleeper.

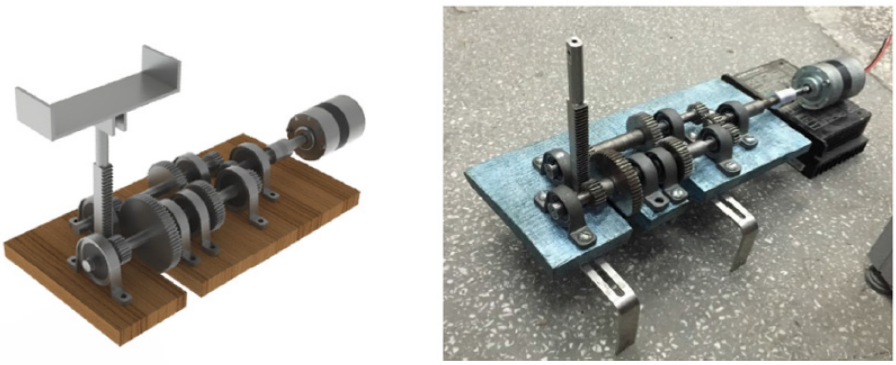

(a) Overview (b) Prototype

Figure 2.8 Energy harvester based on rail track vibration (Zhang et al., 2016) (Reused with permission from Elsevier.)

Piezoelectric energy harvesters have also been explored for railway track systems. Wang et al. (2015) proposed two different theoretical models of piezoelectric energy harvesters, namely patch-type and stack-type, to be mounted at the bottom of a rail track. Wischke et al. (2011) compared the vibration levels of different locations in a rail track

system and reported that the railway sleeper exhibited sufficient vibration to be considered as a potential energy source for piezoelectric harvesters. A field test was subsequently conducted, and the harvested energy successfully powered an MCU. Yuan et al. (2014) proposed and modeled a piezoelectric drum energy harvester mounted at a sleeper bottom. Its effectiveness was validated through the simulation results of a real track: a root-mean-square (RMS) power of 100 mW was generated, and through a 1:10 scale track rig test with a single wheel: an RMS power of 0.1 mW at a wheel speed of 0.5 km/h was generated. The comparison of EM and piezoelectric energy harvesters indicates that the former generates relatively greater watt-level output power.

2.1.2.2 Ocean Waves

Ocean waves represent an appealing and benign option because of their high availability, good predictability, and high energy density (estimated: 2–3 kW/m^2) (Falnes, 2007; Tollefson, 2014; Wang et al., 2015; Viet and Wang, 2018). Falcão (2010) provided a comprehensive overview of the development history and status of WEC systems. Sarmento (2004) summarized nontechnical barriers to the commercialization of large-scale WECs. However, ocean wave energy conversion technologies are still in their infancy thus far.

A representative type of WECs is the point absorber; this has a size smaller than the sea wavelength, and a large number of them can be connected in an array. Point absorbers capture the power from the heave, surge, pitch, or combination of these wave modes through transducers and transmission systems, which are called PTO systems. Liang et al. (2017) developed an EM point absorber with an MMR system operating in heave mode (Figure 2.9) and verified its effectiveness through an ocean field test with an average output power of approximately 21 W. They subsequently designed a self-reacting WEC based on a similar PTO system and tested it in a wave tank (Li et al., 2020). Although the majority of existing point absorbers operate in heave mode, the potential power embodied

in pitch and surge motions is twice that in heave motions (Chaplin and Aggidis, 2007). Pecher and Kofoed (2017) pointed out that pitch and surge motions are favorable for large floating WECs. Babarit et al. (2005) and Pozzi (2018) proposed SEAREV and PeWEC point absorbers, respectively, which operated in surge–pitch mode and used EM generators to realize energy conversion. Thus far, several commercially available EM point absorbers have been reported and tested in practical sea environments; an example is the Smart Power Buoy, with a rated power of 0.3 kW (Resen Waves Company, 2020).

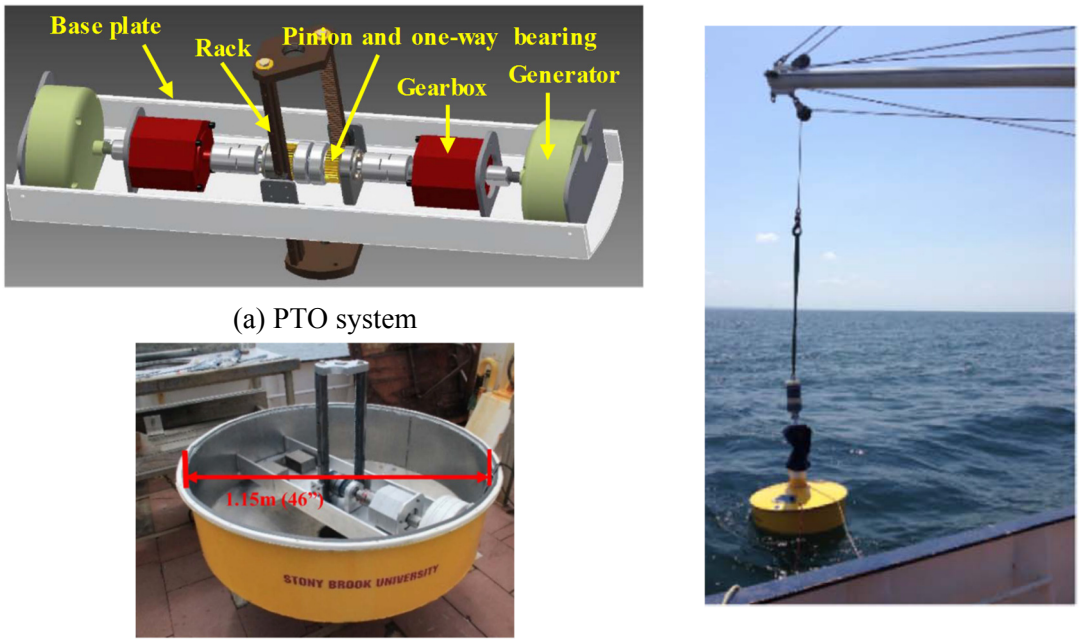

(a) PTO system

(b) Prototype

(c) Field test

Figure 2.9 EM point absorber with MMR (Liang et al., 2017) (Reused with permission from Elsevier.)

The research and development of piezoelectric floating harvesters are mainly in the simulation stage. Burn (1987) designed a floating harvester in which an array of piezoelectric films was connected between a semi-submerged plate and the anchor fixed to the seabed. The buoy heave motion–induced alternate tension and compression in the piezoelectric films had the potential to generate power. Since then, various configurations of piezoelectric floating energy harvesters have been investigated to improve the output performance. Murray and Rastegar (2009) presented a piezoelectric energy harvester for

buoys, in which the interaction with ocean waves was used to excite an array of metal plates with piezoelectric layers. The simulation results showed that average power ranging from 60 to 180 mW could be absorbed by a buoy with a diameter of 3 in. Wu et al. (2015) reported an energy-harvesting buoy, to which several piezoelectric coupling cantilevers were attached. Up to 24 W (RMS power) could be harvested, given that the lengths of the buoy and cantilevers were 20 and 1 m, respectively. Viet et al. (2016) proposed a pitch-type piezoelectric energy harvester with two levers used to amplify the excitation force acting on the piezoelectric material, thus improving the energy harvesting performance. Watt-level power could be harvested in the simulation.

2.1.2.3 Human Motions

Starner and Paradiso (2004) reviewed the potential of harvesting energy from different human activities and reported that the available energy from human body motions, such as walking, is much larger than that from blood pressure and respiration. Since then, energy harvesters based on different transducers have been developed and typically integrated into articles of daily use to capture power from human motions. A well-known device is the previously mentioned energy-harvesting backpack with an internal EM transducer, which required a payload of 38 kg (Rome et al., 2005). Xie and Cai (2015) developed a backpack-based device that could harvest part of the human kinetic energy generated during walking and simultaneously mitigate the accelerative load on the bearer. With a load of 30 kg, the proposed device could produce 6–10.6 W of power at a walking speed of 5.5 km/h, which represents higher efficiency than the device by Rome et al. (2005). Saha et al. (2008) presented an EM energy harvester integrated into a rucksack and harvested power ranging from 0.3 to 2.46 mW during walking and slow running without a payload.

Designing EM energy harvesters with improved power performance for low-frequency human motions is another research direction. Samad et al. (2015) presented a

curved EM system that was superior to other straight energy harvesters working only in a single vibration direction. When installed on a human hand, it generated an average power of 5.2 mW at walking (running) speeds of 0.744–1.86 m/s. Fan et al. (2019) reported an EM energy harvester using a string-suspended and driven rotor. The harvester converted low-frequency vibration to either the rapid rotation motion or high-frequency small twisting vibration of the rotor. The experiment, in which the energy harvester was fixed upside down on a human thigh and the pendant was pulled via a string tethered to a waist belt, delivered an average power of 4.9 mW. Halim et al. (2018) proposed an EM energy harvester with a sprung eccentric rotor structure, tested its effectiveness through a series of pseudo-walking motions, and realized maximum output power at a swing of 1 Hz.

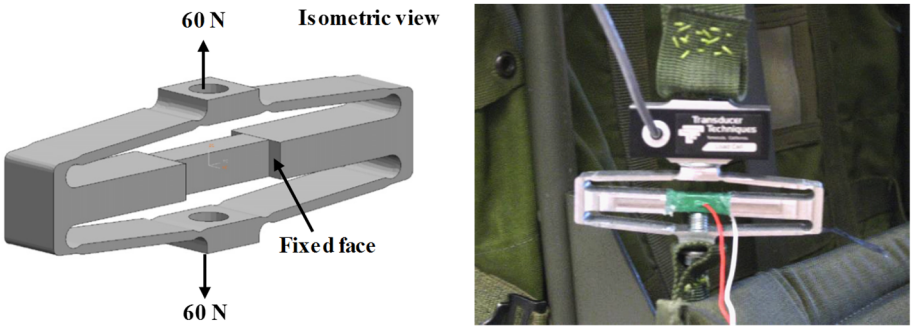

(a) 3D model (b) Prototype

Figure 2.10 Backpack energy harvester with a piezoelectric material stack (Feenstra, 2008)

(Reused with permission from Elsevier.)

Feenstra (2008) replaced the strap buckle of a backpack with a piezoelectric material stack and obtained approximately 0.4 mW of power by measuring the differential force between the wearer and the backpack. The corresponding model and prototype are shown in Figure 2.10. Platt et al. (2005) explored the feasibility of energy harvesting based on piezoelectric materials integrated into knee replacement units. An experiment was performed on a knee replacement model by applying an axial force amplitude of 2.6 kN, and a regulated power of 0.85 mW was obtained. Shenck and Paradiso (2001) embedded

the piezoelectric material into a shoe insole and obtained a peak and average power of 60 and 1.8 mW, respectively, during human walking. These studies have revealed that when no payload was used, the harvested power from human motions was typically low, mostly at the milliwatt level (Zhou et al., 2018; Cai et al., 2020).

2.1.2.4 Vehicles

Traveling vehicles experience vibrations excited by road or track surface roughness and thus have also been investigated as a potential energy source. Using the finite element method, Bayik et al. (2014) simulated the performance of a piezoelectric patch–based energy harvester mounted on the back panel of the cabin of a heavy-duty vehicle. The model predicted an output power of 0.5 μW under a moving operational condition for the 26.6 Hz vibration mode of the back panel. Akkaya (2020) developed a piezoelectric energy harvester installed outside a vehicle to utilize the airflow around a moving vehicle. The maximum output energy was 1.125 mJ when the vehicle traveled at 110 km/h.

A common strategy is to install energy harvesters in vehicle suspensions that experience excessive vibrations. Tavares and Ruderman (2020) conducted a feasibility study on harvesting vibration energy from a piezoelectric transducer installed in a suspension. They estimated an average power of 1.747 mW through numerical simulations of a classical quarter-car suspension (2DOF model) under poor road conditions. Lafarge et al. (2018) proposed the use of a piezoelectric cantilever beam in a vehicle suspension to realize energy harvesting. An in-situ test at traveling speeds of 10 and 30 km/h was conducted, and output power values ranging from 0.001 to 0.021 mW and from 0.01 to 0.07 mW were observed, respectively.

Lee and Choi (2014) installed the piezoelectric material in a vehicle tire and obtained an energy of 380.2 μJ per revolution under a load of 500 kgf and speed of 60 km/h. Xie and Wang (2015a) presented a similar concept of installing the piezoelectric material in a

tire, and their numerically predicted RMS output power of 42.08 W was considerably higher. Figure 2.11 shows a sketch of the piezoelectric tire-energy harvester and the simulated car model.

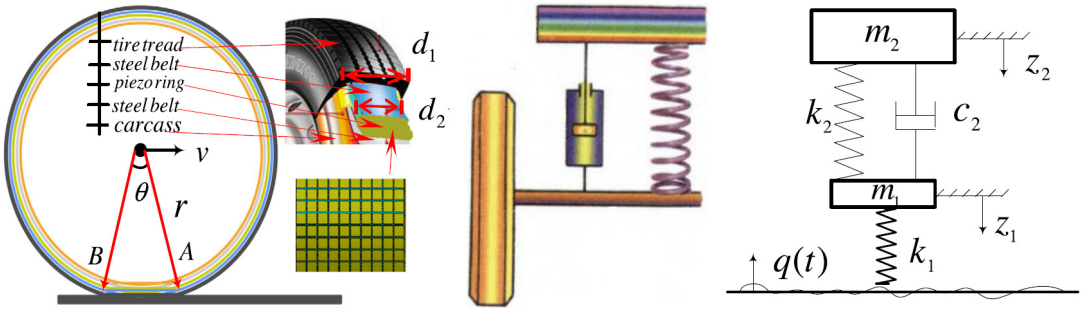

(a) Piezoelectric tire model (b) Quarter-car model

Figure 2.11 Sketch of the piezoelectric tire model and simplified car model (Xie and Wang, 2015a) (Reused with permission from Elsevier.)

The application of EM transducers in suspensions typically forms energy-regenerative suspensions with simultaneous vibration control and energy harvesting functions. Relevant technological developments are reviewed in Subsection 2.2.3.1.

2.1.2.5 Civil Structures

A large number of civil structures subjected to frequent dynamic excitations represent another type of promising and widely available energy source. Sazonov et al. (2009) proposed to power wireless sensors by using an EM generator that can harvest the vibration energy of a bridge induced by passing traffic. They observed a peak power of 12.5 mW at a low excitation frequency of 3.1 Hz. Field tests demonstrated the feasibility of this self-powered wireless sensor system. Jung et al. (2011a) explored the feasibility of harvesting stay cable vibration energy by using an EM energy harvester. A shake table test was performed using the measured acceleration in a real stay cable as the excitation input, and the RMS output power was 27.14 mW under an RMS input acceleration of 74.8 mg. Later, the researchers applied a rotational spring to reduce the static deflection of the spring element, considering the cable inclination. A field test on the full-scale cable

showed that the RMS power was 0.09 mW when the cable acceleration was 17.7 mg; the low power was mainly due to the low machine constant and frequency mismatch (Jung et al., 2012). Kim et al. (2013) further modified their designs by introducing a rotation generator to form a pendulum-based energy harvester. The corresponding field test results showed an average power of 2.60 mW under an RMS cable acceleration of 27 mg.

Cahill et al. (2014) investigated the feasibility of using a piezoelectric energy harvester to harvest energy from passing train–induced bridge vibration and thus power wireless sensors. Their numerical results demonstrated that 588 μW and 24.1 μW could be harvested for passenger and freight trains, respectively. Later, they conducted a field test with a piezoelectric energy harvester on a bridge over which trains passed. They assessed the frequency characteristics based on the harvested energy signal and simultaneously realized monitoring and energy harvesting functions (Cahill et al., 2018).

Table 2.2 summarizes the aforementioned single-function EM and piezoelectric energy harvesters from the perspective of vibration sources. The table is shaded with different colors to distinguish between experimental and numerical studies.

Table 2.2 Survey of the single-function energy harvesters from the perspective of vibration sources

Vibration source	Transducer	Output power (W)[1]	Test		References
			Type	Condition(s)	
Railway track	EM	4×10^{-3}	Field test	10–12 mph (train speed)	Nelson et al., 2008
	Piezoelectric	5.3×10^{-5}	Field test	15 mph (train speed)	
	EM	0.4–3.9	Material testing system (MTS) test	0.25–0.75 in	Nelson et al., 2009
	EM	0.22	Field test	11.5 mph (train speed)	Hansen et al., 2010
	EM	0.5–11.08	MTS test	2.75–3.75 mm, 0.375 Hz	Pourghodrat, 2011
	EM	8.2–47	MTS test	3–5 mm, 1–5 Hz	Wang et al., 2013
	EM	55% (Eff.)	MTS test	6 mm, 1–2 Hz	Zhang et al., 2016
	EM	38–58 V	MTS test	2.5 mm, 0.5–1 Hz	Zhang et al., 2017
	EM	3.5–6.9	Field test	64 km/h (train speed);	Lin et al., 2018
	EM	0.25 J/kg	Sleeper, Inter-city 125 train	195 km/h	Gatti et al., 2016
	Piezoelectric	0–11.6 V, 0–23.36 V	Fatigue testing machine	4 mm, 4 Hz	Wang et al., 2015
	Piezoelectric	395 μJ/train	Field test	\	Wischke et al., 2011
	Piezoelectric	0.55×10^{-4}–1×10^{-4}	1:10 scale track rig test	0.5 km/h (load speed)	Yuan et al., 2014
Human motion	EM	7.4	Normal walking	38 kg load	Rome et al., 2005
	EM	6–10.6	Walking	30kg load, 5.5 km/h	Xie and Cai, 2015
	EM	0.3×10^{-3}–2.46×10^{-3}	Walking and slow running	≈ 0.5 g, 2 Hz for walking; ≈ 1 g, 2.75 Hz for slow running	Saha et al., 2008
	EM	5.185×10^{-3}	Walking (running)	0.744–1.86 m/s	Samad et al., 2015
	EM	0.0159, 0.0049, 0.0034	Hand pulling, leg shaking, arm swinging	\	Fan et al., 2019
	Piezoelectric	0.329×10^{-3}–1.939×10^{-3}	Walking	0.9–1.3 m/s	Feenstra, 2008
	Piezoelectric	8.5×10^{-4}	Force excitation	2600 N	Platt et al., 2005
	Piezoelectric	8.4×10^{-3}	Walking	0.9 Hz walking pace	Shenck and Paradiso, 2001

Ocean wave	EM	21	Field test	\	Liang et al., 2017
	EM	2.61	Wave tank test	Irregular wave	Li et al., 2020
	EM	\	Wave tank test	\	Pozzi, 2018
	EM	0.0003	Field test	\	Toh et al., 201
	Piezoelectric	0.06–0.18	\	1–11.5 m (wave height)	Murray and Rastegar, 2009
	Piezoelectric	24	\	3 m (wave height), 80 m (wave length), 40 m (sea depth)	Wu et al., 2015
	Piezoelectric	103	\	2 m (wave height), 6 s (wave period)	Viet et al., 2016
	Piezoelectric	55 (RMS)	\	2 m (wave height), 15 m (wave length), 3 m (sea depth)	Xie et a., 2014a
Vehicle	Piezoelectric	1.125 mJ	\	110 km/h	Akkaya, 2020
	Piezoelectric	0.001747	\	Poor road condition	Tavares and Ruderman, 2020
	Piezoelectric	0.00001–0.00007	\	30 km/h	Lafarge et al., 2018
	Piezoelectric	380 μJ	\	500 kgf load, 60 km/h	Lee and Choi, 2014
	Piezoelectric	5×10^{-5}	\	Moving condition, 26.6 Hz	Bayik et al., 2014
	Piezoelectric	42.08 (RMS)	\	40 m/s	Xie and Wang, 2015a
Civil structure	EM	0.0125 (Peak)	Field test	Vehicle passes bridge	Sazonov et al., 2009
	EM	0.00046–0.02714 (RMS)	Shake table test	13.6–74.8 mg RMS acceleration	Jung et al., 2011a
	EM	9×10^{-5} (RMS)	Field test	17.7 mg RMS acceleration	Jung et al., 2012
	EM	2.1×10^{-3}–0.0203	Field test	34–160 mg RMS acceleration	Kim et al., 2013
	Piezoelectric	\	Field test	Train passes bridge	Cahill et al., 2018
	Piezoelectric	2.41×10^{-8}–5.88×10^{-7} (RMS)	\	Freight train or passenger train passes bridge	Cahill et al., 2014

Note: 1. The output power in this table might be a bit overestimated because some of the studies regarded the power dissipated by the load resistor as the output power.

2. White background: experimental investigations; shaded background: numerical investigations.

2.2 Dual-function Devices Enabling Simultaneous Energy Harvesting and Vibration Control

2.2.1 What are Dual-function Devices?

Many structural vibration control techniques rely on the energy dissipation mechanism, which is essentially a process that converts structural vibration energy into other energy forms (e.g., heat). The energy conversion mechanism is also the predominant feature of all energy harvesters. In their large-scale implementations installed in structures, vibration-based energy harvesters inevitably modify the dynamics of the structures as a result of extracting a considerable amount of vibration energy from structures. The common ground they share serves as a natural motivation for the integration of vibration-based energy harvesting and structural vibration control functions.

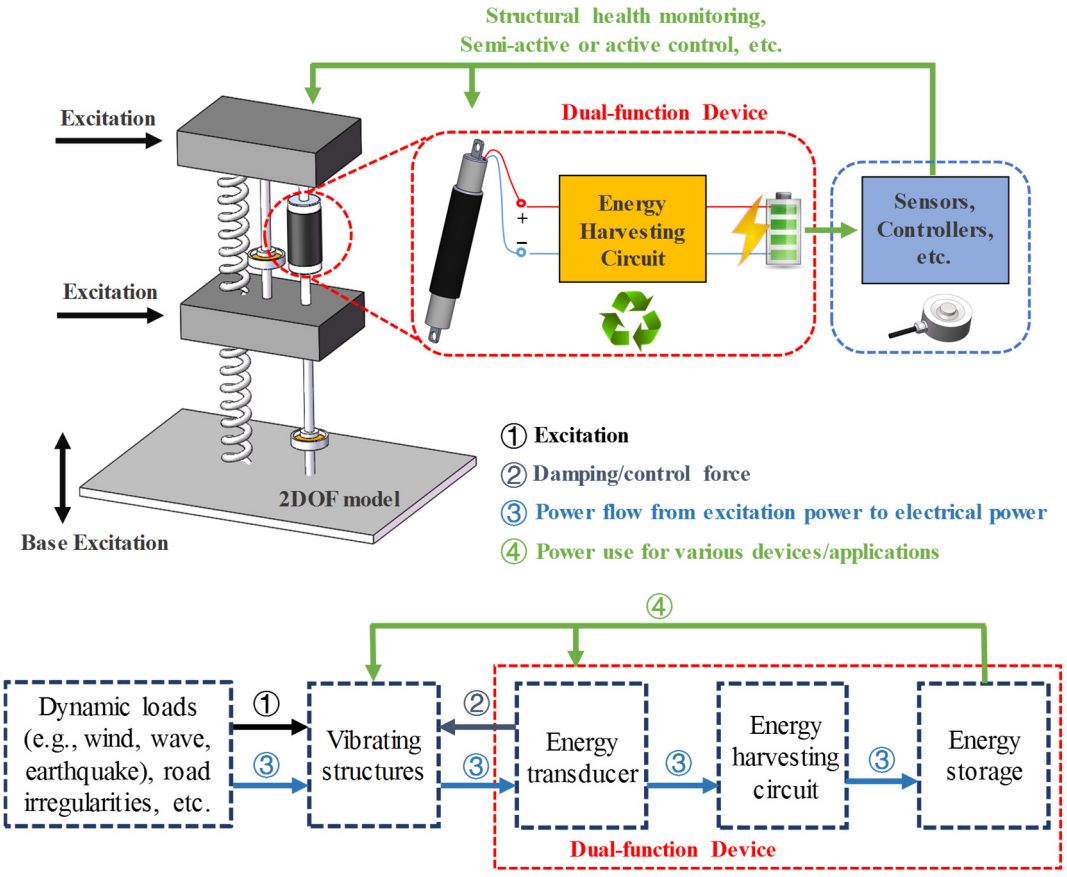

Figure 2.12 General concept and application of a dual-function device

Figure 2.12 presents the general concept and application of dual-function devices. The 2DOF model is a simplified configuration representing the general structure as a potential vibration source. The navy line shows the damping force provided by the dual-function device to the structure (i.e., vibration source), whereas the light blue line shows the power flow from the structural vibration energy to electrical energy converted by the dual-function device that simultaneously provides vibration control and energy harvesting functions. The green line indicates two potential applications of using the harvested power.

The concept of integrating the energy harvesting function into traditional vibration control devices/dampers is appealing due to the following aspects: (1) it justifies the use of large-size energy transducers that are required anyway by the vibration control purpose; (2) the harvested energy is typically comparable to the vibration energy of the host structures, which is usually higher than those of the traditional microscale energy harvesters by orders of magnitude; and (3) the harvested energy can directly supply the energy consumed by sensors, controllers, and other control devices in vibration control systems, which easily justifies the need for and application scenarios of these energy harvesters. Given these aspects, the concept of a self-powered control system (either semi-active or active) also becomes feasible. Although the energy storage of this system is limited owing to the direct usage of the harvested power, dual-function devices play a key role in such a system.

Although many studies on dual-function devices enabling simultaneous energy harvesting and vibration control focused on vehicle suspensions, the potential applications of these devices in other large-scale structures have increasingly elicited interest from civil, mechanical, and electronic engineers in recent years. Figure 2.13 shows several representative applications of dual-function devices in vehicle suspensions, seismic base isolators, tuned mass dampers (TMDs) in structures, and bridge stay cables.

These dual-function devices are often referred to as energy-harvesting dampers, energy-regenerative dampers, or energy-regenerative shock absorbers. Although sometimes used interchangeably, “energy regeneration” and “energy harvesting” have slightly different meanings. The former refers to the reuse of the leftover energy that is part of supplied power but is traditionally wasted to improve power efficiency; the latter refers to the capture of power from the ambient environment to achieve a positive energy gain (e.g., wave energy harvesting). In this regard, “energy regenerative” and “energy harvesting” dampers are often used in the automotive industry and civil structures, respectively. However, for consistency, this thesis adopts the words “energy harvesting” to describe all dual-function devices.

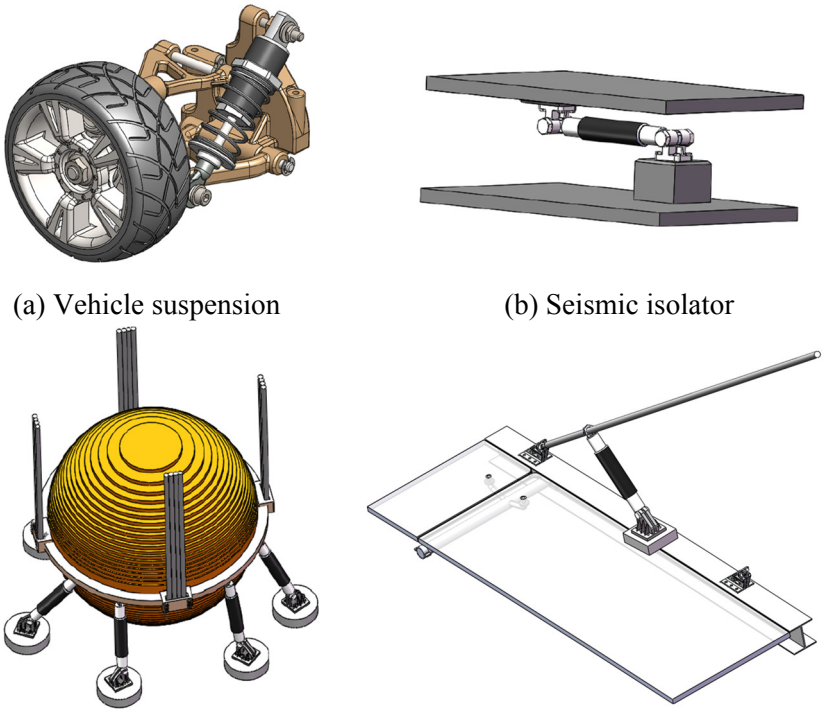

(a) Vehicle suspension (b) Seismic isolator

(c) TMD in a structure (d) Stay cable

Figure 2.13 Representative applications of the dual-function dampers

EM and piezoelectric transducers have been applied for energy conversion in dual-function devices. However, the former type is often preferable in large-scale implementations owing to its relatively large coupling coefficient and output force.

Exploration of the latter type remains relatively limited to date.

The number of publications per year on this topic has increased exponentially over the last decades, as illustrated in Figure 2.14. A comparison of Figures 2.1 and 2.14 indicates that approximately 15% of the studies on vibration-based energy harvesters are related to the dual-function concept.

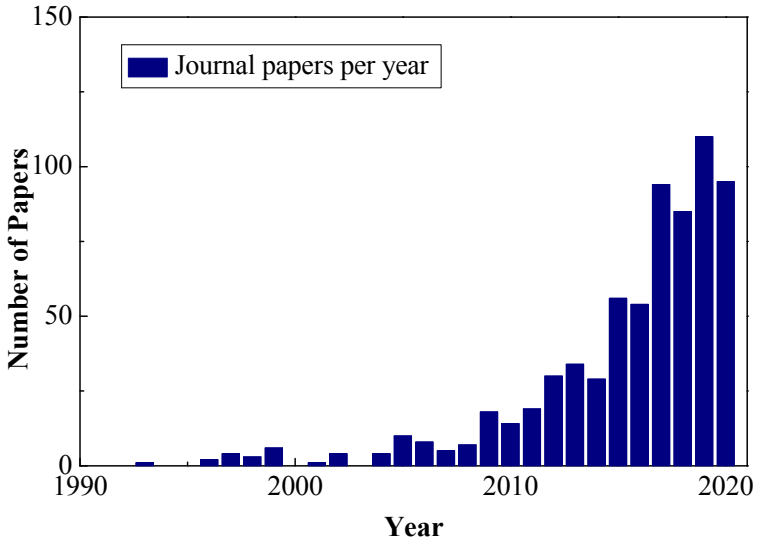

Figure 2.14 Trend of papers in energy-harvesting vibration control (Scopus search keywords: "vibration" and "control" and "energy" and "regenerative" or "harvesting")

2.2.2 Hybrid Energy-harvesting Dampers

Hybrid energy-harvesting dampers fulfill the dual functions using a combination of two separate units: energy harvesting and conventional damper units. The former can supply power to the latter and thus make conventional dampers (e.g., magnetorheological (MR) and hydraulic dampers) highly reliable and energy-saving. In this hybrid strategy, EM transducers are commonly used to generate electrical energy, whereas the damping/control effect is mainly contributed by another type of conventional damper.

2.2.2.1 Hybrid MR Dampers

Cho et al. (2005) integrated an MR damper with an energy-harvesting EM transducer,

wherein the EM transducer supplied the power required by the MR damper for adjusting the damping characteristic. Numerical simulations of a three-story building subjected to seismic loading showed that this proposed system exhibited better performance than conventional MR dampers, with additional reductions of 35.5% and 24.1% in maximum peak acceleration and inter-story drift, respectively. Wang et al. (2009) proposed a self-powered, self-sensing, semi-active control system composed of a rack pinion mechanism, an EM generator, an MR damper, and a control circuit. The EM transducer functioned not only as a velocity sensor but also as a power generator that supplied power to the MR damper. Its effectiveness was validated through the simulation of a self-powered skyhook control for suppressing the dynamic responses of a bridge deck and piers. Jung et al. (2011b) also investigated the utilization of an EM transducer to simultaneously power an MR damper for mitigating the vibration of stay cables and power wireless sensors for estimating cable tension.

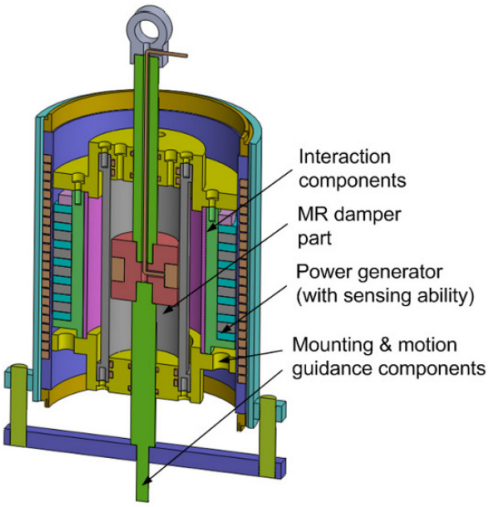

Figure 2.15 Configuration of a self-sensing MR damper with power generation (Chen and Liao, 2012) (Reused with permission from IOP Publishing.)

Given that the EM transducers were not integrated into the dampers and the dual functions were still realized separately in the above-mentioned examples, the above examples may not be regarded as authentic dual-function dampers. Choi and Wereley (2009) constructed a self-powered MR damper that integrated the power generation

component and the MR fluid into one device. Numerical results demonstrated its better isolation performance without using an extra sensor or a control processor. Similarly, Chen and Liao (2012) integrated multiple functions, including energy harvesting, sensing, and damping adjustment, into one specific device (Figure 2.15). The EM relative-velocity sensing strategy was used for signal sensing, and the relative movement between the coils and magnets could generate power and drive the MR damper for damping characteristic adjustment. Later, this proposed energy-harvesting MR damper was applied to a vehicle suspension (Chen et al., 2015). Under general city road conditions and a traveling speed of 45 km/h, an average power of approximately 9.8 W could be harvested, whereas the average power consumed by the MR coils was only 2.68 W. The RMS acceleration could be reduced by 41.7% compared with that of the passive case. A recent experiment on a motorcycle suspension performed by Chen et al. (2018) demonstrated that the self-powered MR suspension could reduce the seat RMS acceleration by 20.7% compared with that of the passive case.

Yang et al. (2020) proposed a self-powered MR elastomer isolation system for the protection of buildings against earthquakes. The isolation system contained an innovative self-powered component that consisted of four EM motors, four gearboxes, a linear bearing, a universal joint, and a gimbal joint. This omnidirectional component could covert all-direction vibrations into electrical energy. Under harmonic excitation with an amplitude of 15 mm at 3 Hz, peak powers of approximately 1 and 0.7 W were observed with excitation directions of 0° and 30°, respectively. The dual-function performance of this system was further tested in a scaled three-story building.

2.2.2.2 Hybrid Hydraulic Dampers

Energy-harvesting hydraulic dampers operate using a mechanism wherein hydraulic fluid transfers the bidirectional displacement of the cylinder to the rotary motions of the hydraulic pump/motor, where the pump is connected to an EM transducer for energy

harvesting. Based on this mechanism, Li and Tse (2013) proposed an energy-harvesting hydraulic damper, in which the hydraulic motor not only converted linear motion into rotation but also accelerated the EM transducer rotation. A test rig result showed that a maximum harvested power of 435.1 W/(m/s) was obtained under a 20 mm excitation amplitude and 0.8 Hz frequency.

Fang et al. (2013) designed and prototyped a hydraulic EM shock absorber with a hydraulic rectifier and an internal accumulator, and focused on output power optimization considering the load resistance and excitation frequency. Li et al. (2014) designed a similar hydraulic rectifier, and characterized the damping and harvesting performance of the hydraulic EM shock absorber. Zou et al. (2019) further studied the working principle of this type of hydraulic EM shock absorber by considering different working modes, such as bounce, pitch, and roll, in a 7DOF full-vehicle suspension model. Simulation results showed that the proposed absorber could harvest an optimal RMS power of 397 W at an external resistance of 15 Ω when a vehicle traveled at 20 m/s on a Class C road. These references provide an approach to optimize energy harvesting from a hydraulic pump using an EM transducer. Mi et al. (2017) explored the application of the hydraulic EM absorber in the bogie suspension of a railway vehicle. The simulation results demonstrated that an average power of 0.3 to 4 kW could be harvested under different installation sites and traveling speeds, and the vibration control performance was comparable to that of conventional dampers.

2.2.3 EHEMD

Notably, EM transducers can be used not only for energy harvesting but also for structural vibration control. The simplest form of a dual-function device is composed of a single EM transducer directly connected to an EHC, as shown by Zhu et al. (2012). Depending on specific application fields, EM dual-function devices often have different names, such as EHEMD, EM damper cum energy harvester, energy-regenerative EM

damper, and energy-regenerative EM shock absorber (Zhu et al., 2012; Li et al., 2012; Shen and Zhu, 2015; Zhang et al., 2016; Xie et al., 2017).

The concept of energy-harvesting dampers first emerged in the field of automotive engineering, and most of these dampers were employed in vehicle suspension systems. Arsem (1971) was among the first to propose the concept of energy-harvesting electric shock absorber for vehicle suspension systems, in which the conventional hydraulic unit was replaced by either EM or piezoelectric transducers that could convert vibration energy into electrical energy. In the late 1980s, the application of EM transducers with adjustable damping in vehicle suspensions was explored for the first time (Karnopp, 1989). In the 1990s, Suda and his coworkers pioneered a hybrid control suspension integrated with EHEMDs to enhance the control performance with reduced energy consumption (Suda and Shiiba, 1996; Suda et al., 1998a, 1998b; Nakano et al., 1999, 2003). Specifically, Suda et al. (1998a, 1998b) applied two EM transducers with self-powered control to improve riding comfort; one worked as an energy generator to power the other one, which worked as an active actuator. This self-powered active control system using both H_∞ control and skyhook control was proved to outperform passive or semi-active systems. Its effectiveness was also validated through its installation in a heavy-duty truck suspension system (Nakano et al., 1999). Nakano et al. (2003) further investigated the feasibility of realizing self-powered active control with a single EHEMD.

The applications of EHEMDs in various types of structures have been proposed and investigated since then. The representative studies are summarized in the following subsections.

2.2.3.1 Vehicle Suspensions

The energy harvested from suspension vibrations can be used to charge back-up power sources and supply electrical loads as a supplement to the vehicle alternator (Zhang

et al., 2016) or to provide power to the semi-active or active control in suspensions (Nakano et al., 2003; Shi et al., 2014).

Abdelkareem et al. (2018a) reported that the potentially harvestable power in shock absorbers ranged from 46 to 7500 W depending on the vehicle categories and operation conditions. For example, it was found to range from 100 to 400 W for a typical passenger car traveling at 97 km/h under good road conditions (Zuo and Zhang, 2013). Zuo and his coworkers (Zuo and Zhang, 2013; Li and Zuo, 2013; Liu, 2016) reported a series of work on energy-harvesting EM shock absorbers, focusing on their feasibility, harvestable power, design, modeling, optimization, semi-active control, and field tests with or without MMR. Using a material test system (MTS), Li et al. (2012) validated that a retrofit rack-pinion-based EM shock absorber could perform like a conventional hydraulic absorber. Later, Liu (2016) modified the shock absorber with a ball screw and an MMR. The road test results demonstrated that the proposed system was superior to the conventional oil shock absorber in terms of energy harvesting capability (with an average power of 5.14 W) and acceleration reduction (>11.12%) when a car traveled on a paved road at 40 mph.

Xie et al. (2017) developed an energy-harvesting suspension with 12 independently controlled EM transducers connected to different load resistors, wherein the adjustable damping can be realized together with power generation according to the road conditions. Power of 16 W was recaptured in an MTS test with an amplitude of 20 mm at 2 Hz. Notably, only pure resistors were connected in this study. Later, Xie et al. (2018) modified the system by using only one EM transducer connected to a tunable resistor to realize damping tuning, and several other EM transducers were connected to a bridge rectifier and battery to realize energy harvesting. Figure 2.16 shows the corresponding prototype and diagram of the energy-harvesting damper designed for vehicle suspensions. Xie et al. (2019) claimed that the proposed system with multiple independent EM transducers had better energy harvesting performance than the single-transducer design proposed by Li

and Zuo (2013).

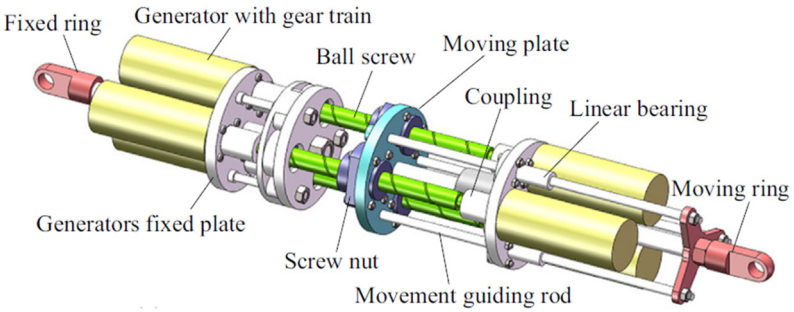

(a) Configuration

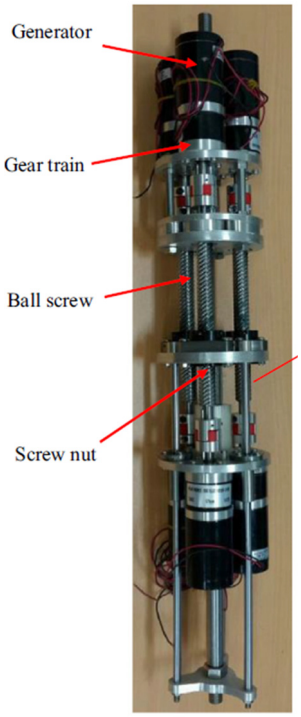

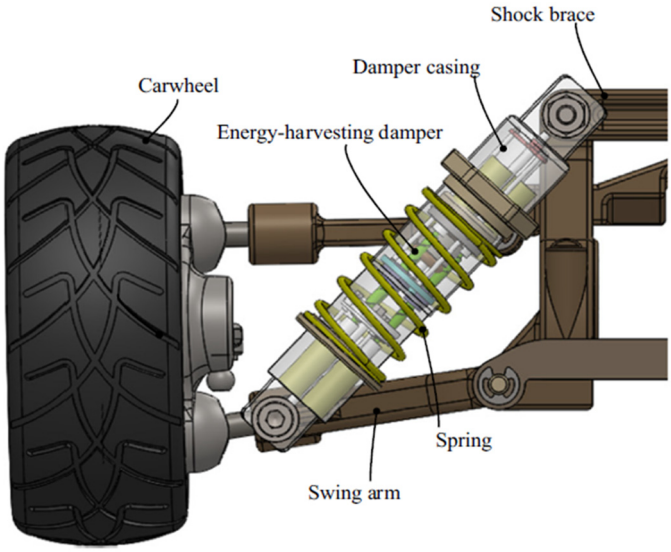

(b) Prototype (c) Damper in the suspension

Figure 2.16 Prototype and schematic of the EHEMD presented by Xie et al. (2018) (Reused with permission from Elsevier.)

Li et al. (2019) presented an energy-harvesting EM shock absorber with real-time damping coefficient adjustment. An equivalent resistance-emulating circuit with energy harvesting function was applied to avoid the damping failure zone in the case of connecting directly to the battery. Series of simulations and experiments on the 2DOF suspension were performed to explore its feasibility, and the corresponding results

demonstrated that the energy harvesting efficiency ranged from 40.72% to 70.55% under harmonic and random road excitations.

Other implementations of EHEMDs serving as shock absorbers in vehicle suspensions can be found in the review by Abdelkareem et al. (2018a).

2.2.3.2 Seat Suspensions

Ning et al. (2018a) proposed a seat suspension system with an energy-saving variable damping characteristic (Figure 2.17), wherein the damping property could be varied through a rotary rheostat. The performance of this system was validated through the installation in a scissor structure. The acceleration of the proposed system was 22.84% lower than that of the passive counterpart, and an RMS power of 1.21 W was measured on a resistor. Later, Ning et al. (2018b) regulated the damping coefficient through a specific circuit, in which a metal–oxide–semiconductor field-effect transistor (MOSFET) was connected in parallel with a resistor. The equivalent resistance was determined based on the duty cycle of the pulse-width modulation (PWM) that drove the MOSFET based on the feedback acceleration signal. In their study, the harvestable RMS power was 1.492 W. Recently, Ning et al. (2019) introduced an in-series torsional spring into the aforementioned seat suspension, wherein the equivalent stiffness could be tuned by changing the damping feature. Although they reported the energy harvesting potential and low energy consumption of the system, no in-depth investigation was performed.

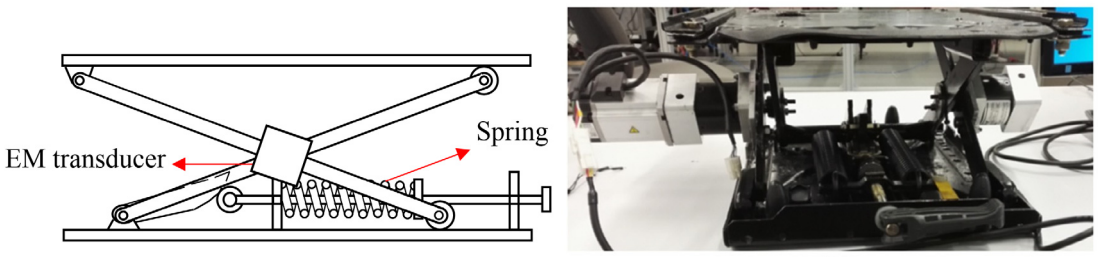

(a) Schematic (b) Prototype

Figure 2.17 Schematic and prototype of a seat suspension with energy-harvesting variable damping characteristics (Ning et al., 2018a) (Reused with permission from Elsevier.)

2.2.3.3 Civil Structures

Seismic base isolators, which protect various types of civil structures against strong earthquakes, share a similar vibration isolation mechanism with vehicle or seat suspensions. Thus, it is not surprising to see the applications of EHEMDs in seismic base isolators for buildings and bridges.

Augé (2003) proposed a magnetic induction damper that was essentially a dual-function EM damper, and explored the active control of building structures under earthquakes. In a numerical study of a six-story building equipped with the proposed dampers in a base isolator and subjected to the scaled El Centro earthquake (scale factor of 2), the harvested power was estimated as 20 kW. However, no detailed technical parameters of the EM transducer and EHC were considered in this preliminary study.

Lu et al. (2014) investigated the feasibility of using an EM transducer to regenerate energy dissipated by the isolator installed in a seismically isolated bridge. Mofidian and Bardaweel (2019) proposed an energy-harvesting isolator that provided vibration isolation and converted part of the vibration energy into electrical energy. Experimental results showed that the isolator could effectively realize oscillation attenuation, particularly for responses higher than 12.5 Hz, and could scavenge 0.115 mW of power under 9.81 m/s^2 ground acceleration. A novel feature of their design is the adoption of a magnetic spring in addition to an elastic mechanical spring.

Shi (2013) studied the feasibility of implementing an EM energy harvester installed on a cable-suspension bridge to mitigate the bridge deck vibration and harvest energy. Power from 616 W to 75 kW could be potentially harvested to power the lights on the bridge when the deck was excited by a mean wind speed of 10 m/s.

Shen et al. (2015) applied the EHEMD concept to the vibration mitigation of bridge

stay cables. They verified its effectiveness through a numerical case study that considered the buffeting vibrations of a full-scale stay cable installed with an EHEMD. Without sacrificing the control performance, the EHEMD could harvest average power from 82.5 mW to 2.40 W under wind speeds of 9 to 15 m/s. Later, Shen et al. (2016a) conducted a corresponding laboratory experiment on a 5.85 m cable with a small-scale EHEMD system, in which approximately 30 and 20 mW (average power) could be harvested under harmonic and random excitations, respectively.

Jamshidi et al. (2017) investigated the design and application of a self-powered EHEMD operating in hybrid modes: an energy-harvesting passive mode and a semi-active mode. A numerical case study of an actual bridge stay cable installed with the proposed system demonstrated that the proposed damper outperformed the conventional passive damper at wind speeds exceeding 10 m/s. The corresponding harvested power met the power demand of MCUs for semi-active operations. Jamshidi et al. (2018) fabricated and tested the proposed system on a small-scale shear frame subjected to ground motion. The vibration amplitude in the semi-active mode was nearly 10 dB less than that in the energy-harvesting passive mode. The energy harvesting efficiency was approximately 30% in the passive mode.

Recently, Kye et al. (2019) designed an EHEMD for stay cables, the operation of which was classified into three modes according to wind speed. The energy harvesting mode was selected when the wind speed was below 6 m/s. The output power in the energy harvesting mode was 174.6 mW in a laboratory experiment corresponding to an acceleration input at a wind speed of 5.4 m/s.

2.2.3.4 Other Structures

Yan et al. (2017) proposed to use a self-sensing EM transducer as a base isolator to protect the space antenna reflector and solar panel against shock or random vibrations

during shipment, launch, and in-orbit deployment. Figure 2.18 illustrates the experimental setup and vibration isolation performance. The system could effectively dampen the second and third modes of the antenna reflector.

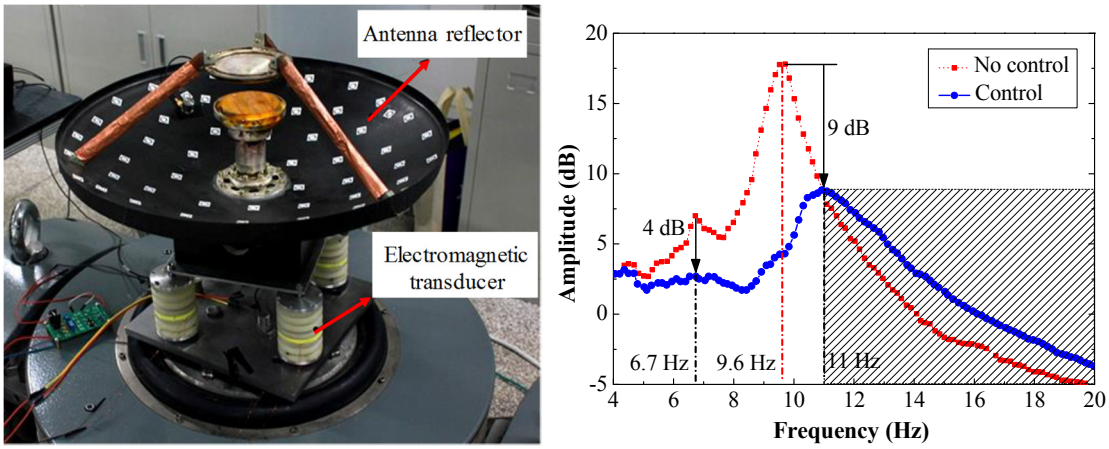

(a) Prototype of the experimental space antenna reflector

(b) Vibration isolation performance

Figure 2.18 Experiment test of an energy-harvesting isolator for a space antenna reflector (Yan et al., 2017) (Reused with permission from IEEE.)

Recently, Li and Zhu (2021) proposed a self-powered actively controlled base isolator using an EM transducer and an H-bridge circuit; the control process was divided into energy-harvesting and energy-consuming periods, and the former could successfully power the latter. Consequently, classical active skyhook control could be realized without an external power supply, and simultaneous energy harvesting and isolation were validated through shake table tests.

2.2.4 Energy-harvesting Piezoelectric Damper

The use of piezoelectric dual-function devices in various mechanical structures has also been investigated. Xie and Wang (2015b) designed a piezoelectric bar to harvest energy from ambient vibrations in a vehicle suspension system, wherein the piezoelectric bar was regarded as a damped spring. Simulation results showed that an RMS power of up to 738 W could be harvested if the piezoelectric bar had a width of 0.015 m and a

height of 0.1 m. Wang et al. (2020) reported a compressive-mode piezoelectric energy harvester that comprised a force amplifier and a piezoelectric stack for application in spring suspensions. Experimental results on a prototype showed that an average power of 13.625 mW could be harvested under an acceleration input of 0.3 g at 46.3 Hz.

Wang and Inman (2012, 2013) designed a dual-function strategy based on two piezoelectric layers; one layer worked as an energy harvester to supply power to the other, which controlled vibrations as an actuator. The design was motivated by the wind spar of a small unmanned aerial vehicle in wind gusts. Wang and Inman (2013) designed this wind spar as a beam-like structure (with a length of 593.7 mm, width of 38 mm, and thickness of 2.38 mm) to fit in a fiberglass composite substrate of 17.8 g.

Khan and Ali (2019) developed an energy-harvesting base isolator composed of a piezoelectric disc embedded in silicone rubber, which exhibited resonance at 56 Hz. The size of the cylinder device was approximately 15 mm (diameter) × 30 mm (height). Approximately 1.8 and 0.51 mW of power were harvested at frequency ratios of 1.4 and 3.5, respectively.

2.2.5 EHTMD

TMDs, also known as dynamic vibration absorbers, are widely applied to suppress vibrations of civil and mechanical structures. A TMD consists of a mass mounted on one or more damped springs. The replacement of conventional dampers (e.g., viscous fluid dampers) in a TMD with dual-function dampers constitutes an EHTMD, wherein the damping energy can be converted and stored by an EHC. Since the 2010s, the applications of EHTMDs in civil structures have been explored by several researchers (Zhu et al., 2011; Ni et al., 2011; Cassidy et al., 2011). Figure 2.19 presents a representative architecture of an EHTMD implemented in a building structure, wherein the EM transducers were adopted as dual-function devices.

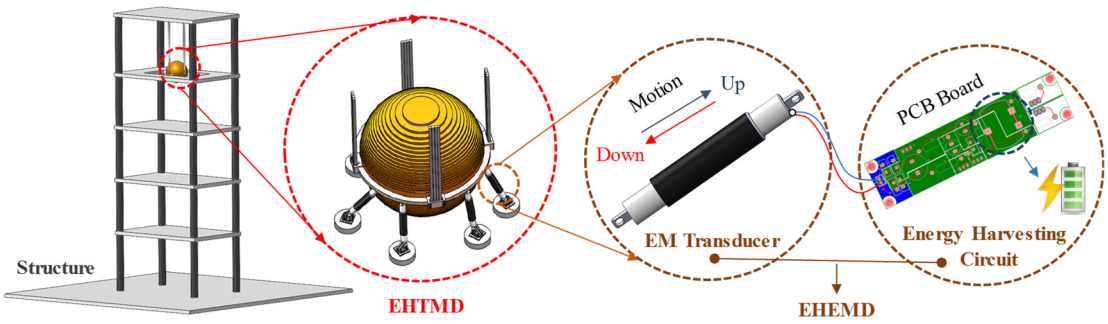

Figure 2.19 A representative design of EHTMD used in a civil structure

Ni et al. (2011) conducted a preliminary study on a 76-story benchmark building subjected to wind excitation and estimated that over 85 kW of damping power was possibly harvested in this building when an appropriate TMD strategy was adopted. Tang and Zuo (2010) proposed an energy-harvesting semi-active series TMD to simultaneously realize vibration control and energy harvesting and numerically estimated its performance in Taipei 101. Later, Tang and Zuo (2012) experimentally validated its effectiveness through a scaled three-story building. Approximately 60 mW of power was harvested, and the acceleration reduction was up to 60% when the building model was subjected to a harmonic force.

In the same year, Shen et al. (2012) developed a small-scale EHTMD prototype that was essentially a pendulum TMD with its pivot connected to a rotary EM transducer and an EHC. The harvested average power was approximately 312.4 mW, and the vibration was approximately 10 dB less than that of the case without EHTMD. Notably, the pendulum EHTMD in this experiment successfully powered a wireless sensor (Figure 2.20). Shen et al. (2016b) also experimentally validated the superior performance of the pendulum EHTMD under the El Centro earthquake with a peak ground acceleration of 0.1 g and obtained approximately 4.7 J of energy. Recently, Shen et al. (2018) examined the power efficiency of the EHTMD installed in a 76-story benchmark building subjected to wind excitation by considering a practical EHC and various types of power losses. With

the increase in wind speed from 4 to 7 m/s, the energy harvesting efficiency increased from 12.8% to 35.9%, which corresponded to an increase in output power from 2.3 to 60.7 W.

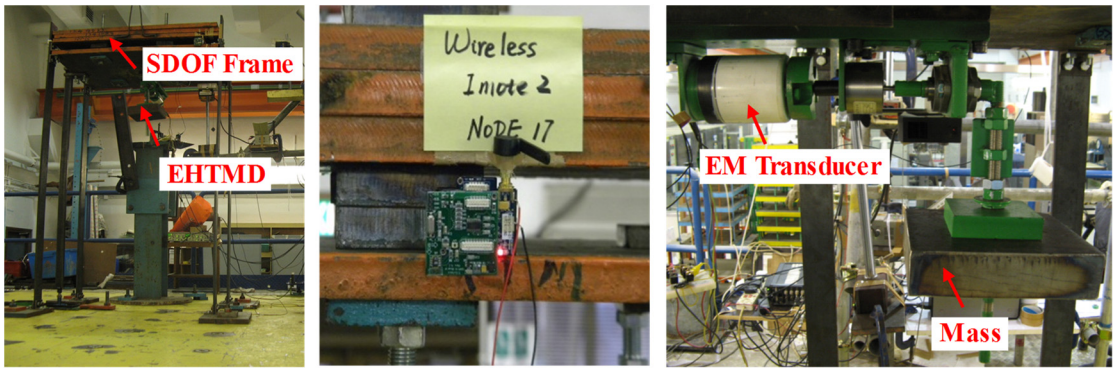

(a) SDOF frame (b) Wireless sensor (c) EHTMD

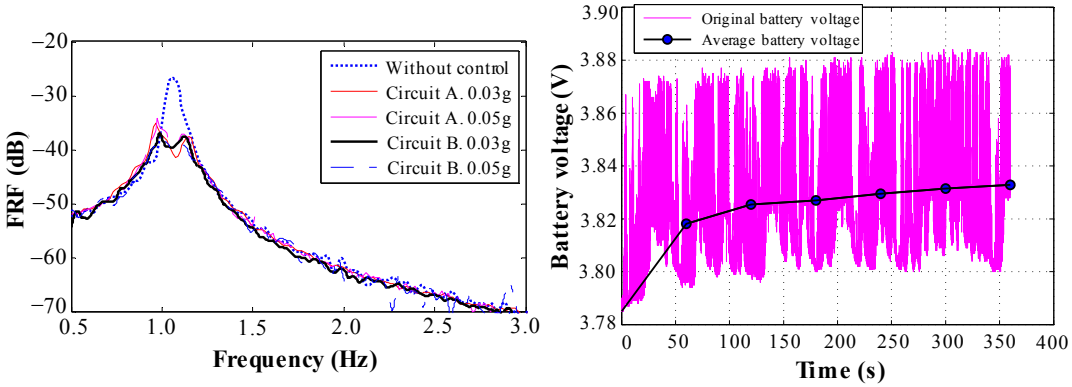

(d) Vibration control performance (e) Battery charging curve

Figure 2.20 Laboratory experiment of a single-story frame installed with EHTMD (Shen et al., 2012) (Reused with permission from Elsevier.)

More recently, Kecik and Mitura (2020) proposed another pendulum EHTMD that consisted of two independent EM harvesting parts. One utilized the oscillation of a levitating magnet in a coil with strong nonlinearity but did not suppress vibrations; the other was mounted at the pivot of the pendulum to dampen vibrations.

Similar to traditional TMDs, the applications of EHTMDs are not limited to building structures. Using an adaptive EHTMD, Caruso et al. (2016) attempted to harvest power from the vibration of a bridge subjected to wind excitation. Numerical results showed that

the amount of harvested power remarkably increased with a slight increase in the attack angle. Specifically, approximately 600 W of power could be harvested at a wind speed of 20 m/s with an attack angle of 2°. Kopylov et al. (2020) explored the implementation of an EHTMD in a vehicle suspension system. By testing the EHTMD in an 11DOF full-scale car model, the RMS carboy acceleration was reduced by 9.6%, and road-holding was enhanced by 5.7% in the case of random road profiles. The RMS power could reach 58 W when the vehicle traveled at a speed of 30 m/s on a Class D road. Yan et al. (2019) explored the feasibility of applying an EHTMD with a resonant circuit in a space rack structure. The output power density was 0.41 W/N, indicating the promising prospect of EHTMD usage for a self-powered electronic device in space engineering. Furthermore, Jahangiri and Sun (2019) used a three-dimensional pendulum EHTMD for offshore wind turbines. The numerical study of the NREL 5MW benchmark wind turbine demonstrated that the EHTMD installed in the nacelle could suppress wind- and wave-induced bidirectional vibrations, and kilowatt-level output power could be harvested.

Yuan et al. (2018) proposed and tested a non-traditional EHTMD configuration, wherein the damping element was installed between the TMD mass and the ground. Different load resistors were connected to search for a good trade-off between the two functions under harmonic excitation. The frequency response function (FRF) curve of the primary mass exhibited a nearly flat shape with a wide frequency band in a large damping case. The optimization of this system under transient response was also investigated (Yuan and Liu, 2018).

Liu et al. (2016) incorporated a TMD with EM shunted resonant damping and validated its effectiveness through a small-scale experiment on an SDOF structure, in which the resonant peak was reduced by 58.7% compared with the case without control.

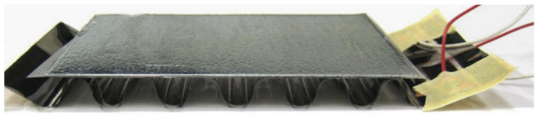

(a) Prototype

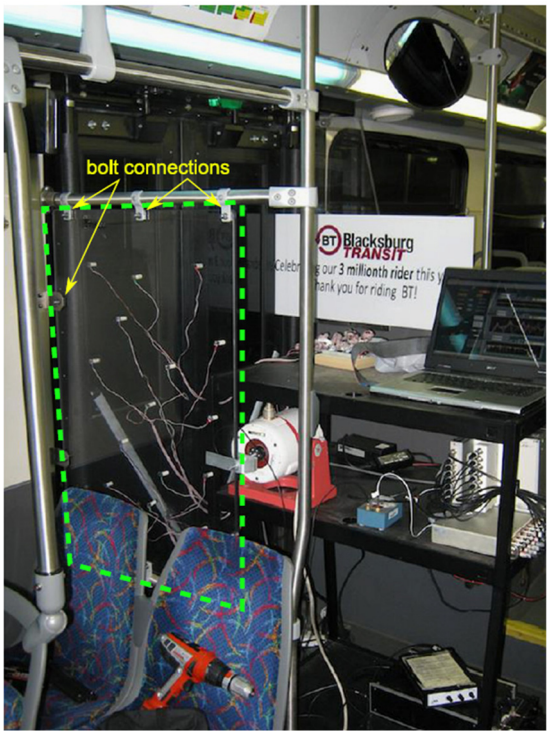

(b) Structural panel installed with energy piezoelectric EHTMD

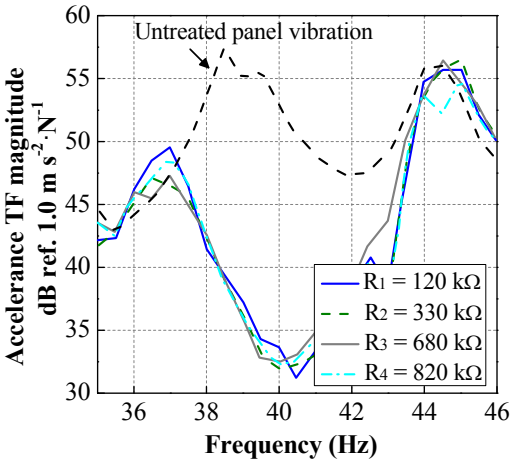

(c) Vibration control performance

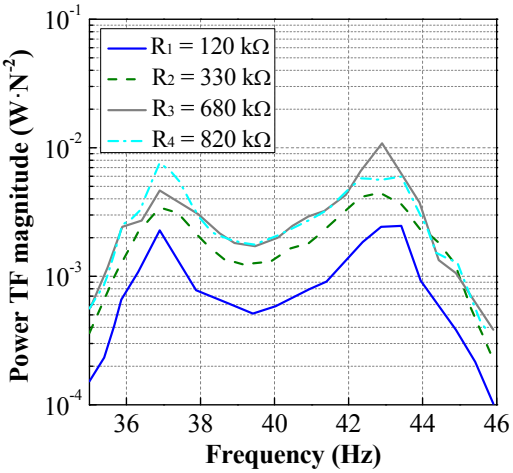

(d) Power generation performance

Note: R_1, R_2, R_3, and R_4 denote the different load resistances.

Figure 2.21 Piezoelectric EHTMD and its performance on a structural panel (Harne, 2013)

(Reused with permission from Elsevier.)

Meanwhile, Xie et al. (2013, 2014b) and Xie and Wang (2016) conducted a series of numerical analyses on piezoelectric energy harvesters in high-rise buildings. Xie et al. (2013) first proposed a piezoelectric coupling cantilever attached to a mass as an EHTMD design and theoretically analyzed its performance in a high-rise building subjected to harmonic motion. Later, Xie and Wang (2016) specifically designed a piezoelectric EHTMD model that comprised a cantilever and two groups of in-series piezoelectric ring harvesters. The in-series ring harvesters were connected by a shaft, which was driven by a rod hinged on the proof mass. The RMS output power was as high as 53.95 kW, and the

optimal energy harvesting efficiency was 38.28%. A matching design of the piezoelectric ring harvester was reported in another early study (Xie et al., 2014b). However, these studies on the piezoelectric EHTMD still remained in the stage of conceptual designs and numerical simulations, and the optimal design was to maximize the power efficiency alone. Pan et al. (2017) reported a different configuration of a piezoelectric EHTMD, wherein the piezoelectric layer was connected between the spring-damping elements and the TMD mass. A small-scale experimental test was conducted with an excitation amplitude of 2 N at 5 Hz, but the average power harvested was only 80 μW. Harne (2013) experimentally studied a piezoelectric EHTMD, in which a circularly corrugated piezoelectric film was regarded as the distributed sparing layer. The effectiveness of the piezoelectric EHTMD was examined by applying the EHTMD to the structural panel of a city bus. An output power of 13.6 μW was obtained when the panel was excited by 2.61 g at 43 Hz. Figure 2.21 illustrates this piezoelectric EHTMD and the corresponding performance.

2.2.6 EHTID

An inerter is a two-terminal device in which the generated force is proportional to the relative acceleration (Smith, 2002). Inerters are typically combined with other elements to further enhance vibration control performance in practical applications. For example, inerter dampers (IDs) combine inerters with a conventional viscous damper, while tuned inerter dampers (TIDs) add another stiffness element to IDs. In recent years, the exploration of energy-harvesting inerter dampers (EHIDs) and EHTIDs has elicited growing interest, in which EM transducers have always been used to replace the viscous dampers in these inerter-based control devices to realize either energy harvesting or self-powered functions. To the best of the authors' knowledge, piezoelectric transducer–based EHIDs or EHTIDs have not been reported in the literature.

For the first time, Zhu et al. (2019) modeled and tested an EHID that can

simultaneously provide large inertance, controllable EM damping, and energy harvesting capability. An average output power of 10 W and efficiency of approximately 30% were observed in their MTS test. Figure 2.22 shows the corresponding prototype and specific configuration of such an EHID.

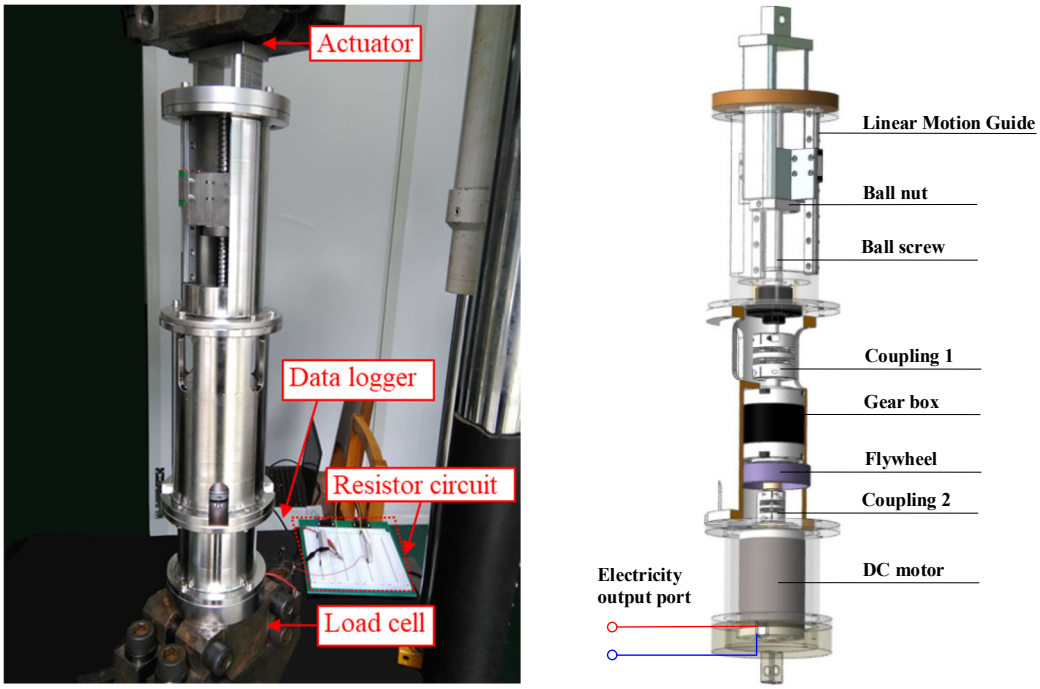

(a) Prototype in MTS test (b) Configuration

Figure 2.22 Prototype and specific configuration of EHID (Zhu et al., 2019) (Reused with permission from Elsevier.)

Marian and Giaralis (2017) investigated the energy harvesting potential in a TMD with an inerter directly connected to the ground. They noticed that the available power generation increased by reducing the inertance and concluded that the optimal absorber was not an optimal energy harvester in the harmonically excited building but the inertance was regarded as a flexible index to realize the trade-off between energy harvesting and vibration suppression. Asai et al. (2018) numerically assessed the vibration control capability and energy harvesting efficiency of an EHTID installed in a building subjected to earthquake ground motion. Later, Sugiura et al. (2020) experimentally characterized the control and harvesting performance of the above-mentioned EHTID, and their results

showed that the energy conversion efficiency increased but the input power decreased compared with the results for the EHEMD in the case of the Kobe earthquake record. Qian et al. (2019) compared two different networks of inerter-based isolators by performing H_2 optimization numerically and evaluated the potentially harvestable power of the isolators. The peak power and average power were recorded as 3.01 kW and 71.77 W, respectively, in the simulation of a five-story building subjected to the Northridge earthquake ground motion. Zhao et al. (2020) analyzed the energy dissipation mechanisms of three different inerter-based networks and explicitly pointed out that the introduction of a grounded inerter reduced the input power to the system. Luo et al. (2017) analyzed a complicated dual-function device that consisted of a resonant shunt EHTMD and an inerter. In a numerical simulation with the Taipei 101 tower, the device improved vibration mitigation by reducing the vibration peak by 35% compared with that of the classical TMD, and the average harvested power was 132.32 W.

2.2.7 Optimization of Dual-function Devices

Notably, when a vibration-based energy harvester is integrated with the vibration control function, a fundamental question on whether these two intended objectives (i.e., energy harvesting and vibration control) are consistent or not naturally arises. When these objectives are conflicting, a trade-off between the optimization is required, whereas when the objectives are consistent, the problem may be simplified as a single-objective optimization. However, these answers to this question are not unique or simple because of the complexity arising from the objective functions, transducer types, damper architectures, and application scenarios. Several insightful studies are summarized in this subsection.

Shen et al. (2019) presented an optimal design of EHEMDs installed in SDOF and multi-degree-of-freedom (MDOF) structures and analytically and numerically validated the consistency of vibration control and energy harvesting objectives under broadband

random excitation, wherein the objective function for vibration control was to minimize the H_2 norm of the structural displacement or acceleration. An intuitive explanation that they provided was that given the constant input power under random excitation, the EHEMD optimized to harvest the maximum power minimized the structural damping power and led to an optimal vibration control performance. However, they also pointed out that the two objectives were inconsistent under harmonic excitation because the input power from the excitation was no longer constant and dependent on the frequency and damping of the structure–EHEMD system.

Abdelkareem et al. (2018b) performed parametric analyses of a 2DOF suspension model considering different driving operation conditions and suspension design parameters. They reported that the optimizations with respect to the harvested power and dynamic control performance (e.g., ride quality and road handling) were inconsistent. However, they claimed that a sufficient amount of suspension energy could be harvested even if the dynamic control was optimized.

Dual-function EHTMDs present an optimization problem involving more parameters, such as frequency and damping ratios. Harne (2013) concluded that the two objectives of EHTMDs attached to a harmonically excited simply supported panel were inconsistent in terms of the optimal mass ratio and load resistance, wherein the specific dual objectives were maximizing the global vibration attenuation and energy harvesting. A similar result was reported by Gonzalez-Buelga et al. (2014), who conducted an SDOF structure–EHTMD analysis by setting the control objective as the minimization of host structure displacement. They concluded that the optimal mass ratios for the two objectives were not identical under harmonic force excitation or harmonic ground motion input.

Under random excitation, Zuo and Cui (2013) numerically optimized the parameters of an EHTMD and found that the optimal parameters for vibration control and energy

harvesting were close, wherein the H_2 optimization was applied in their analysis of the vibrations of the primary structure and harvested power. Zilletti et al. (2012) indicated that the minimization of structural kinetic energy and maximization of the absorbed power of TMDs were consistent in slightly damped structures, but they did not provide theoretical proof. Brennan et al. (2014) investigated an EHTMD in two excitation scenarios and obtained similar conclusions: the EHTMD could effectively realize vibration control and energy harvesting under random force excitation, and no significant difference in power performance was observed when different control criteria were considered. By contrast, under harmonic force excitation, the two optimization objectives were conflicting.

Recently, Shen et al. (2021) separately conducted a theoretical power analysis of an SDOF structure–EHTID system under white noise base excitation and seismic excitation generated by the Kanai–Tajimi earthquake model. The parameters for the optimization of seismic response control and energy harvesting were consistent in the case of white noise input but different in the case of the Kanai–Tajimi model. The parameters discussed included the frequency tuning ratio, damping ratio, inertance-to-mass ratio of EHTID, and period of the primary structure. Notably, only one type of EHTID network was considered in their study.

Table 2.3 summarizes the aforementioned references on dual-function optimization. The studies were mostly based on a linear system. Potential nonlinearities in dual-function systems, such as nonlinear mechanical design (Kremer and Liu, 2017) and the nonlinear effect in EHCs (Loong, 2020), were not considered in the optimizations.

Table 2.3 Survey of dual-function optimization

Target application	Damper type	Model type	Optimization objectives	Excitation type	Consistency	References
Building	EHEMD	SDOF and MDOF models	H_2 optimization for minimizing the response of the host structure H_2 optimization for maximizing the EM damping power	White noise Harmonic excitation	Yes No	Shen et al., 2019
	EHTMD	SDOF model	H_∞ optimization for minimizing the displacement of the host structure H_∞ optimization for maximizing the output power on the load resistor	Harmonic excitation	No	Gonzalez-Buelga et al., 2014
	EHTMD	SDOF model	H_2 optimization for minimizing the responses of the host structure H_2 optimization for maximizing the output power on the load resistor	White noise	Close	Zuo and Cui, 2013
	EHTMD	SDOF model	Different vibration control criteria Maximization of power into EHTMD	White noise Harmonic excitation	Yes No	Brennan et al., 2014
	EHTID	SDOF model	H_2 optimization for minimizing the response of the host structure H_2 optimization for maximizing the EM damping power	White noise Kanai-Tajimi earthquake model	Yes No	Shen et al., 2021
Vehicle suspension	EHEMD	2DOF model	Optimization of ride quality and road handling Maximization of RMS power into EHEMD	Track irregularity	No	Abdelkareem et al. 2018b
Other structures	EHTMD	MDOF plane	Optimization of the spatial average mean-square out-of-plane velocity Optimization of the output power on the load resistor	Harmonic excitation	No	Harne, 2013

2.2.8 Summary and Comparison

Tables 2.4 and 2.5 summarize the studies on EM and piezoelectric dual-function devices, respectively. They show that the number of studies on piezoelectric dual-function devices is much smaller than that on EM dual-function devices. Similar to Table 2.2, Tables 2.4 and 2.5 are shaded using different colors to distinguish between experimental and numerical studies. The EHEMDs used in vehicle suspensions were tested under real driving conditions. The majority of the other studies are still at the laboratory research stage; thus, to explore the engineering application stage, further theoretical and experimental verifications are required.

In addition, the studied implementations of dual-function devices are still limited to several representative applications up to now, such as suspension systems, buildings, and bridges (including bridge cables); the corresponding harvestable power can reach 4, 85, and 75 kW, respectively (Mi et al., 2017; Ni et al., 2011; Shi et al., 2013). This finding demonstrates the prospects of implementing dual-function devices in large-scale applications. Considering the diversified applications of structural vibration control technologies, various potential applications of dual-function devices remain to be explored in the future.

Table 2.6 compares EM and piezoelectric dual-function devices based on past studies. Notably, most of the energy harvesting characteristics of the two types of transducers presented in Table 2.1 are still applicable to dual-function devices. In general, EM dual-function devices show superiority in terms of damping control, compatibility with other structural components and damping mechanisms, and output power performance. Owing to difficulties in manufacturing large piezoelectric transducers, most of the studies on piezoelectric dual-function devices are simulated applications. Meanwhile, a series of laboratory experiments and field tests have been conducted to validate the effectiveness of EM dual-function devices. The coupling coefficients, output

power, and forces of EM dual-function devices can be effectively enhanced using linear-to-rotary motion conversion and a gearbox. Besides electrical bridge rectifiers, MMRs or hydraulic rectifiers have been developed to enable EM dual-function devices to directly output direct current (DC) power. Hence, the technology of EM dual-function devices is relatively mature. It is also convenient to integrate EM transducers with other damper types (e.g., inerters and negative-stiffness elements). To the best of the author's knowledge, such integrations with piezoelectric transducers have not been reported so far. However, this situation does not imply that piezoelectric transducers are unsuitable for dual-function devices. Piezoelectric dual-function devices can be efficient in small-scale applications (e.g., the vibration control of microscale structures), which is a promising area to be explored. Table 2.7 presents two representative usages of the harvested power from dual-function devices: (1) to power wireless sensors in structural health monitoring systems and (2) to realize self-powered semi-active or active vibration control systems by eliminating the need for power supplies.

Figure 2.23 presents a Sankey diagram that summarizes the reviewed studies on dual-function devices from the perspectives of transducers, vibration sources, and device types. The thickness of each flow line indicates the number of related references. The diagram confirms that civil structures and vehicles are two popular application scenarios for dual-function devices, and dual-function devices for other vibration sources (including ocean waves, railway tracks, and human motions) have been given limited attention. This situation implies that many unexplored areas still exist for such promising devices. Examples include vibration suppression on large floating structures and noise and vibration control on railway tracks. For comparison, the reviewed studies on pure energy harvesters without vibration control (i.e., single function) are also included in this Sankey diagram. Such single-function devices have been investigated for all of the aforementioned vibration sources.

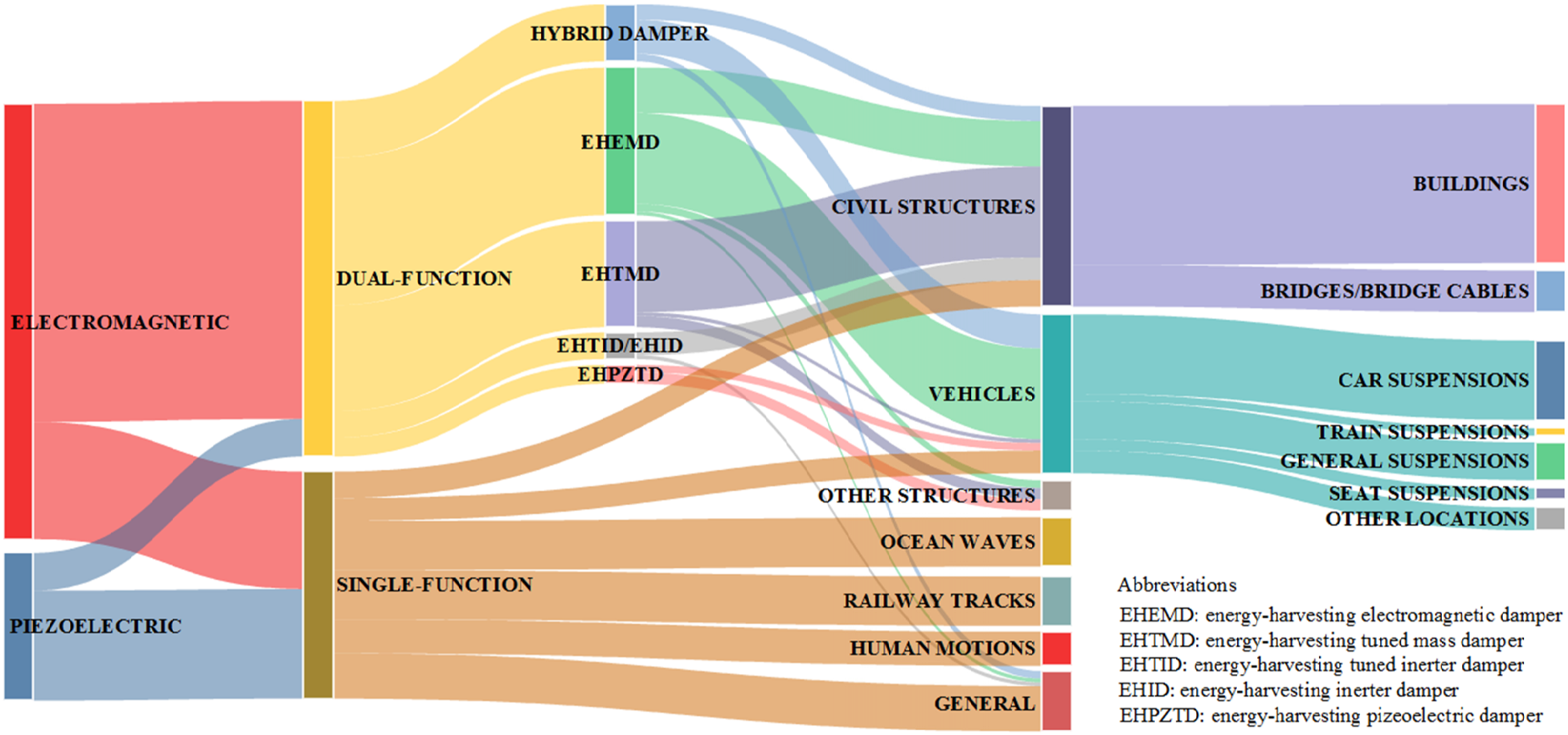

Note: "DUAL-FUNCTION" refers to the devices with functions of simultaneous vibration control and energy harvesting, whereas "SINGLE-FUNCTION" denotes the devices with harvesting function only.

Figure 2.23 Sankey diagram summarizing EM and piezoelectric energy harvesters from three aspects

Table 2.4 Survey of EM dual-function devices

Target applications	Damper type	Application model	Output power (W)[1]	Type of study	Test condition(s)	References
General	EHEMD	\	0.0025–0.274	MTS test	3–11 mm, 2–6 Hz	Zhu et al., 2012
	Hybrid damper[2]	\	\	MTS test	\	Chen and Liao, 2012
	EHID	\	10	MTS test	5 mm, 1 Hz	Zhu et al., 2019
Vehicle suspension	EHEMD	\	0.057–4.302	MTS test	2.5–7.5 mm, 1–2.5 Hz	Zhang et al., 2016
	EHEMD	\	10.13	Bench test	Random road excitation	Shi et al., 2014
	EHEMD	1088 curb mass	100–400 (potential)	Field test	60 mph, Class C	Zuo and Zhang, 2013
	EHEMD	Chevrolet Surburban SUV	19.2	Field test	48 km/h, campus road	Li et al., 2012
	EHEMD	\	16	MTS test	20 mm, 2 Hz	Xie et al., 2017
	EHEMD	2DOF model	~6 (peak)	Motor towing test platform	10m/s, Class C; 5 mm, 3–5 Hz	Li et al., 2019
	Hybrid damper[2]	Motorcycle (Sachs Madass 125)	\	Shaker test	0.03–0.038 m/s, 1 Hz 3.75–5 m, 2 Hz	Chen et al., 2018
	Hybrid damper[3]	\	435.1/(m/s)	MTS test	20 mm, 0.8 Hz	Li and Tse, 2013
	Hybrid damper[3]	Freightliner Cascadia tractor	43–79	Field test	Highway	Mossberg et al., 2012
	Hybrid damper[3]	Passenger car	60–94	Field test	35 km/h, city road	Singh and Satpute, 2015
	EHEMD	4DOF half model (car)	51.54–1289	\	20 km/h, 2Hz, 0.01–0.05 m	Wei and Taghavifar, 2017
	EHEMD	2DOF model (passenger car, bus, off-road vehicle)	105.2–1152	\	60 km/h, Class C	Zhang et al., 2017
	EHEMD	2DOF model (car)	5.14–298.65	\	72 km/h, Class B–D	Liu et al., 2016

	EHEMD	2DOF model (car)	1.1–27.7	\	10–30 m/s, Class A–C	Abdelkareem et al., 2018b
	Hybrid damper[2]	2DOF model (car)	9.8	\	45 km/h, city road	Chen et al., 2015
	Hybrid damper[3]	7DOF model (car)	397 (RMS)	\	20 m/s, Class C	Zou et al., 2019
	Hybrid damper[3]	Railway Vehicle (train)	300–4000	\	60–180 km/h	Mi et al., 2017
	EHTMD	11DOF model (car)	58 (RMS)	\	30 m/s, Class D	Kopylov et al., 2020
Seat suspension	EHEMD	\	1.21 (RMS)	6DOF platform test	Random vibration	Ning et al., 2018a
	EHEMD	\	1.492 (RMS)	6DOF platform test	Random vibration	Ning et al., 2018b
Stay cable	EHEMD	Scaled cable	0.03, 0.02	Shaker test	Harmonic and random force excitation	Shen et al., 2016a
	EHEMD	Scaled cable	0.1746	Shaker test	Free vibration; force excitation (field data)	Kye et al., 2019
	Hybrid damper[2]	Full-scale cable	\	\	Free vibration; force excitation, 2.5–25 mm, 0.5–2 Hz	Jung et al., 2011b
	EHEMD	Full-scale cable	0.0825–2.4	\	Wind excitation, 9–15 m/s	Shen et al., 2015
	EHEMD	Full-scale cable	\	\	Wind excitation, 5–30 m/s	Jamshidi et al., 2017
Building	EHEMD	SDOF frame	\	Shake table test	Random ground motion	Loong and Chang, 2020
	EHEMD	\	0.115×10^{-3}	Shake table test	9.81 m/s^2	Mofidian and Bardaweel, 2019
	Hybrid damper[2]	\	0.7–1 (peak)	Shake table test	15 mm, 3 Hz, excitation direction 0^o or 30^o	Yang et al., 2020
	EHTMD	Scaled 3-story building	0.06	Harmonic force excitation	15 N, 3.3 Hz	Tang and Zuo, 2012
	EHTMD	Single-story fame	0.312	Shake table test	RMS ground acceleration of 0.05 g	Shen et al., 2012

	EHTMD	Single-story fame	\	Shake table test	El Centro motion (peak ground acceleration: 0.1 g)	Shen et al., 2016b
	EHTMD	SDOF model	0.1	\	\	Kecik and Mitura, 2020
	EHTMD	\	0.05	Real-time dynamic substructuring test	\	Gonzalez-Buelga et al., 2014
	EHEMD	6-story building	20,000	\	El Centro motion (scale factor of 2)	Augé, 2003
	EHEMD	20-story building	~1200	\	Random force excitation	Shen et al., 2019
	Hybrid damper[2]	3-story building	\	\	Ground motion	Cho et al., 2005
	EHTMD	76-story building	85,000	\	Wind excitation, 47.25 m/s	Ni et al., 2011
	EHTMD	76-story building	2.3–60.7	\	Wind excitation, 8–25 m/s	Shen et al., 2018
	EHTID	Taipei 101 model	132.32	\	Wind excitation, 39.93 m/s	Luo et al., 2017
	EHTID	5-story building	71.77	\	Northridge motion	Qian et al., 2019
Bridge	EHTMD	Beam-like structure	600	\	Wind excitation, 20 m/s	Caruso et al., 2016
	Hybrid damper[2]	2DOF model	\	\	EI Centro/Northridge motion	Wang et al., 2009
Other structure	EHEMD	Space antenna reflector	\	Shake table test	Random ground motion	Yan et al., 2017
	EHEMD	SDOF model	\	Shake table test	Ground motion	Li and Zhu, 2021
	EHTMD	Space rack structure	0.41/N	Shaker test	Force excitation	Yan et al., 2019
	EHTMD	NREL 5MW wind turbine	kW level	\	Wind excitation, 12 m/s	Jahangiri and Sun, 2019

Note: 1. The output power in this table might be overestimated because several of the studies regarded either the power input of the harvesting damper or dissipated power by the load resistor as the output power.

2. With MR damper

3. With hydraulic damper

4. White background: experimental investigation survey; shaded background: numerical investigation survey.

Table 2.5 Survey of piezoelectric dual-function devices

Target applications	Damper type	Application model	Output power (W)[1]	Type of study	Test condition(s)	References
Vehicle suspension	Piezoelectric damper	\	0.013625	Shaker test	Ground motion , 0.3 g, 46.3 Hz	Wang et al., 2020
	Piezoelectric damper	2DOF model (car)	738	\	35 m/s, random excitation	Xie and Wang, 2015b
Building	EHTMD	SDOF frame	0.00008	Shaker test	Force excitation, 2 N, 5 Hz	Pan et al., 2017
	EHTMD	Beam-like structure with a proof mass	28% (Eff.)	\	Harmonic base motion	Xie et al., 2013
	EHTMD	Beam-like structure with a proof mass	53950	\	Harmonic base motion	Xie and Wang, 2016
Other structure	Piezoelectric damper	\	0.0018	Shake table test	Frequency ratio 1.4	Khan and Ali, 2019
	EHTMD	Structural panel in a city bus	0.0000136	Shaker test	Force excitation, 2.61g, 43 Hz	Harne, 2013
	Piezoelectric damper	Beam-like structure	\	\	\	Wand and Inman, 2013

Note: 1. The output power in this table might be overestimated because several of the studies regarded either the power input of the harvesting damper or dissipated power by the load resistor as the output power.

2. White background: experimental investigations; shaded background: numerical investigations.

Table 2.6 Comparison of EM and piezoelectric dual-function devices

EM dual-function devices	Piezoelectric dual-function devices
• Can provide passive damping during energy transfer.	• Can provide passive damping during energy transfer, but the damping density is low.
• The provided damping has a direct and simple relation with load resistance, and it is easy to control and realize a large damping density.	• Do not focus on optimal damping control in relevant studies but mitigate the vibration response to some extent.
• Easy to integrate with other components, such as inerters and negative-stiffness dampers, for vibration control.	• No references on piezoelectric inerters or negative-stiffness dampers.
• Can be integrated with other damper types (such as hydraulic and MR dampers) as a pure energy transducer.	• Few references on piezoelectric materials integrated into other damping mechanisms.
• Mostly used for large-scale vibration sources.	• Targeted for small mechanical applications in experimental tests, show potential for large-scale civil applications in simulations.
• Mostly used for low-frequency vibration applications.	• The vibration frequencies of the adopted vibration sources are relatively high.
• Show high feasibility of realizing self-powered semi-active or active vibration control in large-scale applications.	• Can realize self-powered semi-active or active vibration control in small-scale mechanical applications.
• The power is in the order of watts to kilowatts in large-scale applications.	• The power in large-scale applications is predicted to reach the watt level, but no corresponding experimental validation is available.
• A series of simulations, laboratory tests, and field tests have been conducted.	• Investigations mainly remain at the simulation stage; the experimental tests are relatively few.
• Control or power performance depends on the EM transducer size, but it is easy to scale up.	• No practical large-size piezoelectric applications, but the size in simulations is up to meter level.
• The motion rectifier mechanism and circuit bridge rectifier can be used for voltage rectification.	• Only circuit bridge rectifier can be adopted for voltage rectification.

Table 2.7 Objectives of the power harvested by dual-function devices

Objectives	Application scenarios	Damper type	References
Wireless sensors in structural health monitoring	• Building	EHTMD	Shen et al., 2012
	• Bridge stay cable	Hybrid damper	Jung et al., 2011b
	• Bridge stay cable	EHEMD	Kye et al., 2019
Semi-active vibration control	• Vehicle suspension	EHEMD	Xie et al., 2017, 2019; Li et al., 2019
	• Vehicle suspension	Hybrid damper	Choi and Wereley, 2009; Chen and Liao, 2012; Chen et al., 2015; Chen et al., 2018
	• Seat suspension	EHEMD	Ning et al., 2018a, 2018b, 2019
	• Structural isolator	Hybrid damper	Yang et al., 2020
	• Building	EHEMD	Jamshidi et al., 2018
	• Building	Hybrid damper	Cho et al., 2005
	• Bridge stay cable	EHEMD	Jamshidi et al., 2017; Kye et al., 2019
	• Bridge deck	Hybrid damper	Wang et al., 2009
	• Unmanned aerial vehicle	Piezoelectric damper	Wang and Inman, 2012, 2013
Active vibration control	• Vehicle suspension	EHEMD	Suda et al., 1998a, 1998b
	• Structural isolator	EHEMD	Li and Zhu, 2021

2.3 Broadband Energy Harvesting

This section reviews the broadband energy harvesting techniques based on frequency tuning methods. The energy harvesting bandwidth can be widened through the utilization of multi-frequency responses by introducing a coupled bimorph cantilever beam (Yang and Yang, 2009) or an array of cantilever beams with different lengths or tip masses (Shahruz, 2006), as well as the utilization of nonlinearity by introducing high magnetic interactions (Mann and Owen, 2010; Lai et al., 2019), a nonlinear spring (Leadenham and Erturk, 2014), or an amplitude limiter (Soliman et al., 2008). However, the two methods generally result in a more complex design configuration than frequency tuning techniques. The pros and cons of various broadband harvesting techniques and a

detailed comparison can be found in Tang et al. (2010) and Maamer et al. (2019). Figure 2.24 shows the number of published papers per year on frequency tuning in vibration-based energy harvesting.

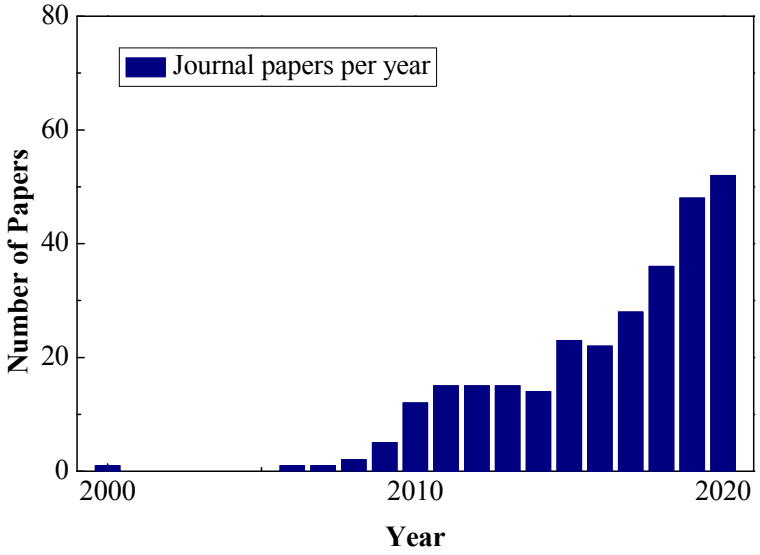

Figure 2.24 Trend of papers in the field of frequency tuning in vibration-based harvester (Scopus search keywords: "frequency" and "tuning" and "energy" and "harvesting")

2.3.1 Impedance Optimization

Frequency tuning methods typically can be categorized into electrical and mechanical tuning methods, wherein the former is essentially realized by adjusting the impedance load. The impedance optimization strategies relevant to the electrical tuning method are reviewed first in this subsection.

Traditional IM has been applied to EHCs to meet the maximum output power condition (Hambley et al., 2013). Zhu et al. (2012) presented a theoretical and experimental study of a linear EM motor connected with four representative circuits when excited by a constant harmonic load. The conditions for maximum output power and efficiency were derived separately, and the corresponding result was consistent with that of the traditional IM strategy. The constant input signal in their derivations assumed that the variation of the EHCs had no effect on the input signal. Such an assumption may not

be true in practical applications when the circuit inevitably affects the dynamics of vibration-based energy harvesters and changes the input signal. The resistance, inductance, and capacitance in the external circuit can be regarded as analogs of the damping, stiffness, and inertance of the primary structure/oscillator, respectively (Firestone, 1933; Zhu et al., 2013; McDaid and Mace, 2013). Ye et al. (2017) conducted a power analysis of an SDOF vibration-based energy harvester. They showed that the generated output power was greatly affected by the excitation frequency and EM damping and stiffness. These parameters influence the structural dynamics of the SDOF harvesters and the EHC efficiency, and thus, such effects should be simultaneously considered to maximize the output power.

Williams et al. (2001) concluded that the maximum output power of an SDOF EM energy harvester corresponds to the following two conditions: (1) the excitation frequency is equal to the natural frequency of the energy harvester, which generates the energy harvester resonance, and (2) the electrical impedance of the load equals the equivalent impedance of mechanical damping. By considering the coil characteristic of an EM harvester, Stephen (2006) found that the maximum output power at a resonance state could be achieved when the load resistance of the circuit was equal to the sum of the coil resistance and electrical analog of the mechanical damping coefficient.

The optimizations in the works by Williams et al. (2001) and Stephen (2006) focused on the ideally resonant state. In a general non-resonant situation, Cheng et al. (2007) determined the maximum power delivered into the electrical load through the complex conjugate of the source impedance and proposed an overall impedance optimization that considered the primary structural characteristic under harmonic excitation. Cammarano et al. (2010) derived a similar optimal result and attempted to retune the resonant state of the energy harvester based on this theory. Later, Cammarano et al. (2014) derived an optimum resistance for a nonlinear energy harvester for a fixed sinusoidal excitation

considering the structural influence by ignoring the internal resistor and inductor of the coil. The analytical results indicated that the optimal resistance was related to several parameters, such as structural frequency, excitation frequency, and mechanical damping.

Similar works have also been reported for piezoelectric harvesters that consider dynamic coupling. Liang and Liao (2011) pointed out that an investigation of harvested power would be misleading if the mechanical dynamics and energy flow of the oscillator were not considered. Liao and Sodano (2018) analyzed the expression of the output power limit for a piezoelectric energy harvester with a resistive circuit, considering the coupling effect, and their result was similar to that for the EM energy harvester reported by Williams and Yates (1996). Liao and Sodano (2009) studied the output power performance of a piezoelectric energy harvester with an *RC* harvesting circuit and analytically determined the optimal impedance. Owing to the strong coupling effect, the energy harvester became a tunable system, and the output performance was enhanced. A similar conclusion regarding an *RL* harvesting circuit was drawn by Renno et al. (2009), who also demonstrated that the introduction of inductive impedance could realize frequency tuning, and thus, a broadband vibration-based energy harvester was formed.

2.3.2 Frequency Tuning

From the mechanical design perspective, vibration-based energy harvesters are effective if their natural frequencies approach the excitation frequencies. However, a slight shift between them results in significant power performance degradation. To handle variable-frequency excitation in practice, different solutions have been proposed to widen the energy harvesting bandwidth. As aforementioned, one of the representative methods is frequency tuning.

2.3.2.1 Electrical Method

The frequency tuning method that adjusts the impedance load of the EHC is

categorized as electrical tuning. Wu et al. (2006) presented a theoretical analysis and experimental study on a piezoelectric cantilever-beam energy harvester with resonant frequency tuning; the harvester had a bimorph structure, with the upper panel used to tune the natural frequency of the beam and the bottom panel used to harvest energy. The natural frequency of the system could be tuned from 91.5 to 94.5 Hz by connecting different capacitances to the upper panel, thereby providing energy harvesting performance with a broader bandwidth. Compared with the untuned system, the energy performance improvement under chirping-frequency excitation and random excitation were 13.4% and 27.4%, respectively. They validated the concept of real-time frequency tuning through an electrical load, although the microcontroller used to sample the excitation frequency and alter the capacitive load in this experiment consumed tens of milliwatts of power. Similar results have been reported by Charnegie (2007), who tuned a bimorph piezoelectric energy harvester by changing the load capacitance. Five different beams were tested, and the maximum frequency change of 5.9 Hz was realized.

Cammarano et al. (2010) put forward the first proof of concept using complex load to tune an EM energy harvester. An experimental frequency tuning range from 57.4 to 66.5 Hz was realized using either a capacitor or inductor. Zhu et al. (2012) presented a more generalized model for an electrically tunable EM harvester and its corresponding experimental validation. Parametric analysis demonstrated that a strong machine constant was required to achieve a wide frequency tuning range. The frequencies of two EM energy harvesters of different scales were successfully tuned by varying the connected capacitive load in the experiment. The micro-scale harvester was tuned by merely 0.23 Hz, and the macro-scale harvester was tuned by 3.8 Hz, with the connected capacitance increasing from 0 to 4000 nF and from 0 to 1400 nF, respectively. Mallick and Roy (2015) presented a bidirectional electrical tuning strategy for an EM energy harvester using complex electric load. The concept of using capacitive and inductive load to tune lower and higher frequencies of the EM harvester, respectively, was experimentally validated

through four different prototypes, wherein the realized tuning upper and lower bounds were 1.8 and 0.6 Hz, respectively.

Notably, these aforementioned electrical tuning approaches were all based on discrete electronic components. Mitcheson et al. (2011) studied for the first time the feasibility of using an H-bridge electronic interface for energy harvesting by synthesize impedance over a continuously variable range. In the experiment on an EM pendulum-type energy harvester, a ±10% change in resonant frequency was achieved by electrically varying the impedance. Later, Toh et al. (2011) demonstrated an application of this electrical tuning method to two different EM wave energy harvesters. The specific design, tuning algorithms, and challenges of the frequency tuning method using an H-bridge electronic circuit interface were presented by Bowden et al. (2014). Note that the electrical tuning methods have also been explored for adaptive vibration control (McDaid and Mace, 2013).

2.3.2.2 Mechanical Method

Peters et al. (2009) attempted to realize frequency tuning using piezoelectric actuation method. Their system consisted of two actuators (a clamped and a free one) and three small hinges, wherein the free actuator worked as an adjustable stiffness element for the system by supplying voltage. In the case study of an EM energy harvester, a frequency tuning range from 42 to 55 Hz was realized. Although the frequency tuning was realized by applying an electrical signal, i.e., different voltages, such a tuning method using piezoelectric actuators was regarded as mechanical tuning.

Challa et al. (2008) utilized magnetic forces to realize frequency tuning and thus improved the energy harvesting performance. A piezoelectric cantilever beam harvester with an initial natural frequency of 26 Hz was adopted to validate this proposed technique involving four magnets; two of the magnets were attached to the free end of the beam,

and the other two were attached to the bottom and top of the enclosure near the beam. They reported a tuning range from 22 to 32 Hz and a power range from 240 to 280 μW at an input acceleration amplitude of 0.08 g. Eichhorn et al. (2008) proposed a frequency tuning approach by applying an axial prestress that was realized by the revolution of a screw. Experimental validation was conducted on a piezoelectric cantilever beam harvester comprising two winds connecting the tip of the beam and the arms, and the results showed that frequency tuning from 292 to 380 Hz could be achieved. Aboulfotoh et al. (2013) designed an energy harvester with tunable frequency based on magnetic forces. Unlike the aforementioned configurations, the harvester consisted of a cantilever beam carrying a magnet as the tip mass, which was placed close to another movable magnet mounted on a motor-driven tray (Figure 2.25). A microprocessor was introduced to detect the excitation frequency and determine the distance between these two magnets, forming a complete control loop to realize real-time frequency tuning. An additional magnet and coil were applied to transfer the vibration energy in this system, and frequency tuning from 4.7 to 9 Hz was realized in the experiment. A similar experimental setup was reported by Zhu et al. (2011). The frequency was tuned from 35 to 68 Hz under tensile loads and from 1.2 to 18 Hz under compressive loads. The tensile and compressive loads were achieved by changing the polarity of the movable magnets. Note that if the interacting magnetic force was high, the system behavior became nonlinear.

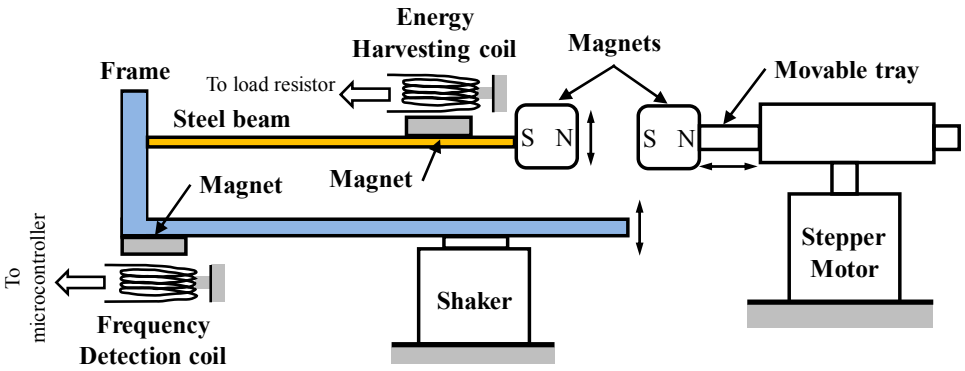

Figure 2.25 Frequency tuning EM energy harvester presented by Aboulfotoh et al. (2013)

(Reused with permission from Elsevier.)

Recently, the concept of self-tuning has been explored for broadband energy harvesting. Thus far, studies on self-tuning have been reported for a string, beam, or rigid plate with a moving mass that tends to move to the equilibrium location along the axis of the base system at a steady state. The equilibrium location depends on the excitation frequencies, and the steady location determines the natural frequencies of the system (Krack et al., 2017). Therefore, such a self-tuning method likely belongs to a nonlinear method. Miller et al. (2013) presented three types of self-tuning vibration-based beam harvesters with a sliding proof mass. Different materials were used to construct the fixed-fixed beam, and the experimental results demonstrated that for a given harmonic excitation, the sliding mass moved automatically along the beam until it reached a position where the natural frequency of the beam matched the excitation frequency. In the experiment, all three types of harvesters displayed self-tuning behavior with a beam length of 6 and 30 cm at frequencies from 45 to 140 Hz and acceleration input from 0.007 to 2 g. According to the experimental results, Krack et al. (2017) provided a theoretical explanation for the self-tuning behaviors based on nonlinear dynamics. Based on this beam–sliding mass configuration, Staaf et al. (2018) proposed and modeled a 4DOF self-tuning energy harvester comprising an array of cantilever beams, wherein a middle beam with a sliding mass was connected by two piezoelectrical cantilevers. The effect of the length of the middle beam on the harvesting performance was analyzed, and a relatively longer beam showed superior performance. Subsequently, they experimentally verified the effectiveness of the proposed numerical model, and investigated the effect of the asymmetric setup corresponding to different piezoelectric cantilever beam lengths and different applied additional mass locations on the self-tuning performance. The results demonstrated that the appropriate asymmetry caused by the different lengths of piezoelectric cantilever beams benefited the tuning performance, whereas the added mass completely locked the frequency tuning function (Staaf et al., 2019). More recently, Bukhari et al. (2020) explored the feasibility of a self-tuning cantilever beam with an EM transducer as the tip mass. The numerical results demonstrated that the natural frequency

of the system varied from 7.2 to 8.4 Hz when the sliding mass moved along the beam. An experiment was performed to verify the numerical analysis and analyze the impacts of friction and backlash that were not considered in the modeling. Different factors of the mass–slider configuration that influence tuning performance have also been investigated. These factors include initial inclination (Yu et al., 2019), integration with repulsive magnets (Yu et al., 2020), and clearance between the slider and the beam (Pillatsch and Miller, 2013).

2.3.3 Summary and Comparison

Table 2.8 summarizes the aforementioned studies on energy harvesters with tunable frequencies. Electrical and mechanical methods for EM or piezoelectric energy harvesters have been tested. In previous studies, the maximum frequency tuning range was approximately 25 Hz for electrical methods (Bowden et al., 2014) and approximately 88 Hz for mechanical methods (Eichhorn et al., 2008). Moreover, it is also noted that the covering frequencies of the piezoelectric harvesters were typically larger than 10 Hz to obtain an effective output.

Table 2.8 Survey of frequency-tuning energy harvesters

Transducer	Methods/Theories	Bandwidth (Hz)	References
Piezoelectric	Electrical load	91.5–94.5	Wu et al., 2006
Piezoelectric	Electrical load	342.6–348.5	Charnegie, 2007
EM	Electrical load	57.4–66.5	Cammarano et al., 2010
EM	Electrical load	91.3–95.1	Zhu et al., 2012
EM	Electrical load	1.05–1.29	Mitcheson et al., 2011
EM	Electrical load	0.94–1.23	Toh et al., 2011
EM	Electrical load	54.5–78.8	Bowden et al., 2014
EM	Electrical load	56.8–59.17	Mallick and Roy, 2015
Piezoelectric	Magnetic	22–32	Challa et al., 2008
Piezoelectric	Prestress	292–380	Eichhorn et al., 2008
EM	Piezoelectric actuator	42–55; 66–89	Peters et al., 2009
EM	Magnetic	4.7–9	Aboulfotoh et al., 2013
EM	Magnetic	35–68; 1.2–18	Zhu et al., 2011
\	Beam–mass sliding	45–140	Miller et al., 2013
Piezoelectric	Beam–mass sliding	360–400	Staaf et al., 2018
EM	Beam–mass sliding	7.2–8.4	Bukhari et al., 2020

2.4 Summary

Figure 2.26 illustrates the potentially harvestable power in the aforementioned simulation or experimental studies, wherein the dot points denote the harvested power from the cited references. The four cases (vehicle suspension, building, bridge/bridge stay cable, and other structures) cover the typical implementation scenarios of the investigated dual-function devices, in which the harvested power can be up to several kilowatts. Such a power level is believed to be sufficient to meet the power requirement for sensors, controllers, computers, or semi-active dampers. However, special caution should be exercised when comparing the harvested power (or power efficiency) presented in Tables 2.3, 2.4, 2.5, and Figure 2.26. Some are based on numerical simulations of ideal and oversimplified situations, whereas others are based on realistic simulations or even experiments that consider various power losses. For example, the output power estimated based on a constant load resistor is considerably higher than that estimated based on practical EHCs. The relationships between overestimated and practical output power are

indicated by the power flow in Figure 2.28, which demonstrates the energy conversion process from excitation power to practical output power in batteries or supercapacitors and the potential power losses. Regarding the power into dual-function devices or into a pure resistor as output power will result in overestimation.

Although both EM and piezoelectric transducers have proven merits in dual-function applications or broadband energy harvesting, EM transducers are easier to scale up, as aforementioned; moreover, they show better harvestable power performance, especially considering that they are more suitable for the low-frequency vibrations and large-scale scenarios that this thesis focuses on. Hence, the EM transducer was employed and systematically investigated in the following chapters of this thesis.

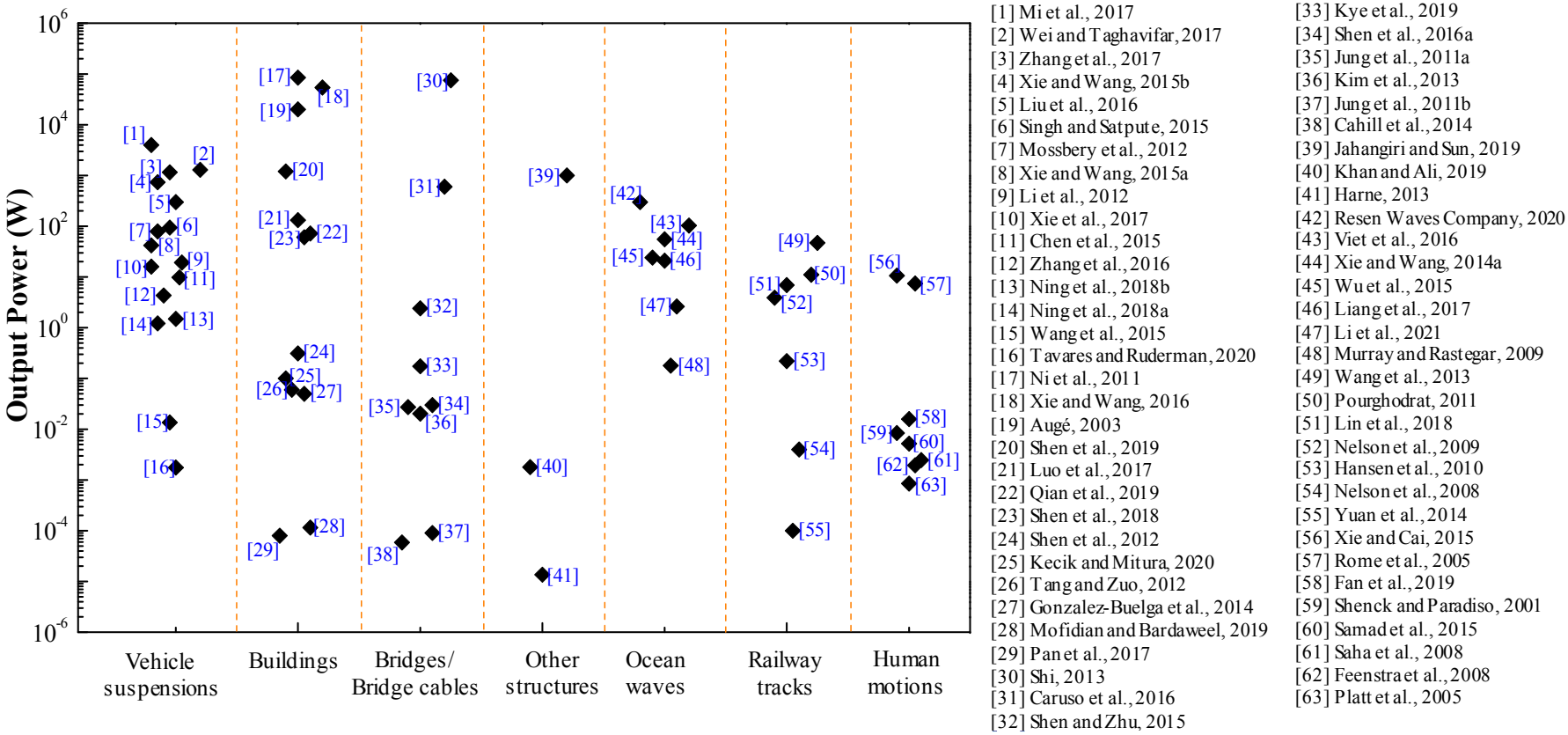

Note: The harvested power in this plot might be overestimated because some studies regarded either the input power into the harvesting damper as or dissipated power by the load resistor as the output power

Figure 2.26 Summary of the harvested power in the aforementioned studies

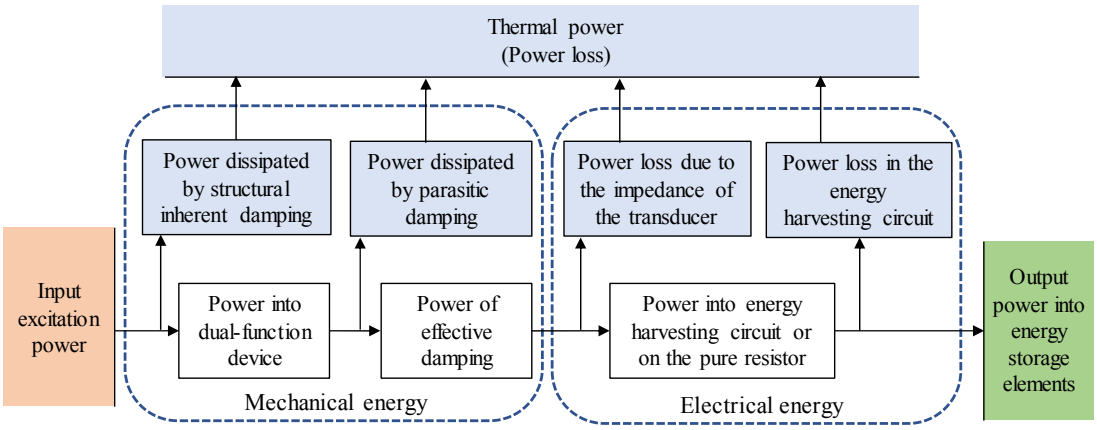

Figure 2.27 Power flow of a structure with dual-function devices

2.5 Research Remarks

Considering the emerging power demand for wireless sensors at remote sites or semi-active/active vibration control strategies, vibration-based energy harvesting techniques offer a reliable, robust, and attractive solution to meet the required demand. Although previous studies have to some extent demonstrated the feasibility of powering wireless sensors or semi-active/active control by using vibration-based energy harvesters, the development of vibration-based energy harvesting techniques and systems remains in its infancy.

This thesis aims to enhance the functionality and performance of vibration-based EM energy harvesters. The underlying principles of this thesis are as follows:

- A strong electromechanical coupling effect between a structure (a vibration source) and a scaled-up energy harvester (including EHC) makes the vibration-based energy harvester a dual-function device with simultaneous vibration control and energy harvesting functions, e.g., EHEMD.
- A strong coupling effect within the energy harvester, i.e., between the harvesting oscillator and the EHC, makes the electrical frequency tuning a possible alternative to mechanical tuning, both of which help to achieve broader energy harvesting bandwidth.

These two strategies, either the integration with vibration control function or the broadband energy harvesting via frequency tuning, is to enhance the functionality and performance of the conventional vibration-based energy harvesters by considering the coupling effect.

According to the literature review, most of the previous studies on either dual-function devices or pure energy harvesters estimated the output power based on a pure resistor. However, such a power assessment usually leads to overestimation owing to the overlook of power loss in EHCs (see Figure 2.27). How to design an EHC that can function as a stable equivalent resistor for practical output power estimation remains an unanswered question. For example, the impedance-emulation EHCs developed in the past exhibited voltage-dependent characteristics and encountered performance degradation under large vibration scenarios.

Although previous studies have to some extent demonstrated the effectiveness of the dual-function devices in different applications, few full-scale experimental tests in civil structures with dual-function devices have been reported. Experimental validations of dual-function devices installed in full-scale structures are of practical significance. Meanwhile, the controllable resistance feature of the EHC naturally inspires an exploration of energy-harvesting adaptive damping, showing better vibration control performance compared with passive damping. In addition to the demonstration of the effectiveness of the dual-function devices, optimization regarding vibration control and energy harvesting performance is another fundamental issue that needs to be addressed.

As for a pure energy harvester with frequency tuning function, insufficient attention has been paid to the harvesting performance optimization while considering different strengths of electromechanical coupling effect. A strong coupling effect makes the classical IM no longer valid. Meanwhile, the electrical frequency tuning approach

becomes an alternative to mechanical tuning. Although energy harvesters with tunable ultra-low frequencies are highly desirable for low-frequency vibration scenarios (such as vibrations of civil structures and ocean waves), few energy harvesters can reach ultra-low-frequency (<1 Hz) even with the use of frequency tuning (electrical or mechanical) technologies.

To fill in the above-mentioned knowledge gaps, this thesis presents systematical investigations on the two types of vibration-based EM energy harvesters, namely dual-function devices and pure energy harvesters with frequency tuning. Table 2.9 summarizes the considered knowledge gaps and the corresponding solutions offered in different chapters. Note that the EM transducer is also termed EMD, EM motor, or EM device in the literature, depending on the focus of the study. This thesis adopts “EMD” in the succeeding chapters for consistency.

Table 2.9 Specific knowledge gaps and the corresponding solutions in this thesis

	Existing knowledge gaps or deficiencies	Solutions
Chapter 3	Nonlinear characteristics of EHC in the previous studies result in performance degradation in larger-vibration scenarios.	Introduce an MCU to realize feed-forward control in EHCs and controllable equivalent constant resistance.
Chapter 4	Performance validation of a passive EHEMD installed in a full-scale structure is desirable.	Conduct a 135 m–long stay cable experiment with an EHEMD consisting of an EMD and an EHC as proposed in Chapter 3.
Chapter 5	Can an energy-harvesting adaptive vibration control strategy be achieved by using EHEMDs?	Investigate the performance of adaptive EHEMDs installed in the secondary suspension of an HST model.
Chapter 6	The question on whether the energy harvesting and vibration control is consistent or not in EHEMD, EHTMD, and EHTID remains unclear.	Individually analyze the coupled systems of an SDOF structure with EHEMD, EHTMD, and EHTID with respect to two optimization objectives.
Chapter 7	How to optimize the impedance of an EM harvester subjected to harmonic or random excitation considering strong coupling effects?	Propose a unified overall impedance optimization strategy that is applicable to different strengths of coupling effects, different structural complexities, and different excitation types. Electrical tuning methods were suggested.
Chapter 8	Few of the existing vibration-based energy harvesters can realize ultra-low frequencies even with the aid of frequency tuning technologies.	Design a DMP-based energy harvester with tunable ultra-low frequencies ranging from 0.2 to 1.4 Hz and validate its energy harvesting performance through shake table tests.
Chapter 9	The performance of the DMP-based WEC under wave excitations is unknown.	Conduct a wave flume test for such a DMP-based WEC to assess its frequency tuning and energy extraction performance.

CHAPTER 3

EM ENERGY HARVESTERS

3.1 Introduction

As mentioned in Chapter 2, EMDs are selected as the energy transducers in vibration-based energy harvesters in this thesis, as they are easier to scale up and more suitable for the low-frequency vibrations and large-scale scenarios that are the focus of this thesis.

When an EMD is connected to an EHC, the impedance characteristic of the EHC determines the energy harvesting performance and damping characteristic of the EM energy harvester. In many energy-harvesting applications, including dual-function dampers, a steady equivalent resistance of the EHC is desirable to maintain the target optimal harvesting or damping performance. Shen and Zhu (2015) adopted a fixed-duty-cycle buck–boost converter as the main part of the EHC, which operated in discontinuous conduction mode (DCM) and continuous conduction mode (CCM) at low and high input voltage, respectively, in an EHEMD installed in a stay cable considering buffeting vibration. In DCM, the inductor current in the EHC is discrete within each switching cycle, whereas CCM corresponds to continuous inductor current. This adopted EHC exhibited a constant resistance characteristic when operating in DCM. However, when the vibration amplitude was high, this EHC operated in CCM and exhibited a reduced equivalent resistance, resulting in the degradation of both vibration control and energy harvesting performance at a high wind excitation level. An improved version of the EHC is desired to overcome this performance limitation.

This chapter presents the basic components of an EM energy harvester, in which an MCU is employed to implement a feed-forward control in the EHC. A duty-cycle-controllable buck–boost converter is adopted as the main part of the EHC. The proposed EHC can achieve the target controllable resistance characteristic and improve the output power efficiency, regardless of whether the buck–boost converter operates in DCM or CCM. In the following sections, the influence of the duty cycle on the equivalent resistance of the EHC, damping performance, and energy harvesting efficiency is introduced first. The equivalent resistance and conversion efficiency of the EHC with or without feed-forward control were experimentally tested, and the results were compared with those of the established Simulink model. Subsequently, the damping characteristic and energy harvesting performance of the EM energy harvester were investigated through cyclic experimental tests.

3.2 Configuration of EM Harvester

The configuration of the EM energy harvester is introduced through two types of the simplest models shown in Figure 3.1. In the first configuration comprising the EMD and EHC, the energy from the vibration sources is directly extracted by the EMD and converted to electrical energy. In the second configuration, wherein an external vibration oscillator is applied, the vibration source induces the oscillator motion, in which the damping energy is converted into electrical energy by the EMD and stored in the EHC. In Figure 3.1, the structural vibration source (e.g., bridge stay cable or vehicle) is simplified as an SDOF structure. It needs to clarify that the harvested power is essentially the to-be-dissipated damping power.

Notably, the basic characteristic that distinguishes the two types of EM energy harvesters in this thesis is whether the EM energy harvester has a significant effect on the vibration source. For example, if the oscillator mass is sufficiently large, the topology in Figure 3.1(b) should represent an EHTMD, which should function as a dual-function device, whereas if the mass is minimal compared with the structural (vibration source)

mass, it should function as a pure vibration-based energy harvester. The first type, i.e., the dual-function damper, is investigated in Chapters 4–6, whereas the second type, i.e., the pure energy harvester, is studied in Chapters 7–9, with a focus on broadband energy harvesting performance. The EMD and EHC are two indispensable components of both types of EM energy harvesters.

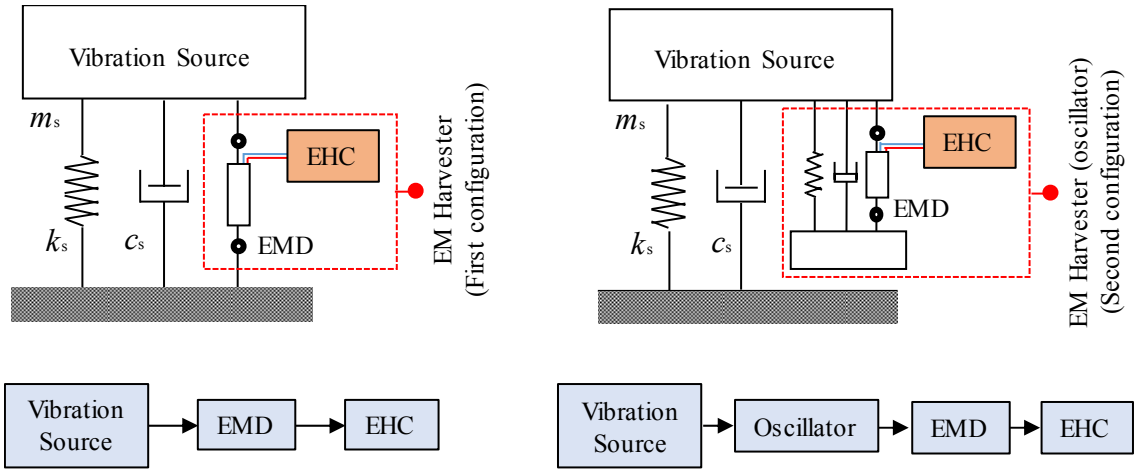

(a) First configuration (b) Second configuration

Note: m_s, k_s, and c_s are the mass, stiffness, and damping coefficients of the vibration source, respectively.

Figure 3.1 Schematic of EM energy harvesters

3.3 EMD

3.3.1 Physical Model

Palomera-Arias (2005) proposed a two-port physical model to represent the EMD wherein the parasitic damping was not included. Note that the EMD provides the parasitic damping c_p owing to various mechanical losses (e.g., friction and iron loss) when the EMD oscillates. Shen (2014) claimed that this parasitic damping cannot be overlooked when modeling an EMD; therefore, he proposed a modified model of the EMD (Figure 3.2), wherein f_p and f_{em} are the parasitic and EM damping forces, respectively; K_{eq} denotes the machine constant (unit: V·s/m or N/A) dependent on the geometric and magnetic properties of the EMD, also known as back electromotive force (EMF) constant and force constant; and R_{coil} and L_{coil} are the coil characteristics. Based on a systematic survey of

the commercially available EM motors, it is found that coil inductance is normally much smaller than coil resistance (Figure 3.3). This finding implies that only if the excitation frequency is as high as hundreds of Hertz, can the coil inductive reactance and resistance reach the same order of magnitude. The symbols U_o and i represent the generated back EMF and the current flowing through the coils, respectively. The main relationship between these parameters is described in the following subsection.

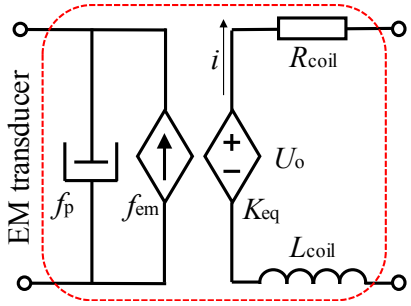

Note: EMD parameters R_{coil} and L_{coil} can be measured using an LCR meter, and K_{eq} and f_p can be estimated through an MTS test with an open circuit.

Figure 3.2 Physical model of the EMD (Shen, 2014)

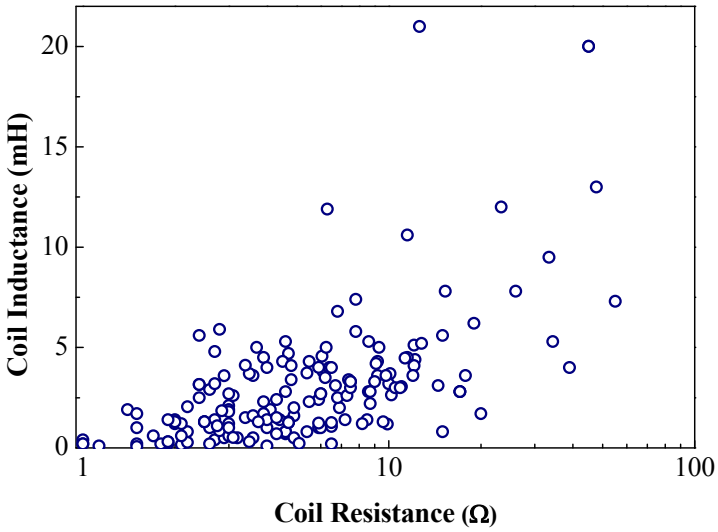

Figure 3.3 R_{coil} and L_{coil} in commercially available motors

3.3.2 Fundamental Principle

As aforementioned, a passive EMD is essentially an EM transducer whose working principle is mainly based on EM induction. According to Faraday's law, a back EMF is

generated in the coil if the coil and magnets move relative to each other. There is a proportional relationship as follows (Palomera-Arias, 2005):

$$U_{\mathrm{o}} = K_{\mathrm{eq}} \dot{x}_{\mathrm{d}} \tag{3.1}$$

where U_{o} is the back EMF; K_{eq} is the machine constant; and $\dot{x}_{\mathrm{d}}$ is the relative velocity between the coils and magnets.

According to Lorentz's law, this back EMF produces a current if the connected circuit is closed. Correspondingly, a damping force is generated as follows:

$$f_{\mathrm{em}} = K_{\mathrm{eq}} i \tag{3.2}$$

where f_{em} is the damping force, and i is the instantaneous current passing through the coils. Palomera-Arias et al. (2008) compared the damping density of the EMD with that of viscous fluid dampers, showing the limit performance of the EMD. To enhance the damping/energy performance, a rotational EMD with linear-to-rotation motion converters (e.g., ball screw and rack-and-pinion converter) and a gearhead are usually used together.

Considering the small value of the coil inductance, its effect is nearly negligible in the case of low-frequency vibration scenarios, such as civil structural vibrations and ocean waves. When an EMD is connected to a constant resistor, the current passing through the coils can be given as follows:

$$i = \frac{U_{\mathrm{o}}}{R_{\mathrm{load}} + R_{\mathrm{coil}}} \tag{3.3}$$

where R_{load} is the load resistance at the terminals. In this regard, the EM damping force and coefficient are given as follows:

$$f_{\mathrm{em}} = \frac{K_{\mathrm{eq}}^2}{R_{\mathrm{load}} + R_{\mathrm{coil}}} \dot{x}_{\mathrm{d}} \tag{3.4}$$

$$c_{\mathrm{em}} = \frac{K_{\mathrm{eq}}^2}{R_{\mathrm{load}} + R_{\mathrm{coil}}} \tag{3.5}$$

Equation (3.5) reveals the damping effect of the EMD with a resistor, which has also been reported by Stephen (2006) and Shen (2014). Considering the aforementioned parasitic damping, the total damping of the EMD is given as:

$$c_{\mathrm{d}} = c_{\mathrm{em}} + c_{\mathrm{p}} \tag{3.6}$$

Evidently, the total damping coefficient of an EMD has a natural boundary:

$$c_{\mathrm{p}} \le c_{\mathrm{d}} \le \frac{K_{\mathrm{eq}}^2}{R_{\mathrm{coil}}} + c_{\mathrm{p}} \tag{3.7}$$

The left item shows the lower limit, representing the open-circuit scenario when $R_{\mathrm{load}} = \infty$ and the EM damping is nearly zero; the right item shows the upper limit, which occurs in the short-circuit case when $R_{\mathrm{load}} = 0$. Equations (3.5–3.7) provide an alternative method to realize damping adjustment by tuning the load resistance.

3.4 EHC

3.4.1 Basic Requirements

The vibration energy in either the first or second configuration is converted into electrical energy by the EMD and further stored in the shunted EHC. In the EHC, the supercapacitor or rechargeable battery is usually used as the energy storage element. The rechargeable battery shows its merits such as high power density and low self-discharge rate (Casciati and Rossi, 2007), but it requires strict charging conditions, i.e., voltage regulation before charging.

In vibration control, an optimal damping coefficient is often required, which can be achieved by selecting a target optimal resistance R_{load}. When the EMD is connected to an EHC, R_{load} refers to the equivalent resistance R_{ehc} of the entire EHC. The variation in the R_{ehc} of the EHC inevitably leads to the deviation from the optimal damping coefficient and degradation of the vibration control performance. In energy harvesting, the classical IM offers the optimal output power in the case of a given power source, thereby also requiring a target optimal resistance. Therefore, an EHC with a nearly constant resistor is

often favorable from the vibration control and energy harvesting perspectives.

3.4.2 Equivalent Resistance Circuit

Previously, a fixed-duty-cycle buck–boost converter was employed as the main part of an EHC because of its steady resistance. Compared with flyback and sepia circuits, the buck–boost converter requires fewer components and a simpler configuration. Lefeuvre et al. (2007) employed a DCM fixed-duty-cycle buck–boost converter in the EHC to match the target resistance. Shen et al. (2015, 2016a) further extended its application to the EHEMD system, in which the fixed-duty-cycle buck–boost converter can only maintain a constant resistance required for vibration control and energy harvesting functions on condition that the circuit operates in DCM.

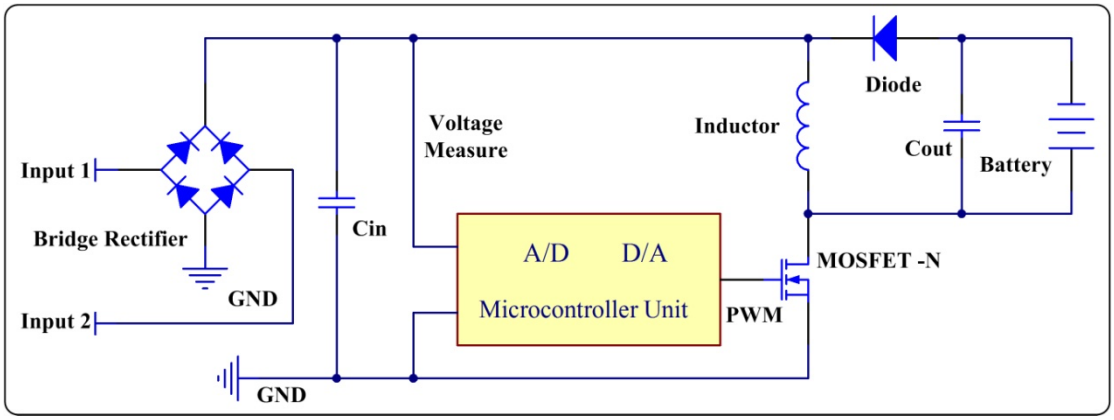

Note: A/D and D/A refer to analog-to-digital and digital-to-analog conversion, respectively.

Figure 3.4 Schematic of the proposed EHC with an MCU

This subsection presents a specially designed EHC with a controllable duty cycle (Figure 3.4). The EHC consists of a full-wave bridge rectifier that transforms alternating current (AC) to DC, an input capacitor to smoothen the rectifier voltage waveform, a classical buck–boost circuit that charges a rechargeable battery, and an MCU to adaptively regulate the duty cycle of the PWM on the basis of the measured rectifier voltage. The two left leads of the MCU are used to sense the rectifier voltage, and the right lead outputs the PWM signal. Compared with the traditional fixed-duty-cycle buck–boost converter, the proposed EHC introduces an MCU that enables the duty cycle

adjustment according to the feed-forward signal (i.e., the measured rectifier output voltage U_{rect}).

In practice, the buck–boost converter operates in DCM when the following condition is met:

$$U_{\text{ind}} < \frac{1-\delta}{\delta}\left(U_{\text{bat}} + U_{\text{F}}\right) \tag{3.8}$$

where U_{bat} is the voltage of the rechargeable battery; U_{F} is the voltage drop on the diode connected to the battery; U_{ind} is the inductor voltage when the MOSFET is turned on; and δ is the duty cycle. Otherwise, the buck–boost circuit operates in CCM. If $U_{\text{F}} << U_{\text{bat}}$, then U_{F} is often negligible. However, U_{F} is not small enough and needs to be considered in the following test. Figures 3.5(a) and 3.5(b) show the typical waveforms of the inductor current and voltage for DCM and CCM, respectively, wherein T_{w} is the duration of each switching cycle, τ in Figure 3.5(a) denotes the charging time within a switching period in DCM, and I_{aver} in Figure 3.5(b) denotes the average current that passes the inductor in CCM. The inductor current is discrete in DCM (i.e., the current falls to zero in each switching cycle), while it is continuous in CCM (i.e., the inductor current is always greater than zero in each switching cycle).

The equivalent resistance of the buck–boost converter can be estimated as follows:

$$R_{\text{eq}} = \begin{cases} \dfrac{2Lf_{\text{w}}}{\delta^2} + \dfrac{R_{\text{on}}}{\delta} & \textit{if DCM} \\ \dfrac{1-\delta}{\delta}\dfrac{U_{\text{rect}}}{\langle i_{\text{bat}} \rangle} & \textit{if CCM} \end{cases} \tag{3.9}$$

where R_{eq} is the equivalent resistance of the buck–boost converter; L is the inductance used in the circuit; R_{on} denotes the static drain-source on-resistance of the MOSFET; U_{rect} is the instantaneous rectifier output voltage; f_{w} is the switching frequency of the PWM; and $\langle i_{\text{bat}} \rangle$ represents the average charging current in a switching cycle in CCM. In addition, R_{on} is typically negligible in comparison with the equivalent resistance R_{eq}. When the input voltage is sufficiently high so that the voltage drop due to the bridge

rectifier is negligible, the average resistance R_{ehc} of the EHC is approximately equal to the equivalent resistance R_{eq} of the buck–boost converter. The "*if* DCM" and "*if* CCM" in Equation (3.9) describe the operation modes of the buck–boost converter.

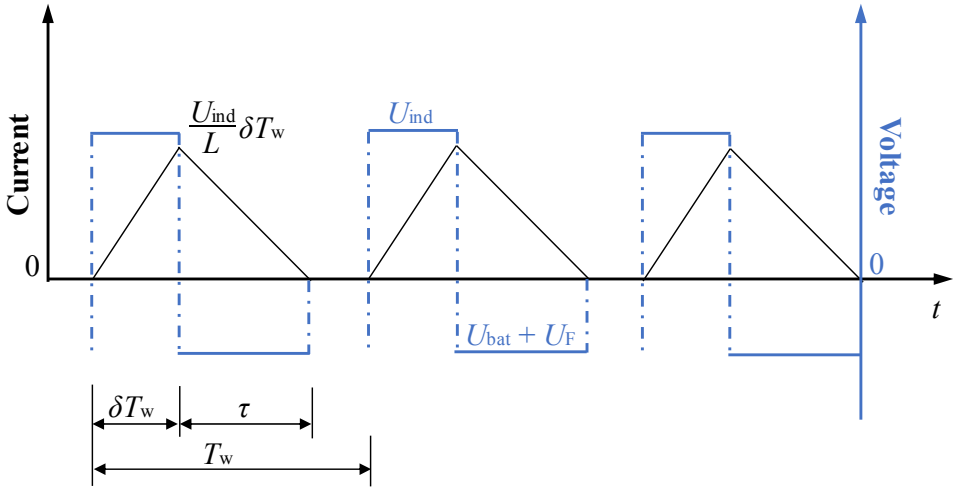

(a) Discontinuous conduction mode (DCM)

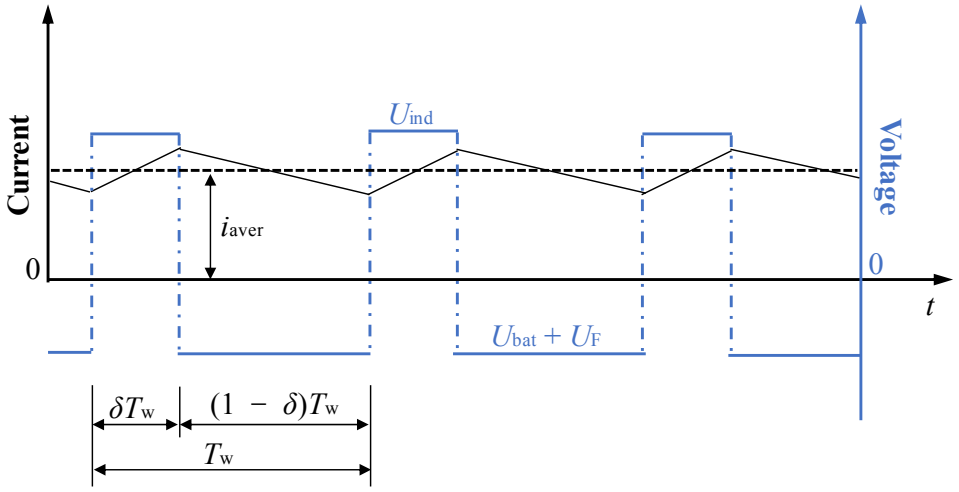

(b) Continuous conduction mode (CCM)

Figure 3.5 Waveform of the inductor current and voltage in the buck–boost converter

According to Equation (3.9), given a fixed duty cycle δ, the buck–boost converter can emulate a constant resistance in DCM. However, the equivalent resistance R_{eq} is dependent on the input voltage U_{rect} in CCM. An increase in the input voltage U_{rect}, which means a large vibration amplitude in the EM energy harvester, generally leads to an increasing charging current and decreasing equivalent resistance R_{eq} of the circuit in CCM.

Equation (3.5) shows that the reduction in R_{eq} leads to a large damping coefficient. In some vibration control applications, the damping coefficient is expected to be maintained close to the optimal value; too large or too small damping coefficients result in the degradation of vibration control performance.

The energy conversion efficiency of the fixed-duty-cycle buck–boost converter can be presented approximately as:

$$\eta_3 = \begin{cases} \dfrac{2Lf_w}{\delta^2 R_{eq}} \dfrac{U_{bat}}{U_{bat}+U_F} & if \text{ DCM} \\ \dfrac{1-\delta}{\delta} \dfrac{U_{bat}}{U_{rect}} & if \text{ CCM} \end{cases} \tag{3.10}$$

where η_3 is the energy efficiency of the buck–boost converter, which represents a sub-efficiency of the harvester, as described in the following subsection. Given a fixed duty cycle, the energy conversion efficiency can maintain a relatively high level in DCM while showing a decreasing trend with increasing input voltage.

The decreased resistance and energy conversion efficiency in CCM represent unfavorable limitations of the fixed-duty-cycle buck–boost converter in the EM energy harvester when subjected to large-amplitude vibrations. However, Equations (3.8) and (3.9) indicate that under a large-amplitude vibration, the desirable resistance can be maintained by two means. First, the buck–boost converter should be kept in DCM even under large vibration amplitudes by increasing the voltage of the rechargeable battery U_{bat} to expand the operational range of DCM. Second, if the duty cycle δ is not fixed, then a CCM buck–boost converter can also realize the target desirable resistance by adjusting the duty cycle δ according to the rectifier voltage U_{rect}. The latter is adopted in this thesis because increasing the battery voltage may cause difficulty in the charging process when the rectifier voltage is much lower than the battery voltage. The duty cycle adjustment is based on the following observations from Equation (3.9): in CCM, an increasing rectifier voltage U_{rect} will lead to a decreasing equivalent resistance of buck–boost converter; but if the duty cycle δ is reduced, then the equivalent resistance R_{eq} increases accordingly.

Consequently, when the rectifier voltage U_{rect} increases in CCM, it is possible to achieve a constant R_{eq} by reducing the duty cycle δ. However, this observation only provides a general direction for the duty cycle adjustment, and the analytical relationship is not available in the literature. Thus, an empirical relationship between U_{rect} and δ to achieve a constant R_{eq} is introduced in the next subsection. Meanwhile, the decrement in duty cycle δ improves the energy conversion efficiency in CCM, according to the aforementioned observation. Therefore, the rectifier output voltage is measured as the feed-forward signal in the duty cycle control.

3.5 Power Flow in Harvester

This subsection presents the power efficiency by discussing the power flow in the entire energy harvesting system. In an energy harvesting process, power losses and consumptions are inevitable when power flows through the EMD and EHC to the battery, as described in Figure 3.6. Consequently, only a portion of the power generated from vibrations can be harvested. The total generated power P_{in} is the summation of the dissipative power P_{p} induced by the parasitic damping, the power loss P_{coil} owing to coil resistance, the power loss P_{brg} owing to the voltage drop of the full-wave bridge rectifier, the power consumption P_{bbc} of the buck–boost converter, and the effective output power P_{out}. All power terms mentioned in this chapter refer to the average power unless otherwise stated. The specific power terms in Figure 3.6 can be calculated as follows:

$$P_{\text{in}} = \frac{1}{T_{\text{w}}}\int_{t_0}^{t_0+T_{\text{w}}} f_{\text{d}}(t)\dot{x}_{\text{d}}(t)\,dt \tag{3.11a}$$

$$P_{\text{p}} = \frac{1}{T_{\text{w}}}\int_{t_0}^{t_0+T_{\text{w}}} c_{\text{p}}(t)\dot{x}_{\text{d}}^2(t)\,dt \tag{3.11b}$$

$$P_{\text{coil}} = \frac{1}{T_{\text{w}}}\int_{t_0}^{t_0+T_{\text{w}}} R_{\text{coil}}(t)i^2(t)\,dt \tag{3.11c}$$

$$P_{\text{out}} = \frac{1}{T_{\text{w}}}\int_{t_0}^{t_0+T_{\text{w}}} U_{\text{bat}}(t)i_{\text{bat}}(t)\,dt \tag{3.11d}$$

$$P_{\mathrm{g}} = \frac{1}{T_{\mathrm{w}}} \int_{t_0}^{t_0+T_{\mathrm{w}}} U_{\mathrm{i}}(t) i(t) dt \tag{3.11e}$$

$$P_{\mathrm{rect}} = \frac{1}{T_{\mathrm{w}}} \int_{t_0}^{t_0+T_{\mathrm{w}}} U_{\mathrm{rect}}(t) i_{\mathrm{rect}}(t) dt \tag{3.11f}$$

$$P_{\mathrm{em}} = P_{\mathrm{in}} - P_{\mathrm{p}} \tag{3.11g}$$

$$P_{\mathrm{brg}} = P_{\mathrm{g}} - P_{\mathrm{rect}} \tag{3.11h}$$

$$P_{\mathrm{bbc}} = P_{\mathrm{rect}} - P_{\mathrm{out}} \tag{3.11j}$$

where f_{d} denotes the damper forces provided by the EMD; $\dot{x}_{\mathrm{d}}$ denotes the relative velocity of the transducer; c_{p} and R_{coil} are the parasitic damping coefficient and coil resistance of the EMD, respectively; i and i_{bat} are the instantaneous current through the coil and into the battery, respectively; $|i|$ is approximately equal to the instantaneous rectifier current i_{rect}; and U_{i} is the instantaneous output voltage from the EMD coil.

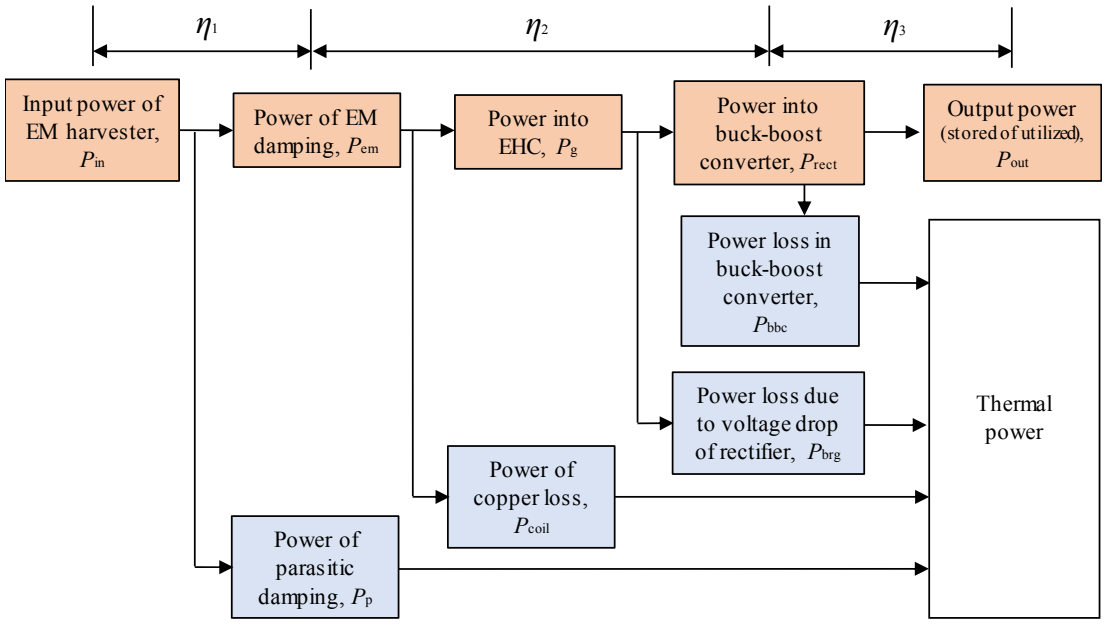

Figure 3.6 Power flow within an EM energy harvester

To quantify the energy harvesting performance, the energy harvesting efficiency of the harvester is defined as follows:

$$\eta = \frac{P_{\text{out}}}{P_{\text{in}}} \tag{3.12}$$

The energy harvesting efficiency in Equation (3.12) can be expressed as the product of three sub-efficiencies, as described in Figure 3.6:

$$\eta = \eta_1 \cdot \eta_2 \cdot \eta_3 \tag{3.13}$$

where

$$\eta_1 = \frac{P_{\text{em}}}{P_{\text{in}}} = \frac{c_{\text{em}}}{c_{\text{em}} + c_{\text{p}}} \tag{3.14a}$$

$$\eta_2 = \frac{P_{\text{rect}}}{P_{\text{em}}} = \frac{R_{\text{eq}}}{R_{\text{eq}} + R_{\text{coil}} + R_{\text{brg}}} \tag{3.14b}$$

$$\eta_3 = \frac{P_{\text{out}}}{P_{\text{rect}}} \tag{3.14c}$$

In the equations above, R_{brg} is the equivalent resistance of the bridge rectifier, which is negligible when the rectifier current is sufficiently large; η_1 describes the conversion efficiency from mechanical input power P_{in} to electrical power P_{em}; η_2 denotes the transmission efficiency from the total electrical power P_{em} to the buck–boost converter (i.e., the rectifier output power P_{rect}); and η_3 is the power efficiency of the buck–boost converter, as presented in Equation (3.10). The equivalent resistance R_{eq} of the buck–boost converter influences the sub-efficiencies as follows:

- A high value of R_{eq} leads to a small c_{em}. Thus, the increase in R_{eq} leads to a low η_1 and a high η_2. However, in the applications of EHEMD, a dual-function damper, the target value of c_{em} should often be set to meet the target damping coefficient required by the vibration control function. Similarly, a constant optimal R_{eq} is usually required to meet the classical IM.
- When the rectifier current i_{rect} is very small, the equivalent resistance of the bridge rectifier is high, which leads to a significantly low efficiency η_2. The power loss due to the voltage drop of the bridge rectifier is negligible when the rectifier current i_{rect} is sufficiently large.

- A large vibration amplitude leads to high rectifier output voltage, rectifier current, inductor current, charging current, and output power. With the increase in vibration amplitude, the sub-efficiency η_2 increases rapidly in DCM owing to the reduced impact of the voltage drop of the rectifier. However, the further increase in the rectifier voltage results in a reduced R_{eq} when the operation transits to CCM; consequently, the sub-efficiency η_2 starts to drop.
- With the proposed feed-forward control, the equivalent resistance R_{eq} is maintained nearly constant in both DCM and CCM, which prevents the drop of the sub-efficiency η_2 when the buck–boost converter operates in CCM under large vibration levels.

3.6 Testing and Simulation of EHC

3.6.1 Experimental Setup

Figure 3.7(a) shows a prototype EHC that was designed and tested in the laboratory. Table 3.1 lists some major parameters of the EHC measured in this test. The value and equivalent series resistance (ESR) of the used electrical components were calibrated using an LCR meter (model No. Hioki 3522-50). An MCU (model No. STC12LE5A60S2) was used to generate a rectangular switching signal to drive the MOSFET. The schematic of the MCU circuit is presented in Appendix 3.9. The adopted MCU was a single-chip MCU based on a high-performance 1T architecture 80C51 CPU. In this experiment, the MCU was powered by a 3.3 V battery. This low-power type MCU had an actual measured power consumption of approximately 30 mW, and the theoretical power consumption in the power-down mode could be as low as 1 mW, according to the specifications from the supplier. The duty cycle δ of the output PWM could be adjusted automatically based on the feed-forward rectifier voltage. The FDV303N MOSFET was selected owing to its low threshold gate voltage and low static drain-source on-resistance. Four Schottky diodes (model No. 20L15T) were used in the full-wave bridge rectifier because of the low forward voltage drop (0.22 V). An aluminum electrolytic capacitor of 680 μF was connected to the bridge rectifier to smoothen the output voltage waveforms U_{rect}. The transient value of U_{rect} was measured by the MCU with the data acquisition and analog-

to-digital conversion functions. Another 10 μF tantalum capacitor was added in parallel with a 1.3 V NiMH rechargeable button battery to reduce the current ripple across the battery. The switch frequency of PWM was 21.6 kHz, and the initial duty cycle was δ = 0.73. A 220 μH inductor was used, resulting in an average resistor of 17.8 Ω (design value) in DCM according to Equation (3.9). A high duty cycle and a low battery voltage (i.e., 1.3 V) were deliberately selected to obtain a low DCM-to-CCM transition voltage (U_{res} = 0.56 V) of the buck–boost converter, which could facilitate the proof-of-concept of using the MCU to adaptively regulate the duty cycle in CCM. It should be noted that the voltage of the rechargeable battery was different from the MCU supply voltage in the experiment. To directly power the MCU using the harvested energy, another boost converter would be needed. This was not done in the current study and is yet to be realized in future study.

Table 3.1 Main measured parameters of EHC in the circuit test

Item	Value	Item	Value
Filter capacitor, C_{in}	680 μF	Static drain-source on-resistance of the MOSFET, R_{on}	0.8 Ω
ESR of filter capacitor, $R_{esr,in}$	4.73 Ω	Initial duty cycle, δ	0.73
Inductor, L	220 μH	Switch frequency, f_w	21.6 kHz
ESR of inductor, $R_{esr,L}$	0.53 Ω	Nominal voltage of charging battery, U_{bat}	1.3 V
Output capacitor, C_{out}	10 μF	Power consumption of MCU	30 mW
ESR of output capacitor, $R_{esr,out}$	2569.8 Ω	Forward voltage of diode, U_F	0.22 V

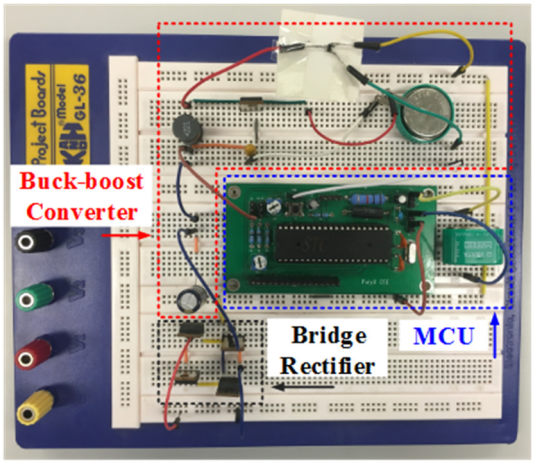

(a) Tested EHC on a breadboard

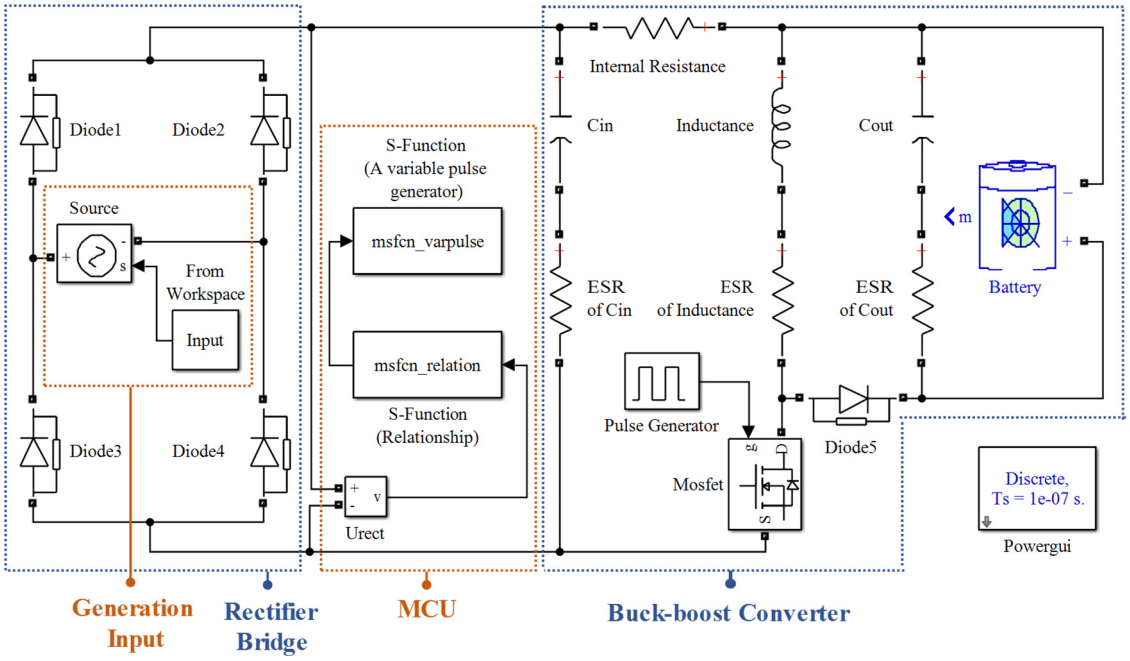

(b) Simulink model of EHC

Figure 3.7 Prototype and modeling of the EHC

3.6.2 Simulink Modeling

Figure 3.7(b) shows the established Simulink model of the tested EHC. The feed-forward control was realized via an S-function to simulate the MCU function. In consideration of the high switching frequency (i.e., 21.6 kHz) of the EHC, the time step was set as 10^{-7} s. The major parameters of the EHC measured in a laboratory were used in the model. An additional resistance of 0.2 Ω (denoted as the internal resistance in Figure 3.7(b)) was simulated to account for the influences of the connecting wires in the

EHC. In the following subsection, the testing and simulation results of the EHC, including the input resistance and efficiency, are presented and compared.

3.6.3 Testing and Simulation Results

The EHCs with fixed and adaptive duty cycles were investigated. In the former case, the duty cycle was fixed at δ = 73%. In the latter case, the duty cycle was fixed in DCM but adaptively adjusted in CCM through the feed-forward control function of the MCU to maintain a constant average resistance of the buck–boost converter. Figure 3.8(a) shows the empirical relationship between the duty cycle and the rectifier voltage obtained through the numerical simulations. The duty cycle changed from 73% to 50% in CCM. Thus far, studies on such a relationship remain limited in the literature. This empirical relationship was implemented in the feed-forward control of the MCU to adaptively adjust the duty cycle. The actual duty cycles obtained in the experiments are also shown in Figure 3.8(a). As can be seen, a satisfactory agreement was observed between the numerical and experimental results.

Figure 3.8(b) shows the corresponding comparison of the average resistance of buck–boost circuits with fixed and adaptive duty cycles. The resistance of the connecting wires, ESR of the inductor, and static drain-source on-resistance of the MOSFET made the actual resistance of the buck–boost converter slightly larger than the theoretical design value in DCM. In the case of the adaptive duty cycle, the buck–boost converter exhibited a nearly constant average resistance, which was close to the target resistance of 17.8 Ω, in both DCM and CCM. In comparison, the average resistance with a fixed duty cycle dropped rapidly once the buck–boost converter entered CCM. This result indicates that the proposed feed-forward control can successfully fulfill the objective, i.e., to maintain a nearly constant average resistance of the EHC through appropriate adjustment of the duty cycle.

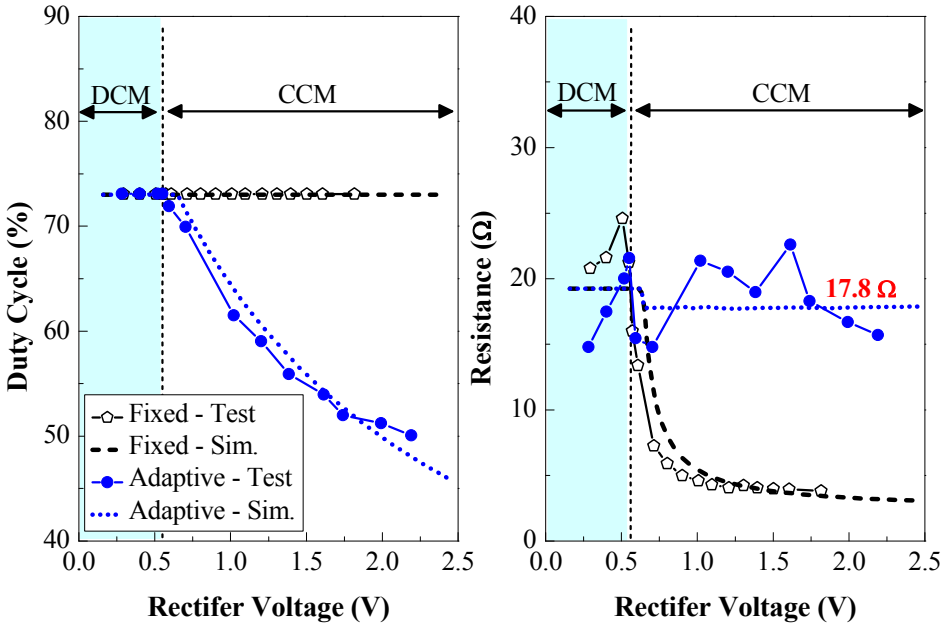

(a) Duty cycle (b) Average resistance

Note: "Fixed" and "Adaptive" stand for the buck–boost converters with fixed and adaptive duty cycles, respectively.

Figure 3.8 Duty cycle and average resistance of the buck–boost converter

In this circuit test, the output power harvested by the proposed circuit with the adaptive duty cycle increased from 4 to 200 mW when the rectifier voltage increased from 0.28 to 2.2 V. The power consumption of the low-power MCU was approximately 30 mW. However, the power consumption of the MCU is not considered in the following sections unless otherwise stated. The output power of the EHC in real applications, such as in large-scale vibration energy harvesters, should be considerably higher than that in this small-scale test. As a result, the power consumption of the MCU should be almost negligible.

Figure 3.9 shows the corresponding comparison of the conversion efficiency η_3. The buck–boost converters with the fixed and adaptive duty cycles showed relatively high charging efficiencies (>80%) in DCM. In CCM, however, the efficiency of the buck–boost converter with the adaptive duty cycle was significantly superior to that without the feed-forward control. The experimental result matched well with the simulation analysis.

The numerical and experimental results indicate that the proposed EHC with a suitable feed-forward control for the duty cycle adjustment could not only maintain a constant average resistance in DCM and CCM but also effectively improve the energy conversion efficiency in EHC.

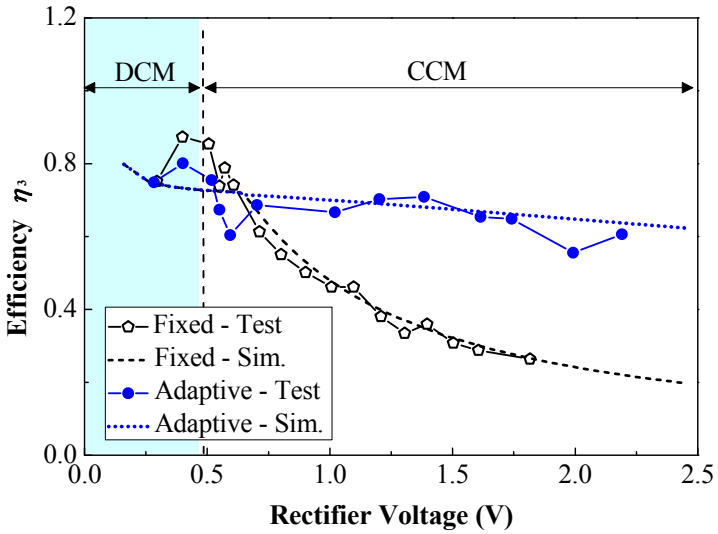

Figure 3.9 Energy efficiency of the buck–boost converter

3.7 Cyclic Tests of EMD plus EHC

3.7.1 Experimental Setup

A commercial linear-motion voice coil motor (Moticont, model No. GVCM-095-051-01) was cyclically tested as a small-scale EMD on an MTS machine (MTS system, Eden Prairie, Minnesota). The same type of motor was employed by Shen et al. (2016a). The diameter and length of this EMD were 95.3 and 45.2 mm, respectively. The motor constant K_{eq} and coil resistance of the EMD were 38 V·sm^{-1} and 9.3 Ω, respectively. Figure 3.10 shows the experimental setup of the cycle tests on a universal testing system, wherein the cyclic tests were conducted at a frequency of 1.5 Hz, with the displacement amplitude ranging from 1 to 15 mm. The displacement and force signals were recorded by a KYOWA data acquisition system (model No. EDX-100A), and the voltages and currents of interest in the EHC were recorded by an oscilloscope (model No. DPO 4104B-L). The EMD was connected to the EHCs with fixed and adaptive duty cycles separately to examine the influence of the proposed feed-forward control in the EHC on the

concerned characteristics of the EM energy harvester. The EHC parameters were identical to those presented in Section 3.6. The major experimental results are presented in the following subsections. Note that this tested system essentially can be regarded as an EHEMD, but it is named EMD plus EHC in this chapter considering the generality of the EM energy harvester.

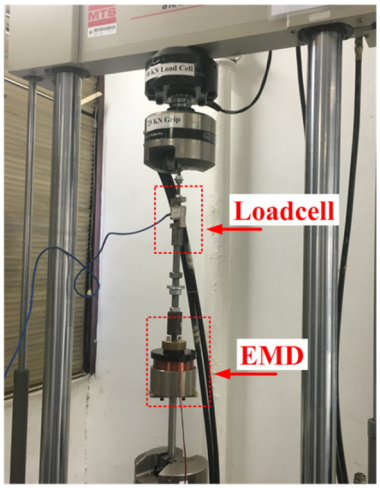

Figure 3.10 Cyclic test setup of EMD plus EHC

3.7.2 Experimental Results

3.7.2.1 Resistance and Damping Coefficient

In a cyclic test, the vibration velocity, which determines the rectifier output voltage, varied in each cycle. When the vibration amplitude was above 1.4 mm, the buck–boost converter partially operated in DCM and partially operated in CCM in each harmonic cycle. The observations of the EHC characteristics under varying vibration magnitudes (i.e., varying rectifier voltages) were similar to those presented in Section 3.6, as shown in Figure 3.11: the buck–boost converter with an adaptive duty cycle offered nearly constant average resistance close to the target value in both DCM and CCM during the cyclic tests. By contrast, without the feed-forward control, the average resistance of the buck–boost converter kept dropping with increasing vibration amplitude.

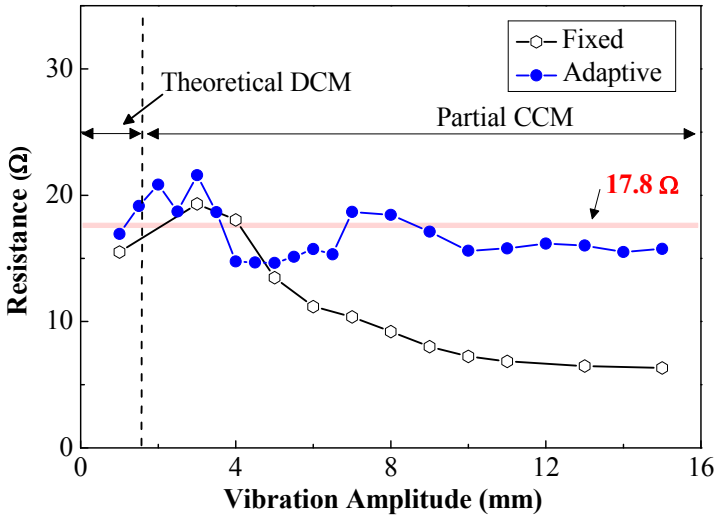

Figure 3.11 Average resistance of the buck–boost converter in a cyclic test

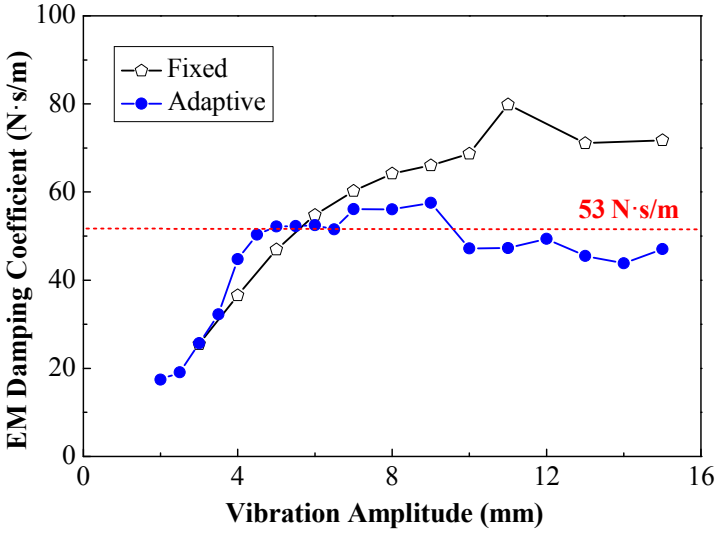

Figure 3.12 EM damping coefficient c_{em} vs. vibration amplitude relationship of the tested EMD plus EHC

Consequently, the variation in average resistance influenced the EM damping coefficient, as shown in Equation (3.5). Figure 3.12 presents the variations in the EM damping coefficient of the tested EMD-EHC with and without feed-forward control under different levels of harmonic excitation. At low vibration levels, the EM damping coefficient was relatively low owing to the influence of the voltage drop of the bridge rectifier. When the vibration amplitude was above 4 mm, the EM damping coefficient of the EMD-EHC with the adaptive duty cycle adjusted by the feed-forward control was kept nearly constant (53 N·s/m). However, in the case of the fixed duty cycle, the EM

damping coefficient kept increasing to approximately 75 N·s/m at a vibration amplitude of 15 mm. This result indicates the benefit of introducing the feed-forward control into the EHC for maintaining a stable damping coefficient (equivalent resistance), which is desirable in many vibration control (energy harvesting) applications. The use of an MCU for semi-active damping adjustment is another potential research direction to be explored in the future.

According to Equation (3.6), the total damping coefficient of the EMD plus EHC was calculated as 85.4 N·s/m, of which the parasitic damping coefficient was approximately 32.4 N·s/m. Figure 3.13 shows a typical damper force–velocity relationship under an excitation frequency of 1.5 Hz and a displacement amplitude of 9 mm. The excitation frequency that represents a typical vibration frequency of civil engineering structures is considerably lower than the switching frequency of the EHC. The slope of the force–velocity relationship was obtained through a linear regression analysis as 89.92 N·s/m, which is close to the total damping coefficient calculated above. The force–velocity relationship was imperfectly linear because of the influence of the moving mass in the EMD.

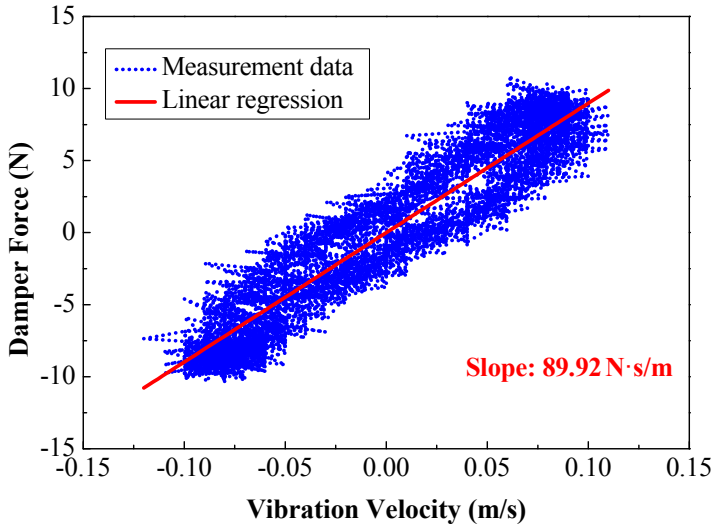

Figure 3.13 Force–velocity relationship of the EMD-EHC at a loading frequency of 1.5 Hz and a loading amplitude of 9 mm

3.7.2.2 Power and Efficiency

Figure 3.14 compares the output power and energy efficiency of the EMD plus EHC with fixed and adaptive duty cycles. In both cases, the output power (i.e., the charging power of the battery) increased rapidly with increasing vibration amplitude. However, the output power in the case of adaptive-duty-cycle control was considerably higher than that with a fixed duty cycle at a large vibration amplitude. For example, the output power values under adaptive and fixed duty cycles were 140 and 85 mW, respectively, at a vibration amplitude of 15 mm. Accordingly, the total energy efficiency in the case of the adaptive duty cycle was as high as 18%, approximately 2.5 times that with the fixed duty cycle. The improvement in output power and energy efficiency demonstrates that the adaptive control enabled by the MCU can efficiently improve the energy harvesting performance of the EM energy harvester. Figure 3.14 also shows the power consumption of the MCU, which was not considered in the calculation of the output power. The comparison indicates the power deficit and surplus under small and large vibration amplitudes, respectively. As explained in Section 3.6, the power consumption of the MCU should be negligible in a large-scale application, and thus, the positive output power can be expected.

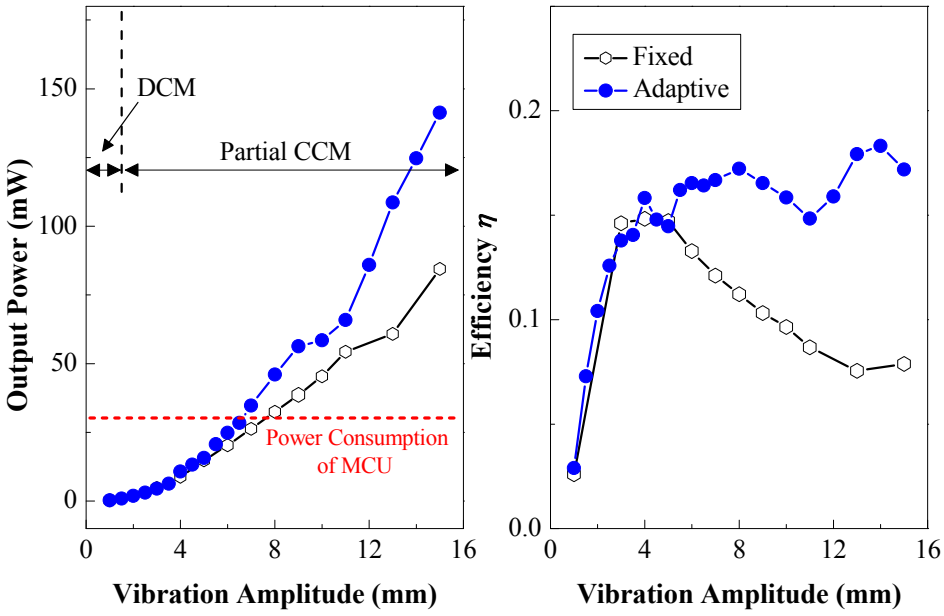

(a) Output power (b) Efficiency η

Figure 3.14 Energy harvesting performance of EMD plus EHC

Figure 3.15 shows three sub-efficiencies of the EMD plus EHC with an adaptive duty cycle. As can be seen, the electromechanical coupling coefficient η_1 was low because the friction effect led to a large equivalent parasitic damping coefficient c_p at small vibration levels. According to Equation (3.6), this sub-efficiency can be considerably improved by minimizing the friction of the EMD. The sub-efficiency η_2 was also low at a small vibration level because of the impact of the voltage drop caused by the bridge rectifier, and this sub-efficiency kept increasing with the rectifier voltage until the voltage drop was nearly negligible in comparison with the rectifier voltage. Thus, the sub-efficiency η_2 can be improved in large vibration amplitudes. The sub-efficiency η_3 of the buck–boost converter was extremely high in DCM and dropped slightly in CCM, which is consistent with the observation from Figure 3.9.

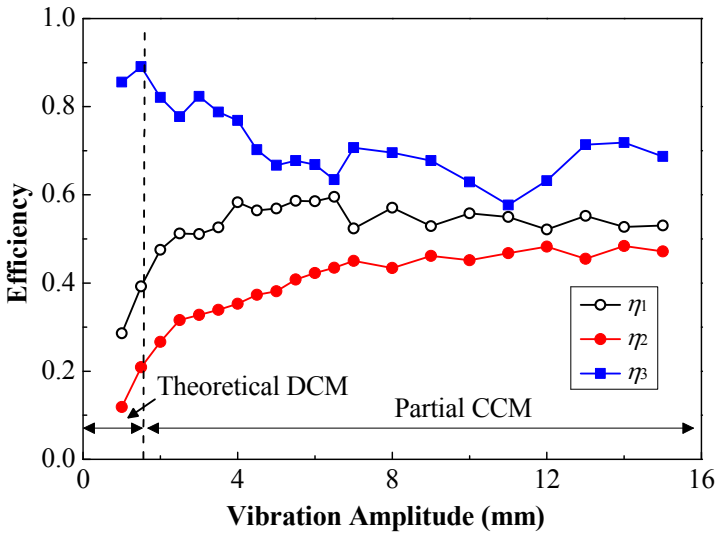

Figure 3.15 Sub-efficiencies of the EMD plus EHC

3.8 Summary

This chapter presents the basic components of an EM energy harvester, i.e., the EMD and EHC. The EMD plus EHC (can be regarded as an EHEMD) could maintain a stable characteristic over a wide vibration range by employing a low-power MCU to implement a feed-forward control in the EHC. The PWM duty cycle in the EHC can be automatically adjusted based on the real-time voltage measurement. Consequently, the buck–boost converter with adaptive-duty-cycle control can maintain a nearly constant resistance in a

wide operation range. Such a feed-forward control strategy avoided one deficiency associated with the fixed-duty-cycle buck–boost converter previously used in the EMD plus EHC, i.e., the equivalent resistance of the fixed-duty-cycle EHC kept decreasing when operating in CCM. The effectiveness of the EMD plus EHC was systematically investigated through a series of studies, including simulations and tests of the proposed EHC with adaptive-duty-cycle control, and the experimental characterization of the improved system through cyclic tests. The experimental and numerical investigations of the proposed EHC with the adaptive duty cycle showed satisfactory agreement. The major conclusions of these investigations are as follows:

1) On the basis of the empirical relationship between the rectifier voltage and duty cycle, the MCU-enabled feed-forward control could successfully maintain a nearly constant equivalent resistance of the buck–boost converter in DCM and CCM. Consequently, the designed EMD plus EHC could have a stable damping coefficient under a wide range of vibration levels, which is a favorable feature in vibration control applications.
2) The stable equivalent resistance of the EHC can efficiently enhance the output power and improve the energy harvesting efficiency of the EMD plus EHC when the buck–boost converter operated in CCM under large vibration amplitudes corresponding to a large voltage input. A total energy efficiency of approximately 18% was obtained in the laboratory tests of the designed system, which is approximately 2.5 times that of the system with a fixed duty cycle in a large vibration scenario.

3.9 Appendix A: Feed-forward Control Scheme in EHC

The detailed feed-forward control scheme in the EHC is shown in Figure 3.16. The MCU circuit mainly consisted of a reset circuit, a crystal oscillating circuit, an MCU, and an A/D input circuit.

The reset circuit was connected to the “RESET” pin and the battery, mainly included an electrolytic capacitor of 10 μF and a resistor of 10 kΩ. Its function was to send a signal

to the MCU and then activate other circuits once powered on.

The crystal oscillating circuit was connected to the “XTAL1”, “XTAL2”, and “GND” pins. The circuit contained two monolithic capacitors of 22 pF and a crystal oscillator of 11.0592 MHz, generating a clock signal for the MCU operation.

The A/D input circuit was used to limit the voltage input to the MCU. In the case wherein the rectified voltage is much higher than the normal operation voltage of STC12LE5A60S2 (3.3 V), the MCU may burn out. Therefore, the three 10 kΩ resistors in series were for voltage control. The highest allowable rectified voltage could be enhanced to approximately 10 V. A battery was used to supply power to the MCU.

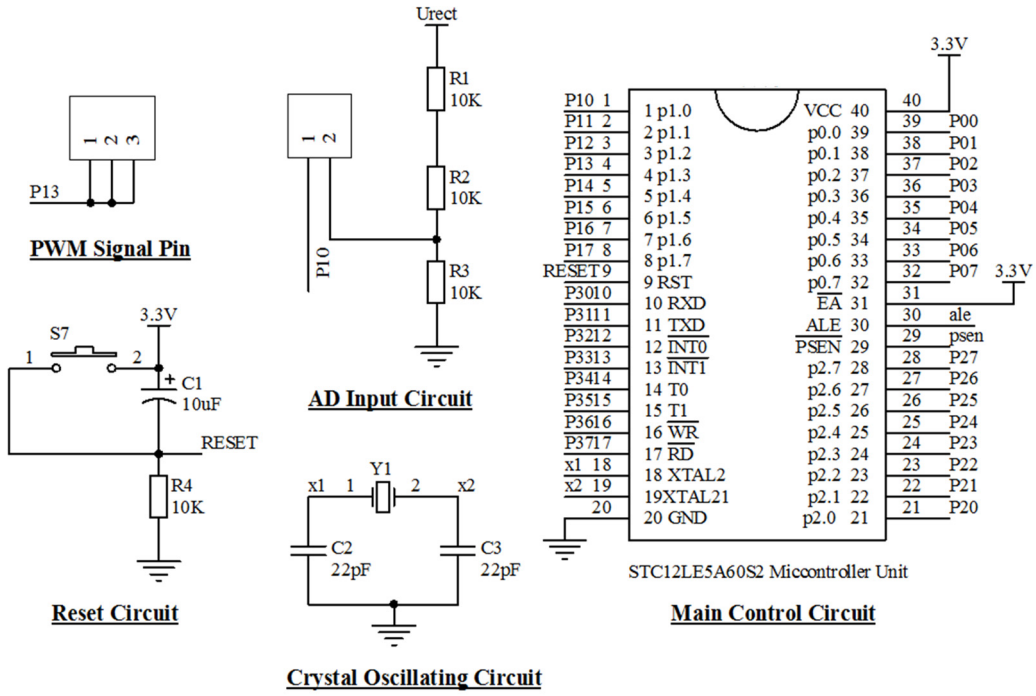

Figure 3.16 Detailed schematic of the MCU circuit

The corresponding printed circuit board (PCB) for the MCU circuit was designed using industry-standard computer-aided design tools (Figure 3.17a). The prototype of the MCU circuit board is displayed in Figure 3.17(b).

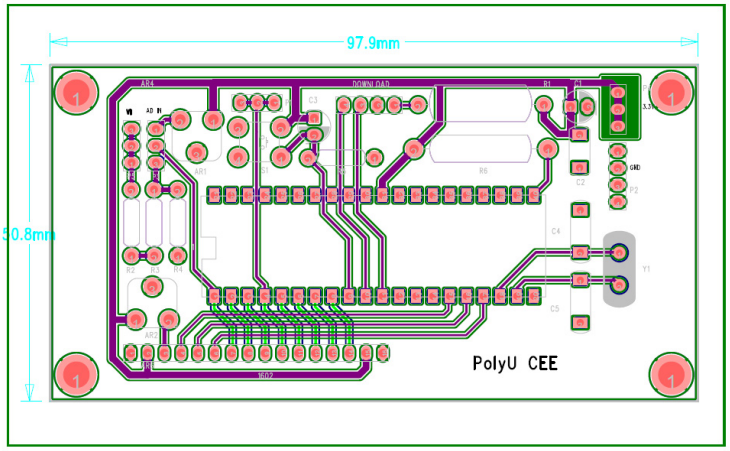

(a) PCB layout

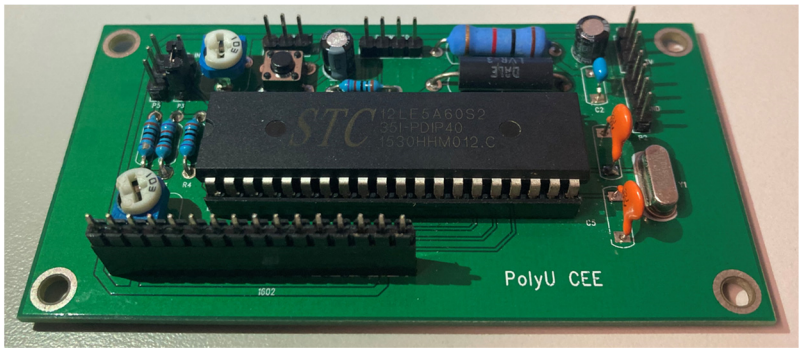

(b) Photo of the MCU circuit

Figure 3.17 PCB of the MCU circuit

CHAPTER 4

EHEMD FOR A FULL-SCALE BRIDGE CABLE

4.1 Introduction

Zhu et al. (2012) proposed the concept of EHEMD, and they were among the first to develop smart dampers with simultaneous vibration attenuation and energy harvesting functions in civil structures (Zhu et al., 2012; Shen et al., 2012, 2016a). They explored the feasibility of an EHEMD installed in a stay cable, considering the buffeting vibrations numerically (Shen and Zhu, 2015), and conducted a corresponding laboratory experiment involving a 5.85 m cable with a small-scale EHEMD system under a series of harmonic and random excitations (Shen et al., 2016a). In their studies, a fixed-duty-cycle buck–boost converter was used as the main part of the EHC, exhibiting an unstable equivalent resistance and lower power efficiency in CCM. The deficiencies of the early version of EHEMDs (i.e., performance degradation in a large vibration scenario) have been identified in Chapter 3. To clarify, the large vibration scenario refers to the vibration case where the velocity of the damper is large enough so that the corresponding inductor voltage is larger than the threshold between DCM and CCM of the EHC. One possible solution is to introduce the MCU feed-forward control into the EHC. In addition, the experimental validation of an EHEMD in a full-scale structure is of practical significance.

This chapter describes the test of the EHEMD with the EHC developed in Chapter 3 in a full-scale cable. The dynamic modeling of the bridge cable is not included in this chapter, considering its similarity with the modeling in the work by Shen et al. (2015). Some results are quite similar to those in Chapter 3 and are not presented again. First, a large EHEMD prototype to be adopted for large-scale applications was designed and

fabricated. Then, the improved EHEMD (with MCU) was applied to a 135 m–long bridge stay cable in the laboratory, and the feasibility and performance of the proposed EHEMD were validated through a series of dynamic tests of the full-scale cable.

4.2 EHEMD Prototype

4.2.1 EMD

In view of the low damping density of a linear EMD, the EHEMD design as shown in Figure 4.1(a) was adopted. A ball screw with a large lead angle was used to transform the linear motion into rotary motion. Consequently, a rotational EM transducer (SONGGANG motor, model No. O6SGN) with a gearhead was used in the EMD. The relationship between the linear displacement of the two terminals of the EHEMD and the rotation angle of the rotational EM transducer is given as follows:

$$\theta_{\text{em}} = \frac{2\pi\alpha}{l_{\text{bs}}} x \tag{4.1}$$

where α is the gear ratio; l_{bs} is the ball-screw lead; and x and θ_{em} are the linear displacement of the two terminals and the rotational angle of the used EMD, respectively. By selecting the appropriate screw lead and gear ratio, the ball screw and gearhead together accelerate the relative velocity between the permanent magnets and conductive material, achieving a high energy density.

The fabricated EHEMD with an open circuit was cyclically tested on an MTS machine first by applying the gearhead with a 1:12.5 gear ratio (Figure 4.1(b)). Figure 4.2 shows the MTS test results. The slope of the regression line in Figure 4.2(a) represents the machine constant of the EMD, that is, $K_{\text{eq}} \approx 640$ N/A. Owing to the introduction of the ball-screw and gearhead, the friction action was quite significant and dense oscillations occurred in this scenario (Figure 4.2(b)). The final equivalent parasitic damping can be modeled as the superposition of viscous damping and Coulomb damping (Zhu et al., 2012):

$$c_{\mathrm{p}} = \frac{2F_{\mathrm{fric}}}{\pi^2 fd} + c_{\mathrm{pv}} \tag{4.2}$$

where f and d are the excitation frequency and amplitude, respectively; $F_{\mathrm{fric}} \approx 0.16$ kN is the magnitude of the friction; and $c_{\mathrm{pv}} \approx 9$ kN·s/m is the parasitic viscous damping coefficient. Consequently, the equivalent parasitic damping coefficient in this scene was approximately 22 kN·s/m. Note that the modeling of the parasitic damping of the EMD is simplified as a constant in the following chapters unless otherwise stated. Other parameters of the EMD used for the subsequent cable test are summarized in Table 4.1.

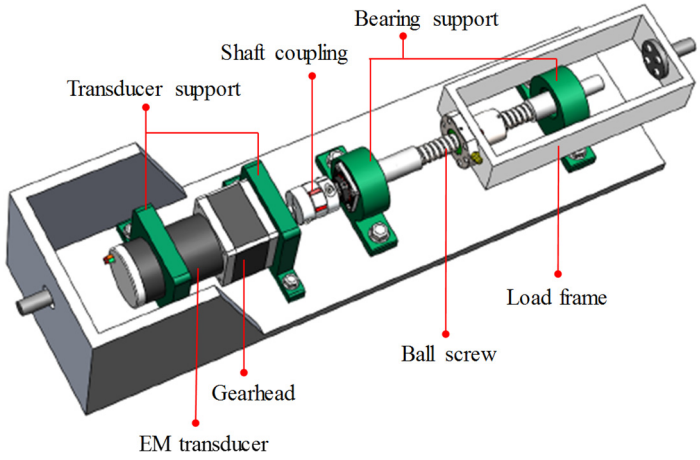

(a) 3D drawing

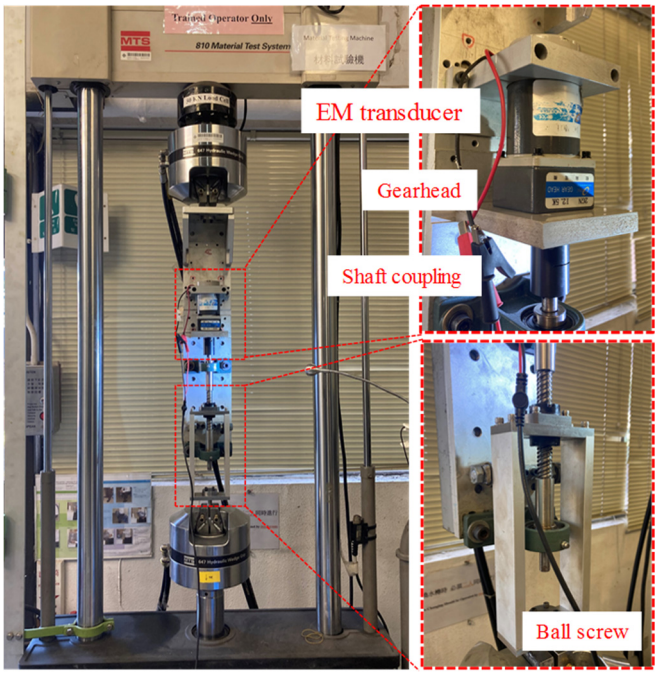

(b) Tested prototype

Figure 4.1 EHEMD prototype (without circuit) for the full-scale cable test

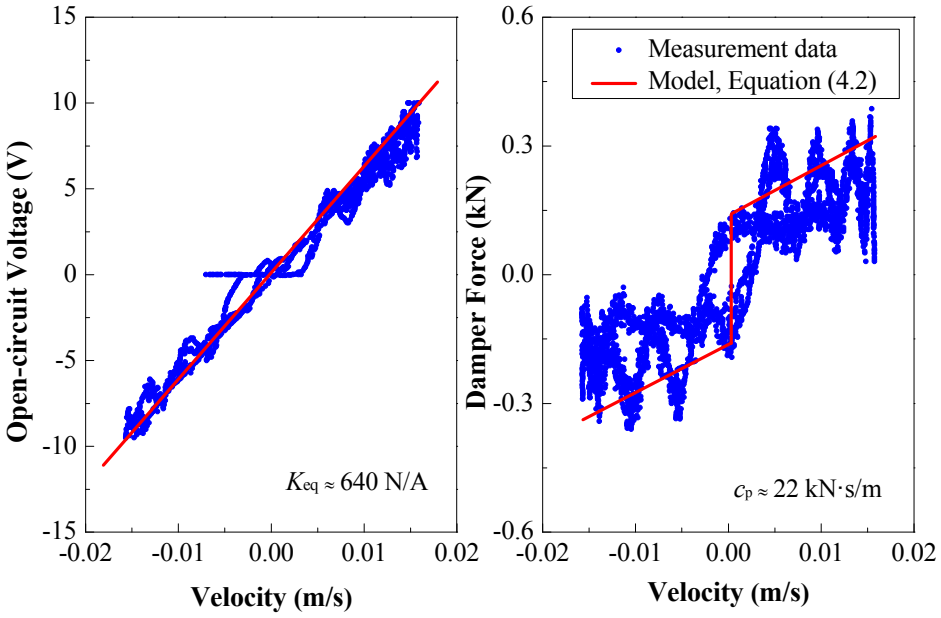

(a) Open-circuit voltage–velocity (b) Parasitic damping–velocity

Figure 4.2 Experimental characterization of EHEMD with open circuit (Li et al., 2020)

Table 4.1 Main parameters of the EMD for the cable test

Items	Parameters	Value
Finalized EMD	Machine constant, K_{eq}	640 N/A
	Coil resistance, R_{coil}	7.5 Ω
	Coil inductance, L_{coil}	13.35 mH
Ball screw	Ball screw lead, l_{bs}	16 mm
	Ball screw shaft diameter, D_{bs}	16 mm
	Ball screw design stroke, S_{bs}	50 mm
Gearhead	Gear ratio, α	1:12.5
Load frame	Length of frame, l_f	726 mm

4.2.2 EHC

An EHC similar to that presented in Chapter 3 was used in the EHEMD. To match the optimal value (Equation (4.3)) for the first vibration mode of the cable, the average resistance of the EHC was set as 7.5 Ω, considering the parasitic damping coefficient beforehand. This value also satisfied the classical IM theory for maximum output power. Consequently, the inductance and the initial duty cycle in the EHC were set to 68 μH and 0.63, respectively. In CCM, the duty cycle was adjusted by the MCU, wherein the

adjustment strategy was determined through a similar mean as presented in Chapter 3.

4.3 Cable Experiment

Bridge stay cables are often susceptible to excessive vibrations owing to their low inherent damping (Yamaguchi, 1998; Xu and Yu, 1998; Johnson et al., 2007). Viscous fluid dampers are commonly used to mitigate stay cable vibrations. In this subsection, the EHEMD involving the proposed EHC with feed-forward control was applied to a full-scale stay cable model to simultaneously perform vibration control and energy harvesting functions. However, the stay cable with a traditional EHEMD was not tested, and thus, the direction performance comparison between the EHEMDs with adaptive and fixed duty cycles could not be performed in this section.

4.3.1 Experimental Setup

A 135 m–long stay cable was tested in the laboratory. The tested cable consisted of 12 compactly twisted steel strands and a high-density polyethylene protection layer (Figure 4.3). The diameter of each strand was 15.2 mm, with allowed bias from −0.2 to +0.4 mm. The major parameters of this stay cable are shown in Table 4.2. A preliminary sine sweep test revealed that the first three frequencies of the cable without any damper were approximately 1.1, 2.2, and 3.3 Hz. Figure 4.4 shows the schematic of the test setup, including the used facilities and sensors, and Figure 4.5 presents the prototype of the EHEMD installed in the cable. The dynamic exciter (model No. HEV-1000) and the EHEMD were installed at $0.12l$ and $0.05l$ away from the right anchorage, respectively, where l is the total cable length. Four accelerometers (model No. DH187E series) and three displacement laser sensors (model No. KEYENCE, LK-503) were installed at certain locations to measure the concerned vibration responses. One load cell (model No. EVT-14C2-2T) was installed between the exciter and the cable to measure the excitation force, and another (model No. SINOCERA CL-YB-3 300k) was connected between the EHEMD and cable to measure the damping force provided. According to Kovacs (1982), the optimal damping coefficient corresponding to the maximized modal damping ratio

for a particular vibration mode of a stay cable is as follows:

$$c_{\mathrm{opt,j}} = \frac{ml\omega_{\mathrm{f}}}{2\pi j\left(x_{\mathrm{c}}/l\right)} \tag{4.3}$$

where m and l are the cable unit mass and length, respectively; ω_{f} is the fundamental circular frequency of the cable; x_{c} is the distance from the cable anchorage to the damper; and j denotes the concerned j^{th} vibration mode. Accordingly, the optimal viscous damping coefficient for the aforementioned damper location was estimated as 49.45 kN·s/m for the fundamental vibration mode. Notably, the optimal damping coefficients corresponding to different vibration modes were also different.

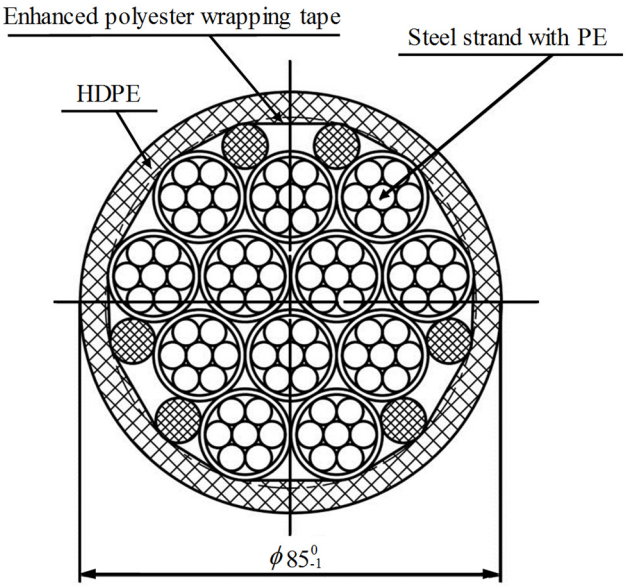

Note: HDPE denotes high-density polyethylene.

Figure 4.3 Cross section of the tested cable (OVM Co. Ltd, 2014)

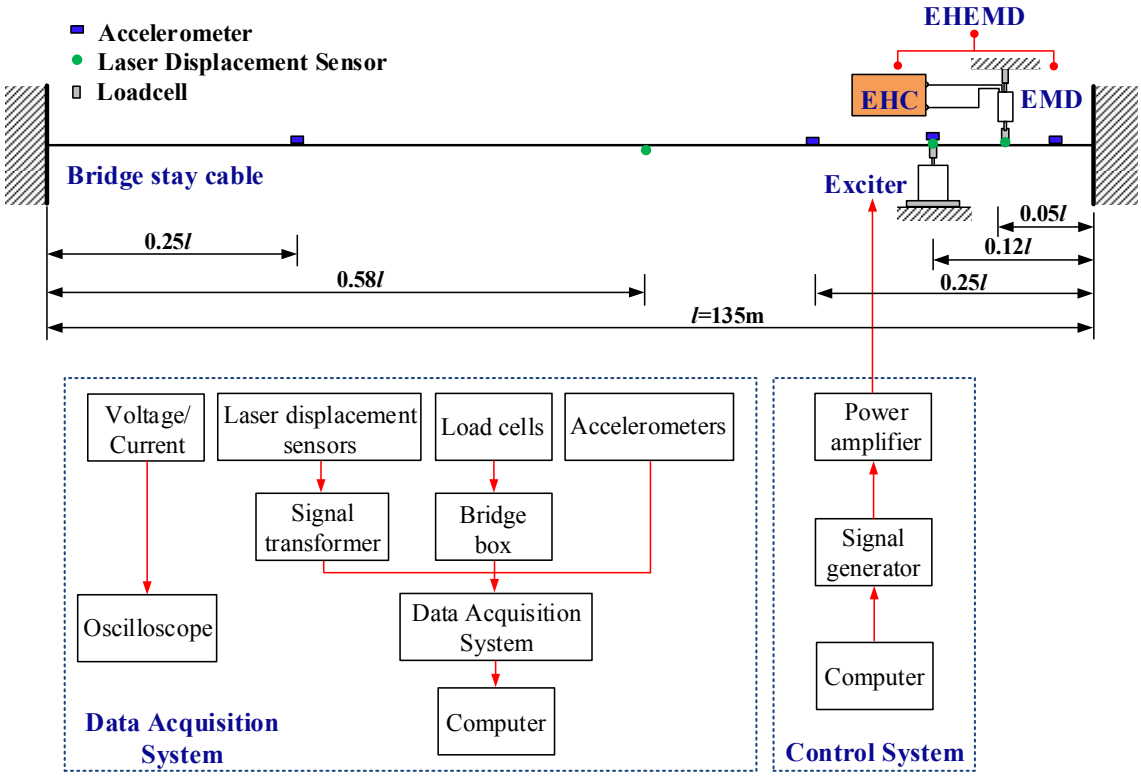

Figure 4.4 Schematic of the EHEMD with the stay cable

Table 4.2 Main parameters of the full-scale bridge cable (OVM Co. Ltd, 2014)

Parameter	Value
Cable length, l	135 m
Cable unit mass, m	16.65 kg/m
Young's modulus	195 GPa
Diameter	85 mm
Cross-sectional area	5.675×10^{-3} m^2
Applied tension	1200 kN
Yielding load	3120 kN

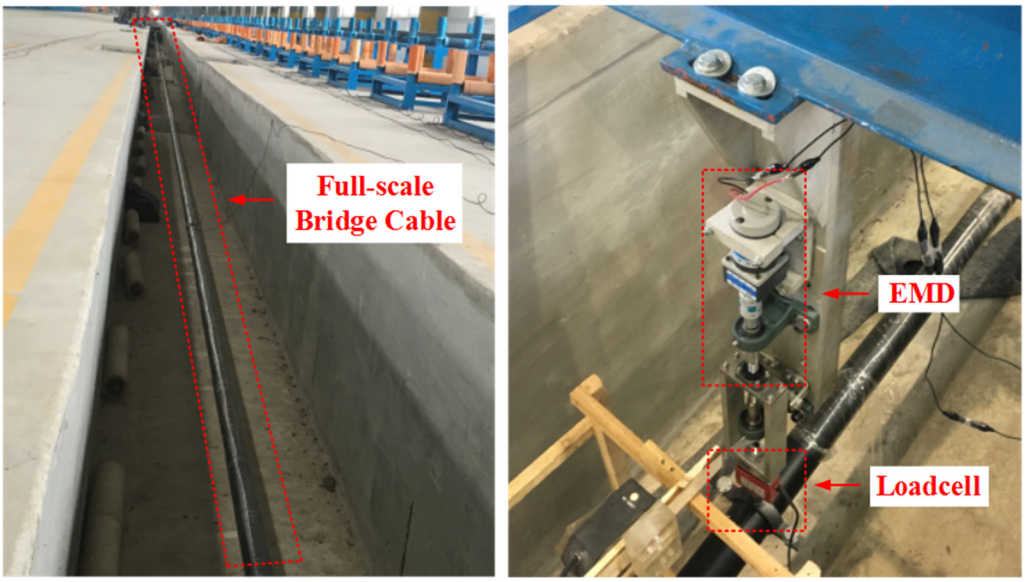

Figure 4.5 Photos of the experimental setup of the full-scale cable test

4.3.2 Experimental Results

4.3.2.1 Vibration Control Performance

The stay cable was excited by the harmonic excitations of different levels. The damper force, cable responses, and generated voltage all increased with the excitation level. Figure 4.6 shows the measured average resistance of the EHC under a harmonic excitation that corresponded to the third vibration mode (i.e., 3.3 Hz). Figure 4.6(a) shows the variation in average resistance of the buck–boost converter with different peak rectifier voltages, representing different vibration levels (see Figure 4.8). The resistance was generally kept nearly constant and close to the design target value of 7.5 Ω in the entire test, although the buck–boost converter partially operated in CCM. Figure 4.6(b) demonstrates the relationship between the average rectifier voltage and rectifier current for five loading cycles, which also characterizes the average input resistance of the buck–boost converter. The nearly linear relationship between the rectifier voltage and current demonstrates that the converter could emulate a constant resistor. The slope in this figure, which represents the average resistance, was identified as approximately 7.5 Ω, also very close to the design target value.

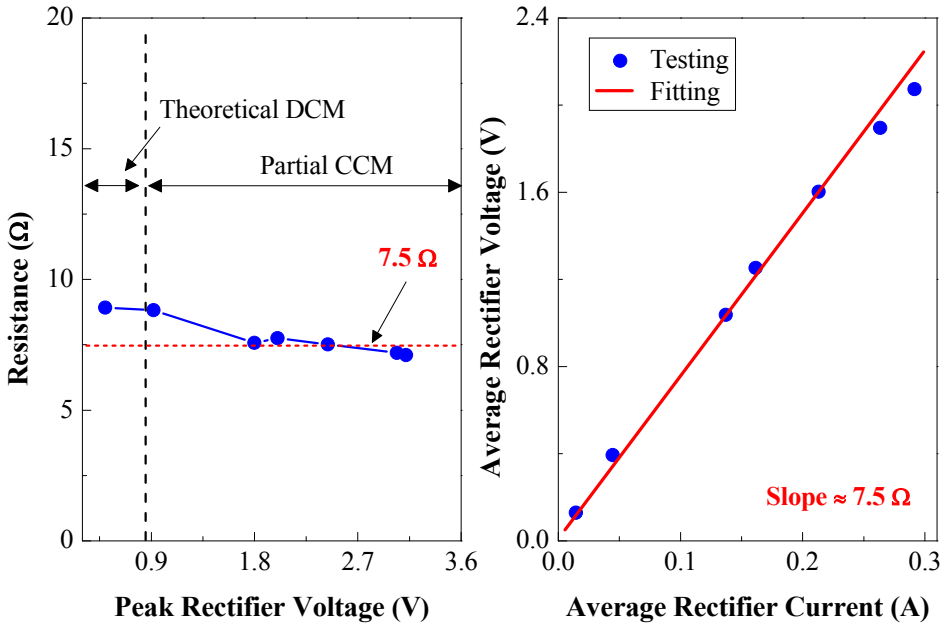

(a) Average resistance (b) Average voltage–current

Figure 4.6 Average resistance of EHC in the cable test

Figure 4.7 compares the steady displacement responses at the damper location under a harmonic excitation of 2 Hz for three cases: the EMD was connected to an open circuit, a pure resistor (7.5 Ω), and the proposed EHC. The open-circuit case involving zero EM damping represented an uncontrolled case; the pure-resistor case consisting of an EMD connected to a constant resistor represented an ideal situation with a steady and constant damping coefficient; and the EHC case represented an EHEMD designed to perform dual functions and maintain a steady resistance feature. Compared with the EMD connected to an open circuit, the dual-function EHEMD offered a significant reduction (approximately 67.4%) in the vibration responses, indicating the effective vibration control performance of the EHEMD. Moreover, the vibration mitigation performance of the EHEMD was nearly identical to that of the pure-resistor case, which demonstrates that the proposed EHC with an adaptive duty cycle could effectively emulate a target constant resistor and that the EHEMD could offer desirable vibration mitigation performance. As a passive damper, the EHEMD does not compromise the optimal control performance by introducing the function of energy harvesting.

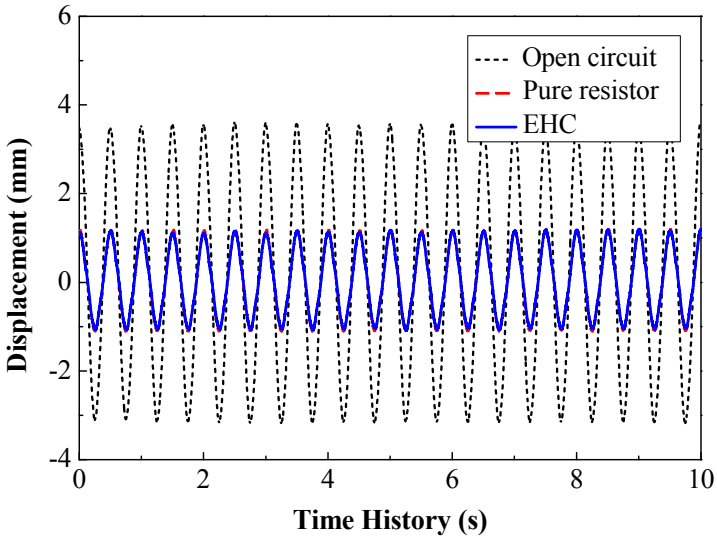

Figure 4.7 Control performance of EHEMD in the cable test

4.3.2.2 Energy Harvesting Performance

Figure 4.8(a) shows the variation in rectifier output voltages with the vibration levels under an excitation frequency of 3.3 Hz, wherein the vibration levels are expressed using the RMS acceleration at the 1/4-span of the cable. As can be seen, the peak and average U_{rect} increased with the vibration level. The threshold for the transition from DCM to CCM was $U_{thres} \approx 0.89$ V. Once the transient U_{rect} exceeded this threshold, the MCU started to adjust the duty cycle according to the feed-forward signal of U_{rect}. In addition, the initial power transferred to the EHEMD could be calculated using Equation (3.11a). The results can be observed in Figure 4.8(b); the input power increased from 0.46 to 6.3 W.

Figure 4.9 shows the corresponding variations in charging power and overall efficiency. With increasing vibration levels, the output power increased from 1 to 200 mW, and 200 mW is considered sufficient to power some commercial wireless sensors in structural health monitoring applications (Lynch and Loh, 2006; Priya, 2005). Thus, the experimental result demonstrates the prospect of EHEMD to simultaneously perform vibration control and energy harvesting functions in real civil structures.

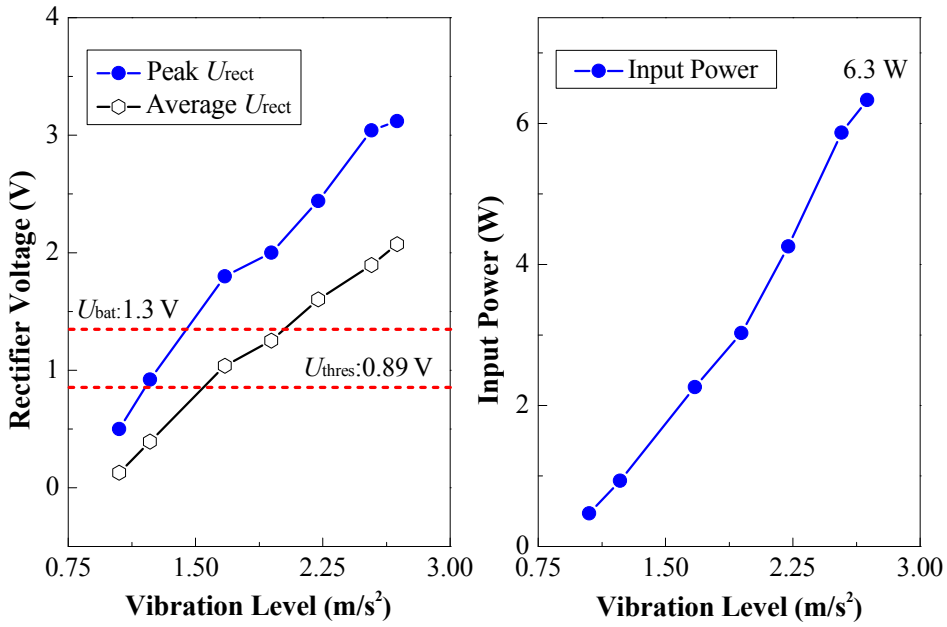

(a) Rectifier voltage (b) Input power

Figure 4.8 Rectifier voltage at different vibration levels

The corresponding energy harvesting efficiency was very low (only 3%) in this full-scale cable experiment, which can be attributed to two reasons. First, the parasitic damping coefficient of the EMD was too large, thereby leading to a low conversion efficiency η_1 from the mechanical power to electrical power. The power loss caused by the parasitic damping was more significant under small vibration amplitudes. Second, as predicted by Equations (3.10) and (3.14), the power loss due to R_{coil}, R_{on}, and $R_{esr,L}$ in this application was high, given the small value of the design resistance of the EHC. In general, the energy harvesting efficiency was relatively low at small vibration levels and tended to be stable with increasing vibration levels. This trend is consistent with the observation in Figure 3.14(b).

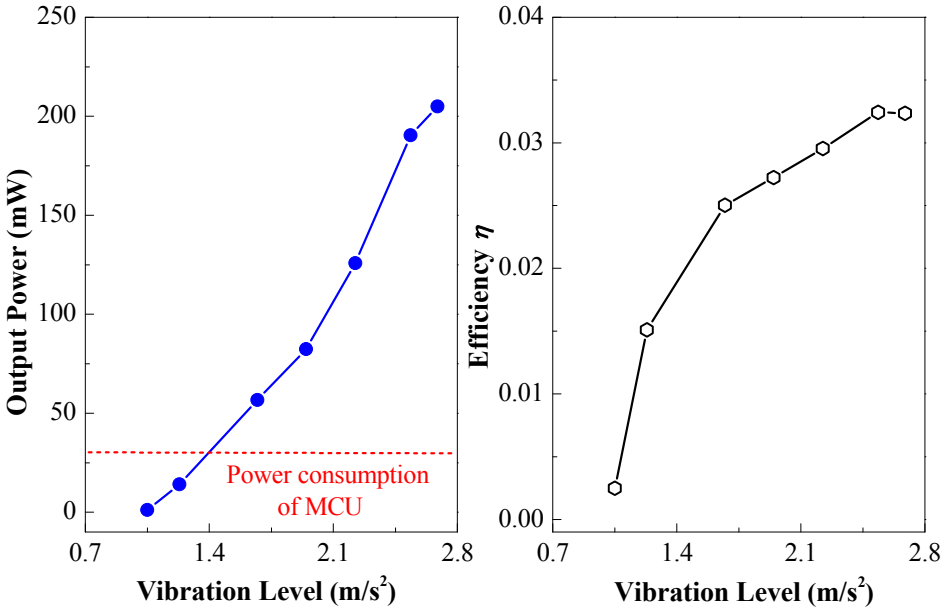

(a) Output power (b) Efficiency η

Figure 4.9 Output power and efficiency of EHEMD in the cable test

4.4 Summary

The EMD and EHC together form an EHEMD, a device for simultaneously suppressing structural vibration responses and harvesting vibration energy. This chapter presents the design and fabrication of an improved EHEMD with a large energy density. The EHEMD was tested in a 135 m–long stay cable. The major conclusions are as follows:

1) When applied to the full-scale cable test, the EHEMD demonstrated its capability of fulfilling simultaneous vibration control and energy harvesting functions. The vibration control performance was comparable to that of a passive EMD connected to a pure resistor, with approximately 67% further reduction in vibration amplitude in comparison to that with an open circuit; moreover, the peak output power of 200 mW was achieved in the dynamic tests, which is sufficient for powering some wireless sensors in structural health monitoring. This proof-of-concept test demonstrates the promising prospect of applying the EHEMD in large-scale structures for vibration control and energy harvesting.
2) A total energy efficiency of 3% was obtained in the full-scale cable tests of the EHEMD system. The low efficiency was mainly due to the small design resistance of the EHC

and the relatively large coil resistance and parasitic damping. It needs to be improved in future studies. A stable damping coefficient close to the optimal value is always desirable in cable vibration control. In this sense, the proposed EHEMD with a nearly constant resistance can improve the vibration control performance in cable tests. This benefit is yet to be validated in future studies.

CHAPTER 5

ADAPTIVE CONTROL IN HST SUSPENSION USING EHEMD

5.1 Introduction

Following the passive EHEMD introduced in the last chapter, this chapter proposes and investigates a novel HST secondary suspension employing two adaptive EHEMDs with energy harvesting and adaptive damping functions. The major part of the EHC in this chapter is also an adaptive-duty-cycle buck–boost converter, in which the sensing information is the train speed instead of the rectifier voltage. Consequently, the variable optimal damping coefficient can be realized at different train speeds by tuning the duty cycle of the EHC. This proposed secondary suspension is associated with the advantages of energy regeneration and adaptive vibration control, provided that the adaptive damping coefficient can be properly adjusted based on the train speed. Compared with MR damper–based adaptive suspension systems, EHEMDs can not only realize energy harvesting but also effectively avoid damper performance degradation due to overheating (temperature-induced changes in the physical properties of MR fluids). Furthermore, the proposed control topology, in which only the duty cycle regulation consumes nearly negligible power, is much simpler than those in the literature (e.g., Wang et al., 2015).

The rest of this chapter is organized as follows: Section 5.2 introduces the modeling of the HST and track irregularities. Section 5.3 presents the proposed energy-harvesting adaptive vibration damping. Section 5.4 numerically investigates the energy harvesting and vibration control performance when the HST secondary suspension is equipped with

adaptively controlled EHEMDs. Section 5.5 provides the main results and findings.

5.2 HST and Track Model

The 17DOF HST model developed by Zong et al. (2013) was adopted in this study, as shown in Figure 5.1. This model consists of one car body, two bogies, and four wheels, with the corresponding DOFs depicted in Figure 5.1 and explained in Table 5.1. The secondary lateral suspension is the most critical element affecting the car body vibrations. Two EHEMDs are installed in the secondary suspension to replace the original lateral passive dampers.

The governing equations of the motions for each part can be expressed accordingly. The dynamics of the car body are characterized by lateral, roll, and yaw motions:

$$\begin{aligned} m_{\mathrm{c}}\ddot{y}_{\mathrm{c}} =& -k_{2\mathrm{y}}\left(y_{\mathrm{c}}+l\phi_{\mathrm{c}}-h_1\theta_{\mathrm{c}}-y_{\mathrm{t1}}-h_3\theta_{\mathrm{t1}}\right)-k_{2\mathrm{y}}\left(y_{\mathrm{c}}-l\phi_{\mathrm{c}}-h_1\theta_{\mathrm{c}}-y_{\mathrm{t2}}-h_3\theta_{\mathrm{t2}}\right)\\ &-c_{2\mathrm{y}}\left(\dot{y}_{\mathrm{c}}+l\dot{\phi}_{\mathrm{c}}-h_2\dot{\theta}_{\mathrm{c}}-\dot{y}_{\mathrm{t1}}-h_5\dot{\theta}_{\mathrm{t1}}\right)-c_{2\mathrm{y}}\left(\dot{y}_{\mathrm{c}}-l\dot{\phi}_{\mathrm{c}}-h_2\dot{\theta}_{\mathrm{c}}-\dot{y}_{\mathrm{t2}}-h_5\dot{\theta}_{\mathrm{t2}}\right) \end{aligned} \tag{5.1}$$

$$\begin{aligned} J_{\mathrm{cz}}\ddot{\phi}_{\mathrm{c}} =& -k_{2\mathrm{y}}l\left(y_{\mathrm{c}}+l\phi_{\mathrm{c}}-h_1\theta_{\mathrm{c}}-y_{\mathrm{t1}}-h_3\theta_{\mathrm{t1}}\right)+k_{2\mathrm{y}}l\left(y_{\mathrm{c}}-l\phi_{\mathrm{c}}-h_1\theta_{\mathrm{c}}-y_{\mathrm{t2}}-h_3\theta_{\mathrm{t2}}\right)\\ &-c_{2\mathrm{y}}l\left(\dot{y}_{\mathrm{c}}+l\dot{\phi}_{\mathrm{c}}-h_2\dot{\theta}_{\mathrm{c}}-\dot{y}_{\mathrm{t1}}-h_5\dot{\theta}_{\mathrm{t1}}\right)+c_{2\mathrm{y}}l\left(\dot{y}_{\mathrm{c}}-l\dot{\phi}_{\mathrm{c}}-h_2\dot{\theta}_{\mathrm{c}}-\dot{y}_{\mathrm{t2}}-h_5\dot{\theta}_{\mathrm{t2}}\right)\\ &-k_{2\mathrm{x}}b_2^2\left(\phi_{\mathrm{c}}-\phi_{\mathrm{t1}}\right)-c_{2\mathrm{x}}b_3^2\left(\dot{\phi}_{\mathrm{c}}-\dot{\phi}_{\mathrm{t1}}\right)-k_{2\mathrm{x}}b_2^2\left(\phi_{\mathrm{c}}-\phi_{\mathrm{t2}}\right)-c_{2\mathrm{x}}b_3^2\left(\dot{\phi}_{\mathrm{c}}-\dot{\phi}_{\mathrm{t2}}\right) \end{aligned} \tag{5.2}$$

$$\begin{aligned} J_{\mathrm{cz}}\ddot{\theta}_{\mathrm{c}} =& k_{2\mathrm{y}}h_1\left(y_{\mathrm{c}}+l\phi_{\mathrm{c}}-h_1\theta_{\mathrm{c}}-y_{\mathrm{t1}}-h_3\theta_{\mathrm{t1}}\right)+k_{2\mathrm{y}}h_1\left(y_{\mathrm{c}}-l\phi_{\mathrm{c}}-h_1\theta_{\mathrm{c}}-y_{\mathrm{t2}}-h_3\theta_{\mathrm{t2}}\right)\\ &c_{2\mathrm{y}}h_2\left(\dot{y}_{\mathrm{c}}+l\dot{\phi}_{\mathrm{c}}-h_2\dot{\theta}_{\mathrm{c}}-\dot{y}_{\mathrm{t1}}-h_5\dot{\theta}_{\mathrm{t1}}\right)+c_{2\mathrm{y}}h_2\left(\dot{y}_{\mathrm{c}}-l\dot{\phi}_{\mathrm{c}}-h_2\dot{\theta}_{\mathrm{c}}-\dot{y}_{\mathrm{t2}}-h_5\dot{\theta}_{\mathrm{t2}}\right)\\ &-k_{2\mathrm{z}}b_2^2\left(\theta_{c}-\theta_{\mathrm{t1}}\right)-k_{2\mathrm{z}}b_2^2\left(\theta_{\mathrm{c}}-\theta_{\mathrm{t1}}\right)-c_{2\mathrm{z}}b_3^2\left(\dot{\theta}_{\mathrm{c}}-\dot{\theta}_{\mathrm{t1}}\right)-c_{2\mathrm{x}}b_3^2\left(\dot{\theta}_{\mathrm{c}}-\dot{\theta}_{\mathrm{t1}}\right) \end{aligned} \tag{5.3}$$

The dynamics of the front and rear bogies, which are denoted by the subscript $i = 1$, 2, respectively, are expressed as:

$$\begin{aligned} m_{\mathrm{t}}\ddot{y}_{\mathrm{ti}} =& k_{2\mathrm{y}}\left(y_{\mathrm{c}}-(-1)^{\mathrm{i}}l\phi_{\mathrm{c}}-y_{\mathrm{ti}}-h_1\theta_{\mathrm{c}}-h_3\theta_{\mathrm{ti}}\right)+c_{2\mathrm{y}}\left(\dot{y}_{\mathrm{c}}-(-1)^{\mathrm{i}}l\dot{\phi}_{\mathrm{c}}-\dot{y}_{\mathrm{ti}}-h_2\dot{\theta}_{\mathrm{c}}-h_5\dot{\theta}_{\mathrm{ti}}\right)\\ &-k_{1\mathrm{y}}\left(y_{\mathrm{ti}}-l\phi_{\mathrm{ti}}-h_4\theta_{\mathrm{ti}}-y_{\omega(2\mathrm{i}-1)}\right)-k_{1\mathrm{y}}\left(y_{\mathrm{ti}}-l\phi_{\mathrm{ti}}-h_4\theta_{\mathrm{ti}}-y_{\omega(2\mathrm{i})}\right)\\ &-c_{1\mathrm{y}}\left(\dot{y}_{\mathrm{ti}}-l\dot{\phi}_{\mathrm{ti}}-h_4\dot{\theta}_{\mathrm{ti}}-\dot{y}_{\omega(2\mathrm{i}-1)}\right)-c_{1\mathrm{y}}\left(\dot{y}_{\mathrm{ti}}-l\dot{\phi}_{\mathrm{ti}}-h_4\dot{\theta}_{\mathrm{ti}}-\dot{y}_{\omega(2\mathrm{i})}\right) \end{aligned} \tag{5.4}$$

$$
\begin{aligned}
J_{\mathrm{tz}}\ddot{\phi}_{\mathrm{ti}} &= k_{2\mathrm{x}}b_2^2\left(\phi_{\mathrm{c}}-\phi_{\mathrm{ti}}\right)+c_{2\mathrm{x}}b_3^2\left(\dot{\phi}_{\mathrm{c}}-\dot{\phi}_{\mathrm{ti}}\right)\\
&\quad -k_{1\mathrm{y}}l_1\left(y_{\mathrm{ti}}+l_1\phi_{\mathrm{ti}}-h_4\theta_{\mathrm{ti}}-y_{\omega(2\mathrm{i}-1)}\right)+k_{1\mathrm{y}}l_1\left(y_{\mathrm{ti}}+l_1\phi_{\mathrm{ti}}-h_4\theta_{\mathrm{ti}}+y_{\omega(2\mathrm{i})}\right)\\
&\quad -c_{1\mathrm{y}}l_1\left(\dot{y}_{\mathrm{ti}}+l_1\dot{\phi}_{\mathrm{ti}}-h_4\dot{\theta}_{\mathrm{ti}}-\dot{y}_{\omega(2\mathrm{i}-1)}\right)+c_{1\mathrm{y}}l_1\left(\dot{y}_{\mathrm{ti}}+l_1\dot{\phi}_{\mathrm{ti}}-h_4\dot{\theta}_{\mathrm{ti}}+\dot{y}_{\omega(2\mathrm{i})}\right)\\
&\quad -k_{1\mathrm{x}}b_1^2\left(\phi_{\mathrm{ti}}-\phi_{\omega(2\mathrm{i}-1)}\right)-k_{1\mathrm{x}}b_1^2\left(\phi_{\mathrm{ti}}-\phi_{\omega(2\mathrm{i})}\right)-c_{1\mathrm{x}}b_1^2\left(\dot{\phi}_{\mathrm{ti}}-\dot{\phi}_{\omega(2\mathrm{i}-1)}\right)-c_{1\mathrm{x}}b_1^2\left(\dot{\phi}_{\mathrm{ti}}-\dot{\phi}_{\omega(2\mathrm{i})}\right)
\end{aligned}
\tag{5.5}
$$

$$
\begin{aligned}
J_{\mathrm{tx}}\ddot{\theta}_{\mathrm{ti}} &= k_{2\mathrm{y}}h_3\left(y_{\mathrm{c}}-(-1)^{\mathrm{i}}l\phi_{\mathrm{c}}-\dot{y}_{\mathrm{ti}}-h_1\theta_{\mathrm{c}}-h_3\theta_{\mathrm{ti}}\right)+c_{2\mathrm{y}}h_5\left(\dot{y}_{\mathrm{c}}-(-1)^{\mathrm{i}}l\dot{\phi}_{\mathrm{c}}-\dot{y}_{\mathrm{ti}}-h_2\dot{\theta}_{\mathrm{c}}-h_5\dot{\theta}_{\mathrm{ti}}\right)\\
&\quad +k_{2\mathrm{z}}b_2^2\left(\theta_{\mathrm{c}}-\theta_{\mathrm{ti}}\right)+c_{2\mathrm{z}}b_3^2\left(\dot{\theta}_{\mathrm{c}}-\dot{\theta}_{\mathrm{ti}}\right)\\
&\quad +k_{1\mathrm{y}}h_4\left(y_{\mathrm{ti}}+l\phi_{\mathrm{ti}}-h_4\theta_{\mathrm{ti}}-y_{\omega(2\mathrm{i}-1)}\right)+k_{1\mathrm{y}}h_4\left(y_{\mathrm{ti}}-l\phi_{\mathrm{ti}}-h_4\theta_{\mathrm{ti}}-y_{\omega(2\mathrm{i})}\right)\\
&\quad +c_{1\mathrm{y}}h_4\left(\dot{y}_{\mathrm{ti}}+l\dot{\phi}_{\mathrm{ti}}-h_4\dot{\theta}_{\mathrm{ti}}-\dot{y}_{\omega(2\mathrm{i}-1)}\right)+c_{1\mathrm{y}}h_4\left(\dot{y}_{\mathrm{ti}}-l\dot{\phi}_{\mathrm{ti}}-h_4\dot{\theta}_{\mathrm{ti}}-\dot{y}_{\omega(2\mathrm{i})}\right)\\
&\quad -2k_{1\mathrm{z}}b_1^2\theta_{\mathrm{ti}}-2c_{1\mathrm{z}}b_1^2\dot{\theta}_{\mathrm{ti}}
\end{aligned}
\tag{5.6}
$$

The dynamics of the four wheelsets (j = 1, 2 for two wheelsets in the front bogie, i = 1; and j = 3, 4 for two wheelsets in the rear bogie, i = 2) are expressed as follows:

$$
\begin{aligned}
m_{\omega}\ddot{y}_{\omega\mathrm{j}} &= k_{1\mathrm{y}}\left(y_{\mathrm{ti}}-(-1)^{\mathrm{j}}l\phi_{\mathrm{ti}}-\dot{y}_{\omega\mathrm{j}}-h_4\theta_{\mathrm{ti}}\right)+c_{1\mathrm{y}}\left(\dot{y}_{\mathrm{ti}}-(-1)^{\mathrm{j}}l\phi_{\mathrm{ti}}-\dot{y}_{\omega\mathrm{j}}-h_4\dot{\theta}_{\mathrm{ti}}\right)\\
&\quad -2f_{22}\left[\frac{\dot{y}_{\omega\mathrm{j}}}{V}\left(1+\frac{\sigma r_0}{b}\right)-\phi_{\omega\mathrm{j}}\right]-k_{\mathrm{gy}}y_{\omega\mathrm{j}}+2\left(\frac{\sigma r_0}{Vb}\dot{y}_{\mathrm{aj}}+\frac{\sigma r_0^2}{Vb}\dot{\theta}_{\mathrm{c1j}}\right)+k_{\mathrm{gy}}\left(y_{\mathrm{aj}}+r_0\theta_{\mathrm{c1j}}\right)
\end{aligned}
\tag{5.7}
$$

$$
J_{\omega\mathrm{z}}\ddot{\phi}_{\omega\mathrm{j}} = k_{1\mathrm{x}}b_1^2\left(\phi_{\omega\mathrm{j}}-\phi_{\mathrm{ti}}\right)-2f_{11}\left(\frac{b\lambda_{\mathrm{e}}}{r_0}y_{\omega\mathrm{j}}+\frac{b^2}{V}\dot{\phi}_{\omega\mathrm{j}}\right)+k_{\mathrm{gf}}\phi_{\omega\mathrm{j}}+2f_{11}\frac{b\lambda_{\mathrm{e}}}{r_0}\left(y_{\mathrm{aj}}+r_0\theta_{\mathrm{c1j}}\right)
\tag{5.8}
$$

Specifically, the lateral and yaw gravitational stiffness, k_{gy} and $k_{\mathrm{g}\varphi}$, are calculated as follows:

$$
k_{\mathrm{gy}} = \frac{W\lambda_{\mathrm{e}}}{b}
\tag{5.9}
$$

$$
k_{\mathrm{g}\varphi} = -Wb\lambda_{\mathrm{e}}
\tag{5.10}
$$

The random track irregularities experienced by the wheelsets are typically described by the power spectral densities (PSDs) of the lateral alignment parameter y_{aj} and cross-level parameter θ_{clj}. The one-sided PSD functions of German high-speed railways, which are obtained by analyzing a large number of measured field data, can be defined as follows (Claus and Schiehlen, 1998; Lei, 2017):

$$\text{Lateral alignment: } S_{\mathrm{a}}(\Gamma)=\frac{A_{\mathrm{a}}\Gamma_{\mathrm{c}}^{2}}{\left(\Gamma^{2}+\Gamma_{\mathrm{r}}^{2}\right)\left(\Gamma^{2}+\Gamma_{\mathrm{c}}^{2}\right)} \tag{5.11a}$$

$$\text{Cross-level: } S_{\mathrm{c}}(\Gamma)=\frac{\frac{A_{\mathrm{v}}}{b^{2}}\Gamma_{\mathrm{c}}^{2}\Gamma^{2}}{\left(\Gamma^{2}+\Gamma_{\mathrm{r}}^{2}\right)\left(\Gamma^{2}+\Gamma_{\mathrm{c}}^{2}\right)\left(\Gamma^{2}+\Gamma_{\mathrm{s}}^{2}\right)} \tag{5.11b}$$

where Γ is the spatial frequency (rad/m), and the unit of $S(\Gamma)$ is m^2/rad/m. Considering the relationship between the temporal and spatial frequencies, we have:

$$\omega = V\Gamma \tag{5.12}$$

and the RMS of the PSDs expressed with respect to the two frequencies should be equal:

$$S(\omega)d\omega = S(\Gamma)d\Gamma \tag{5.13}$$

The corresponding PSD functions in the temporal frequency are given as:

$$S_{\mathrm{a}}(\omega)=\frac{A_{\mathrm{a}}V^{3}\Gamma_{\mathrm{c}}^{2}}{\left(\omega^{2}+\left(V\Gamma_{\mathrm{r}}\right)^{2}\right)\left(\omega^{2}+\left(V\Gamma_{\mathrm{c}}\right)^{2}\right)} \tag{5.14a}$$

$$S_{\mathrm{c}}(\omega)=\frac{\frac{A_{\mathrm{v}}}{b^{2}}V^{3}\Gamma_{\mathrm{c}}^{2}\omega^{2}}{\left(\omega^{2}+\left(V\Gamma_{\mathrm{r}}\right)^{2}\right)\left(\omega^{2}+\left(V\Gamma_{\mathrm{c}}\right)^{2}\right)\left(\omega^{2}+\left(V\Gamma_{\mathrm{s}}\right)^{2}\right)} \tag{5.14b}$$

where V is the train speed, and ω is the temporal frequency, given in the unit rad/s. The key parameters in Equations (5.1–5.14) are listed in Appendix 5.6.

In this numerical study, the passive secondary suspension c_{2y} is replaced by the adaptive EHEMDs. The governing equation of motion is reconstructed as:

$$\mathbf{M}\ddot{\mathbf{X}}+\mathbf{C}\dot{\mathbf{X}}+\mathbf{K}\mathbf{X}=\mathbf{F}_{\mathrm{r}}\mathbf{w}+\mathbf{F}_{\mathrm{d}}\mathbf{u} \tag{5.15}$$

where **M**, **C**, and **K** are the 17 × 17 mass, damping, and stiffness matrix of the HST model, respectively; **w** represents the track irregularities; **u** is the control force provided by EHEMDs; and $\mathbf{F_r}$ and $\mathbf{F}_{\mathrm{d}}$ are the coefficient matrices corresponding to the track irregularities and the installation of the EHEMDs, respectively.

$$\mathbf{w}=\left[\,y_{\mathrm{a1}}\;\; y_{\mathrm{a2}}\;\; y_{\mathrm{a3}}\;\; y_{\mathrm{a4}}\;\; \theta_{\mathrm{c11}}\;\; \theta_{\mathrm{c12}}\;\; \theta_{\mathrm{c13}}\;\; \theta_{\mathrm{c14}}\;\; \dot{y}_{\mathrm{a1}}\;\; \dot{y}_{\mathrm{a2}}\;\; \dot{y}_{\mathrm{a3}}\;\; \dot{y}_{\mathrm{a4}}\;\; \dot{\theta}_{\mathrm{c11}}\;\; \dot{\theta}_{\mathrm{c12}}\;\; \dot{\theta}_{\mathrm{c13}}\;\; \dot{\theta}_{\mathrm{c14}}\,\right]^{T} \tag{5.16}$$

The product of $\mathbf{F_r}$ and $\mathbf{w}$ can be regarded as the excitation acting on the HST. $\mathbf{X}$ is the response vector:

$$\mathbf{X} = \left[y_c \;\; \phi_c \;\; \theta_c \;\; y_{t1} \;\; \phi_{t1} \;\; \theta_{t1} \;\; y_{t2} \;\; \phi_{t2} \;\; \theta_{t2} \;\; y_{\omega 1} \;\; \phi_{\omega 1} \;\; y_{\omega 2} \;\; \phi_{\omega 2} \;\; y_{\omega 3} \;\; \phi_{\omega 3} \;\; y_{\omega 4} \;\; \phi_{\omega 4} \right]^T \tag{5.17}$$

Equation (5.15) can be rewritten in a state-space form:

$$\dot{\mathbf{Z}} = \mathbf{A}\mathbf{Z} + \mathbf{B}_w \mathbf{w} + \mathbf{B}_d \mathbf{u} \tag{5.18}$$

where

$$\mathbf{Z} = \begin{bmatrix} \mathbf{X} \\ \dot{\mathbf{X}} \end{bmatrix} \tag{5.19a}$$

$$\mathbf{A} = \begin{bmatrix} \mathbf{0} & \mathbf{I} \\ -\mathbf{M}^{-1}\mathbf{K} & \mathbf{M}^{-1}\mathbf{C} \end{bmatrix} \tag{5.19b}$$

$$\mathbf{B}_w = \begin{bmatrix} \mathbf{0} \\ \mathbf{M}^{-1}\mathbf{F}_r \end{bmatrix} \tag{5.19c}$$

$$\mathbf{B}_d = \begin{bmatrix} \mathbf{0} \\ \mathbf{M}^{-1}\mathbf{F}_d \end{bmatrix} \tag{5.19d}$$

where $\mathbf{I}$ is an identity matrix.

Table 5.1 Definitions of the 17 DOFs in the HST model (Zong et al., 2013)

	Component	Lateral	Yaw	Roll
Car body		y_c	ϕ_c	θ_c
Bogie	Leading bogie	y_{t1}	ϕ_{t1}	θ_{t1}
	Rear bogie	y_{t2}	ϕ_{t2}	θ_{t2}
Wheelset	Leading bogie leading wheelset	$y_{\omega 1}$	$\phi_{\omega 1}$	
	Leading bogie trailing wheelset	$y_{\omega 2}$	$\phi_{\omega 2}$	
	Rear bogie leading wheelset	$y_{\omega 3}$	$\phi_{\omega 3}$	
	Rear bogie trailing wheelset	$y_{\omega 4}$	$\phi_{\omega 4}$	

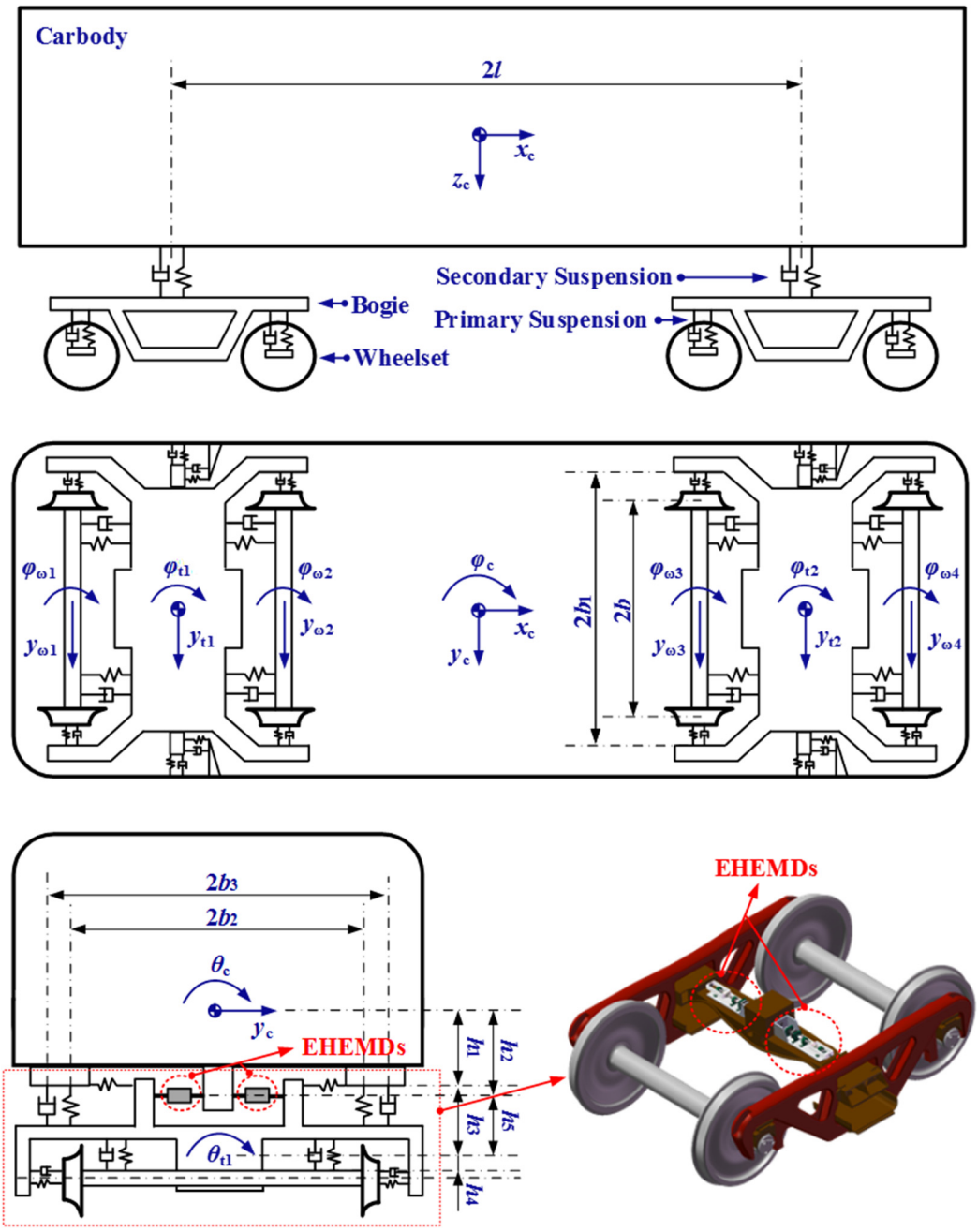

Figure 5.1 17DOF model of HST with EHEMDs

5.3 Energy-harvesting Adaptive Damping

5.3.1 Optimal Damping

The optimal damping of the HST secondary lateral suspension depends on the train speed (Shi and Zhu, 2018). Large and small damping coefficients are required at low and high train speeds, respectively, to achieve favorable vibration suppression performance. Therefore, an adaptive adjustment of the damping coefficient c_{2y} based on the train speed

is highly desirable. It needs to mention that the damping coefficient c_{2y} is provided by two symmetrically viscous dampers. Given the models of the HST and track irregularities, the optimal damping coefficient is a function of the train speed. The relationship between the optimal damping coefficient of each damper and the train speed, which is unavailable in the literature, was first determined numerically in this study through the following optimization:

$$J := \min_{c_d \in [c_{low}, c_{up}]} \sqrt{\frac{\sum_{i=1}^{n} (\ddot{y}_{ci})^2}{n}} \tag{5.20}$$

where J denotes the objective function; $\ddot{y}_{ci}$ is the lateral acceleration of the car body at time i; n is the number of data points in the selected time window, recorded acceleration data length; and c_{low} and c_{up} represent the lower and upper bounds of c_d, respectively, due to the practical constraints; specifically, $c_p \le c_d \le (c_p + K_{eq}^2/R_{coil})$ (see Chapter 3). Equation (5.20) presents a single-parameter optimization problem with the optimization objective of minimizing the RMS lateral acceleration of the car body.

Figure 5.2 shows the obtained optimal relationship for the considered HST model, with the optimization objective of minimizing the RMS lateral acceleration of the car body. The optimal damping coefficient c_d of one passive viscous damper decreased from 26.5 to 12 kN·s/m when the train accelerated. A cubic polynomial fitting was applied in this study to obtain an approximate relationship:

$$c_{d,opt} = \frac{c_{2y,opt}}{2} = \mathbf{D}\begin{bmatrix} V^3 & V^2 & V & 1 \end{bmatrix}^T \quad (100 \le V \le 340) \tag{5.21}$$

where $\mathbf{D} = [1.6754 \times 10^{-6}, -0.0011, 0.1492, 20.9804]$ is the coefficient matrix. Notably, four identical passive dampers were installed in the secondary lateral suspensions (two for both front and rear bogies) in the original train model. A fixed passive damping coefficient of $c_d = 26$ kN·s/m (equal to $c_{2y} = 52$ kN·s/m) was set for each viscous damper (Zong et al., 2013), which can perform well only at low train speeds in accordance with Figure 5.2.

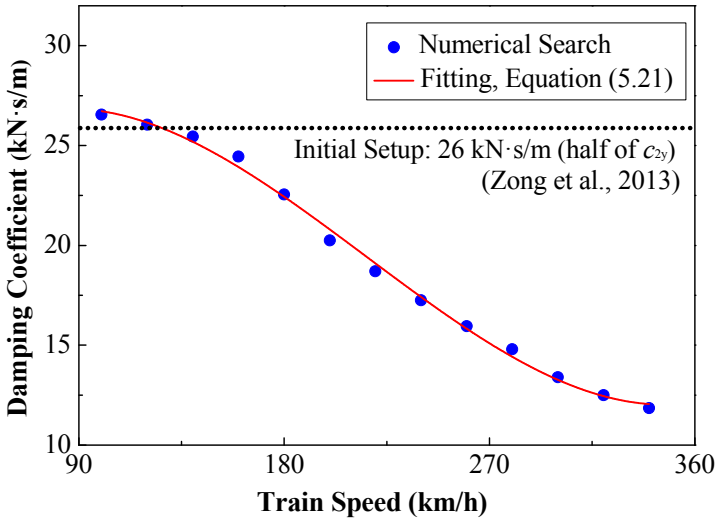

Figure 5.2 Optimal damping coefficient c_d of one passive damper installed in the secondary lateral suspension at different train speeds

5.3.2 EHEMD with Adaptive Damping and Energy Harvesting

5.3.2.1 EMD

The presented EHEMD is composed of an EMD and an adaptive-duty-cycle EHC, wherein the EMD can transform the vibration energy into electricity through the relative motion between the coils and permanent magnets, and the EHC stores the generated power and functions as an adaptive equivalent resistor. The detailed description of EHEMD can be found in Chapter 4. The influence of the coil inductance L_{coil} is negligible, considering its small value and the low-frequency (<20 Hz) vibration in HSTs.

The original passive viscous dampers in the secondary lateral suspensions are replaced by four EHEMDs installed at the same locations. Therefore, the damping coefficient c_{2y} is provided by:

$$c_{2y} = 2c_d = 2\left(c_{em} + c_p\right) \tag{5.22}$$

where c_d is the total damping coefficient provided by each EHEMD. To meet the variable optimal condition of the damping coefficient at different train speeds (Figure 5.2), the load resistance should be tuned adaptively. Such variation in the equivalent resistance can be realized by adjusting the duty cycle of the EHC as mentioned in Chapter 3.

5.3.2.2 EHC Design

The EHC components used in this chapter are nearly the same as the description in Figure 3.4. Just notably, the MCU herein enables the adaptive adjustment of the duty cycle of the PWM waves according to the train speed sensing, as shown in Figure 5.3. A detailed elaboration of these symbols can be found in Chapter 3.

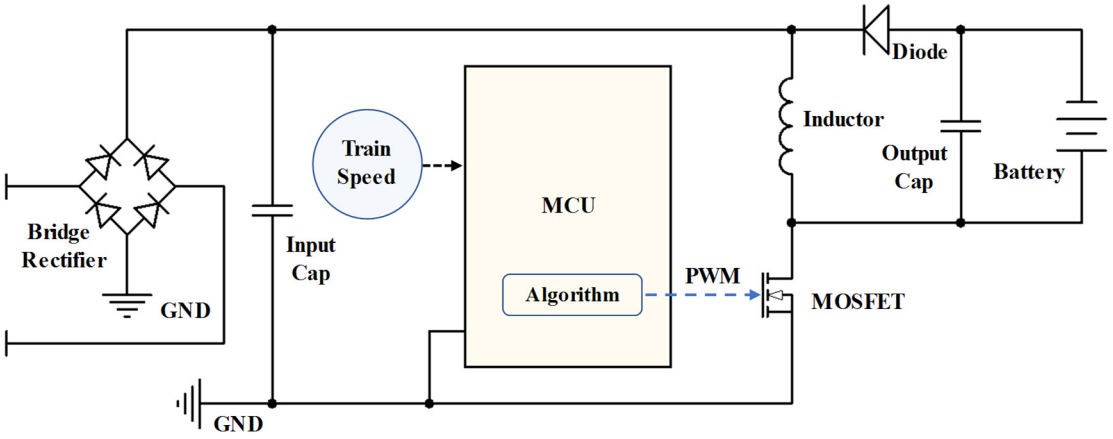

Figure 5.3 Schematic of the EHC in energy-harvesting adaptive damping

To achieve the optimal damping $c_{\mathrm{d,opt}}$ specified in Equation (5.21), the on-demand EM damping coefficient $c_{\mathrm{em,opt}}$ of each EHEMD, the equivalent resistance $R_{\mathrm{eq,opt}}$ of the buck–boost converter, and the duty cycle δ_{opt} of PWM are as follows:

$$c_{\mathrm{em,opt}} = c_{\mathrm{d,opt}} - c_{\mathrm{p}} \tag{5.23a}$$

$$R_{\mathrm{eq,opt}} = \frac{K_{\mathrm{eq}}^2}{c_{\mathrm{em,opt}}} - R_{\mathrm{coil}} \tag{5.23b}$$

$$\delta_{\mathrm{opt}} = \begin{cases} \dfrac{4Lf_{\mathrm{w}}}{\left(R_{\mathrm{on}}^2 + 8Lf_{\mathrm{w}}R_{\mathrm{eq,opt}}\right)^{1/2} - R_{\mathrm{on}}} & \textit{if DCM} \\ \dfrac{U_{\mathrm{rect}}}{\langle i_{\mathrm{bat}} \rangle R_{\mathrm{eq,opt}} + U_{\mathrm{rect}}} & \textit{if CCM} \end{cases} \tag{5.23c}$$

Taking the DCM operation mode as an example, the fitting relationship between the train speed and the optimal duty cycle can be given as:

$$\delta_{\text{opt}} = \frac{4Lf_{\text{w}}}{\left(R_{\text{on}}^2 + 8Lf_{\text{w}} \left(\frac{K_{\text{eq}}^2}{\mathbf{D}\left[V^3 \;\; V^2 \;\; V \;\; 1 \right]^T - c_{\text{p}}} - R_{\text{coil}} \right) \right)^{1/2} - R_{\text{on}}} \tag{5.24}$$

Consequently, the optimal relationship between the train speed and damping coefficient is converted to the relationship between the train speed and control signal (i.e., the duty cycle δ_{opt}).

5.3.2.3 Adaptive Control Strategy

The control strategy is illustrated in Figure 5.4. Given the relationship between the optimal damping coefficient and train speed in Equation (5.21), the target EM damping coefficient, equivalent resistance, and duty cycle corresponding to different train speeds can be obtained by using Equation (5.23). This relationship between the train speed and duty cycle (i.e., Equation (5.24)) can be programmed into the MCU beforehand. With train speed sensing, the PWM wave with the corresponding duty cycle can be generated by the MCU and fed to the MOSFET. Consequently, an approximately target damping force is provided to the HST secondary suspension. When the sensed train speed changes, the duty cycle should be adjusted adaptively. The buck–boost converter will partially operate in CCM if the rectifier voltage is larger than the threshold (Equation (3.8)), leading to the degradation of the vibration control performance. In this numerical study, the nominal voltage of the rechargeable battery was set as 110 V, which is equal to the typical emergency power supply voltage in an HST system. With this battery voltage, the buck–boost converter could maintain its operation mainly in DCM when the train speed ranged from 100 to 340 km/h (Figure 5.10). Notably, even if the buck–boost converter with other design parameters is expected to operate in CCM, a solution to realize the target resistance is still found by sensing the rectifier voltage and adjusting the duty cycle in CCM (see Chapter 3).

In the whole control strategy, the EHEMD works as an adaptive viscous damper with an adjustable damping coefficient and an energy harvesting function. The input signal is

the sensed train speed, and the output is the optimal damping force on the HST. The optimal damping force is realized by adjusting the duty cycle of the PWM wave to achieve the target equivalent resistance of the EHC. During the provision of the damping force to the HST, the vibration energy is partially converted to electrical energy and stored in the EHC rechargeable battery.

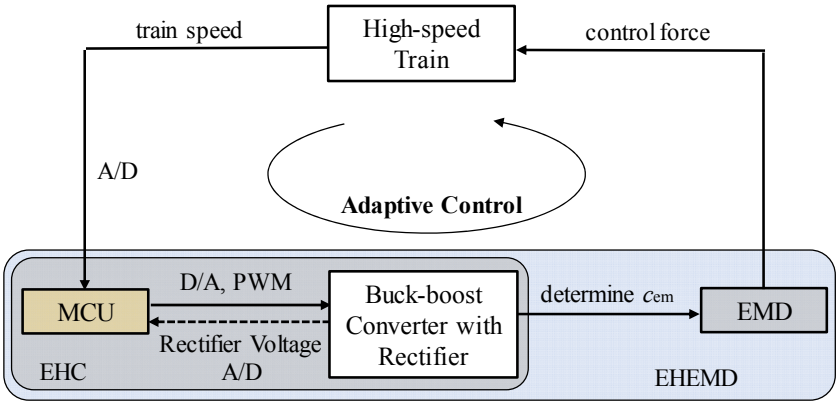

Figure 5.4 Energy-harvesting adaptive control strategy

The abovementioned control strategy shown in Figure 5.4 is essentially a feed-forward control, in which only the MCU consumes power. However, the power consumption of MCUs is considerably lower than the harvested power (often greater than 10 W, as shown in the following section). Given that the optimal equivalent resistance is determined to achieve the desired vibration control performance at different train speeds, it is unlikely to maintain an optimal output power or power efficiency.

5.4. Dynamic Simulation and Performance Evaluation

5.4.1 Simulink Model

This subsection introduces the established Simulink model for the HST model with adaptively controlled EHEMDs (Figure 5.5). The time step was set as 10^{-7} s, considering the high switching frequency (equal to 20 kHz) of the PWM wave in the EHC. The EMD parameters were assumed as c_p = 7 kN·s/m, R_{coil} = 5 Ω, K_{eq} = 500 N/A in this numerical study. The parameters of the electronic elements, such as the forward voltage of the diodes, on-resistance of the MOSFET, and ESR of the used inductor and capacitor, are presented

in Table 5.2. For the sake of comparison, two different control strategies were applied:

(1) Energy-harvesting passive control (EHPC): A buck–boost converter with a fixed duty cycle was adopted as the main part of the EHC, wherein the duty cycle was fixed as 75%; an initial equivalent resistor R_{eq} = 8 Ω (Equation (3.9)) was generated, and the EM damping coefficient c_{em} was 19 kN·s/m (Equation (3.5)) when the EHC operated in DCM. Each EHEMD could provide a damping coefficient c_d of 26 kN·s/m, considering the parasitic damping coefficient c_p of 7 kN·s/m. This value is close to the setting of the passive viscous dampers originally used in the HST model.

(2) Energy-harvesting adaptive control (EHAC): The duty cycle of the buck–boost converter was adaptively adjusted based on the train speed.

For the sake of brevity, hereafter, parameters such as the equivalent resistance, EM damping, and power items are for a single EHEMD only (one of four EHEMDs), unless otherwise stated.

Table 5.2 Main parameters of the EHC in EHAC and EHPC

Parameter	Value	Parameter	Value
Filter capacitor, C_{in}	240 μF	Switch frequency, f_w	20 kHz
ESR of filter capacitor, $R_{esr,in}$	0.2 Ω	Forward voltage of diode, U_F	0.22 V
Inductor, L	100 μH	Static drain-source on-resistance of the MOSFET, R_{on}	0.8 Ω
ESR of inductor, $R_{esr,L}$	0.53 Ω	Nominal voltage of rechargeable battery, U_{bat}	110 V
Output capacitor, C_{out}	10 μF	Power consumption of MCU	ignored
ESR of output capacitor, $R_{esr,out}$	0.18 Ω		

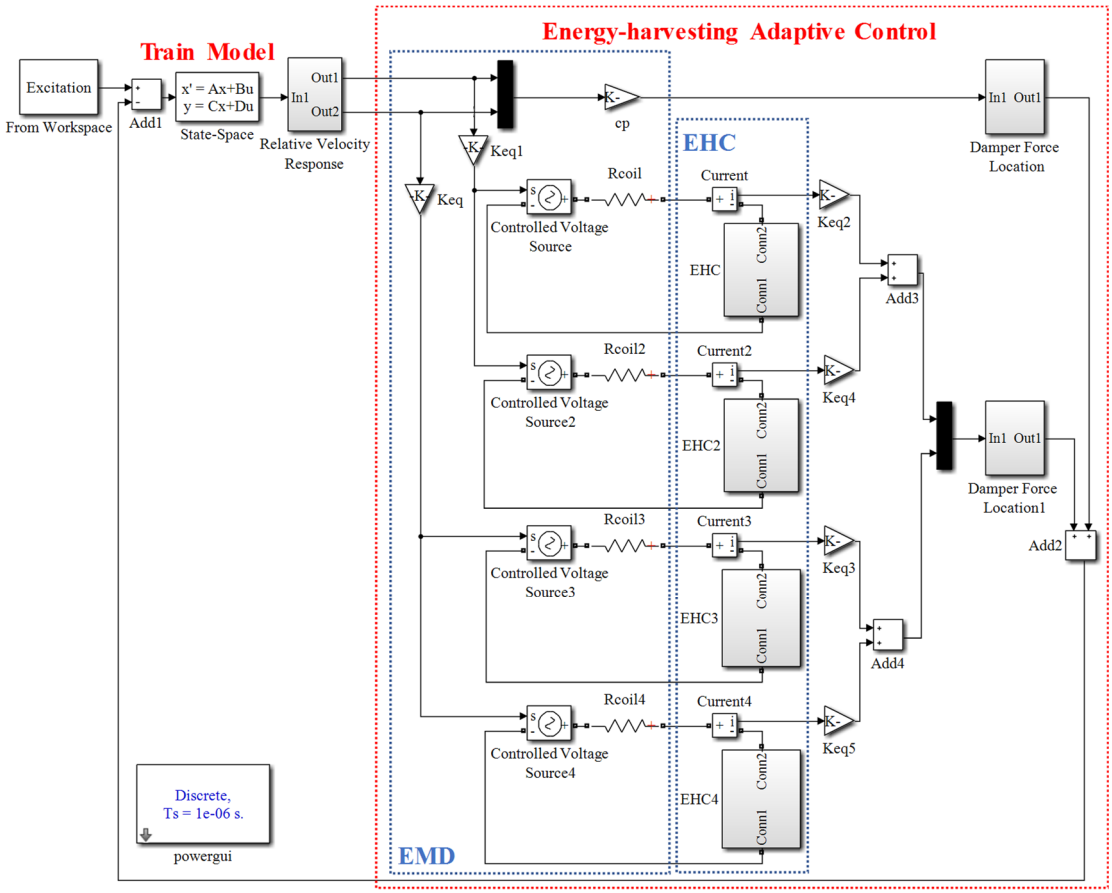

(a) Overall system

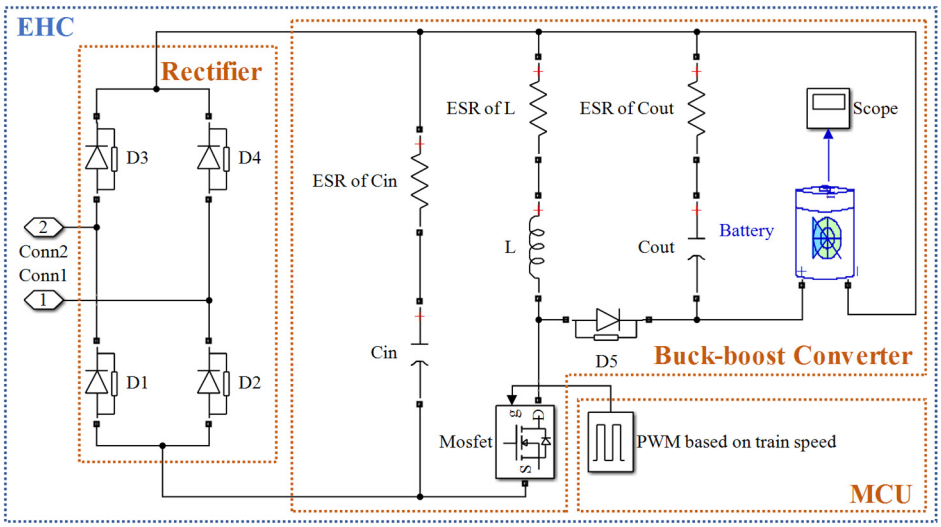

(b) EHC

Figure 5.5 Simulink model for HST with EHAC

5.4.2 Track Irregularities

Figures 5.6 and 5.7 show the simulated track irregularities in the lateral alignment

and cross-level, respectively, whereby subfigures (a) and (b) show the time histories and the corresponding PSDs, respectively. As observed in Figures 5.6 and 5.7, the simulated PSDs agree well with the analytical expressions in Equation (5.14).

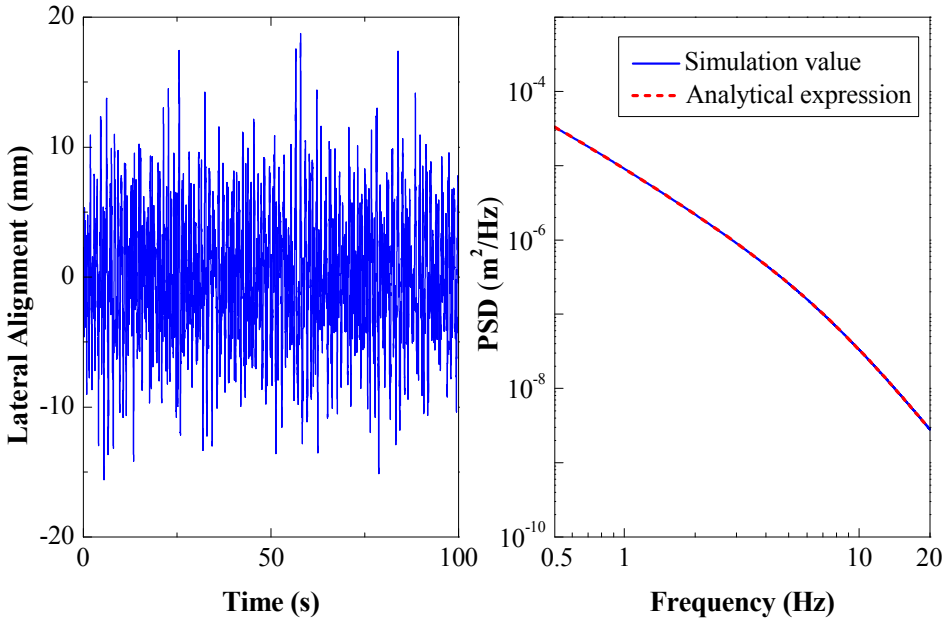

(a) Time history (b) PSD

Figure 5.6 Lateral alignment of the track irregularities

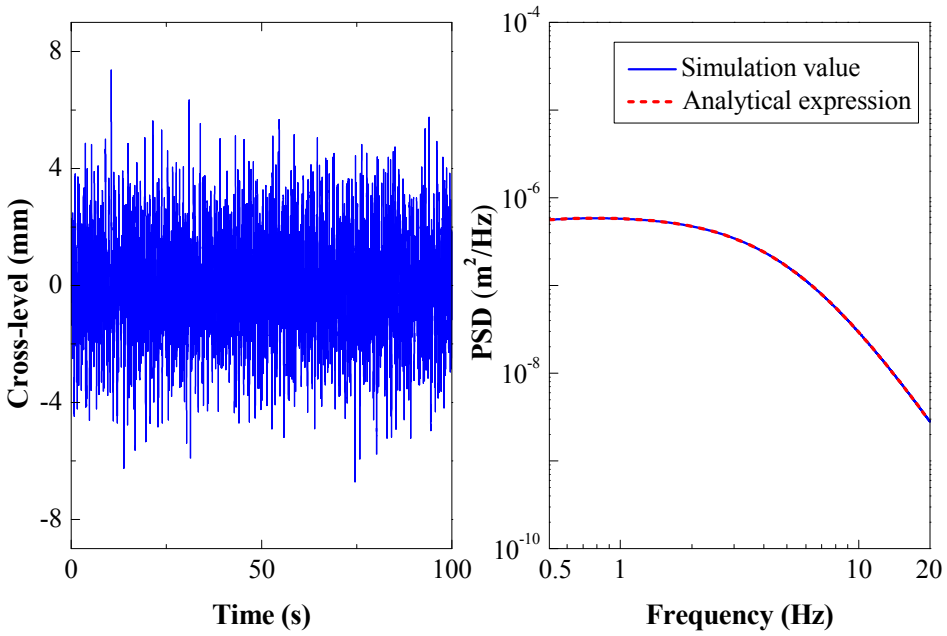

(a) Time history (b) PSD

Figure 5.7 Cross-level of the track irregularities

The random track irregularities were then converted to the excitation force acting on the wheelsets. Figure 5.8 shows a representative lateral excitation force acting on the leading bogie leading wheelset. The RMS force in this case was approximately 1.025 kN.

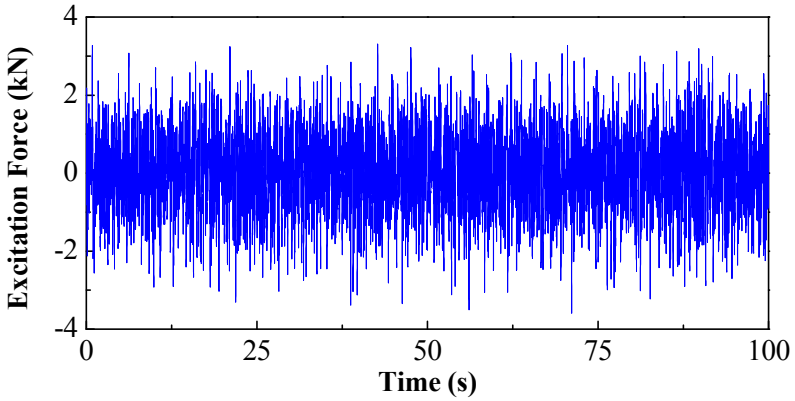

Figure 5.8 Time history of the lateral excitation force on the front bogie leading wheelset at a speed of 200 km/h

5.4.3 Circuit Characteristics

Figure 5.9(a) shows the duty cycle of the EHAC, adaptively adjusted in accordance with the empirical relationship shown in Equation (5.24). The duty cycle changed from 77% to 30% when the train speed increased from 100 to 340 km/h. Notably, the train speed 340 km/h is below the critical speed for this HST model. It has been confirmed by a pole-zero analysis, which is not included in this thesis. The fixed duty cycle of the EHPC is plotted in Figure 5.9(a) for comparison. Figure 5.9(b) shows the average equivalent resistance of the EHC in the EHAC and EHPC cases. In the EHAC case, the equivalent resistance generally increased with the increase in the train speed. The equivalent resistance of the EHAC matched well with the design target at each train speed, with a maximum error of merely 2%. In contrast, the average resistance in the EHPC case dropped and shifted away from the fixed value of 8 Ω with the increasing train speed, because the fixed-duty-cycle (i.e., 75%) buck–boost converter mainly operated in CCM when the train speed exceeded 200 km/h.

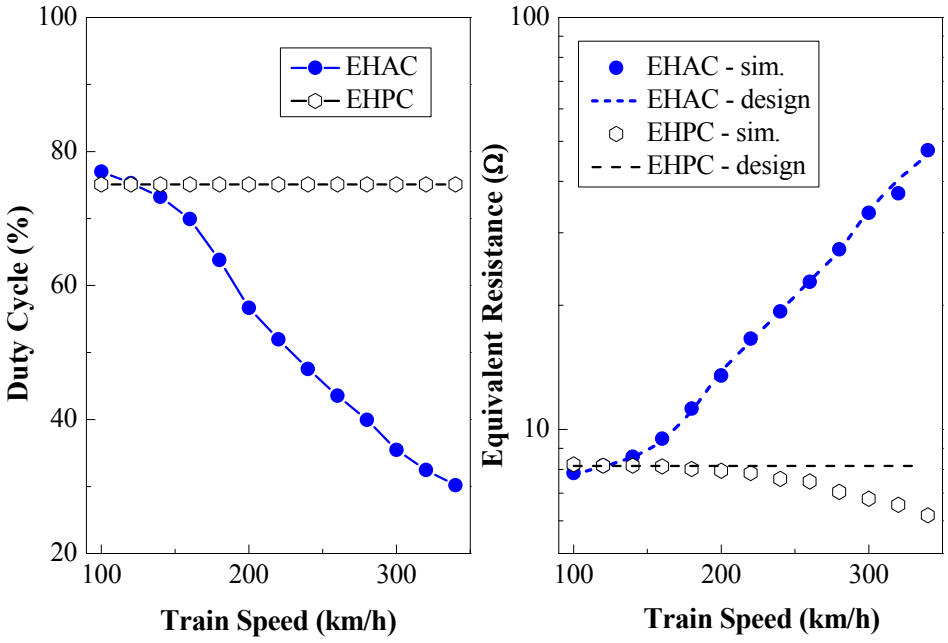

(a) Duty cycle (b) Equivalent resistance

Figure 5.9 Duty cycle and equivalent resistance for two different control strategies (EHAC and EHPC)

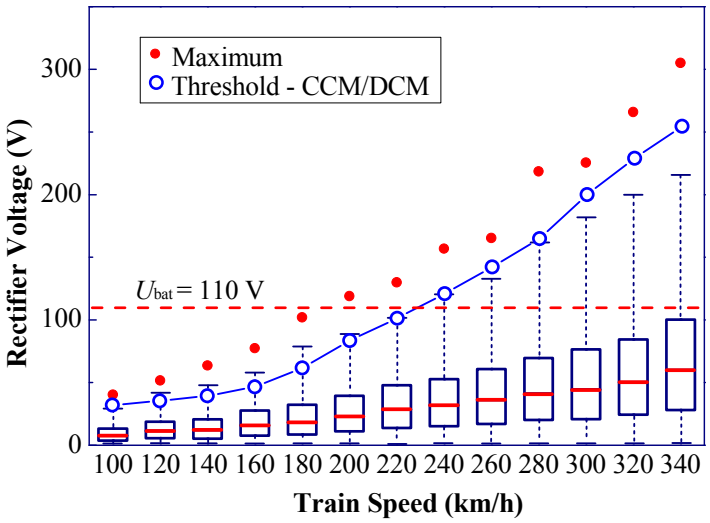

Figure 5.10 Box–whisker plot and rectifier voltage at different train speeds

Figure 5.10 shows the statistical results (in the form of a box-and-whisker plot) of the rectifier voltage in the EHAC case. For each train speed, the whisker range represents 1–99% of the rectifier voltage, and the red point is the maximum rectifier voltage. The theoretical transition threshold between DCM and CCM increased from 32.9 to 254.9 V with the increasing train speed owing to the decreasing duty cycle. The threshold voltage

mostly covered the rectifier voltages at each train speed, implying that the adaptive adjustment of the duty cycle in the EHAC case made the EHC mainly operate in DCM most of the time, and thus, the target optimal damping was maintained.

5.4.4 Vibration Suppression Performance

Figure 5.11 shows the damper force versus damper velocity relationship in the EHAC and EHPC cases at a train speed of 300 km/h. The slope of the force–velocity curve denotes the EM damping coefficient of the installed EHEMD. The provided EM damping coefficient of EHAC was approximately 6.49 kN·s/m, which is very close to the optimal design value of 6.40 kN·s/m. The EHPC shows a bilinear curve with a relatively smaller damping coefficient of 19 kN·s/m at a low vibration velocity and an increased damping coefficient at a high vibration velocity, and they corresponded to DCM and CCM operations, respectively. A linear regression analysis of the numerical data shows that the overall damping coefficient of EHPC was approximately 22.58 kN·s/m, which considerably deviates from the initial design value.

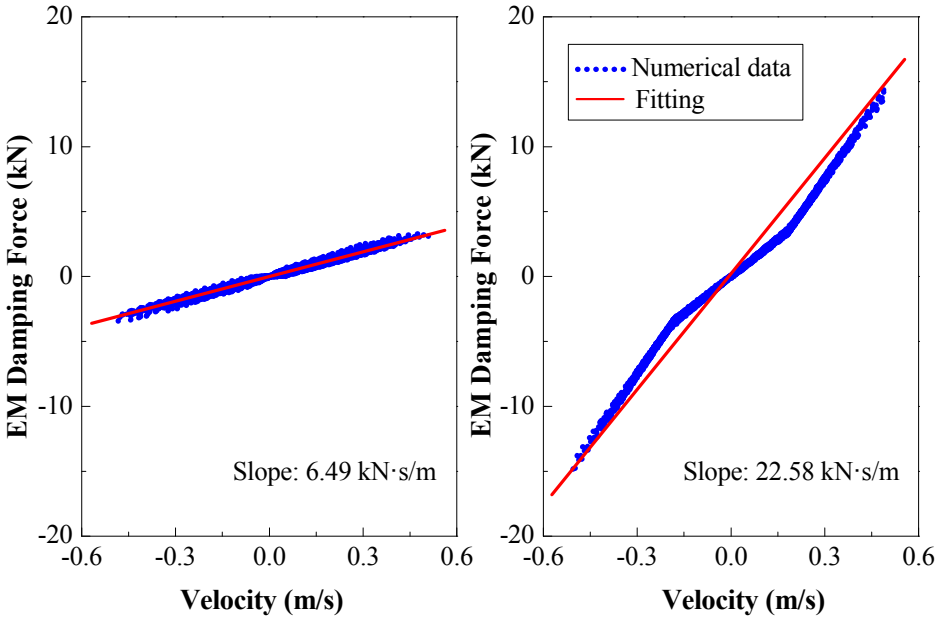

(a) EHAC (b) EHPC

Figure 5.11 Damping force vs. velocity curves at 300 km/h

Figure 5.12(a) illustrates the variation of the EM damping coefficients within the concerned train speed range. The numerical results of EHAC agree well with the optimal design target. The maximum relative error of 3% occurred at a relatively low train speed, which is attributed to the voltage drop of the bridge rectifier. This comparison demonstrates that the proposed EHEMD can successfully realize adaptive damping tuning through the MCU-controlled buck–boost converter. Note that each bogie was equipped with two EHEMDs. The target EM damping coefficient of each EHEMD can be determined using Equation (5.23a). By contrast, the EHPC significantly deviated from the optimal design values. The EHPC even could not maintain the initially set fixed damping coefficient (19 kN·s/m) when the train speed increased.

Figure 5.12(b) summarizes the RMS lateral acceleration of the car body at different train speeds using different control strategies; the case with a viscous damper represents the result with a fixed damping coefficient of c_d = 26 kN·s/m (i.e., c_{2y} = 52 kN·s/m) that was used in the original train model. The control performance of EHAC and EHPC at a low train speed was very close; however, at a relatively high train speed (e.g., 340 km/h), the vibration reduction achieved by the EHAC was ~40% and ~27% greater than those achieved by the EHPC and a pure viscous damper, respectively. These comparisons demonstrate the benefits of the adaptive damping enabled by the EHEMDs, particularly at a high train speed when vibration problems become more crucial for ride comfort. It is noted that owing to the performance degradation in CCM, the EHPC at a large train speed resulted in even worse control performance compared with the pure viscous damper originally used in the HST model.

The lateral acceleration time histories at three different train speeds, namely 100, 200, and 300 km/h, are presented in Figure 5.13. The comparison demonstrates the effectiveness of the proposed adaptive control with EHEMD(s) in the HST, especially at high speeds.

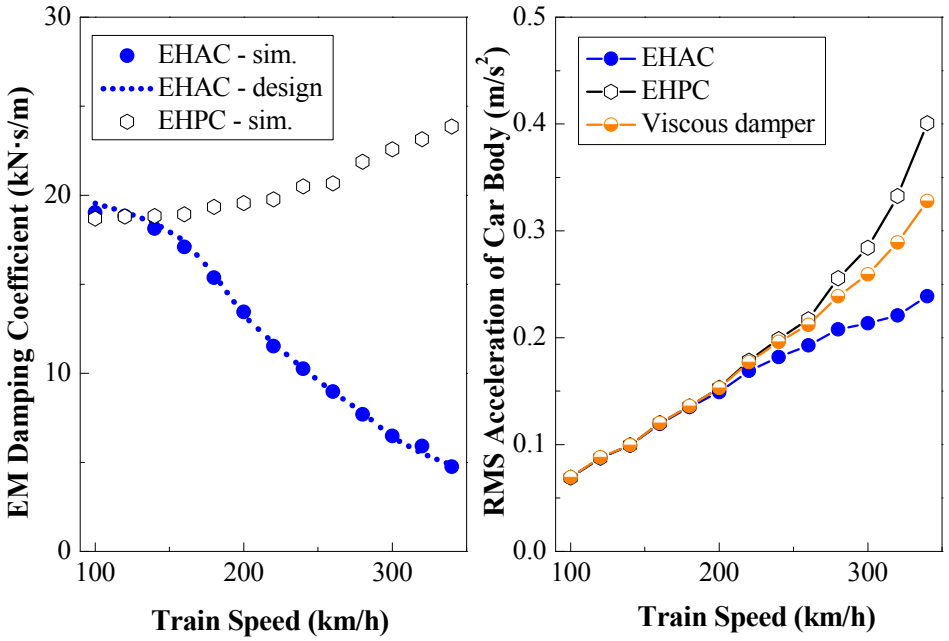

(a) EM damping of one EHEMD (b) RMS acceleration

Figure 5.12 Control performance of different control strategies

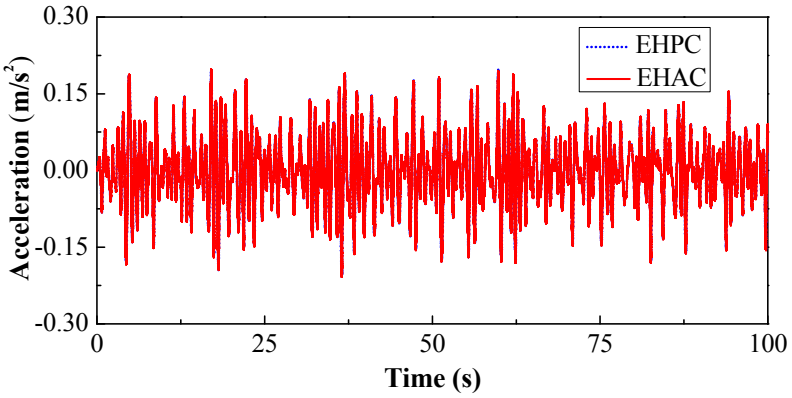

(a) 100 km/h

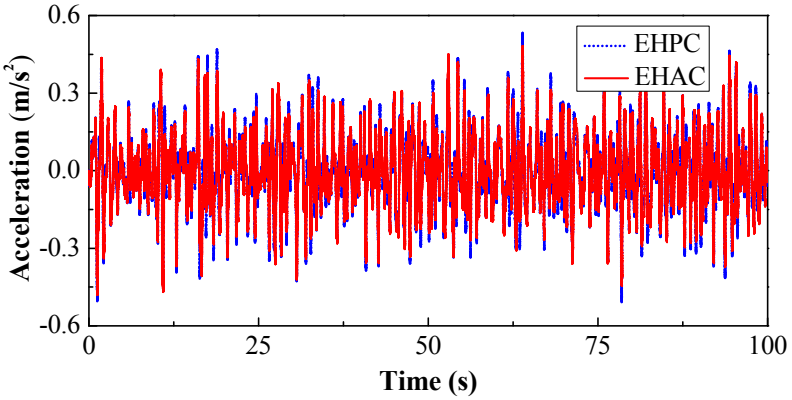

(b) 200 km/h

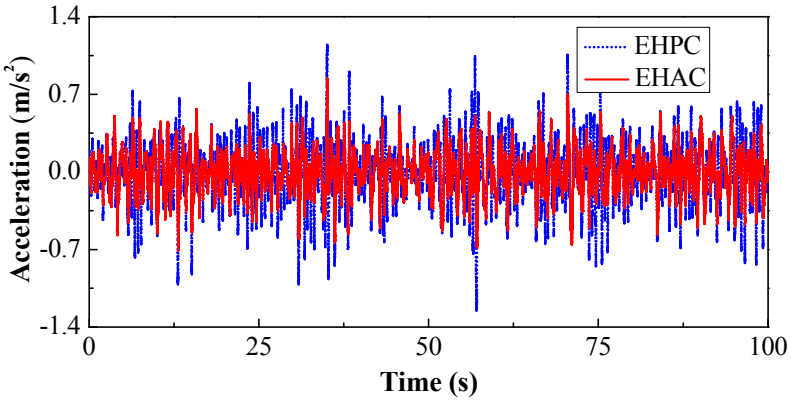

(c) 300 km/h

Figure 5.13 Lateral acceleration time histories of the car body at three train speeds

5.4.5 Energy Harvesting Performance

Figure 5.14(a) presents the input and output powers of the EHAC at different train speeds. The input power and output power monotonically increased from 38.2 to 423 W and from 10.7 to 125.3 W, respectively, with the increase in train speed from 100 to 340 km/h. This result demonstrates that the adaptive control with EHEMD(s) can effectively harvest the vibration energy from the traveling HST. Figure 5.14(b) shows the corresponding efficiency. The sub-efficiency η_1 decreased because the design target damping decreased with the increase in train speed (Figure 5.2). Accordingly, the design resistance increased with the increase in train speed, leading to the increasing sub-efficiencies η_2 and η_3. The overall efficiency η reached a maximum value of 35% at a speed of 240 km/h. The comparison of Figure 5.14(a) and (b) demonstrates that an optimal power efficiency does not correspond to the maximum output power.

Taking the train speed of 200 km/h as an example, Figure 5.15 illustrates the power distribution of the total input power of EHAC, of which 34.23% was dissipated by the parasitic damping and 34.31% was stored in the battery as effective output power. The corresponding average output power was approximately 61.9 W, which is likely sufficient to power the low-power MCU used in semi-active/active control systems or numerous wireless sensors. Notably, the percentages of power losses in the bridge rectifier and converter can be reduced at higher speeds when the design resistance and the generated

voltage are larger.

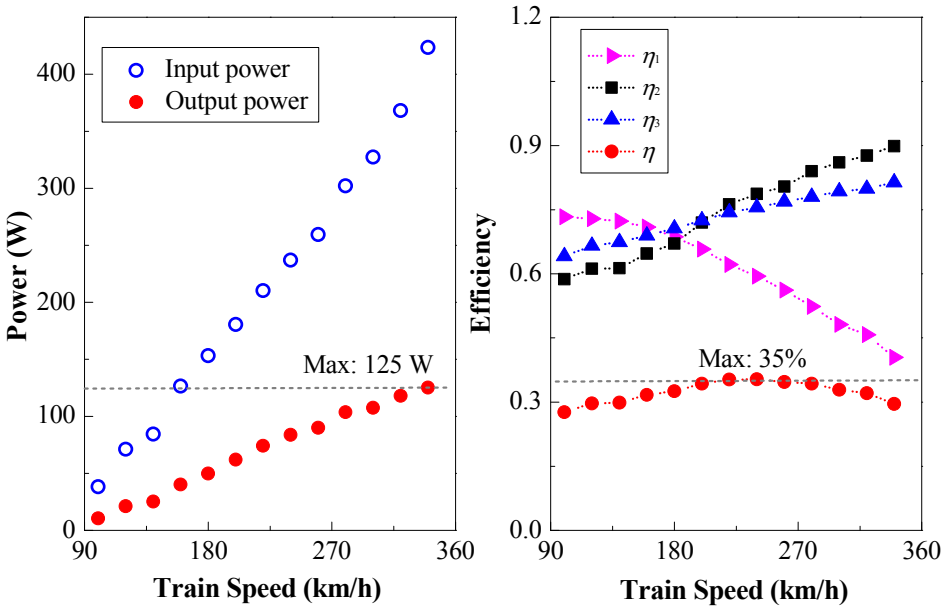

(a) Power (b) Efficiency

Figure 5.14 Harvesting performance at different train speeds: EHAC

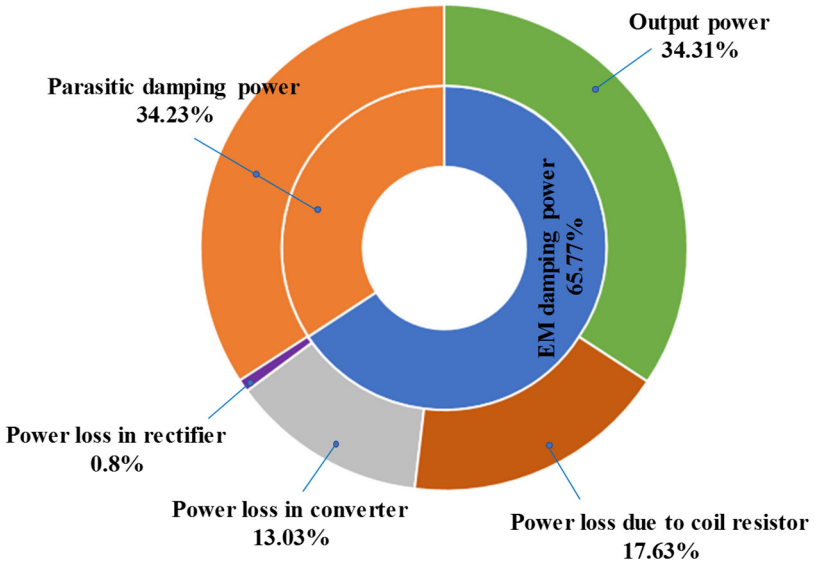

Figure 5.15 Power distribution of input power under a speed of 200 km/h

The aforementioned power results are obtained from one EHEMD in the front bogie. Considering all four installed EHEMDs, of which two are in the front bogie and the others are in the rear bogie, Table 5.3 compares the corresponding energy harvesting results of

the EHAC and EHPC. The EHPC generally could capture more power owing to the dramatically higher input power, although the power harvesting efficiency was lower. The total input power of EHAC at the train speed of 340 km/h was up to 1948.2 W, but approximately 2787.5 W less than that of EHPC. Notably, in the case of the same control strategy, the amounts of power harvested by the EHEMDs installed in the front and rear bogies were slightly different. However, all of them operated in DCM most of the time. Given the similarity, the individual results are not presented for brevity. The results in Figure 5.12 and Table 5.3 demonstrate that the optimizations of energy harvesting and vibration control (minimization of the RMS lateral acceleration of the car body) were inconsistent when the adaptively controlled EHEMDs were applied to the HST suspension. This conclusion is similar to the observation by Abdelkareem et al. (2018b). Considering the major function of the secondary suspension, the vibration control performance should be given priority when a trade-off must be made between two objectives in the EHEMD design.

Table 5.3 Energy harvesting results of EHAC and EHPC (four EHEMDs) under four different train speeds

Train speed (km/h)	EHAC		EHPC	
	Output power (W)	Output efficiency (%)	Output power (W)	Output efficiency (%)
100	40.47	27.56	41.62	28.12
200	244.92	34.28	242.02	29.19
300	469.84	32.88	690.66	24.59
340	589.82	30.27	1046.24	22.09

5.5 Summary

This chapter proposes an energy-harvesting adaptive vibration-damping strategy implemented in the HST secondary suspension using dual-function adaptive EHEMDs. Each EHEMD is composed of an EMD and an EHC. In the proposed EHAC, the duty cycle of PWM waves in the EHC is adaptively adjusted based on the train speed, and thus

the buck–boost converter can always emulate a target resistance and produce an optimal equivalent damping coefficient within the concerned train speed range, wherein the optimization objective is to minimize the RMS lateral acceleration of the car body. The effectiveness of the proposed suspension with EHAC to improve vibration suppression was numerically verified through a 17DOF HST model. For comparison, an EHPC with a fixed duty cycle was simulated in parallel. The main conclusions are given as follows:

1) The empirical relationship between the train speed and optimal damping coefficient of the secondary lateral suspension was obtained, showing that the optimal damping coefficient gradually decreases with increasing train speed.
2) Through the MCU-enabled duty cycle adjustment in EHC, the equivalent resistance could be adaptively adjusted to realize the optimal damping coefficients at different train speeds.
3) Although the EHPC can simultaneously realize vibration damping and energy harvesting functions, it cannot guarantee optimal vibration control performance owing to its fixed nature. Compared with the traditional passive viscous dampers in HSTs, the EHPC showed a similar control performance at a low train speed but a worse vibration control performance at a high train speed because of the influence of CCM.
4) Compared with EHPC, EHAC could improve the vibration control performance by 40% at a high train speed. EHAC could also outperform pure viscous dampers in the secondary lateral suspension of HSTs.
5) The output power of EHPC was generally higher than that of EHAC. The performance comparison of EHAC and EHPC indicates that the optimizations of energy harvesting and vibration control in the HST suspension are inconsistent.
6) The output power in the case of EHAC ranged from 40.5 to 589.8 W within the considered train speed range (100–340 km/h), which will likely be sufficient to power numerous wireless sensors for train monitoring or MCUs used in semi-active/active vibration control.

The numerical results demonstrate that the proposed system can successfully realize energy-harvesting adaptive vibration control. Further experimental validations on the accuracy of the numerical simulations and the effectiveness of the proposed adaptive control with EHEMD(s) need to be conducted. Notably, the applications of the energy-harvesting adaptive vibration damping enabled by EHEMD(s) are certainly not limited to HST suspensions.

5.6 Appendix: Parameters of the HST and Track Model

Table 5.4 Main parameters of the HST model (Zong et al., 2013)

Symbol	Parameter description
$m_\omega\, m_t\, m_c$	Mass of wheelset (1,750 kg), bogie (3,296 kg), and car body (32,000 kg)
$J_{\omega z}\, J_{tz}\, J_{cz}$	Yaw moment of inertia of wheelset (1,400 kgm^2), bogie (2,100 kgm^2), and car body (2.24×10^6 kgm^2)
$J_{tx}\, J_{cx}$	Roll moment of inertia of bogie (1,900 kgm^2) and car body (75,000 kgm^2)
W	Load per wheelset (1.117×10^5 N)
$k_{1x}\, k_{2x}$	Double of primary (2.9×10^7 N/m) and secondary longitudinal stiffness (3.4×10^5 N/m)
$k_{1y}\, k_{2y}$	Double of primary (1.5×10^7 N/m) and secondary lateral stiffness (3.5×10^5 N/m)
$k_{1z}\, k_{2z}$	Double of primary (1.33×10^6 N/m) and secondary vertical stiffness (6.8×10^5 N/m)
$c_{1x}\, c_{2x}$	Double of primary (0 N·s/m) and secondary longitudinal damping (5.0×10^5 N·s/m)
$c_{1y}\, c_{2y}$	Double of primary (0 N·s/m) and secondary lateral damping (initial: 5.2×10^4 N·s/m; determined by the proposed EHEMD)
$c_{1z}\, c_{2z}$	Double of primary (3.0×10^4 N·s/m) and secondary vertical damping (1.6×10^5 N·s/m)
$h_1\, h_2$	Vertical distance from car body center of gravity to secondary spring (0.763 m) and damper (0.78 m)
$h_3\, h_4\, h_5$	Vertical distance from bogie frame center of gravity to secondary spring (0.0245 m), primary suspension (−2085 m) and secondary lateral damper (0.2175 m)
$l\, l_1$	Half of bogie center pin spacing (9 m) and wheelbase (1.25 m)
$b\, b_1\, b_2\, b_3$	Half of wheelset contact distance (0.7465 m), primary suspension spacing (lateral, 1 m), secondary spring spacing (lateral, 1 m), and secondary vertical damper spacing (lateral, 1 m)
r_0	Wheel rolling radius (0.4575 m)
V	Vehicle speed (100–340 km/h)
$f_{11} f_{22}$	Longitudinal creep (1.12×10^7) and lateral coefficient (9.98×10^6)
λ_e	Effective wheel conicity (0.05)
σ	Wheelset roll coefficient (0.05)
$\Gamma_c\, \Gamma_r\, \Gamma_s$	Truncated wavenumber (0.438, 0.8246, 0.0206 rad/m)
$A_a\, A_v$	Scalar factor of lateral alignment (10.8×10^{-7} rad m) and cross-level (6.125×10^{-7} rad m)
$k_{gy}\, k_{g\varphi}$	Lateral and yaw gravitational stiffness

CHAPTER 6

ANALYSIS OF STRUCTURES WITH DUAL-FUNCTION DAMPERS

6.1 Introduction

A rational design of a dual-function damper should address optimization regarding the dual objectives—vibration control and energy harvesting performance. Shen et al. (2019) analytically and numerically validated the consistency of the dual objectives in the optimization of EHEMD(s) installed in randomly excited SDOF and MDOF structures. However, when an EHEMD is integrated into a TMD or TID to form an EHTMD or EHTID, the dual-objective optimization problem becomes more complicated because of the additional parameters to be determined. This chapter first reviews the dual-objective optimization consistency in the SDOF structure–EHEMD coupled system. Then, a damped randomly excited SDOF structure in which an EHTMD or EHTID has been installed is analyzed, aiming to answer the fundamental and unaddressed question of whether the optimizations of vibration control and energy harvesting are consistent or contradictory in these two relatively complicated scenarios.

An EHTMD is a TMD with dual functions (vibration control and energy harvesting), whereby the EMD is the damping element in the TMD. A large mass ratio of TMD enhances the vibration control effect. Some researchers thus believe that a large mass ratio of EHTMD may reduce the harvested power because of the significantly suppressed vibrations of the primary structures. In this chapter, the closed-form solutions for the optimal parameters of an EHTMD installed in an SDOF structure are given with

consideration of structural damping. The solutions indicate that the dual objectives to maximize the harvested power of the EHTMD and minimize structural kinetic energy are essentially consistent in this optimization problem. In addition, the general expression of the power efficiency in the EHTMD is presented, and the optimal power efficiency is derived. The influence of the mass ratio of EHTMD and the inherent damping ratio of the primary structure on the power efficiency is investigated mathematically. An SDOF numerical example was analyzed to validate the efficacy and accuracy of the analytical study.

Similar to EHTMD, an EHTID is a dual-function inerter-based device with an energy harvesting function. Since the concept of an inerter was proposed, different inerter-based networks have been developed for vibration control, and some designs have been integrated with an energy harvesting function. This chapter presents the analytical input excitation power (total damping power) of an SDOF structure installed with an EHTID considering 10 different inerter-based networks. Numerical case studies were conducted to validate the analytical expression of the input excitation power, and a corresponding conditional power distribution analysis was conducted to briefly analyze which network is suitable for applications in a dual-function damper.

The following three assumptions (simplifications) were adopted in the analyses:

(1) The random force was assumed to be ideal white noise or band-limited white noise.

(2) The structures installed with dual-function dampers (including EHEMD, EHTID, and EHTID) were assumed to be linearly elastic.

(3) The EMD part of the dual-function dampers only provided a damping characteristic.

6.2 EHEMD

The derivation in this section is similar to that in Shen et al. (2019), who adopted the

objective function for vibration control that minimized the H_2 norm of the structural displacement or acceleration. However, the control objective in this section is to minimize the structural kinetic energy.

6.2.1 System Modeling

Figure 6.1 shows a typical coupled system with a damped SDOF structure and an EHEMD. In the figure, m, k, and c denote the mass, stiffness, and damping coefficients, respectively. The subscripts 0 and 1 denote the SDOF structure and EHEMD system, respectively. The specific components of an EHEMD can be found in Chapter 3. In this configuration, the EHEMD damping power, which is essentially the total generated power P_{in} (power transferred into the EM energy harvester, see Figure 3.6 in Chapter 3), is regarded as the potentially harvestable power, namely the gross EHEMD output power. The influence of the EMD parameters on the power efficiency is discussed later.

The governing equation for the structural configuration (Figure 6.1) subjected to an external force is as follows:

$$m_0\ddot{x}_0 + (c_0 + c_1)\dot{x}_0 + k_0 x_0 = F \tag{6.1}$$

where x_0 is the absolute displacement response, and the overdot denotes the differential with respect to time. The corresponding dimensionless velocity transfer function of the SDOF structure $H_{0\text{-}1}$ is given as follows:

$$H_{0\text{-}1} = \left(\frac{1}{m_0\omega_0}\right)\frac{sj}{(sj)^2 + 2(\xi_0 + \xi_1)sj + 1} \tag{6.2}$$

where $j = (-1)^{1/2}$; $s = \omega/\omega_0$; $\omega_0 = (k_0/m_0)^{1/2}$ is the natural frequency of the SDOF structure; ω is the excitation frequency; and $\xi_0 = c_0/2m_0\omega_0$ and $\xi_1 = c_1/2m_0\omega_0$ are the damping ratios contributed by structural inherent damping and EHEMD damping, respectively.

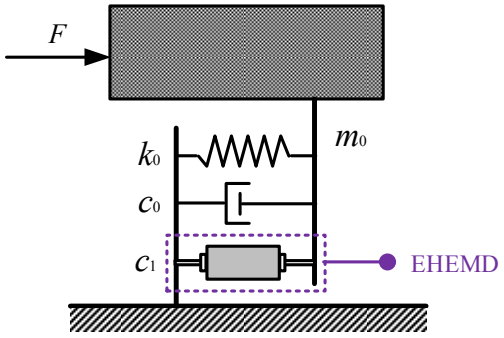

Figure 6.1 A damped SDOF structure–EHEMD coupled system

6.2.2 Performance Assessment

When the structure is subjected to white-noise force excitation, the gross output power P_d of the EHEMD and the kinetic energy P_k of the SDOF structure can be expressed as follows:

$$P_d = 2S_0\omega_0^2 m_0 \xi_1 \int_{-\infty}^{+\infty} |H_{0\text{-}1}|^2 \, ds \tag{6.3}$$

$$P_k = \frac{1}{2} S_0 m_0 \omega_0 \int_{-\infty}^{+\infty} |H_{0\text{-}1}|^2 \, ds \tag{6.4}$$

where S_0 is the constant PSD of the random force excitation (unit: $N^2 \cdot s/rad$). The kinetic energy P_k is essentially proportional to the square of the H_2 norm of the structural velocity (i.e., the steady-state variance of structural velocity under white noise excitation). Equations (6.3) and (6.4) represent two key performance indices of the EHEMD for energy harvesting and vibration control, respectively.

With the integral computation given in Appendix 6.7, the total excitation power P_{ex} can be calculated as follows (Shen, 2014; Clough and Penzien, 2003):

$$P_{ex} = P_d + P_s = \frac{\pi S_0}{m_0} \tag{6.5}$$

where P_{ex} is the excitation power and is equal to the total damping power of the entire system, that is, the sum of the EHEMD damping power P_d (i.e., EHEMD output power) and structural damping power P_s. In a stationary response, the change rate of structural vibration energy is approximately zero. Equation (6.5) is an approximate estimation if the excitation is a band-limited white noise excitation covering the fundamental frequency of

the SDOF structure. Equation (6.5) indicates that the total damping power is a constant that depends only on the mass of the SDOF structure and the PSD of the random excitation. The inherent damping power P_s of the SDOF structure is given as follows:

$$P_s = 2S_0\omega_0^2 m_0 \xi_0 \int_{-\infty}^{+\infty} |H_{0\text{-}1}|^2 \, ds = 4\xi_0 \omega_0 P_k \tag{6.6}$$

Such a relationship determines the gross power efficiency, defined as the ratio of the output power to the total excitation power:

$$\eta_{em} = \frac{c_1}{c_0 + c_1} = \frac{\xi_1}{\xi_0 + \xi_1} \tag{6.7}$$

Equation (6.7) reveals that a larger EHEMD damping coefficient c_1 results in higher power efficiency. From this perspective, the objectives of vibration control and energy harvesting are consistent with each other, whereby a larger EHEMD damping coefficient c_1 results in a higher EHEMD output power and a lower structural kinetic energy (proportional to the structural inherent damping power). Note that this optimization-consistency conclusion regarding the EHEMD was also pointed out by Shen (2014), who set the reduction of the FRF magnitude attributed to the EHEMD as the measure of the vibration control performance.

6.2.3 Numerical Validation

A numerical case study was conducted to validate the conclusion. The structural parameters were as follows: $m_0 = 3$ kg and $\omega_0 = 18.25$ rad/s. All subsequent power/energy results in this subsection are normalized by the input excitation power $\pi S_0/m_0$. Thus, the EHEMD output power herein is equivalent to the power efficiency η_{em}. The conversion efficiency η inside the EMD is regarded as 1.

Figure 6.2 shows the SDOF structural vibration responses, including displacement, velocity, and acceleration, with the variation of the EHEMD damping ratio, wherein the structural inherent damping ratio was set as 0.03. The result suggests that the vibration response could be effectively reduced by increasing the damping ratio, which has also

been pointed out by Shen (2014).

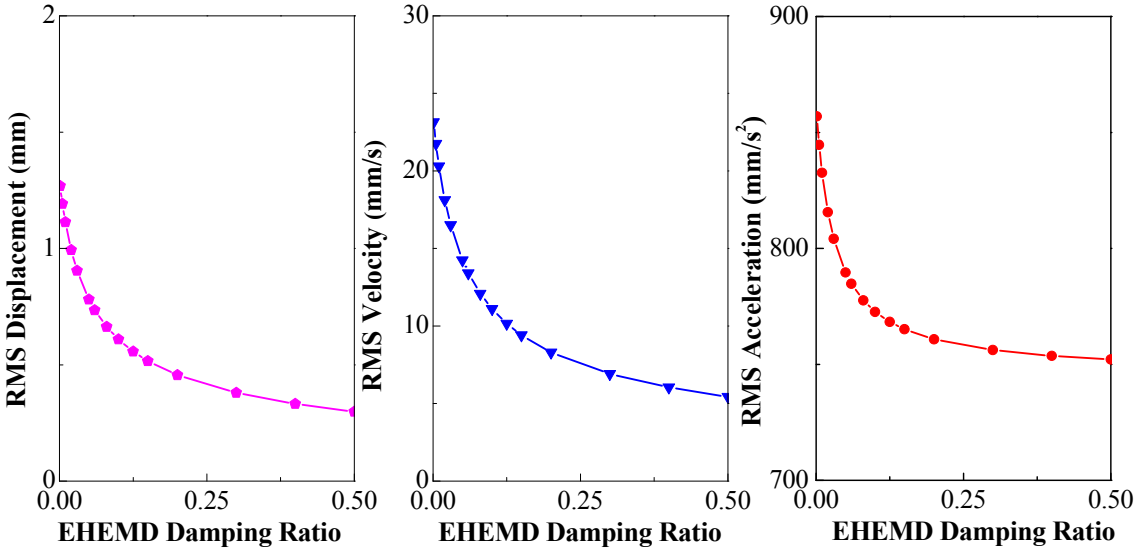

(a) Displacement (b) Velocity (c) Acceleration

Figure 6.2 Vibration response of an SDOF structure installed with an EHEMD ($\xi_0 = 0.03$)

Figure 6.3(a) shows the power items in the power flow of the damped SDOF structure–EHEMD coupled system when subjected to a random excitation force. As the EHEMD damping ratio increased, the input excitation power (total damping power) was relatively stable, as predicted by Equation (6.5), whereas the EHEMD output power increased. Accordingly, the structural inherent damping power and kinetic energy decayed with increasing EHEMD damping ratio. This result implies that a large EHEMD damping ratio benefits both the EHEMD output power enhancement and structural kinetic energy reduction, which to some extent demonstrates the consistency between the objectives of vibration control and energy harvesting.

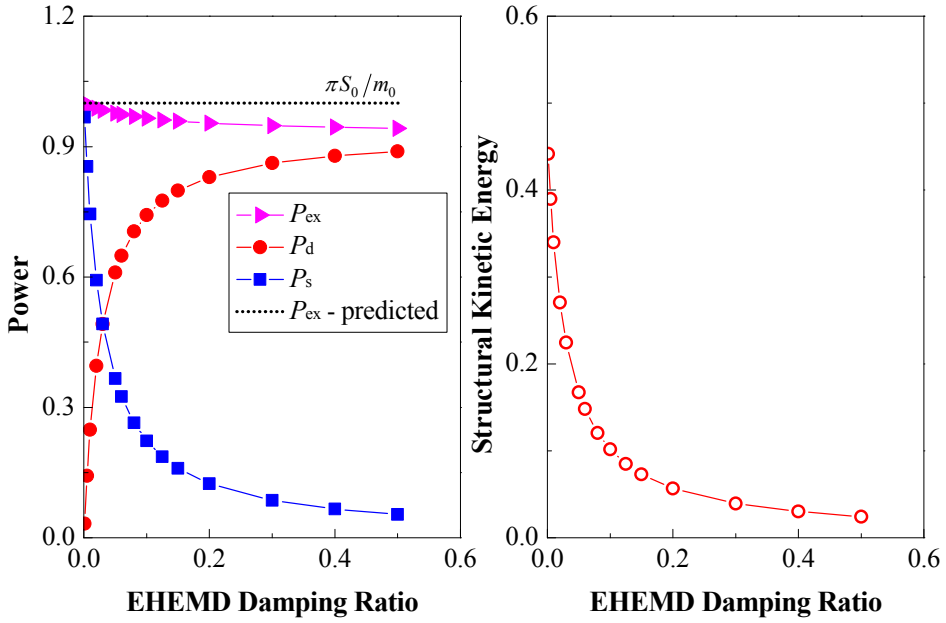

(a) Power items (b) Structural kinetic energy

Figure 6.3 Variation of power and energy items with the EHEMD damping ratio ($\xi_0 = 0.03$)

6.2.4 Discussions

(1) In a randomly excited damped SDOF structure–EHEMD coupled system, the energy harvesting and vibration control in the EHEMD are generally consistent if the vibration control objective is to minimize the vibration responses (including displacement, velocity, and acceleration) of the SDOF structure or the structural kinetic energy.

(2) If the control objective is to minimize the H_2 norm of the structural relative velocity in consideration of the structural inherent damping, the consistency conclusion can be directly applied in the case of ground motion, wherein the total input excitation power is $\pi m_0 S_0$.

(3) In a trivial case wherein the structural inherent damping ratio is ignored ($\xi_0 = 0$), the EHEMD output power is equal to the excitation power, which is independent of the EHEMD damping ratio, but a larger EHEMD damping ratio benefits the vibration control performance.

6.3 EHTMD

The SDOF structure–EHTMD coupled system has not been analytically investigated in previous studies. This section investigates this coupled system for the first time and presents the closed-form solutions for the optimal parameters to realize consistency, as well as the analytical effects of the mass ratio and structural inherent damping on the dual objectives.

6.3.1 System Modeling

Figure 6.4 shows the simplified model of a damped SDOF structure installed with an EHTMD. In this section, the subscript 2 represents the TMD. To realize the energy harvesting function, an EMD is employed to provide the damping required in the TMD, and an EHTMD that converts the damping power to electricity is formed. Similar to the analysis of the EHEMD, the EHTMD damping power is defined as the gross EHTMD output power, representing the potentially harvestable power.

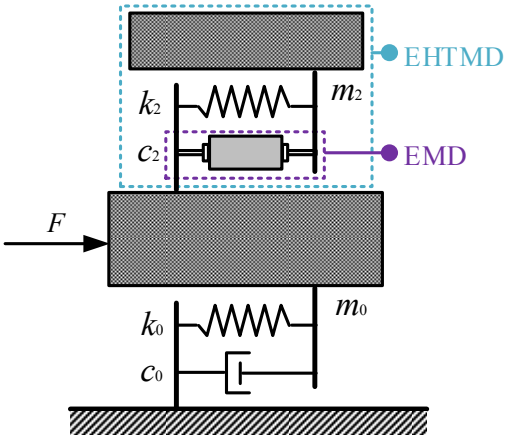

Figure 6.4 Typical configuration of a damped SDOF structure with EHTMD

6.3.2 Closed-form Solution under Forced Vibration

When the primary structure is subjected to force excitation, the governing equation of the damped SDOF structure and TMD system is as follows:

$$\begin{bmatrix} m_0 & 0 \\ 0 & m_2 \end{bmatrix}\begin{bmatrix} \ddot{x}_0 \\ \ddot{x}_2 \end{bmatrix}+\begin{bmatrix} c_0+c_2 & -c_2 \\ -c_2 & c_2 \end{bmatrix}\begin{bmatrix} \dot{x}_0 \\ \dot{x}_2 \end{bmatrix}+\begin{bmatrix} k_0+k_2 & -k_2 \\ -k_2 & k_2 \end{bmatrix}\begin{bmatrix} x_0 \\ x_2 \end{bmatrix}=\begin{bmatrix} F \\ 0 \end{bmatrix} \tag{6.8}$$

where x_0 and x_2 are the absolute displacement responses. Because the EMD only provides the equivalent damping effect (i.e., c_2), Equation (6.8) is always adoptable and independent of the strength of the coupling effect in the EHTMD. Accordingly, the dimensionless transfer functions of the relative velocity between the TMD and the structure $H_{0\text{-}2}$, and the velocity of the SDOF structure H_0 are respectively given as follows:

$$H_{0\text{-}2} = \left(\frac{1}{m_0\omega_0}\right)\frac{B_0 + B_1(sj) + B_2(sj)^2 + B_3(sj)^3}{A_0 + A_1(sj) + A_2(sj)^2 + A_3(sj)^3 + A_4(sj)^4} \tag{6.9a}$$

$$H_0 = \left(\frac{1}{m_0\omega_0}\right)\frac{C_0 + C_1(sj) + C_2(sj)^2 + C_3(sj)^3}{A_0 + A_1(sj) + A_2(sj)^2 + A_3(sj)^3 + A_4(sj)^4} \tag{6.9b}$$

where

$$A_0 = \gamma^2 \qquad B_0 = 0 \qquad C_0 = 0$$

$$A_1 = 2\xi_0\gamma^2 + 2\xi_2\gamma \qquad B_1 = 0 \qquad C_1 = \gamma^2$$

$$A_2 = \gamma^2 + 1 + \mu\gamma^2 + 4\xi_0\xi_2\gamma \qquad B_2 = 0 \qquad C_2 = 2\xi_2\gamma$$

$$A_3 = 2\xi_2\mu\gamma + 2\xi_2\gamma + 2\xi_0 \qquad B_3 = 1 \qquad C_3 = 1$$

$$A_4 = 1$$

where $\gamma = \omega_2/\omega_0$ is the frequency tuning ratio between the TMD and structure; $\mu = m_2/m_0$ is the mass ratio; and $\xi_0 = c_0/2m_0\omega_0$ and $\xi_2 = c_2/2m_2\omega_2$ are the damping ratios of the structure and TMD, respectively. Similar to the EHEMD, the EHTMD output power P_d and the SDOF structural kinetic energy P_k are regarded as performance indices for energy harvesting and vibration control, respectively:

$$P_d = 2S_0\omega_0^2 m_0\xi_2\gamma\mu\int_{-\infty}^{+\infty}|H_{0\text{-}2}|^2\,ds \tag{6.10}$$

$$P_k = \frac{1}{2}S_0 m_0\omega_0\int_{-\infty}^{+\infty}|H_0|^2\,ds \tag{6.11}$$

Adopting the derivatives of Equations (6.10) and (6.11) with respect to the damping ratio ξ_2 and frequency tuning ratio γ can provide the optimal conditions, which are identical for these two performance indices, demonstrating the consistency between energy harvesting and vibration control in the EHTMD. Although a similar conclusion regarding traditional

TMDs was reported by Zilletti et al. (2012), only approximate solutions were provided in their study. Following their observation, the present study provides the exact closed-form solutions for the two optimal conditions as follows:

$$\xi_{2,\text{opt}} = \frac{\sqrt{2}\mu^2(1+\mu)}{4\xi_0\left\{\left[\frac{\mu}{\xi_0}\left(\lambda-\frac{1}{2}(1+\mu)\right)\sqrt{\mu\lambda}-\mu^2\lambda\right]\left(\frac{\mu}{\xi_0}\sqrt{\mu\lambda}-\mu^2\right)\right\}^{1/2}} \tag{6.12a}$$

$$\gamma_{\text{opt}} = \left\{\frac{\mu^2-\frac{\mu}{\xi_0}\sqrt{\mu\lambda}}{2\left[\frac{\mu}{\xi_0}\left(\frac{1}{2}(1+\mu)-\lambda\right)\sqrt{\mu\lambda}+\mu^2\lambda\right]}\right\}^{1/2} \tag{6.12b}$$

where $\lambda = 1 + \mu - \xi_0^2$ is a dimensionless parameter. Equation (6.12b) provides a real frequency ratio when $\xi_0 < ((1 + \mu - (\mu^2+\mu)^{1/2})/2)^{1/2}$.

The total input excitation power can be calculated as follows (Clough and Penzien, 2003):

$$P_{\text{ex}} = P_{\text{d}} + P_{\text{s}} = \frac{\pi S_0}{m_0} \tag{6.13}$$

The expression is identical to Equation (6.5), representing the total excitation power in the case of an SDOF structure subjected to white noise excitation. Note that the expression of the structural inherent damper power is the same as Equation (6.6). Accordingly, the gross power efficiency is as follows:

$$\eta_{\text{em}} = \frac{P_{\text{d}}}{P_{\text{ex}}} = \frac{\xi_2\gamma\mu\left(4\xi_0\xi_2^2\gamma+4\xi_0^2\xi_2\gamma^2+\xi_0\gamma^3+\xi_2+\xi_0\gamma^3\mu\right)}{(\xi_2+\xi_0\gamma)(\xi_2\gamma+\xi_0+\xi_2\gamma\mu)\left(4\xi_0\xi_2\gamma+1+\gamma^2+\gamma^2\mu\right)-\gamma(\xi_2+\xi_0\gamma)^2-\gamma(\xi_2\gamma+\xi_0+\xi_2\gamma\mu)^2} \tag{6.14}$$

Notably, Equation (6.14) is a general form of the TMD power efficiency, and it is suitable for different design parameters of the TMD (either optimal or non-optimal design). Substituting the optimal conditions in Equation (6.12) into Equation (6.14) gives the optimal power efficiency as:

$$\eta_{\text{opt}} = \frac{P_{\text{d}}}{P_{\text{ex}}} = \frac{4\xi_0\left(\xi_0^2 - \lambda\right)\sqrt{\mu^3\lambda} + \mu^4 + 2\mu^3\left(1-2\xi_0^2\right) + \mu^2\left(1+4\xi_0^4\right) + 4\mu\xi_0^2\left(1-\xi_0^2\right)}{\left[\mu^2 + \mu\left(1-4\xi_0^2\right) + 4\xi_0^4 - 4\xi_0^2\right]^2} \tag{6.15}$$

Given a slightly damped primary structure (i.e., ξ_0 is very small), the high-order terms of ξ_0 are negligible, and Equation (6.15) can be approximately simplified as:

$$\eta_{\text{opt}} \approx 1 - \frac{4\xi_0}{\sqrt{\mu(1+\mu)}} \tag{6.16}$$

An empirical threshold of $\xi_0 < 0.1(\mu^2+\mu)^{1/2}$ is suggested because Equation (6.16) is only suitable for low structural damping. It is evident that a larger mass ratio μ of the EHTMD enhances the energy harvesting performance, whereas a larger inherent damping ratio ξ_0 of the structure has a negative impact on power efficiency. Meanwhile, it is well known that a larger mass ratio of TMD offers a better control effect, regardless of which control criterion is applied. A review of the optimized vibration response can be found in the study (Warburton, 1982). Therefore, it can be concluded that a larger mass ratio of EHTMD benefits energy harvesting and vibration control performance simultaneously. Such a conclusion has never been reported in the literature.

From the vibration control perspective, this power efficiency reveals the control performance of TMD under a given criterion to some extent. In the optimal cases, the structural damping power and kinetic energy are minimized, and they can be approximately expressed under low structural damping as follows:

$$P_{\text{s, opt}} \approx \frac{4S_0\xi_0\pi}{m_0\sqrt{\mu(1+\mu)}} \tag{6.17a}$$

$$P_{\text{k, opt}} \approx \frac{S_0\pi}{m_0\omega_0\sqrt{\mu(1+\mu)}} \tag{6.17b}$$

A part of the excitation power is dissipated by the primary structure due to the existence of ξ_0. However, a relatively large mass ratio of TMD can effectively reduce the structural damping power or kinetic energy, revealing the benefit from the vibration control perspective. This result may also shed light on the optimization of power

distribution in TMD-controlled structures.

6.3.3 Numerical Validation

The same numerical model and normalization strategy in Subsection 6.2.3 are adopted. Figure 6.5 illustrates the performance indices of the EHTMD under a fixed structural damping ratio $\xi_0 = 0.03$ and fixed mass ratio of EHTMD $\mu = 0.03$. The overall trends of the EHTMD output power and structural kinetic energy were nearly opposite to the variations of the damping and frequency tuning ratios. The optimal points for the maximization of the EHTMD output power and minimization of the structural kinetic energy were identical, with the parameters $\xi_2 = 0.0874$ and $\gamma = 0.9887$, which agree with the theoretical prediction by Equation (6.12). The corresponding EHTMD output power and structural kinetic energy after normalization were $P_d = 0.558$ and $P_k = 0.20$, respectively, which are consistent with Equation (6.15).

Numerous optimization criteria have been proposed for TMDs. Therefore, TMDs or EHTMDs may be designed using different criteria other than the optimal conditions proposed in this study. The optimal condition presented in Equation (6.12) is equivalent to the H_2 minimization of structural velocity. Three other control criteria that disregard structural inherent damping, as listed in Table 6.1, were also considered in this section for comparison.

Figure 6.6 shows the variations of the EHTMD output power and structural kinetic energy with increasing structural inherent damping, wherein the mass ratio of TMD was fixed at $\mu = 0.03$. The following can be observed: (1) The optimal condition (i.e., Equation (6.12)) offered a superior vibration control and energy harvesting performance over the other design criteria (see Table 6.1) that ignored structural inherent damping in the optimization. This finding demonstrates the accuracy and effectiveness of the closed-form derivation in this chapter. (2) The existence of structural inherent damping degraded the EHTMD output power but improved the vibration control effect. (3) At a low level of

structural inherent damping, however, the different TMD design criteria led to similar vibration control and energy harvesting performance.

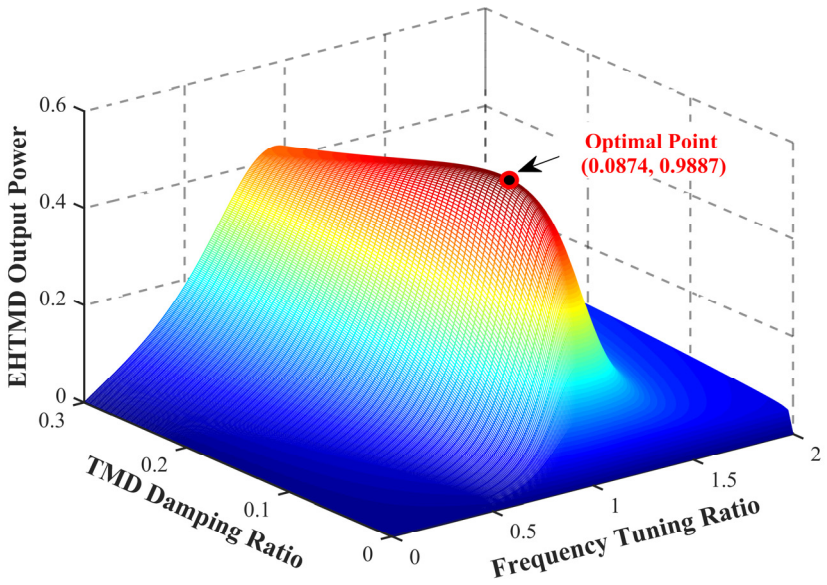

(a) EHTMD output power

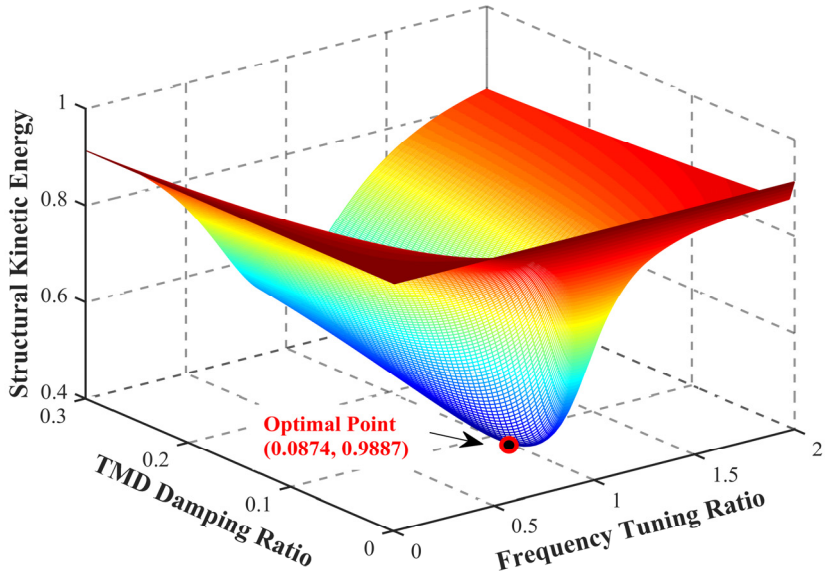

(b) Structural kinetic energy

Figure 6.5 Variation in the performance indices with the damping ratio (ξ_2) and frequency tuning ratio (γ) of EHTMD ($\mu = \xi_0 = 0.03$), and the optimal conditions predicted by Equation (6.12)

Table 6.1 Optimization criteria of TMDs with and without consideration of zero inherent damping

Optimization Criterion	Optimal Parameters
H_2 for velocity - Minimize structural kinetic energy - Consider structural inherent damping	See Equation (6.12)
H_2 for velocity (Warburton, 1982) - Minimize structural kinetic energy - Ignore structural inherent damping	$\xi_2 = \left\{\frac{\mu}{4}\right\}^{1/2}$, $\gamma = \left\{\frac{1}{1+\mu}\right\}^{1/2}$
H_2 for displacement (Warburton, 1982) - Minimize RMS displacement - Ignore structural inherent damping	$\xi_2 = \left\{\frac{\mu(4+3\mu)}{8(1+\mu)(2+\mu)}\right\}^{1/2}$, $\gamma = \frac{1}{1+\mu}\left\{\frac{2+\mu}{\mu}\right\}^{1/2}$
H_∞ for displacement (Ormondroyd and Den Hartog, 1982) - Minimize the maximum displacement - Ignore structural inherent damping	$\xi_2 = \left\{\frac{3\mu}{8(1+\mu)}\right\}^{1/2}$, $\gamma = \frac{1}{1+\mu}$

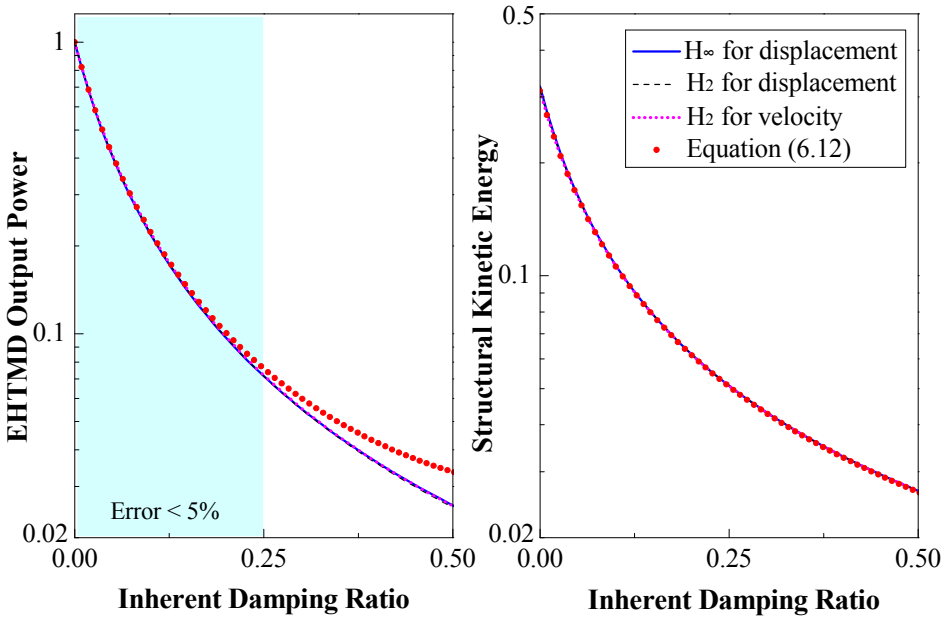

(a) EHTMD output power (b) Structural kinetic energy

Figure 6.6 Comparison of the performance of different TMD design criteria considering structural inherent damping (μ = 0.03)

Figure 6.7 compares the performance under different TMD mass ratios. The following can be observed: (1) A larger mass ratio simultaneously benefited the energy harvesting efficiency and vibration control effects, regardless of which TMD design criterion was applied. (2) With an increment in the mass ratio, the superiority of the proposed optimal conditions in terms of the EHTMD output power and structural kinetic energy became increasingly evident compared with other TMD design criteria.

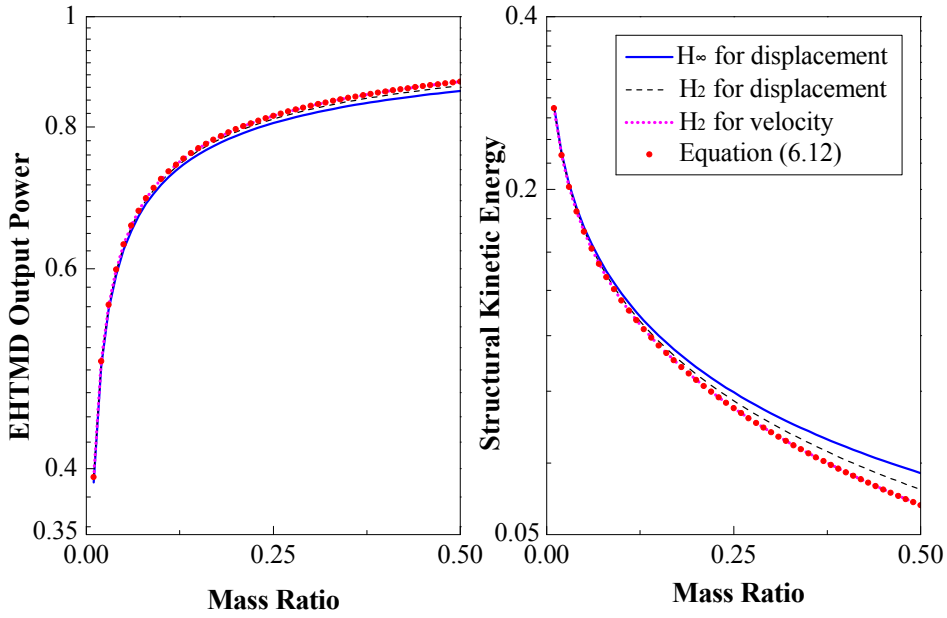

(a) EHTMD output power (b) Structural kinetic energy

Figure 6.7 Comparison of the performance of different TMD design criteria considering various mass ratios of TMD ($\xi_0 = 0.03$)

Figure 6.8 demonstrates the effect of the detuned TMD parameters on the harvesting performance. The optimal parameters were determined according to Equation (6.12). The EHTMD output power was insensitive to the slight detuning of the damping and frequency ratios. However, when the damping ratio significantly deviated from the optimal value ($\xi_2 = 2\xi_{2,opt}$), the performance degradation became increasingly apparent.

The EHTMD can be implemented for potential application scenarios, such as civil structures and vehicle suspensions, as traditional TMDs. The actual mass ratio might be smaller than the designed value due to the influence of the passengers or cargos. This

potential mass ratio change would also degrade the vibration control and energy harvesting performance. For a special case study where setting the initial optimal parameters for μ = 0.03, the actual mass ratio was 0.027 (10% change), the structural kinetic energy and EHTMD output power decreased by18% and 5%, respectively.

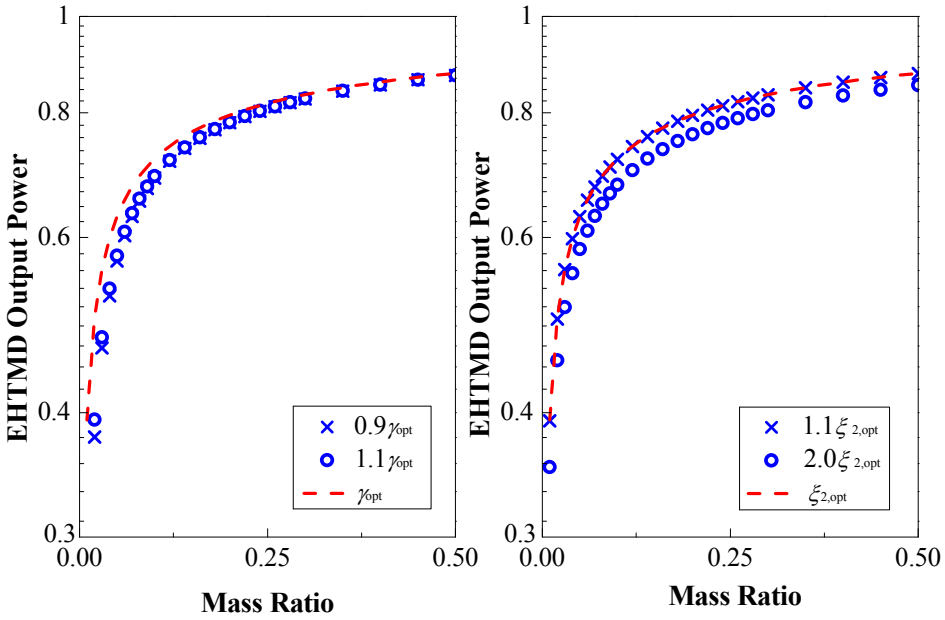

(a) Frequency tuning ratio (b) EHTMD damping ratio

Figure 6.8 Sensitivity of energy harvesting performance to detuned parameters

Figure 6.9 compares the power efficiency computed using the approximate and exact expressions. The power efficiency was also evaluated numerically through a dynamic simulation of the entire system under broadband random excitation (0–500 Hz). The corresponding results computed directly from the input and output powers are also depicted in Figure 6.9. The numerical results showed excellent agreement with the exact mathematical expression (i.e., Equation (6.15)). Meanwhile, the approximation (i.e., Equation (6.16)) offered a satisfactory evaluation of power efficiency only at a low level of structural inherent damping. The relative error was approximately 14% at the proposed empirical threshold (i.e., $0.1(\mu^2+\mu)^{1/2} \approx 1.8\%$). Such an approximation is inapplicable to a relatively large structural inherent damping.

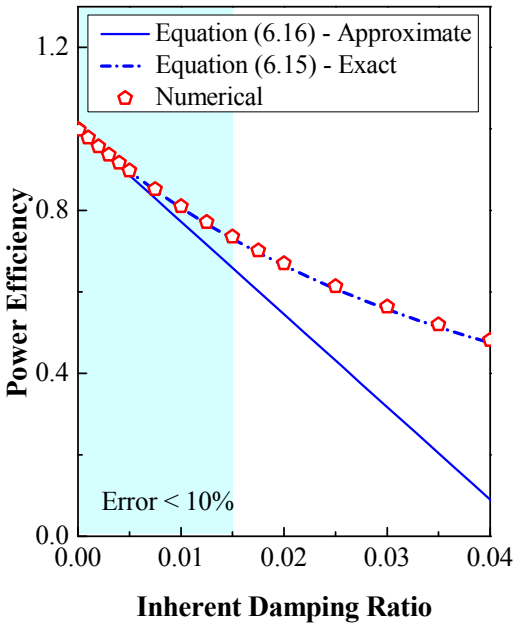

Figure 6.9 Comparison of power efficiency using approximate and exact expressions ($\mu = 0.03$)

6.3.4 Discussions

(1) When an EHTMD is optimized to minimize the H_2 norm of structural velocity considering structural inherent damping, the performance objectives of vibration control and energy harvesting are identical and can be simultaneously optimized.

(2) When an EHTMD is designed using other TMD optimization criteria for vibration control, the energy harvesting performance of the EHTMD becomes suboptimal. However, if the structural inherent damping and TMD mass ratio are small, then the deviation from the optimal performance will be limited, and the two performance objectives of the EHTMD will still be approximately consistent.

(3) Ignoring the structural inherent damping in the TMD optimization results in slightly suboptimal parameters of the EHTMD. It may also erroneously indicate that all of the excitation power is absorbed by the EHTMD and the primary structure does not dissipate any power. The closed-form solution that considers structural inherent damping not only provides accurate optimal conditions but also enables analyses of the power distribution between the structure and EHTMD and the corresponding power efficiency.

(4) Although the presented derivation in this section is based on force excitation, it may also provide some insight into a structure subjected to random ground motions,

wherein the total excitation power is proportional to the sum of the structural and EHTMD masses. A larger EHTMD mass enhances the total excitation power transferred into the system and benefits the power harvesting. Given that the total excitation power is the sum of the EHTMD output power and structural inherent damping power, the maximization of the former leads to the minimization of the latter. This observation implies that the maximum output power of EHTMD is consistent with the minimum H_2 norm of the relative velocity between the controlled structure and the ground. However, the optimal conditions for a seismically excited structure will be different from those derived in this chapter and need to be numerically searched, as a closed-form solution may not exist.

(5) The expressions of the power conversion efficiency and power distribution in Equations (6.15) and (6.16) are not only of interest to the novel EHTMDs but also shed light on the optimization of classical TMDs with respect to power distribution.

6.4 EHTID

6.4.1 System Modeling

Figure 6.10 shows the configuration of an SDOF structure with a two-terminal inerter-based damper, in which the damping part is provided by the EMD to provide energy harvesting capacity. Under force excitation, the corresponding dimensionless transfer function of the relative velocity between the two terminals of the damper is given as follows:

$$H_{0\text{-}3} = \left(\frac{1}{m_0\omega_0}\right)\frac{sj}{(sj)^2 + \left(2\xi_0 + Z_b / m_0\omega_0^2\right)(sj) + +1} \tag{6.18}$$

where Z_b is the impedance of the damper network, also known as the transfer function of the damping force with respect to the velocity. In this section, 10 different inerter-based networks are considered, as shown in Figure 6.11. Network II series include two two-component networks, and the corresponding impedance is shown in Equation (6.19), whereas Network III series refer to three-component topologies that correspond to the impedance in Equation (6.20). Strictly speaking, the Network II series is called ID,

whereas the Network III series is called TID.

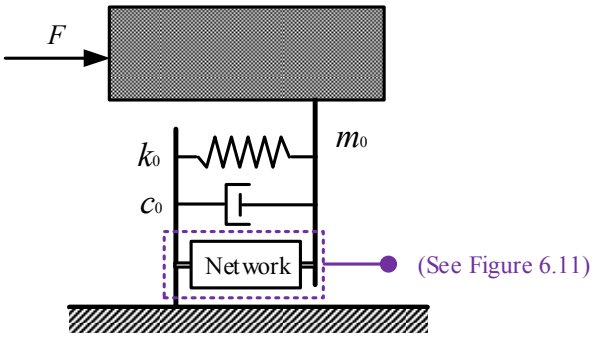

Figure 6.10 A damped SDOF structure with a two-terminal damper

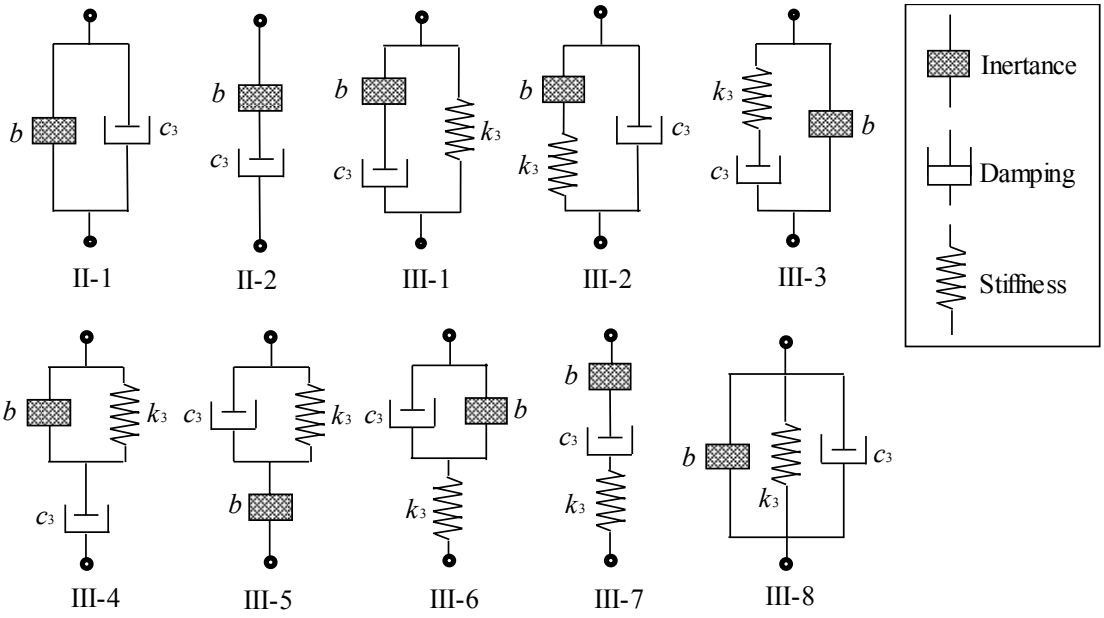

Figure 6.11 Inerter-based networks

$$Z_{\text{I1-1}} = b\kappa + c_3 \tag{6.19a}$$

$$Z_{\text{I1-2}} = \frac{bc_3\kappa}{b\kappa + c_3} \tag{6.19b}$$

where $\kappa = \omega j$; c_3, k_3, and b are the damping, stiffness, and inertance coefficients, respectively, in the inerter-based dampers, if any.

$$Z_{\text{III-1}} = \frac{bc_3\kappa^2 + bk_3\kappa + c_3k_3}{b_3\kappa^2 + c_3\kappa} \tag{6.20a}$$

$$Z_{\text{III-2}} = \frac{bc_3\kappa^2 + bk_3\kappa + c_3k_3}{b\kappa^2 + k_3} \tag{6.20b}$$

$$Z_{\text{III-3}} = \frac{bc_3\kappa^2 + bk_3\kappa + c_3k_3}{c_3\kappa + k_3} \tag{6.20c}$$

$$Z_{\text{III-4}} = \frac{bc_3\kappa^2 + c_3k_3}{b\kappa^2 + c_3\kappa + k_3} \tag{6.20d}$$

$$Z_{\text{III-5}} = \frac{bc_3\kappa^2 + bk_3\kappa}{b\kappa^2 + c_3\kappa + k_3} \tag{6.20e}$$

$$Z_{\text{III-6}} = \frac{bk_3\kappa + c_3k_3}{b\kappa^2 + c_3\kappa + k_3} \tag{6.20f}$$

$$Z_{\text{III-7}} = \frac{bc_3k_3\kappa}{bc_3\kappa^2 + bk_3\kappa + c_3k_3} \tag{6.20g}$$

$$Z_{\text{III-8}} = b\kappa + c_3 + \frac{k_3}{\kappa} \tag{6.20h}$$

By substituting Equations (6.19) or (6.20) into Equation (6.18), the velocity transfer function can be obtained accordingly.

6.4.2 Excitation Power Analysis

Similar to the analysis of the EHEMD and EHTMD, the total excitation power under white-noise excitation can be calculated as Equation (6.5). The structural inherent damping power in this scene is given as:

$$P_{\text{s}} = S_0 c_0 \omega_0 \int_{-\infty}^{+\infty} \left| H_{0\text{-}3} \right|^2 ds \tag{6.21}$$

and the damping power of the inerter-based damper is given as:

$$P_{\text{d}} = S_0 c_3 \omega_0 \int_{-\infty}^{+\infty} \left| \rho H_{0\text{-}3} \right|^2 ds \tag{6.22}$$

where $H_{0\text{-}3}$ is the relative velocity between two terminals of the inerter network; $\rho H_{0\text{-}3}$ is the relative velocity experienced by the damping element c_3; and ρ, given in Equations (6.23) and (6.24), represents the velocity transfer efficiency to some extent.

$$\rho_{\text{II-1}} = 1 \tag{6.23a}$$

$$\rho_{\text{II-2}} = \frac{b\kappa}{b\kappa + c} \tag{6.23b}$$

$$\rho_{\text{III-1}} = \frac{b\kappa}{b\kappa + c_3} \tag{6.24a}$$

$$\rho_{\text{III-2}} = 1 \tag{6.24b}$$

$$\rho_{\text{III-3}} = \frac{k_3}{c_3\kappa + k_3} \tag{6.24c}$$

$$\rho_{\text{III-4}} = \frac{b\kappa^2 + k_3}{b\kappa^2 + c_3\kappa + k_3} \tag{6.24d}$$

$$\rho_{\text{III-5}} = \frac{b\kappa^2}{b\kappa^2 + c_3\kappa + k_3} \tag{6.24e}$$

$$\rho_{\text{III-6}} = \frac{k_3}{b\kappa^2 + c_3\kappa + k_3} \tag{6.24f}$$

$$\rho_{\text{III-7}} = \frac{bk_3\kappa}{bc_3\kappa^2 + bk_3\kappa + c_3k_3} \tag{6.24g}$$

$$\rho_{\text{III-8}} = 1 \tag{6.24h}$$

With the integral computation, the total excitation power for most networks could be analytically obtained, as presented in Table 6.2, wherein "Null" indicates that no analytical solution was obtained, and the result in the adjacent bracket represents a numerical estimation obtained in the next subsection. For comparison, the results for an EHTMD and a single EHEMD are also summarized in the table. Table 6.2 demonstrates that introducing an inerter into the damper does not further increase the input excitation power; in particular, a grounded inerter results in reduced excitation power into the system. From this perspective, these inerter-based strategies do not benefit energy harvesting. However, it needs to mention that whether the inerter benefits the potential EHTID output power highly depends on the effect of the inertance on the power distribution of the total excitation power, which is numerically analyzed in the next subsection.

For a given inertance, the input excitation power will be nearly constant. In this regard, the minimization of the structural damping power (related to the structural kinetic energy) corresponds to the maximization of the potential EHTID output power. Vibration control and energy harvesting are consistent with each other, similar to the EHTMD analysis in Section 6.3.

Table 6.2 Input excitation power of an SDOF structure with different inerter-based networks

Strategy/Network	Excitation power (force excitation)	Excitation power (acceleration ground input)
EHTMD	$\pi S_0/m_0$	$\pi(m_0 + m_2)S_0$
EHEMD	$\pi S_0/m_0$	$\pi m_0 S_0$
II-1	$\pi S_0/(m_0 + b)$	$\pi m_0^2 S_0/(m_0 + b)$
II-2	Null ($\pi S_0/m_0$)	Null ($\pi m_0 S_0$)
III-1	Null ($\pi S_0/m_0$)	Null ($\pi m_0 S_0$)
III-2	$\pi S_0/m_0$	$\pi m_0 S_0$
III-3	Null ($\pi S_0/(m_0 + b)$)	Null ($\pi m_0^2 S_0/(m_0 + b)$)
III-4	$\pi S_0/m_0$	$\pi m_0 S_0$
III-5	$\pi S_0/m_0$	$\pi m_0 S_0$
III-6	$\pi S_0/m_0$	$\pi m_0 S_0$
III-7	$\pi S_0/m_0$	$\pi m_0 S_0$
III-8	$\pi S_0/(m_0 + b)$	$\pi m_0^2 S_0/(m_0 + b)$

6.4.3 Numerical Validation

The same numerical model in Subsection 6.2.3 was adopted, and the structural inherent damping ratio was set as 0.03. The power results are normalized by the excitation power (i.e., $\pi S_0/m_0$) when a viscous damper (or EHEMD) was connected. The aforementioned networks were applied to the model by considering different inerter ratios β (= b/m_0). Note that the optimal conditions for these networks, if existing, were obtained numerically with a constrained EHTID damping coefficient ($5 \leq c_3 \leq 1000$ N·s/m) and stiffness ($0.1\omega_0 \leq (k_3/b)^{1/2} \leq 10\omega_0$). The optimization objectives were to minimize the structural kinetic energy and maximize the EHTID output power, which were approximately consistent.

Figure 6.12 shows the normalized input excitation power of an SDOF structure with different networks of EHTIDs. All networks with a grounded inerter, specifically Networks II-1, III-3, and III-8, resulted in decreased input excitation power, which agrees well with the theoretical analysis in Table 6.2.

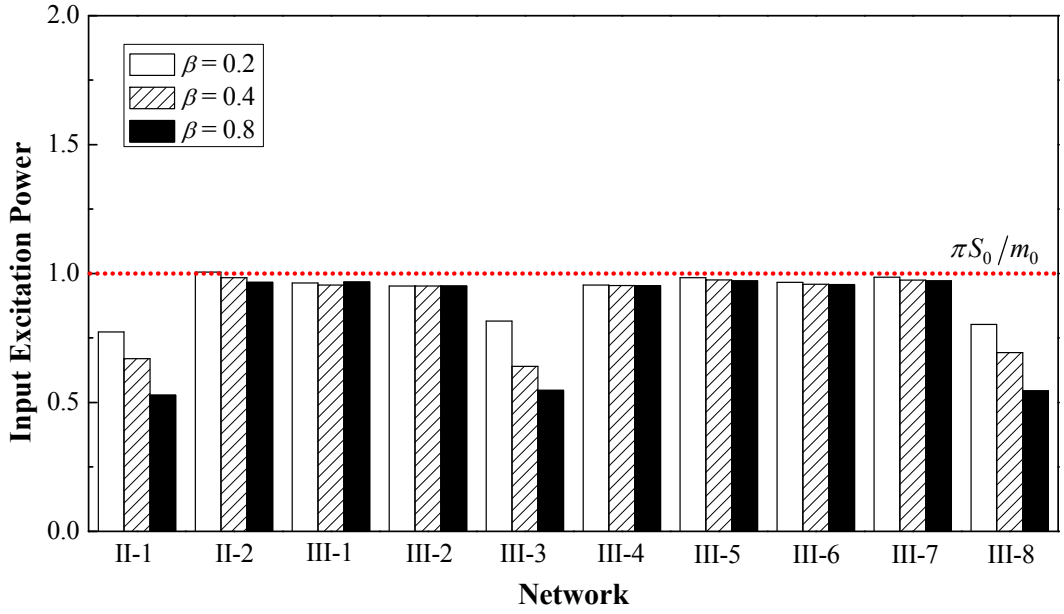

Figure 6.12 Input excitation power of an SDOF structure with EHTID ($\xi_0 = 0.03$)

Moreover, Figure 6.13 presents the corresponding input excitation damping (total damping power) and EHTID output power under different inerter ratios from 0.01 to 0.8. The theoretical prediction of the input excitation power matched well with the numerical results, which demonstrates the accuracy of the theoretical derivation (i.e., Equations (6.18–6.24)). Moreover, under the optimal condition for the minimization of structural kinetic energy, the following was observed:

(1) Increased inertance in a grounded inerter generally resulted in a lower EHTID output power and input excitation power, although most of the input power could be distributed into the EHTID (Figure 6.13(a), (e), and (k)), whereas an increased ungrounded inerter did not affect the input excitation power but led to different power distribution performance.

(2) In the cases of Networks III-2, III-4, and III-6, neither the EHTID output power P_d nor the structural inherent damping power P_s were significantly influenced by increased inertance, indicating that the power items in these networks were insensitive to inertance variation.

(3) In the cases of Networks II-2, III-1, III-5, and III-7, an increased inerter resulted in the distribution of more power into the EHTID, thereby enhancing the EHTID output power and reducing the structural inherent damping power that is proportional to the

structural kinetic energy.

In the case of a fixed inerter ratio $\beta = 0.2$ and taking Network III-7 as an example, Figure 6.14 presents the concerned performance of the structure–EHTID system under a structural inherent damping ratio of $\xi_0 = 0.03$. The overall trend of the EHTID output power was nearly opposite to that of the structural inherent damping power/kinetic energy, similar to the results for EHTMD in Figure 6.5. The optimal conditions for these two indices were nearly identical (25.5 N·s/m, 229.5 N/m). Note that a similar trend can be obtained for other networks if the inerter ratio is given. This result indicates that given a fixed inerter ratio, the vibration control and energy harvesting objectives of the EHTID are consistent.

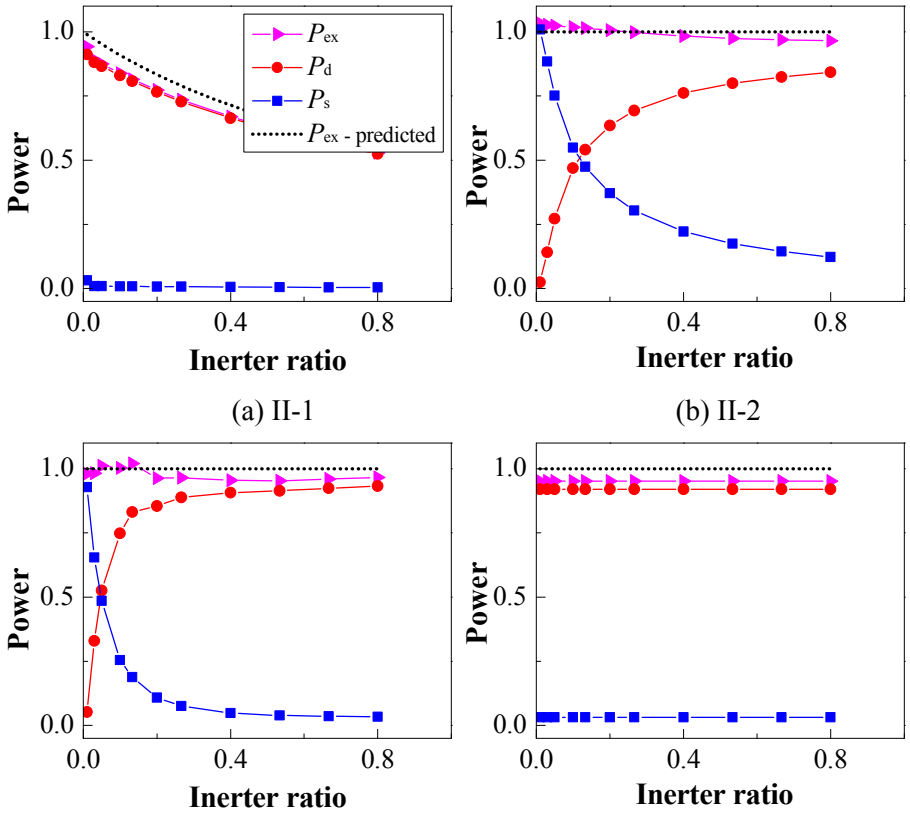

(a) II-1 (b) II-2

(c) III-1 (d) III-2

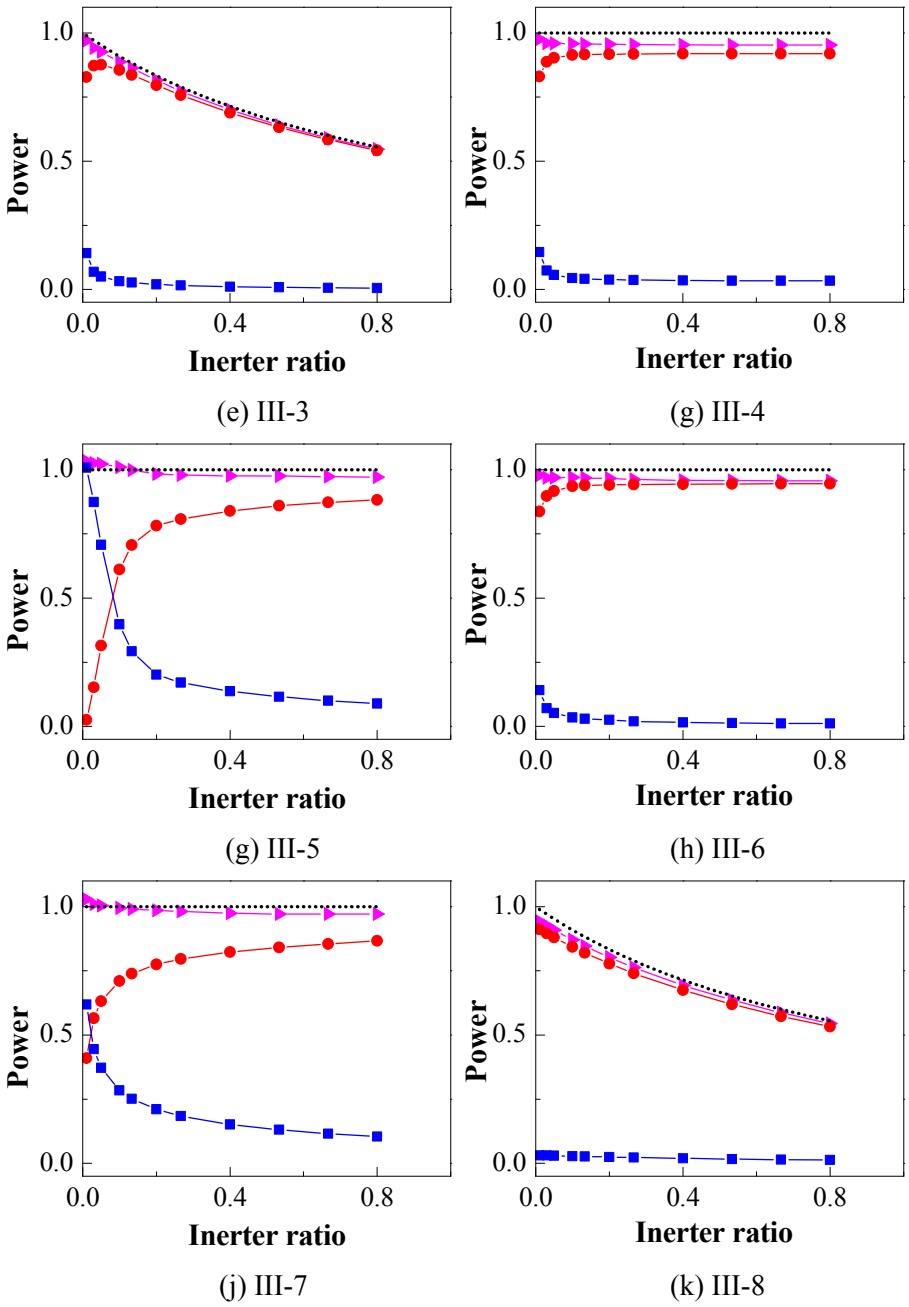

(e) III-3 (g) III-4

(g) III-5 (h) III-6

(j) III-7 (k) III-8

Figure 6.13 Power distribution in different networks of EHTIDs (ξ_0 = 0.03)

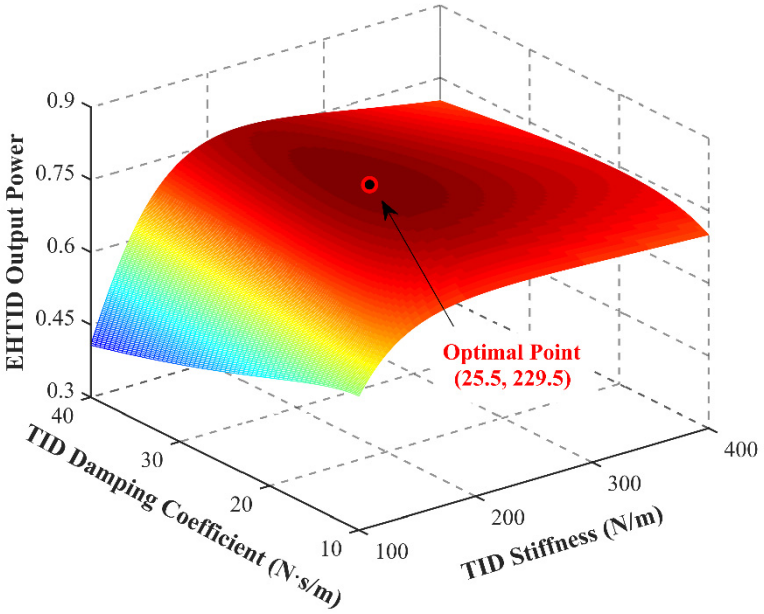

(a) EHTID output power

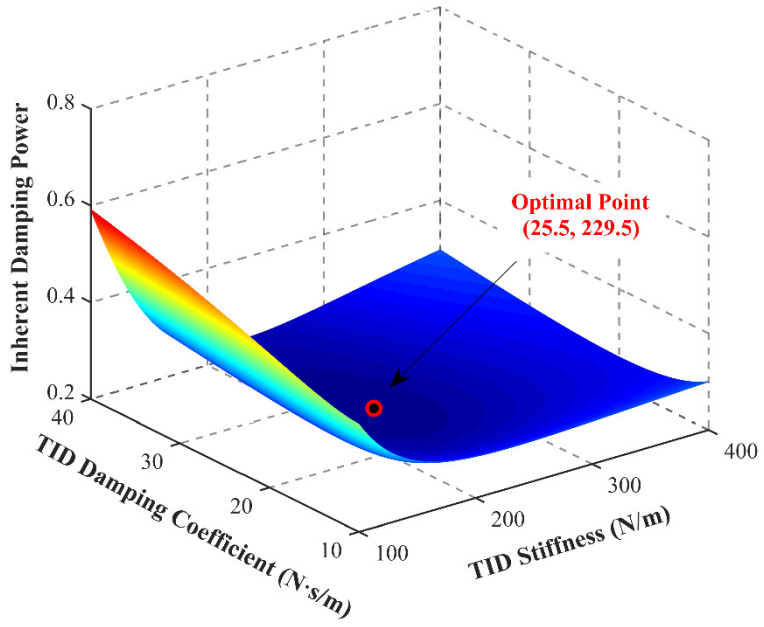

(b) Structural inherent damping power

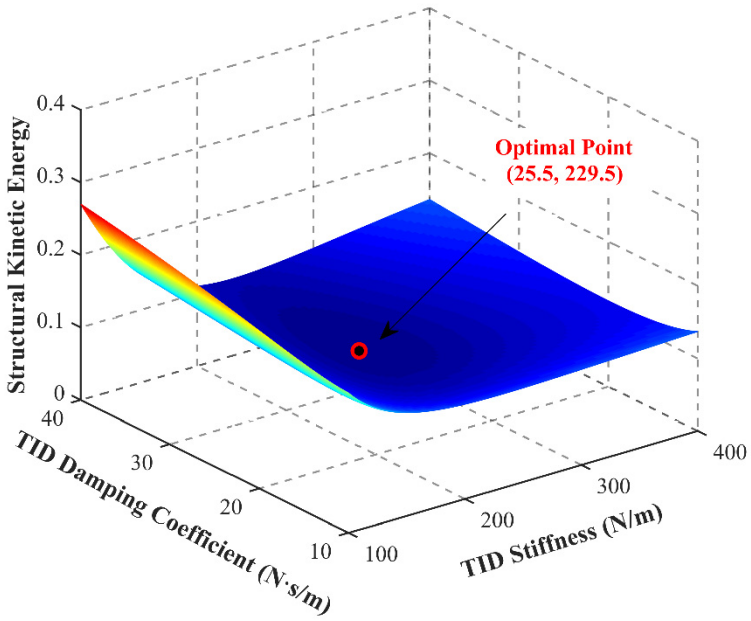

(c) Structural kinetic energy

Figure 6.14 Variation in the performance indices with EHTID damping coefficient (c_3) and stiffness (k_3) under conditions $\xi_0 = 0.03$ and $\beta = 0.2$

6.4.4 Discussions

(1) Given a fixed inertance, vibration control and energy harvesting are consistent if the EHTID is designed to minimize the structural kinetic energy/inherent damping power.

(2) Introducing the inertance cannot increase the excitation power inputted into the entire system; in particular, a grounded inerter might reduce this input excitation power, regardless of force excitation or ground acceleration excitation. In this regard, if the structural inherent damping is ignored, the increasing inertance shows no positive effect on energy harvesting. If the inherent damping is considered, a specific analysis of the power distribution of the employed inerter-based network is required.

(3) In a damped SDOF–EHTID coupled system subjected to random excitation, the increasing grounded inertance reduced the input excitation power and the EHTID output power, which confirms the negative effect from an energy harvesting perspective. As for the ungrounded-inerter-based networks, a larger inertance is preferable for Networks II-2, III-1, III-5, and III-7 considering the dual-function enhancement with increased inertance; the inertance showed limited impact on the

power distribution for the other three networks, thereby raising the question of whether the inerter is necessary for an energy harvester.

(4) Considering that the input excitation power is independent of the inertance ratio for the ungrounded-inerter-based networks, the maximization of the EHTID output power naturally corresponds to the minimization of the structural inherent damping power. Thus, the dual-objective optimizations in the EHTID with an ungrounded inerter should be consistent.

6.5 Power Efficiency within EMD

The target optimal damping coefficient c_{opt} ($c_{1,\text{opt}}$, $c_{2,\text{opt}}$, $c_{3,\text{opt}}$) governs the selection of the EMD. As mentioned in Chapter 3, the upper and lower limits of the achievable damping coefficients of an EMD correspond to $R_{\text{load}} = 0$ and ∞, respectively. Therefore, a proper selection of the EMD parameters should be done to meet the requirement $c_{\text{p}} < c_{\text{opt}} < (c_{\text{p}} + K_{\text{eq}}^2/R_{\text{coil}})$, i.e., Equation (3.6).

In addition, the EMD damping power is regarded as the gross output power of the concerned damper in the previous sections of this chapter. In reality, only a portion of the gross output power can be finally harvested in an energy storage element. The net output power of EMD depends on another power conversion efficiency η (see Equation (3.13)), which is determined by the characteristics of the EMD and the load resistance of the EHC. If the power of the load resistance R_{load} is regarded as the net output power, the power conversion efficiency inside the EMD can be expressed as:

$$\eta = \frac{K_{\text{eq}}^2 R_{\text{load}}}{c_{\text{p}} \left(R_{\text{load}} + R_{\text{coil}} \right)^2 + K_{\text{eq}}^2 \left(R_{\text{load}} + R_{\text{coil}} \right)} \tag{6.25}$$

Combining Equations (3.5) and (6.25) yields:

$$\eta = \frac{\left(c_{\text{opt}} - c_{\text{p}} \right)\left(c_{\text{p}} + K_{\text{eq}}^2 / R_{\text{coil}} - c_{\text{opt}} \right)}{c_{\text{opt}} \, K_{\text{eq}}^2 / R_{\text{coil}}} \tag{6.26}$$

Therefore, the selection of the EMD parameters represents another complex optimization problem to achieve the maximum power conversion efficiency η, which

cannot be analytically discussed because of the lack of empirical relations among K_{eq}, R_{coil}, and c_p of EMDs. A general conclusion is that a large ratio of K_{eq}^2/R_{coil} and a small parasitic damping c_p of an EMD can enhance the power conversion efficiency η. The unity power conversion efficiency $\eta_{em} = 1$ only occurs when R_{coil} and c_p approach zero. The numerical optimization of η is outside the scope of this analytical study, and thus, only the gross output power of EMD is discussed above.

6.6 Summary

This chapter first reviews the consistency between the two-objective optimization for the SDOF structure–EHEMD coupled system presented by Shen (2014) and validates its effectiveness through a numerical case study. Then, two relatively more complicated scenarios, i.e., the SDOF structure–EHTMD system and SDOF structure–EHTID system, are analytically investigated. The analysis of the three structure–damper systems that represent common passive control strategies in civil structures, to some extent, clarifies the ambiguity in dual-function dampers.

In the case of EHTMDs, this chapter presents a closed-form solution to the optimal parameters of an EHTMD installed in a damped structure subjected to random excitation, whereby the optimization objectives are to minimize the kinetic energy (calculated by relative velocity) of the controlled structure and maximize the EHTMD output power. The major results and conclusions are summarized as follows:

1) Vibration control and energy harvesting are generally consistent in an EHTMD installed in a damped structure subjected to broadband random excitation, wherein the excitations might be random forces or ground motions.
2) A larger mass ratio of the EHTMD benefits both vibration control and energy harvesting performance. This observation is different from what has been reported in previous studies.
3) The energy harvesting performance of the EHTMD is insensitive to slight parameter detuning.

4) The general expressions of the power efficiency and power distributions will shed light on the power-based optimization of classical TMDs installed in damped structures.

In the case of EHTIDs, this chapter presents an analytical solution to the total damping power of an SDOF structure with 10 EHTID networks. The power distribution of the total damping power was analyzed numerically. Using the same two objectives as those for the EHTMD, the major results are summarized as follows:

5) In the case of broadband random excitation, either by random force or ground motion, the grounded inerter reduced the excitation input power and the EHTID output power, which is not recommended from the perspective of energy harvesting.
6) In networks with ungrounded inerters, the energy harvesting and vibration control in an EHTID installed in a damped structure are still generally consistent, even when the inerter ratio is varied.
7) A larger inerter ratio generally benefits energy harvesting and vibration control simultaneously for the ungrounded-inerter-based networks, except Networks III-2, III-4, and III-6.
8) Given a fixed inerter ratio, regardless of which network is applied, the two objectives in the EHTID are consistent.

Note that the aforementioned conclusions are obtained on the condition of random excitation. However, under harmonic excitation, the excitation power transferred to the structure with dual-function dampers (EHEMD, EHTMD, and EHTID) should be highly dependent on the frequency and damping, and thus, the optimizations of the two objectives in the dampers should not be consistent anymore.

6.7 Appendix: Integral Computation

Equations (6.27) and (6.28) present the integral computations for the typical transfer functions of SDOF and 2DOF structures, respectively:

$$\int_{-\infty}^{+\infty}\left|\frac{B_0+B_1\kappa}{A_0+A_1\kappa+A_2\kappa^2}\right|^2 \mathrm{d}\omega=\frac{\pi\left(B_0^2 A_2/A_0+B_1^2\right)}{A_1 A_2} \tag{6.27}$$

$$\int_{-\infty}^{+\infty}\left|\frac{B_0+B_1\kappa+B_2\kappa^2+B_3\kappa^3}{A_0+A_1\kappa+A_2\kappa^2+A_3\kappa^3+A_4\kappa^4}\right|^2 d\omega$$

$$=\pi\frac{A_0 B_3^3\left(A_0 A_3-A_1 A_2\right)+A_0 A_1 A_4\left(2B_1 B_3-B_2^2\right)-A_0 A_3 A_4\left(B_1^2-2B_0 B_2\right)+A_4 B_0^2\left(A_1 A_4-A_2 A_3\right)}{A_0 A_4\left(A_0 A_3^2+A_1^2 A_4-A_1 A_2 A_3\right)} \tag{6.28}$$

CHAPTER 7

OVERALL IMPEDANCE OPTIMIZATION IN EM ENERGY HARVESTERS

7.1 Introduction

Chapters 4–6 focus on the first category, i.e., the dual-function EM energy harvester. Power enhancement was realized by scaling up the energy harvester whose machine constant is typically sufficiently large, so that the device could be coupled with the vibration sources.

This chapter investigates the electrical load optimization for energy harvesters in the second category, i.e., single-function EM energy harvesters, which mainly refers to a harvester that has no significant effect on the vibration sources. In addition to the EMD and EHC, this configuration typically contains an oscillating structure.

As reviewed in Chapter 2, the optimal electrical load for an EM energy harvester under harmonic excitation has been explored by Cheng et al. (2007) and Cammarano et al. (2010) in the electrical and mechanical domains, respectively. However, the optimal conditions of vibration-based energy harvesters under random excitation, an arguably more common type of environmental vibration, are rarely investigated. Another apparent deficiency is the focus given to SDOF energy harvesters by the majority of previous optimization studies, even though the energy harvesters may sometimes be MDOF structures (Tang and Zuo, 2011; Tang and Yang, 2012; Xiao et al., 2016; Hu et al., 2018). For example, Tang and Zuo (2011) suggested the use of dual-mass systems to enhance

the EM vibration energy harvesting performance. Xiao et al. (2016) introduced an improved MDOF harvester by adding piezoelectric elements between every two oscillators. Despite different MDOF configurations have been proposed to enhance energy harvesting performance, optimization of the electrical load in these cases has not yet been addressed. Hence, the optimizations presented in the previous studies provided incomplete answers to individual cases. This chapter presents a unified solution for vibration-based energy harvesters based on the overall impedance optimization strategy, which can be applied to either SDOF or MDOF energy harvesters under different excitations with strong or weak electromechanical coupling effects. This chapter is organized as follows: After the introduction section, the classical IM strategy is first presented. Thereafter, the vibration-based EM energy harvester is entirely represented by an alternative equivalent circuit in the electrical domain on the basis of the dynamic analogy between mechanical and electrical systems. With such an equivalent circuit model, the optimal conditions for output power and efficiency are derived mathematically under various excitation types. Subsequently, numerical models were established to simulate six different scenarios (SDOF and MDOF harvesters under resonant, non-resonant, and random excitations) and validate the proposed overall impedance optimization strategy. Finally, the brief conclusions are summarized.

7.2 Classical IM

7.2.1 Voltage Source

The traditional IM in electronics refers to the practice of designing the load impedance to maximize the power transfer. Figure 7.1 shows a representative electrical model with a voltage source U_s and internal impedance (capacitance C_s, inductance L_s, and resistance R_s). The corresponding source impedance Z_s is given as:

$$Z_s = R_s + \left(\omega L_s - \frac{1}{\omega C_s} \right) j \tag{7.1}$$

where ω is the frequency of the voltage source. To maximize the average power transfer to the load, the load impedance Z_{load} should be the complex conjugate of the source

impedance; if this condition is met, the phenomenon is commonly known as the classical IM.

$$Z_{\text{load}} = R_{\text{load}} + \chi_{\text{load}}\, j \tag{7.2}$$

where

$$R_{\text{load}} = \text{Re}\left(Z_{\text{s}}\right) = R_{\text{s}} \tag{7.3a}$$

$$\chi_{\text{load}} = -\text{Im}\left(Z_{\text{s}}\right) = \frac{1}{\omega C_{\text{s}}} - \omega L_{\text{s}} \tag{7.3b}$$

where Re(·) and Im(·) denote the real and imaginary parts of the concerned impedance, respectively; and R_{load} and χ_{load} are the load resistance and reactance, respectively. Hereafter, the IM strategy that does not consider the dynamics of mechanical structures is referred to as the classical IM for simplicity.

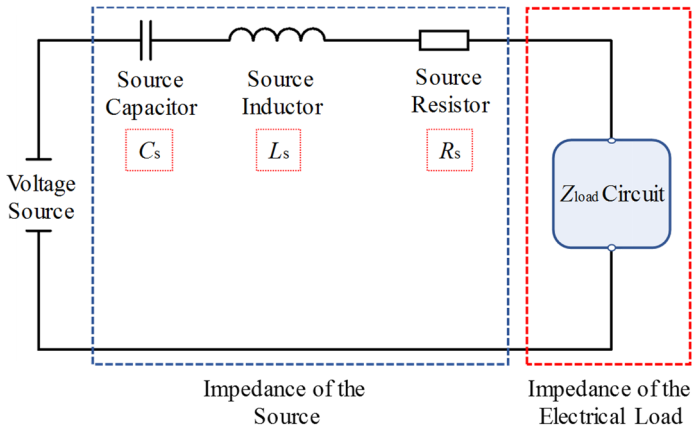

Figure 7.1 Classical IM in the circuit with a voltage source that requires the load impedance to be the complex conjugate of the source impedance

7.2.2 Current Source

For a circuit with a current source or complex electric network, the Thévenin's theorem presents a standard technique to convert a complex circuit into an equivalent simplified one with a voltage source in a series connection with an internal impedance:

- *The Thévenin equivalent voltage U_{Th} is the open-circuit voltage at the output terminals of the original circuit.*

- *The Thévenin equivalent impedance Z_{Th} can be calculated across the terminals by using the formulae for series and parallel circuits after replacing the current and voltage sources with open and short circuits, respectively.*

Figure 7.2 shows a classical electric circuit with a current source. The corresponding Thévenin parameters are as follows:

$$V_{\mathrm{Th}} = i_{\mathrm{s}} Z_{\mathrm{Th}} \tag{7.4}$$

$$Z_{\mathrm{Th}} = R_{\mathrm{Th}} + \chi_{\mathrm{Th}}\, j \tag{7.5}$$

where i_{s} is the source current, and R_{Th} and χ_{Th} are the Thévenin equivalent resistance and reactance, respectively. Accordingly, the optimal output impedance for the maximum power transfer can be calculated as follows:

$$R_{\mathrm{load}} = R_{\mathrm{Th}} = \frac{R_{\mathrm{s}}}{1 + R_{\mathrm{s}}^2 \left(\omega C_{\mathrm{s}} - \dfrac{1}{\omega L_{\mathrm{s}}} \right)^2} \tag{7.6a}$$

$$\chi_{\mathrm{load}} = -\chi_{\mathrm{Th}} = \frac{-\left(\omega C_{\mathrm{s}} - \dfrac{1}{\omega L_{\mathrm{s}}} \right) R_{\mathrm{s}}^2}{1 + R_{\mathrm{s}}^2 \left(\omega C_{\mathrm{s}} - \dfrac{1}{\omega L_{\mathrm{s}}} \right)^2} \tag{7.6b}$$

Equations (7.3) and (7.6) contain the frequency ω, implying that the optimal impedance is only for the maximum output power with a known harmonic input frequency. Equations (7.3) and (7.6) assume a constant voltage or current source independent of the selected load impedance. However, random inputs (excitation sources) with a broad frequency bandwidth are common in vibration-based energy harvesting. The circuit dynamics are coupled with structural dynamics. Therefore, the variation of load impedance in the circuit may affect the power input into the circuit, and the coupling effect of the mechanical and electrical systems must be properly considered. In this regard, the classical IM theory provides an insufficient solution that cannot be directly applied to optimize the vibration-based energy harvester. Therefore, an overall impedance optimization method is presented in the subsequent section.

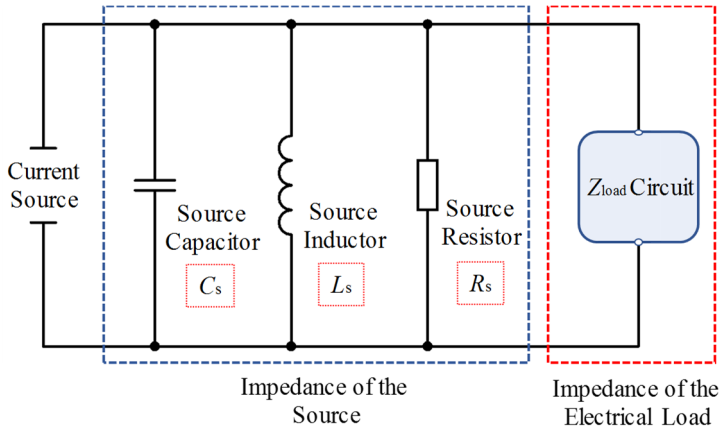

Figure 7.2 Classical IM in the circuit with a current source, source impedance, and load impedance

7.3 Overall Impedance Optimization in SDOF Harvester

7.3.1 Structural and Electrical System

Figure 7.3 shows the classical configuration of a vibration-based EM energy harvester (oscillator), which comprises an SDOF primary structure and an EMD connected to an EHC. Herein, SDOF describes the dynamics of the mechanical structure. However, if the circuit dynamics are considered, then the degrees of freedom of the entire system might be more than one.

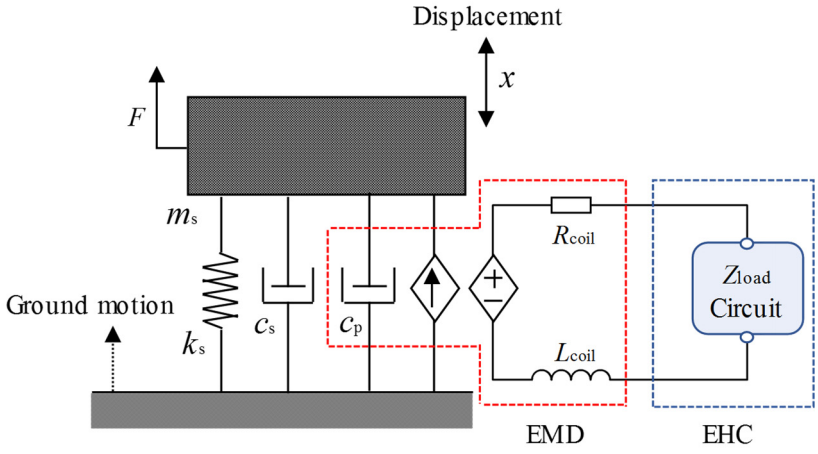

Figure 7.3 Schematic of a typical vibration-based EM energy harvester

The SDOF structure consists of a mass m_{str}, stiffness k_{str}, and inherent damping c_{str}. The EMD provides the parasitic damping c_p owing to various mechanical losses, such as

friction and iron loss. As shown in Figure 7.3, structural vibration generates an EMF in the EMD during energy transformation. The EMF further generates a current flowing through the attached harvesting circuit and internal impedance of the EMD. Meanwhile, an EM force proportional to the current is generated and acts against the primary structural oscillation. Hence, the EMD contributes parasitic damping and EM forces to the mechanical structures, which may affect the structural vibrations, as previously mentioned.

7.3.2 Equivalent Circuit Representation

Figure 7.3 shows a coupled electromechanical system. The following expressions are presented based on the analogy between the electrical components and mechanical structures (Firestone, 1933; Zhu et al., 2013):

$$i = \frac{F}{K_{\text{eq}}} \tag{7.7a}$$

$$U = K_{\text{eq}}\dot{x} \tag{7.7b}$$

$$L_{\text{str}} = \frac{K_{\text{eq}}^2}{k_{\text{str}}} \tag{7.7c}$$

$$C_{\text{str}} = \frac{m_{\text{str}}}{K_{\text{eq}}^2} \tag{7.7d}$$

$$R_{\text{p}} = \frac{K_{\text{eq}}^2}{c_{\text{p}}} \tag{7.7e}$$

$$R_{\text{str}} = \frac{K_{\text{eq}}^2}{c_{\text{str}}} \tag{7.7f}$$

where F is the excitation force; $\dot{x}$ is the relative velocity between two terminals of the EMD; K_{eq} is the machine constant (also known as back EMF constant and force constant) of the EMD; c_{p} is the parasitic damping introduced by the EMD; L_{str}, C_{str}, and R_{str} are the structural equivalent inductance, capacitance, and resistance, respectively; and R_{p} represents the equivalent resistance corresponding to parasitic damping. The expressions

in Equation (7.7) are known as mobility analogy. The coupled system shown in Figure 7.3 can then be represented by an alternative equivalent circuit (Figure 7.4) that is entirely in the electrical domain. In this dynamic analogy, the dynamic force on the SDOF structure corresponds to an electrical current generator, and the vibration velocity corresponds to the voltage across the electrical elements. Notably, this topology is also applicable to the energy harvester subjected to ground motion. In Figure 7.4, the left blue block represents the equivalent part of the mechanical structure, and the red block represents the EMD. In this equivalent circuit, most of the electrical elements are connected in parallel.

When the classical IM, i.e., Equation (7.2), is applied, the optimal load impedance is determined based on the EMD impedance (i.e., R_{coil} and L_{coil}), while the dynamics of the mechanical system and the parasitic damping R_p of the EMD in Figure 7.4 are ignored. The classical IM certainly cannot provide an optimal solution in this case.

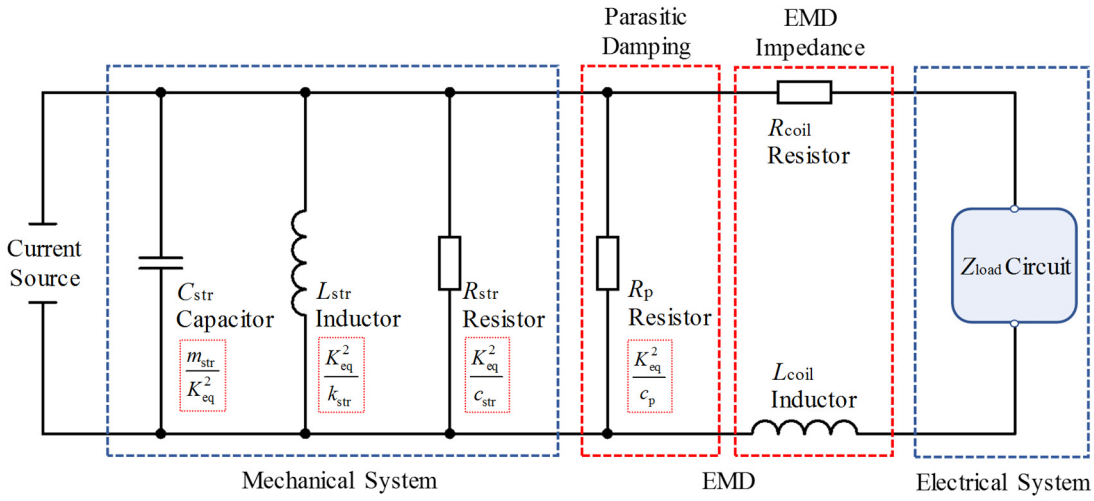

Figure 7.4 Representation of the electromechanical coupled system of an SDOF energy harvester using an equivalent circuit

7.3.3 Weakly Coupled System

In certain cases with small K_{eq} and c_p, the EMD produces small forces. Thus, the influence of the EMD connected to the EHC on the overall dynamics is nearly negligible. Consequently, the entire system becomes weakly coupled; that is, the input voltage to the

EMD is mainly determined by the mechanical dynamics of the SDOF structure and remains nearly constant if the major mechanical and excitation parameters are fixed. In this case, the equivalent circuit can be simplified as Figure 7.5, with an independent voltage source input connected to the EMD. The quantitative definition of the coupling strength to classify weakly and strongly coupled systems will be studied in future works.

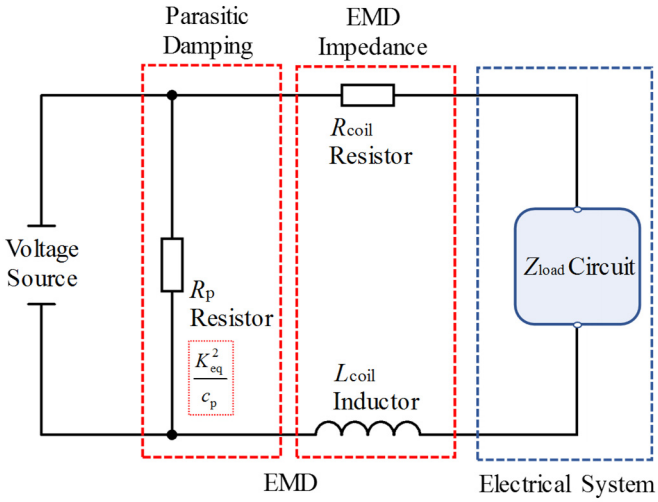

Figure 7.5 Representation of the weakly coupled system of an SDOF energy harvester using an equivalent circuit

If the voltage source represents a harmonic input, then the optimal impedance for the maximum output power can be easily obtained through the aforementioned Thévenin equivalent circuit analysis:

$$R_{load} = R_{Th} = R_{coil} \tag{7.8a}$$

$$\chi_{load} = -\chi_{Th} = -\omega L_{coil} \tag{7.8b}$$

This condition is consistent with the result in Equation (7.2) for the classical IM, which demonstrates that the classical IM can be applied to weakly coupled systems. This conclusion can also be extended to the weakly coupled MDOF energy harvester. Compared with the circuit shown in Figure 7.1 for the classical IM, the topology in Figure 7.5 shows an additional resistor R_p to represent the parasitic damping of the EMD. However, the existence of the parasitic damping does not influence the optimal load

impedance in this case, because the voltage source is treated as a short circuit in the calculation of the Thévenin equivalent impedance.

However, the abovementioned IM does not correspond to the optimal power efficiency in the circuit shown in Figure 7.5. The optimal power efficiency condition, which differs from the IM condition, is discussed in detail in Subsection 7.3.4.2. It is also noteworthy that Equation (7.8) is only suitable for the optimal output power with harmonic input/excitation. If the voltage source is replaced by a constant power source in Figure 7.5, then the optimal power efficiency condition, instead of the IM condition, should lead to the maximum output power. This conclusion is relevant to the optimization under random excitation in the following section.

7.3.4 Strongly Coupled System

7.3.4.1 Overall IM under Harmonic Excitation

Given a strong electromechanical coupling system, the SDOF energy harvester can be described by the equivalent circuit shown in Figure 7.4. Given a harmonic excitation (a harmonic force or ground motion), i.e., a harmonic current source with frequency ω, the Thévenin equivalent impedance can be obtained by analyzing the circuit topology in Figure 7.4:

$$\begin{aligned} Z_{\mathrm{Th}} &= \frac{1}{\frac{1}{R_{\mathrm{str}}}+\frac{1}{R_{\mathrm{p}}}+\omega C_{\mathrm{str}} j-\frac{j}{\omega L_{\mathrm{str}}}}+R_{\mathrm{coil}}+\omega L_{\mathrm{coil}} j \\ &= R_{\mathrm{Th}}+\chi_{\mathrm{Th}} j \end{aligned} \tag{7.9}$$

If the entire energy harvesting system is treated as a single circuit, then the maximum output power under harmonic excitation can be obtained by applying the overall IM. The optimal load impedance should be the complex conjugate of the Thévenin equivalent impedance:

$$R_{\text{load}} = R_{\text{Th}} = \frac{R_{\text{p+str}}}{1 + R_{\text{p+str}}^2 \left(\omega C_{\text{str}} - 1/\omega L_{\text{str}}\right)^2} + R_{\text{coil}} \quad \text{Electrical domain}$$

$$= \frac{\omega^2 K_{\text{eq}}^2 \left(c_{\text{str}} + c_{\text{cp}}\right)}{\omega^2 \left(c_{\text{str}} + c_{\text{p}}\right)^2 + \left(\omega^2 m_{\text{str}} - k_{\text{str}}\right)^2} + R_{\text{coil}} \quad \text{Mechanical domain} \tag{7.10a}$$

$$\chi_{\text{load}} = -\chi_{\text{Th}} = \frac{-R_{\text{p+str}}^2 \left(1/\omega L_{\text{str}} - \omega C_{\text{str}}\right)}{1 + R_{\text{p+str}}^2 \left(\omega C_{\text{str}} - 1/\omega L_{\text{str}}\right)^2} - \omega L_{\text{coil}} \quad \text{Electrical domain}$$

$$= \frac{-\omega K_{\text{eq}}^2 \left(k_{\text{str}} - \omega^2 m_{\text{str}}\right)}{\omega^2 \left(c_{\text{str}} + c_{\text{p}}\right)^2 + \left(\omega^2 m_{\text{str}} - k_{\text{str}}\right)^2} - \omega L_{\text{coil}} \quad \text{Mechanical domain} \tag{7.10b}$$

where $R_{\text{p+str}} = R_{\text{p}}R_{\text{str}}/(R_{\text{p}} + R_{\text{str}})$ is the total resistance considering R_{p} and R_{str} in parallel connection. This optimal condition, which is excitation frequency–dependent, is consistent with the conclusions reported by Cheng et al. (2007) and Cammarano et al. (2010) who derived in electrical and mechanical domains, respectively.

Equation (7.10) indicates that the optimal load impedance in the strongly coupled system depends not only on the EMD characteristics (i.e., R_{p}, R_{coil}, and L_{coil}) but also on the structural characteristics, such as the equivalent resistor R_{str}, capacitor C_{str}, and inductor L_{str}. The result theoretically demonstrates that the structural (oscillator's) mechanical characteristics should be considered during the impedance optimization of the EM energy harvester. The classical IM method can be extended to the optimization of the EHC in the vibration-based EM energy harvester by properly considering the overall (electrical and mechanical) impedance. It is evident that the realization of IM depends on not only the EHC characteristics (simplified as Z_{load} in this chapter) but also the coupling effect of the system. For simplicity, this strategy is hereafter referred to as the overall IM. Liao and Liang (2018) made similar observations for piezoelectric energy harvesters.

In an ideal case in which the primary structure is designed in resonance with the harmonic excitation with a frequency ω:

$$k_{\text{str}} = m_{\text{str}}\omega^2 \tag{7.11a}$$

$$\omega L_{\text{str}} = \frac{1}{\omega C_{\text{str}}} \tag{7.11b}$$

The optimal condition shown in Equation (7.10) can be simplified as:

$$R_{\text{load}} = R_{\text{str+p}} + R_{\text{coil}} \tag{7.12a}$$

$$\chi_{\text{load}} = -\omega L_{\text{coil}} \tag{7.12b}$$

If the coil inductance is negligible, Equation (7.12a) provides a result consistent with that previously reported by Stephen (2006) for a resonant state. Williams et al. (2001) indicated that the optimal electrical load impedance equaled the mechanical equivalent impedance in a resonant state. However, Equation (7.12) indicates that this conclusion is true only if the coil resistance R_{coil} of the EMD is negligible.

The energy harvester in a resonant state certainly presents an ideal situation for maximizing the output power, while Equation (7.10) presents a general case in which the harmonic excitation frequency may deviate from the designed frequency of the energy harvester.

7.3.4.2 Power Efficiency

As mentioned in Chapter 3, in the energy conversion process, various power losses and consumptions occur inevitably when the power flows through the entire system. Only a portion of the vibration power can be harvested. The power efficiency is also an index of common interest in energy harvesting performance evaluation. This subsection represents the power efficiency index in the equivalent circuit model. Zhu et al. (2012) and Shen et al. (2016a) presented the overall power efficiency as the products of several sub-efficiencies:

$$P_{\text{out}} = P_{\text{ex}} \cdot \eta = P_{\text{in}} \cdot \eta_1 \cdot \eta_2 \cdot \eta_3 \tag{7.13}$$

where P_{out} is the average output power from the energy harvester; P_{ex} is the average excitation power inputted into the entire system and is equal to the total damping power

of the oscillator; η is the overall power efficiency in the entire system; η_1 denotes the ratio of the power in the branch with R_{coil} and Z_{load} to the total power consumption of the equivalent circuit; η_2 is the ratio of the output power on the load resistance R_{load} to the power consumed by this branch; and η_3 represents the power conversion ratio of the EHC. In practice, various types of circuits have been proposed to realize energy harvesting and synthetic impedance functions, such as H-bridge (Mitcheson et al., 2011) and buck–boost converter, as mentioned in Chapter 3. Dell'Anna et al. (2018) summarized the recently proposed power circuits on energy-neutral designs. For simplicity, the power consumption by the load resistance R_{load} is regarded as the output power in this chapter, and η_3 is equal to 1. It is also noteworthy that all of the power items in this chapter are average power unless otherwise stated.

The following aspects should be pointed out: (1) Owing to the introduced R_{str}, the excitation power of the oscillator is equal to the total mechanical input power but might be larger than the power transferred into the EMD (P_{in}); that is, $P_{ex} \geq P_{in}$ (see Chapter 3 for the definition of P_{in}). When $R_{str} = \infty$ ($c_{str} = 0$), $P_{ex} = P_{in}$. (2) Owing to the simplified EHC represented by a pure load resistor R_{load}, the effect of the bridge rectifier is neglected; therefore, the sub-efficiencies η_1 and η_2 in this chapter are slightly different from the expressions in Chapter 3.

Considering the equivalent circuit shown in Figure 7.4, the ideal capacitor or inductor elements consume no power in a cycle, and only the resistors in the circuit are energy-consuming or -dissipating elements. Thus, the other two sub-efficiencies can be expressed as:

$$\eta_1 = \frac{R_{p+str}\cos^2\theta_e}{R_{load} + R_{coil} + R_{p+str}\cos^2\theta_e} \tag{7.14a}$$

$$\eta_2 = \frac{R_{load}}{R_{load} + R_{coil}} \tag{7.14b}$$

The corresponding overall power efficiency is as follows:

$$\eta = \frac{R_{\text{p+str}} \cos^2 \theta_{\text{e}}}{R_{\text{load}} + R_{\text{coil}} + R_{\text{p+str}} \cos^2 \theta_{\text{e}}} \cdot \frac{R_{\text{load}}}{R_{\text{load}} + R_{\text{coil}}} \tag{7.15}$$

where θ_{e} represents the phase angle between the current and voltage in the branch containing R_{coil}, L_{coil}, and Z_{load} (Figure 7.6).

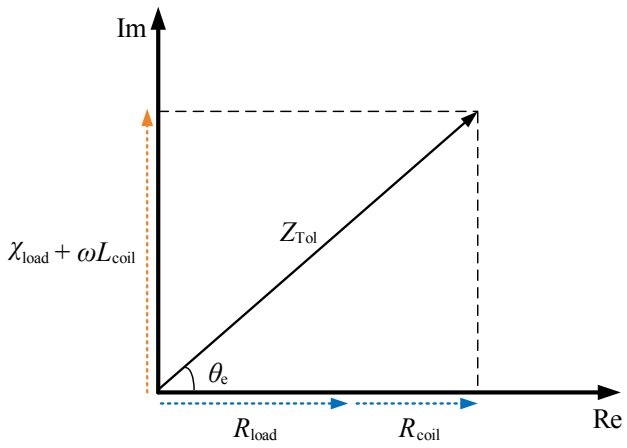

Figure 7.6 Impedance vector diagram for the EMD and EHC

If

$$\chi_{\text{load}} = -\omega L_{\text{coil}} \quad (\text{i.e.,} \quad \cos\theta_{\text{e}} = 1) \tag{7.16a}$$

$$R_{\text{load}} = \sqrt{R_{\text{coil}}^2 + R_{\text{coil}} R_{\text{p+str}}} \tag{7.16b}$$

the optimal power efficiency can be achieved as:

$$\eta_{\text{opt}} = \frac{\sqrt{R_{\text{coil}}^2 + R_{\text{coil}} R_{\text{p+str}}}\, R_{\text{p+str}}}{R_{\text{p+str}} \left(\sqrt{R_{\text{coil}}^2 + R_{\text{coil}} R_{\text{p+str}}} + R_{\text{coil}} \right) + \left(\sqrt{R_{\text{coil}}^2 + R_{\text{coil}} R_{\text{p+str}}} + R_{\text{coil}} \right)^2} \tag{7.17}$$

Equation (7.16) demonstrates that the optimal power efficiency requires the load reactance to be the opposite number of the coil reactance. Equations (7.10) and (7.16) indicate that the optimal impedance values for the maximum output power and power efficiency are considerably different under harmonic excitation. This difference occurs because the input excitation power P_{ex} under harmonic excitation varies with the electrical load. Consequently, the maximum power efficiency does not lead to the maximum output power. Similar conclusions have also been reported by Liao and Sodano (2009) for

piezoelectric energy harvesters.

Given a small coil inductance of the EMD and low-frequency excitation, the reactance shown in Equation (7.16a) will be nearly negligible. Thus, a pure resistive load can be used to optimize the efficiency. In this situation, only Equation (7.16b) can be adopted to obtain the optimal efficiency shown in Equation (7.17).

Equations (7.16) and (7.17) do not depend on the structural characteristics, such as m_{str} and k_{str}, but on structural inherent damping (c_{str} or R_{str}). Therefore, the mechanical and electrical systems in the optimal power efficiency are coupled through the equivalent resistance R_{str} only. In real applications, the inherent damping of the energy harvesting structures is always minimized to enhance the efficiency. If the structural inherent damping becomes negligible ($c_{str} << c_p$), the equivalent resistance R_{str} becomes extremely large, and the system becomes decoupled in terms of power efficiency. Consequently, the optimal conditions in Equation (7.16) can be simplified as:

$$\chi_{load} = -\omega L_{coil} \tag{7.18a}$$

$$R_{load} = \sqrt{R_{coil}^2 + R_{coil} R_p} \tag{7.18b}$$

for the weakly coupled system. This result is identical to that derived by Zhu et al. (2012), who ignored any coupling effect.

7.3.4.3 Impedance Optimization under Random Excitation

Since AC power sources typically have a fixed frequency, random power sources rarely appear in the power electronic discussions. However, random excitation is common in vibration-based energy harvesters. By replacing the harmonic current source in Figure 7.4 with a white noise random source, Equations (7.10) and (7.12) are no longer applicable because of the undetermined excitation frequency. Accordingly, the optimization of vibration-based energy harvesters under random excitation has received limited attention.

Shen et al. (2019) analyzed the stochastic vibrations of an SDOF energy harvester, in which the EMD was represented by a damping element. Their PSD analysis could provide the input excitation power with a resistive load as follows:

$$P_{\text{ex}} = \begin{cases} \pi m_{\text{str}} S_0 & \textit{if random gound motion} \\ \pi S_0 / m_{\text{str}} & \textit{if random force excitation} \end{cases} \tag{7.19}$$

where S_0 represents the PSD of the random ground motion or force excitation. If the equivalent circuit in Figure 7.4 is considered, then the input excitation power of the open circuit can be expressed as:

$$P_{\text{ex}} = \pi S_{\text{I}} / C_{\text{str}} \tag{7.20}$$

where the average input excitation power only depends on the PSD of the random current source S_{I} and the structural equivalent capacitor C_{str} in the circuit.

Considering the broadband characteristic of excitations, a pure resistive EHC is preferable in the case of random excitation. Although the variation of load resistance may change the system overall damping, Equation (7.20) shows that the input excitation power remains constant under white noise excitation. The constant input excitation power implies that the maximum output power and power efficiency can be achieved simultaneously by using Equation (7.16), which is different from the conclusion in the harmonic excitation case. Given a negligible coil inductance of the EMD, Equation (7.16b) provides a satisfactory solution to achieve the maximum output power and power efficiency under random excitation. The optimal power efficiency is described by Equation (7.17). A pure resistive EHC is assumed in the previous discussion, considering that the addition of reactance to the output circuit may lower the power efficiency or even the input excitation power.

7.4 Overall Impedance Optimization in MDOF Harvester

7.4.1 MDOF Harvester

To expand the frequency bandwidth of energy harvesters, a number of MDOF energy

harvesters with different structures have been proposed recently (Tang and Zuo, 2011; Hu et al., 2018; Tang and Yang, 2012). However, the optimization of the electrical load in these MDOF energy harvesters, especially when subjected to random input, has been rarely investigated. This subsection introduces the impedance optimization in a general MDOF energy harvester under harmonic and random excitations.

An MDOF harvester can be similarly represented by an equivalent electric circuit, as shown in Figure 7.7. Under ground motion excitation, either harmonic or random, the current sources 1 to N are in phase and proportional, whereas under force excitation, these current sources may have different frequencies and magnitudes if the external forces on each mass are independent.

The inherent damping of the MDOF harvester that leads to power loss always needs to be minimized. As discussed later in Subsection 7.5.4.3, the inherent damping of a slightly damped structure is often negligible compared with the damping contributed by the EMD; thus, the equivalent resistors $R_{\text{str\_i}}$ (i = 1, ⋯, N) can be removed. In this situation, the Thévenin equivalent impedance can be calculated as follows:

$$Z_{\text{Th}} = \frac{1}{\dfrac{1}{Z_{\text{str\_2}}} + \dfrac{1}{R_{\text{p}}} + \omega C_{\text{str\_1}} j - \dfrac{j}{\omega L_{\text{str\_1}}}} + R_{\text{coil}} + \omega L_{\text{coil}} j \tag{7.21}$$

where the form $Z_{\text{str\_i}}$ can be obtained as:

$$Z_{\text{str\_i}} = \begin{cases} \dfrac{1}{1/Z_{\text{str\_i+1}} + \omega C_{\text{str\_i}} j} + \omega L_{\text{str\_i}} j & (\text{i} = 2, 3, \cdots, N-1) \\ -j/\omega C_{\text{str\_N}} + \omega L_{\text{str\_N}} j & (\text{i} = N) \end{cases} \tag{7.22}$$

The optimal output impedance can be calculated directly as the complex conjugate of Z_{Th}. Notably, this optimal impedance for output power is frequency-dependent and only suitable for harmonic excitation. Under a resonant state (i.e., the excitation frequency is equal to the natural frequency), the optimal impedance for the MDOF harvester becomes identical to that for the SDOF scenario (i.e., Equation (7.12)).

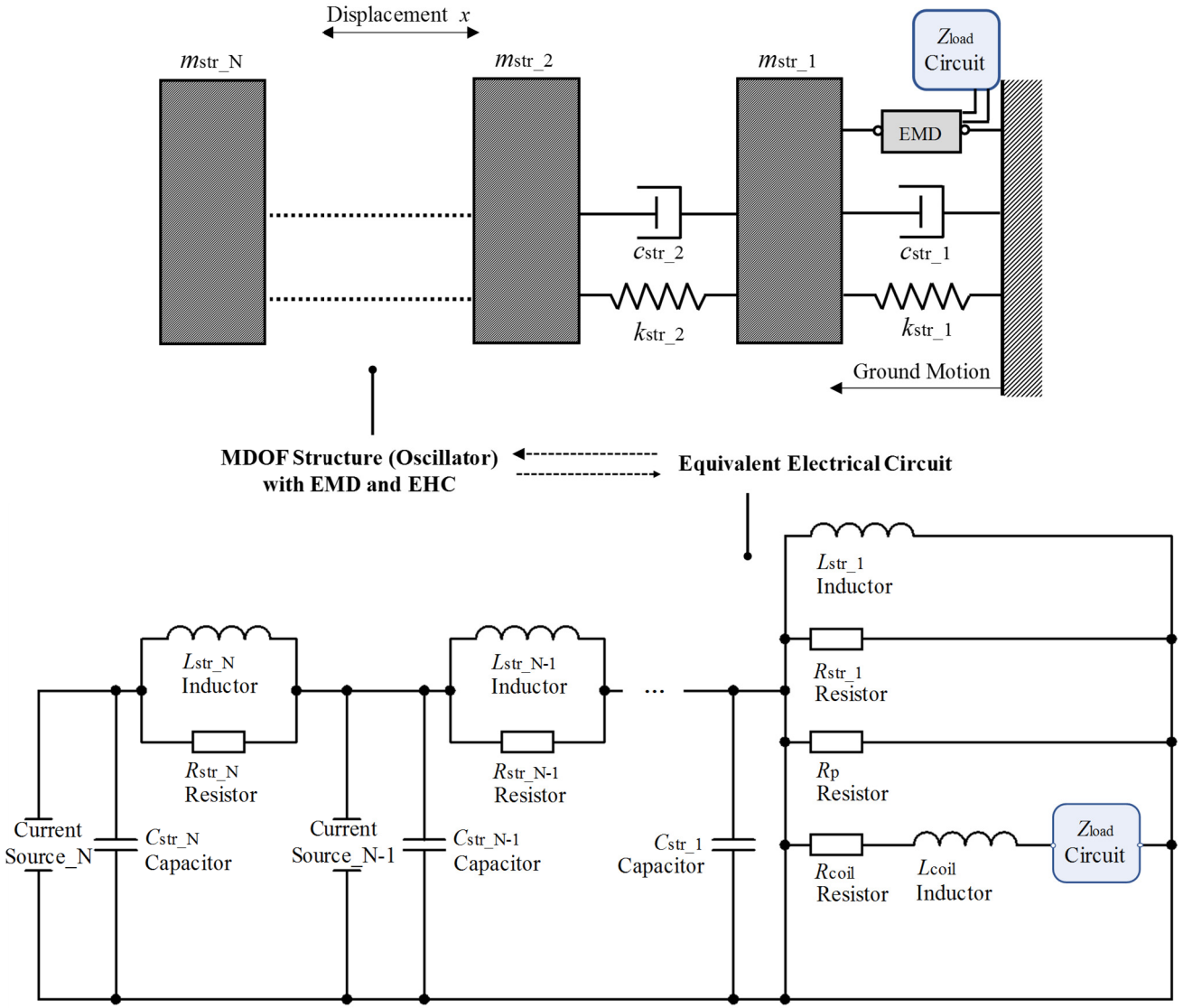

Figure 7.7 Representation of the coupled system of an MDOF energy harvester using an equivalent circuit

Similar to the SDOF case, a pure resistive output circuit is preferred for the MDOF energy harvester under random excitation. Given the fixed structural characteristics and PSD of the random input, the excitation power transferred to the MDOF harvester under white noise excitation is nearly constant and independent of the load resistance change (Shen et al., 2019). Considering the constant input excitation power, the maximum output power should be consistent with the maximum power efficiency. In the case that the structural inherent damping and coil inductance are minimal, Equation (7.18b), introduced in Subsection 7.3.4.3, can be still applied to the MDOF energy harvester to obtain the optimal impedance. Low structural inherent damping is highly desirable in vibration-based energy harvesters to achieve a satisfactory energy conversion ratio. Otherwise, a high structural inherent damping ratio will dissipate the majority of the input excitation power and lead to trivial output power. The effect of the inherent damping is briefly discussed in the subsequent section.

7.4.2 Summary of Overall Impedance Optimization

The optimal impedance for the maximum output power is theoretically derived in this section, considering different types of excitations (harmonic and random). Table 7.1 summarizes the optimal electrical load that maximizes the output power in different scenarios and the corresponding assumptions.

Table 7.1 Optimal conditions for output power in different scenarios

Structural type	Excitation	Load impedance
SDOF/MODF (weak coupling)	Harmonic	Equation (7.8)
	Random[1]	Equation (7.18b)
SDOF (strong coupling)	Harmonic	Equation (7.10)
	Random[1]	Equation (7.16b)
MDOF (strong coupling)	Harmonic	Equation (7.21)
	Random[2]	Equation (7.18b)

Note: 1. The coil inductance is assumed to be negligible.

2. The coil inductance and structural inherent damping are assumed to be negligible.

7.5 Numerical Validation

7.5.1 Simulink Model

This section introduces the dynamic simulations of SDOF and 2DOF energy harvesters. Figure 7.8 shows the simulation model of the SDOF harvester established in the Matlab/Simulink environment. The time step was set as 10^{-4} s to guarantee accurate circuit signals. The EMD was modeled using the measured parameters of a real linear-motion EM device (Moticont, model No. GVCM-095-051-01) in Chapter 3: machine constant K_{eq} = 38 N/A, parasitic damping coefficient c_p = 32.4 N·s/m, coil resistance R_{coil} = 9.3 Ω, and coil inductance L_{coil} = 5 mH. The influence of such a small coil inductance is often negligible in low-frequency vibrations. In the numerical simulations described in this chapter, the coil inductance was ignored unless otherwise stated. Depending on the sign of the optimal reactance value χ_{load}, either a load capacitor or a load inductor should be connected. Two types of ground motion, harmonic and random, were separately applied to the concerned energy harvesters. The inherent damping of the structure was ignored; thus, $P_{ex} = P_{in}$ in the numerical validation.

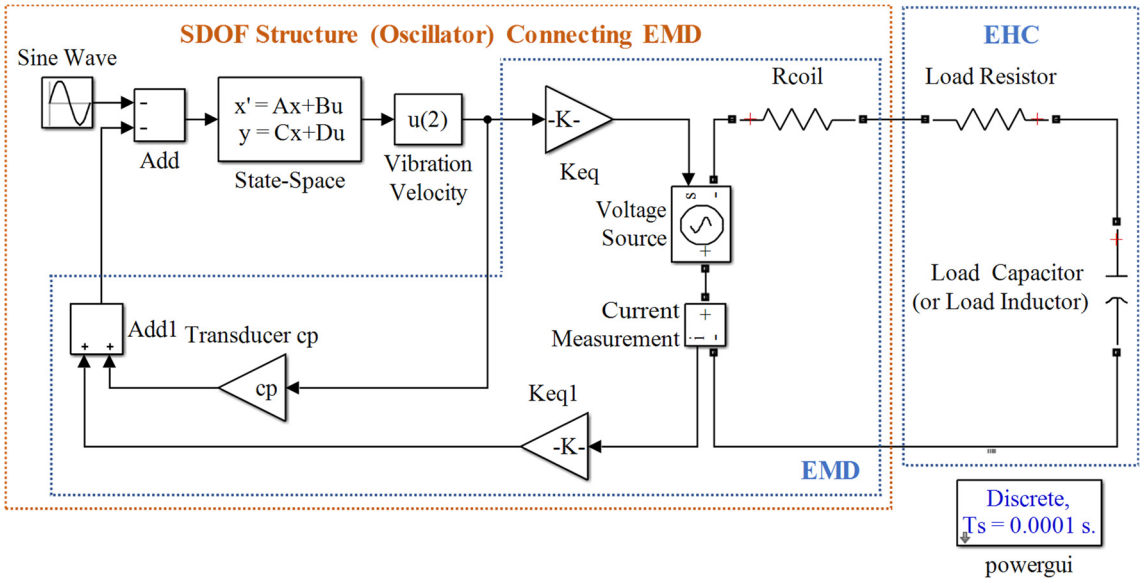

Figure 7.8 Simulink model for the SDOF energy harvester

The 2DOF energy harvester was simulated in a way similar to the SDOF energy harvester simulation. Table 7.2 lists the main parameters of the numerical models and

excitations for the SDOF and 2DOF energy harvesters. The mass and stiffness were determined to be compatible with the selected machine constant. Cases 1 and 2 represent the resonant and non-resonant cases of the SDOF energy harvester. Cases 4 and 5 represent the resonant and non-resonant cases of the 2DOF energy harvester, where the resonant case corresponds to the second frequency. The harmonic excitation frequencies and the natural frequencies in these cases are shown in Figure 7.9. Cases 3 and 6 represent the cases for white noise excitation with sufficiently broad frequency bands.

Table 7.2 Main parameters of the harvesters and excitation

Structural types		Parameters	Value
SDOF	Structural parameters	Structural mass, m_{str}	3 kg
		Structural stiffness, k_{str}	10^3 N·m^{-1}
		Natural frequency, f_{res}	2.91 Hz
	Excitation cases	Case 1, harmonic, f_{ex}	2.91 Hz
		Case 2, harmonic, f_{ex}	2.50 Hz
		Case 3, random, f_{ex}	0–500 Hz
2DOF	Structural parameters	Structural mass, m_{str_2}	0.8 kg
		Structural stiffness, k_{str_2}	300 N·m^{-1}
		Structural mass, m_{str_1}	8 kg
		Structural stiffness, k_{str_1}	3 kN·m^{-1}
		1st-order resonant frequency, f_{res_1}	2.63 Hz
		2nd-order resonant frequency, f_{res_2}	3.61 Hz
	Excitation cases	Case 4, harmonic, f_{ex}	3.61 Hz
		Case 5, harmonic, f_{ex}	3.50 Hz
		Case 6, random, f_{ex}	0–500 Hz

7.5.2 Optimal Impedance Results

Figure 7.9 shows the variations of optimal load resistance R_{load} and reactance χ_{load} based on the overall IM (i.e., Equations (7.10) and (7.21), respectively) for the maximum output power under harmonic excitation. The optimal values of the two parameters (R_{load} and χ_{load}) are functions of the excitation frequency. In Figure 7.9(a), the curve shapes of

the resistance and reactance are symmetrical and anti-symmetrical, respectively. At the resonant frequency, the optimal resistance was maximum, whereas the optimal reactance was nearly zero. In Figure 7.9(b), the number of peaks in the optimal resistance is equal to the number of DOFs. In the SDOF and 2DOF cases, the varying optimal resistance had a low bound of R_{coil} = 9.3 Ω, which was determined based on the classical IM without considering the structural impedance (i.e., Equation (7.3a)). The required reactance is realized in the simplest way by connecting either an inductor or a capacitor in the output circuit.

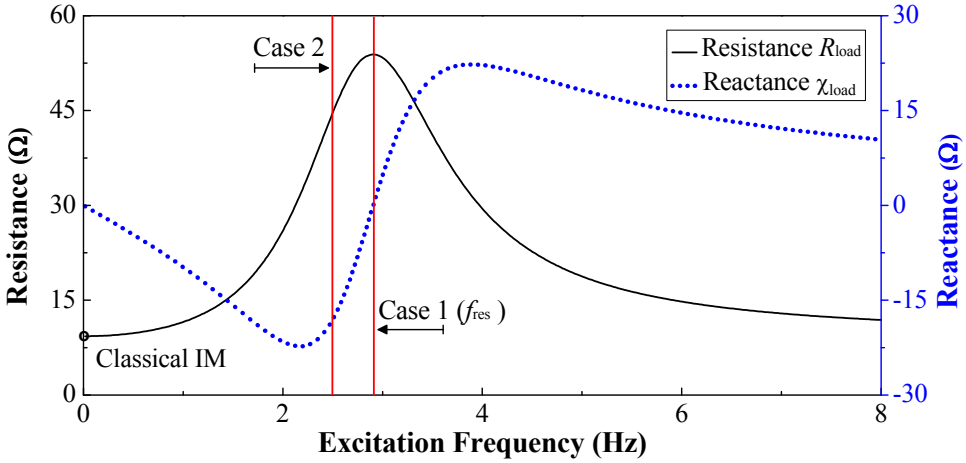

(a) SDOF energy harvester

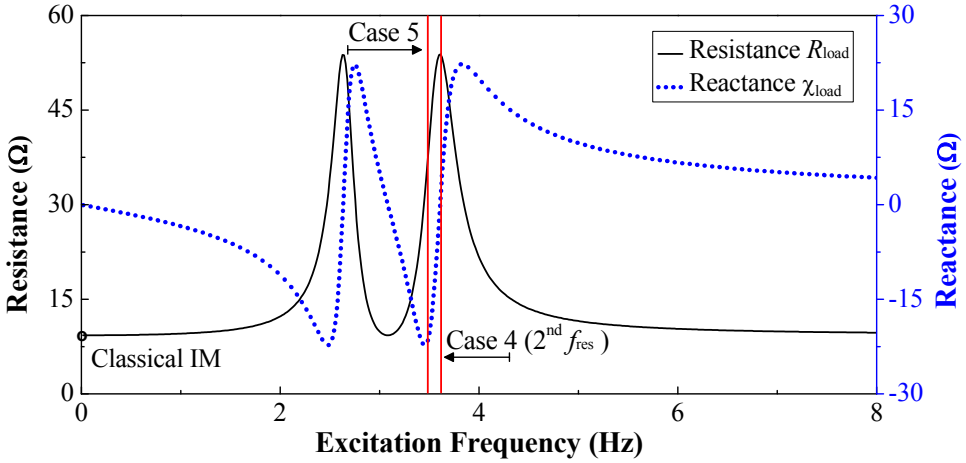

(b) 2DOF energy harvester

Figure 7.9 IM results for harmonic excitation, depicting the frequency dependence of the optimal impedance

Figure 7.9 highlights the frequencies corresponding to Cases 1, 2, 4, and 5. The corresponding optimal values for the output power can be read as follows:

$$\text{Case 1, Equation (7.12):}\quad R_{\text{load}} \approx 54\,\Omega,\quad \chi_{\text{load}} \approx 0\,\Omega \tag{7.23a}$$

$$\text{Case 2, Equation (7.10):}\quad R_{\text{load}} \approx 45\,\Omega,\quad \chi_{\text{load}} \approx 18\,\Omega \tag{7.23b}$$

$$\text{Case 4, Equation (7.12):}\quad R_{\text{load}} \approx 54\,\Omega,\quad \chi_{\text{load}} \approx 0\,\Omega \tag{7.23c}$$

$$\text{Case 5, Equation (7.21):}\quad R_{\text{load}} \approx 40\,\Omega,\quad \chi_{\text{load}} \approx 20\,\Omega \tag{7.23d}$$

Under random excitation (Cases 3 and 6), the optimal resistance is determined for the maximum efficiency as follows:

$$\text{Optimal efficiency, Equation (7.18):}\quad R_{\text{load}} \approx 22.4\,\Omega,\quad \chi_{\text{load}} \approx 0\,\Omega \tag{7.24}$$

which is frequency-independent.

In another case, the classical IM is also considered for comparison in the following subsection:

$$\text{Classical IM:}\quad R_{\text{load}} = R_{\text{coil}} = 9.3\,\Omega,\quad \chi_{\text{load}} \approx 0\,\Omega \tag{7.25}$$

7.5.3 Simulation Results of SDOF Harvester

7.5.3.1 Case 1: Resonant SDOF Harvester

In Case 1, the SDOF energy harvester was subjected to a harmonic excitation, whose frequency equaled to the resonant frequency of the mechanical structure. Figure 7.10(a) illustrates the variations of P_{in} and P_{out} with the load resistance R_{load} in Case 1. The total input power P_{in} increased monotonically with the load resistance, whereas the output power curve exhibited a peak value. The load resistance R_{load} = 54 Ω corresponded to the maximum output power P_{max} = 28.7 mW, which validates the theoretical prediction by Equation (7.23a). The optimal output power of the overall IM was significantly enhanced by 100% compared with the result for the classical IM, as shown by the dashed line. This comparison demonstrates that during the impedance optimization in vibration-based energy harvesting, the primary structure and EMD must be considered, rather than

directly implementing the classical IM.

Figure 7.10(b) shows the variations of power efficiency with the load resistance. The maximum power efficiency did not occur simultaneously with the maximum output power owing to the varying input power. The maximum power efficiency occurred when the resistance R_{load} was equal to 22 Ω, which agrees well with the theoretical prediction by Equation (7.24). The efficiency reached only 41% because the relatively large parasitic damping and coil resistance were considered in this numerical model.

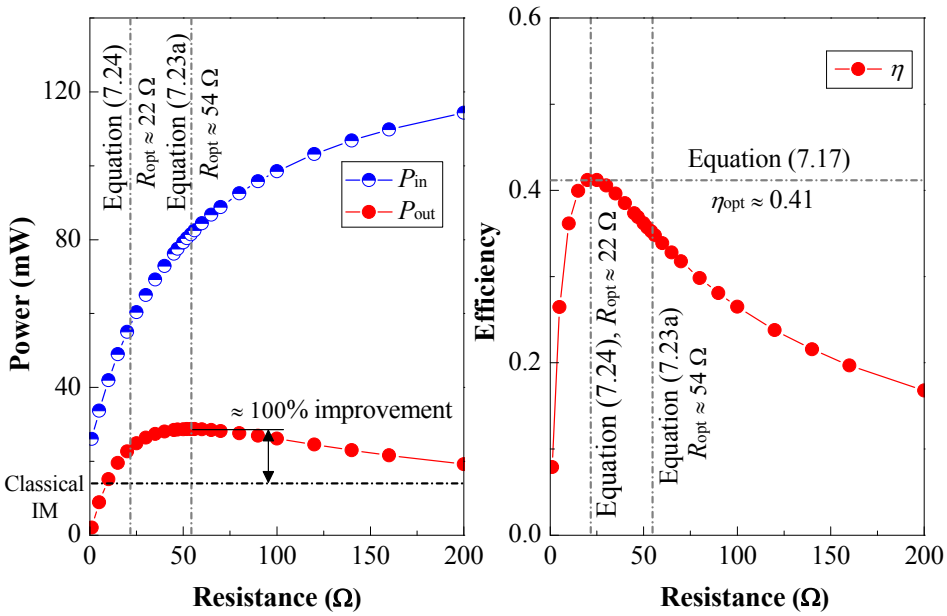

(a) Input and output power (b) Power efficiency

Figure 7.10 Energy harvesting performance vs. R_{load} in a resonant state for SDOF energy harvester

7.5.3.2 Case 2: Non-resonant SDOF Harvester

In Case 2, the SDOF energy harvester was subjected to a harmonic excitation, whose frequency was less than the structural resonant frequency. As mentioned in Subsection 7.5.2, the optimal impedance for output power can be predicted as R_{load} = 45 Ω and χ_{load} = 18 Ω (C_{load} = 3.5 mF). Figures 7.11 and 7.12 show the corresponding harvesting performance under the fixed optimal resistance and capacitance, respectively. The output power varied significantly with the increasing load resistance when the capacitance was

fixed; however, after the output power reached its peak value, it was insensitive to the capacitance and only dropped slightly with the further increase in capacitance. This insensitivity was mainly due to the large parasitic damping and coil resistance considered for the EMD. The effect of the optimal capacitance should be evident when a significantly small parasitic damping and coil resistance are adopted.

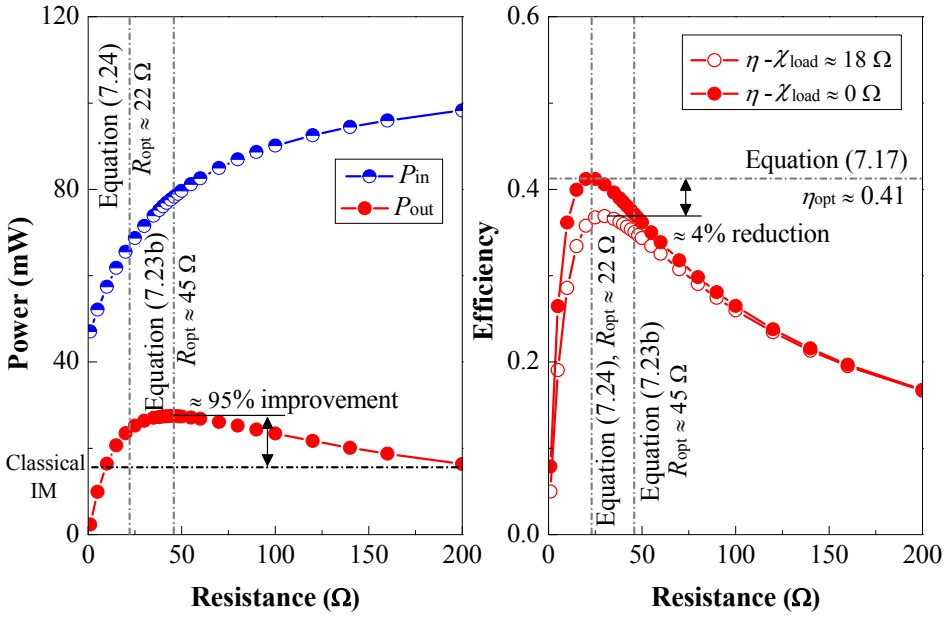

(a) Input and output power (b) Power efficiency

Figure 7.11 Energy harvesting performance vs. R_{load} in a non-resonant state for the SDOF harvester

The optimal output power when the overall IM framework was adopted (Figure 7.11(a) was approximately 95% higher than that when the classical IM was adopted. Figure 7.11(b) shows the variations of power efficiency with the load resistance R_{load} under load reactance of 18 and 0 Ω. Both curves indicate that the optimal load resistance for the maximum output power did not correspond to the maximum power efficiency. The existence of the reactance in the load slightly decreased the peak power efficiency, and the maximum power efficiency (i.e., 41%) occurred in a pure resistive load circuit when R_{load} = 22 Ω, as predicted by Equation (7.24).

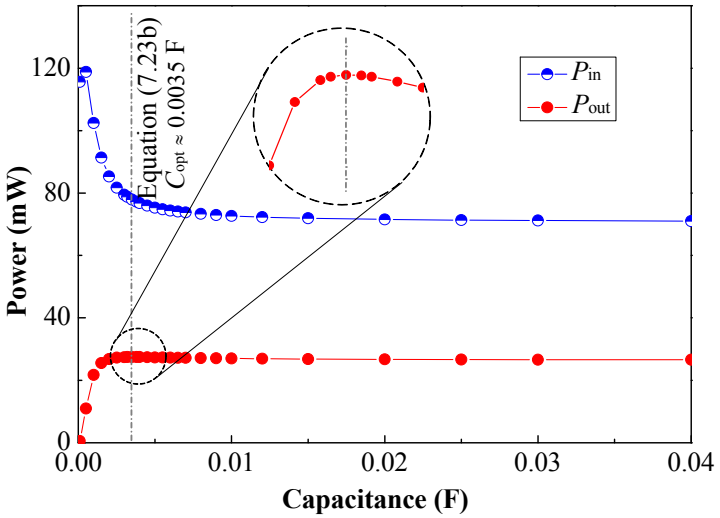

Figure 7.12 Input and output power vs. C_{load} in a non-resonant state for the SDOF energy harvester

7.5.3.3 Case 3: Randomly Excited SDOF Harvester

A pure load resistance R_{load} = 22 Ω was adopted when the SDOF energy harvester was subjected to a broadband random ground motion. Figure 7.13 shows the PSD of the input ground acceleration, which represents a white noise input. This excitation bandwidth ranged from 0 to 500 Hz with a constant PSD value of approximately 0.01 $(m/s^2)^2/Hz$.

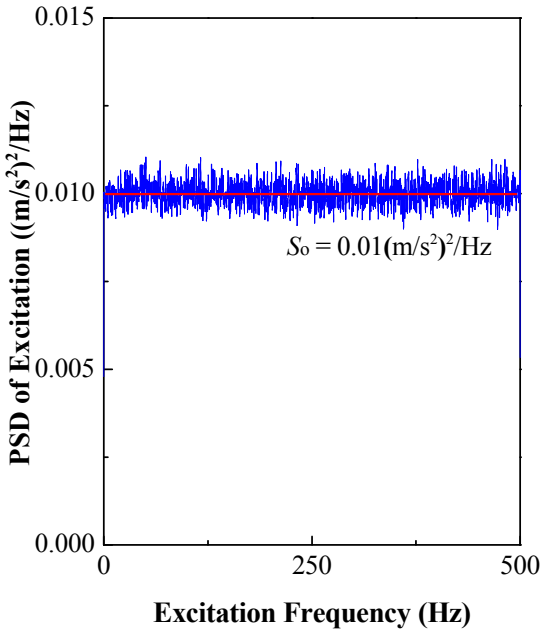

Figure 7.13 PSD of the random ground acceleration

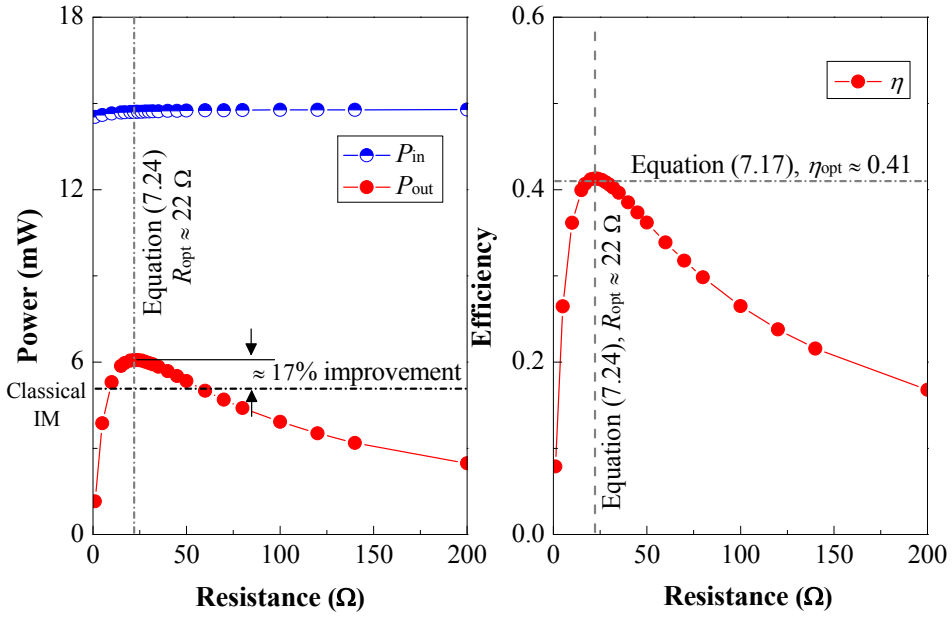

(a) Input and output power (b) Power efficiency

Figure 7.14 Energy harvesting performance vs. R_{load} in random excitation for the SDOF harvester

Figure 7.14 illustrates the output power and power efficiency variations with the load resistance in Case 3. The total input power P_{in} was nearly constant, as predicted, and was independent of the load resistance change. Consequently, the maximum output power and power efficiency occurred simultaneously when the load resistance $R_{load} = 22$ Ω, and the maximum power efficiency was 41%. These results accurately agree with the prediction in Subsection 7.5.2. The output power when the optimal load resistance was adopted was 17% higher than that when the classical IM was adopted. This improvement demonstrates the benefit of using the proposed optimal impedance for power efficiency in designing vibration-based EM energy harvesters under random excitation. The classical IM cannot provide an optimal solution for the output power and power efficiency.

7.5.4 Simulation Results of 2DOF Harvester

This subsection presents the simulation results of the 2DOF energy harvester under different excitations. As the 2DOF structure represents a more general case compared with the SDOF one, additional parametric analyses are included in this subsection to

examine the effects of different factors.

7.5.4.1 Cases 4 and 5: Harmonically Excited 2DOF Harvester

Case 4 presents the resonant case in which the 2DOF energy harvester was excited with a harmonic frequency equal to its second-order natural frequency. The optimal impedance values for the output power and power efficiency were 54 and 22 Ω, respectively. The observations in the energy harvesting performance are similar to those reported for Case 1 and thus are not reported here. The output power determined with the overall IM was nearly twice that determined with the classical IM.

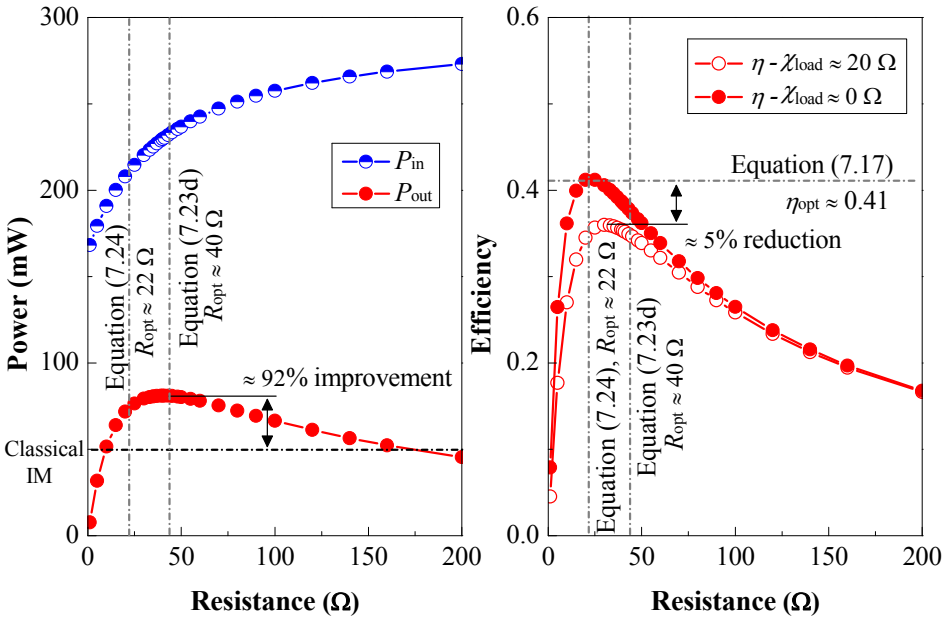

(a) Input and output power (b) Power efficiency

Figure 7.15 Energy harvesting performance vs. R_{load} in a non-resonant state for the 2DOF harvester

Case 5 represents the non-resonant case with an excitation frequency of 3.5 Hz. The theoretical optimal impedance for the output power was 40 Ω and 2.2 mF, while the optimal impedance for the power efficiency was 22 Ω. The observations are similar to those for Case 2 (Figure 7.15). The maximum output power and power efficiency did not occur simultaneously under harmonic excitation. The power efficiency when a capacitor was connected to the system was lower than that under a pure resistive circuit.

Cases 4 and 5 show the energy harvesting performance of two individual frequencies. By applying the overall IM strategy to other harmonic frequencies of excitations, the energy harvesting performance over the frequency range can be obtained. Figure 7.16 presents the FRF of the normalized output power obtained through a series of simulations. The envelope corresponding to the classical IM is also illustrated for comparison. In comparison with the classical IM, the overall IM strategy can significantly improve the output power, especially near the resonant range, under harmonic excitation. This comparison demonstrates the importance of load impedance optimization in the performance of vibration-based energy harvesters.

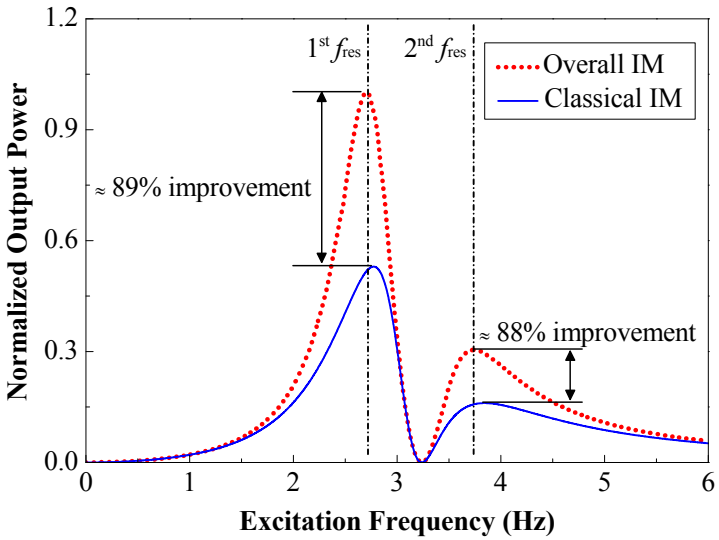

Figure 7.16 Overall tuning performance: 2DOF harvester

7.5.4.2 Case 6: Randomly Excited 2DOF Harvester

Under random excitation, the optimal impedance values for the maximum output power and power efficiency are identical (i.e., Equation (7.24)). Figure 7.17 shows the corresponding energy harvesting performance under random ground motion, wherein the ground acceleration is the same as that described in Subsection 7.5.3.3. The variations of energy harvesting performance are similar to those of the SDOF harvester in Case 3. The optimal output power and power efficiency occurred at the predicted location. The power was approximately 17% higher than that corresponding to the classical IM. This result demonstrates the effectiveness of the proposed optimal impedance optimization for the

MDOF energy harvester under random excitation.

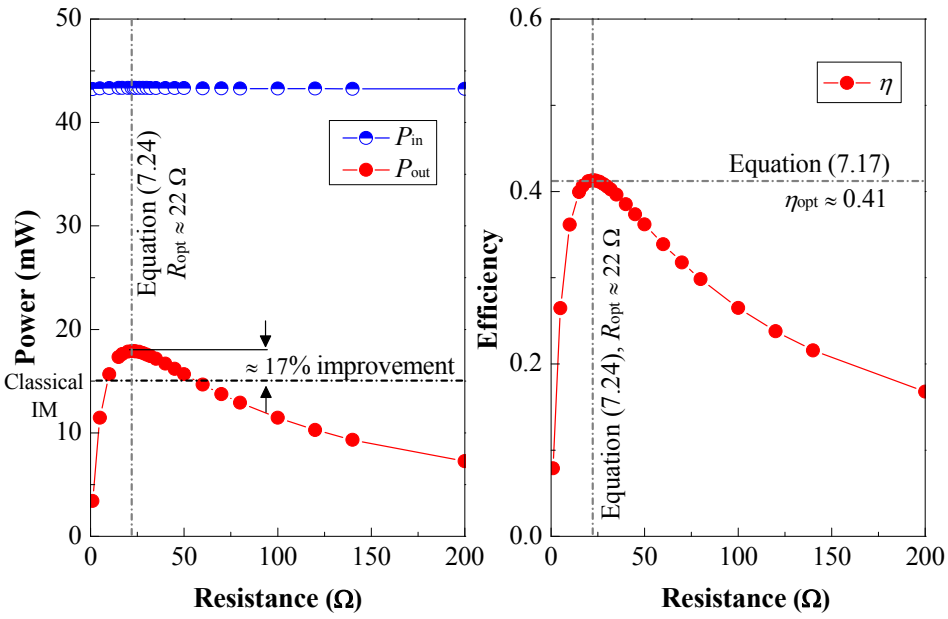

(a) Input and output power (b) Power efficiency

Figure 7.17 Energy harvesting performance vs. R_{load} under random excitations for the 2DOF harvester

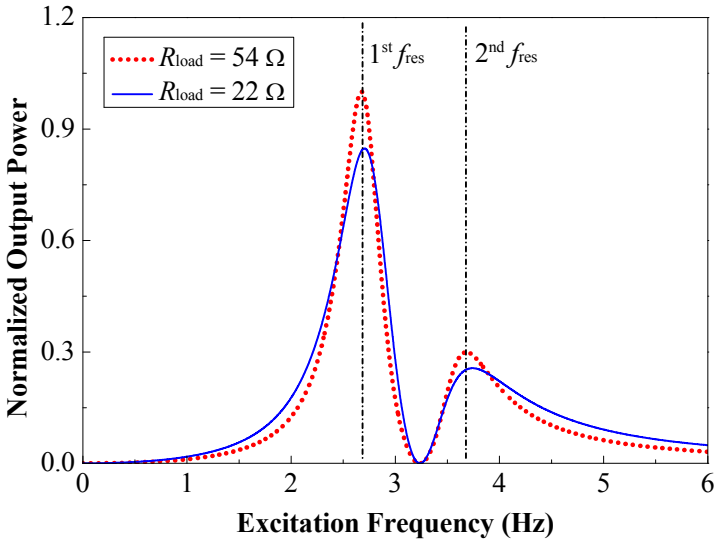

Figure 7.18 Output power FRF comparison for the 2DOF harvester

Although the random ground motion is approximately white noise, the vibration of the 2DOF system remains dominated by the natural frequencies. Specifically, the input to the EMD is a filtered signal, which is no longer white noise. If the vibration is dominated

by the natural frequencies, the question is whether the optimal impedance setting for a resonant state is adoptable for a random case or not. Figure 7.18 compares the output power FRFs under the optimal impedance settings for resonance (i.e., Equation (7.23c)) and random excitation (i.e., Equation (7.24)). The former produced higher power corresponding to the resonant peaks than the latter. However, the optimal impedance defined in Equation (7.24) led to a 13.6% improvement in the total output power compared with Equation (7.23c) when considering the area under the curves, which represents the total output power under random excitation. This result demonstrates the necessity and benefit of adopting different optimal impedance settings for a random case, as proposed in this chapter, instead of an optimal impedance setting for resonance.

7.5.4.3 Effect of Structural Inherent Damping

The structural inherent damping was ignored in the aforementioned numerical case studies. This subsection examines the effect of structural inherent damping (i.e., R_{str}) on the optimal impedance and output power, by using Case 4 as an example.

In Case 4, for the second-order resonance, Equation (7.23c) shows the optimal impedance if structural inherent damping is neglected. With the consideration of structural inherent damping, the optimal impedance values and output power changed as the inherent damping ratio of the mechanical structure increased (Figure 7.19). A large damping ratio led to a large discrepancy in the output power (Figure 7.19(b)). However, the structural inherent damping ratio must be minimized with consideration of power efficiency in real applications. For a low damping ratio (e.g., second-order damping ratio $\zeta_{str\_2} < 4\%$), the difference in output power was minimal (5% error). Similar results occurred in the random excitation case. These observations justify that slight structural damping can typically be ignored in the aforementioned numerical simulations.

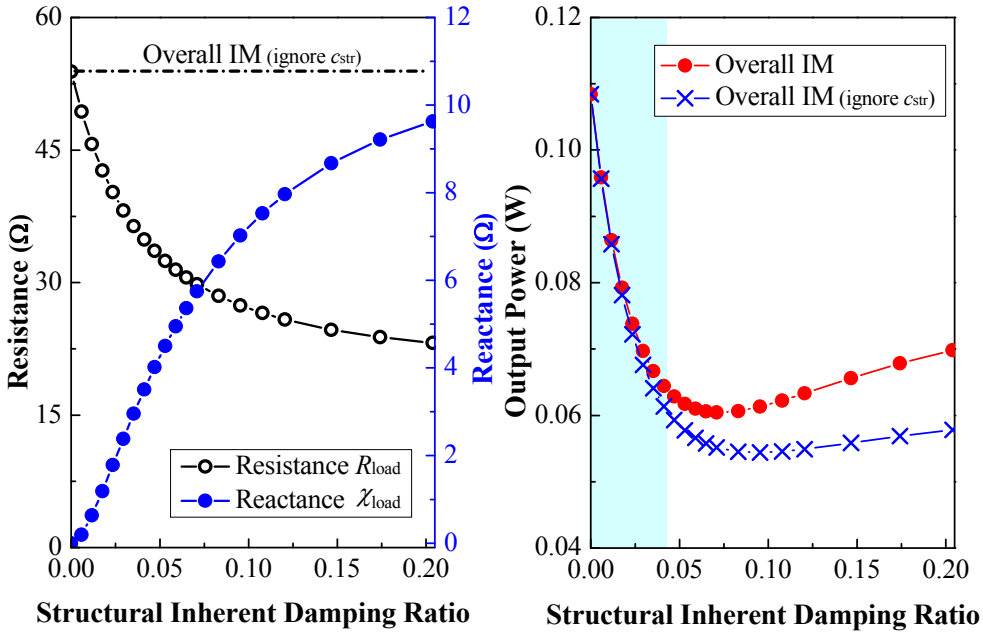

(a) Optimal impedance (b) Output power

Figure 7.19 Influence of inherent damping under harmonic excitation

7.6 Summary

This chapter presents a unified strategy for overall impedance optimization considering the structural and electrical dynamics in vibration-based EM energy harvesters. General equivalent circuit models of SDOF or MDOF harvesters were developed. Subsequently, the corresponding optimal impedance for the maximum output power and power efficiency was theoretically derived, considering different types of excitations (harmonic and random). Numerical case studies were conducted to validate the effectiveness and accuracy of the proposed overall impedance optimization. Based on the results of the theoretical derivation and numerical simulations, the following major conclusions can be drawn:

1) The classical IM in power electronics cannot guarantee realization of the maximum output power in vibration-based EM energy harvesters with a strong coupling effect between electrical and mechanical systems.
2) The dynamic analogy between mechanical and electrical systems enables the representation of an SDOF or MDOF energy harvester using an equivalent circuit

model. This equivalent representation provides a convenient and straightforward tool for optimizing the load impedance of the EHC.

3) Under harmonic excitation, the overall IM, which considers the equivalent impedance of the primary structure and EMD, can achieve the maximum output power in vibration-based energy harvesters. The corresponding optimal impedance values are thus frequency-dependent.
4) Under harmonic excitation, the maximum output power does not correspond to the maximum power efficiency. The optimal solution for the maximum power efficiency is dependent on structural inherent damping and EMD parasitic damping. Incorporating reactance in the harvesting circuit may degrade the power efficiency. Thus, a pure resistive circuit is preferable from the power efficiency perspective.
5) Under random excitation, the maximum output power and power efficiency can be achieved simultaneously, given the relatively low damping level of the primary structure of an energy harvester. Therefore, the optimal impedance for the maximum power efficiency can be applied in a random excitation case. Such optimal impedance is frequency-independent if the coil inductance is negligible.
6) If the inherent damping of an energy harvester structure is low, then neglecting structural inherent damping in the overall impedance optimization will have a minimal influence on the energy harvesting performance under harmonic or random excitation.

It is noteworthy that the energy harvesting performance can be enhanced by adjusting either the electrical or mechanical systems. This chapter only focuses on the optimization of the electrical impedance of EHCs. However, given the equivalent conversion between the mechanical structures and electric circuits, the proposed methodology in this chapter will also shed light on the optimal design of the mechanical part.

CHAPTER 8

DMP-BASED ENERGY HARVESTER

8.1 Introduction

This chapter proposes a DMP-based energy harvester with a tunable ultra-low frequency range (<1 Hz), in which the frequency tuning function is realized by relocating the two individual masses, and an unpractical pendulum length for ultra-low frequency is avoided, overcoming the shortcomings of traditional pendulums. The proposed device is still a resonant-type SDOF energy harvester. The DMP-based harvester was designed to (1) validate the overall impedance optimization theory of the SDOF configuration in Chapter 7 and (2) serve as an ultra-low-frequency vibration oscillator in the floating-point absorber studied in Chapter 9.

Ocean wave frequencies vary significantly in the range of 0.1–1 Hz, which often considered an ultra-low frequency range in mechanical vibrations (Liu et al., 2019; Toffoli and Bitner-Gregersen, 2017). As reviewed in Chapter 2, although various design configurations have been proposed to generate resonance at low frequencies (Fan et al., 2019; Wu et al., 2018; Li and Jing, 2019), most of them were intended for vibrations caused by human movements (~1 Hz) and machinery vibrations (<10 Hz). Few can realize ultra-low natural frequencies (<1 Hz), even with frequency tuning technologies. Thus, an energy harvester with an ultra-low natural frequency (<1 Hz) is highly desirable for WECs.

This chapter first presents the conceptual design and basic dynamics of the DMP-

based energy harvester. The small-amplitude assumption is adopted, and its effect on the power estimation error is discussed accordingly. A corresponding fabricated prototype was tested through free vibration and shake table tests. In the free vibration test, the mechanical frequency tuning performance and the softening nonlinear characteristics were evaluated. Subsequently, in the shake table test, the optimal impedance for different excitation types was determined to validate the overall impedance optimization theory and clarify the impedance selection in the next chapter. During the shake table test, the EHC described in Chapter 3 was applied to verify the practical energy harvesting performance. Finally, the major conclusions of this chapter are summarized.

8.2 Development of DMP-based energy harvester

8.2.1 Conceptual Design

The natural frequency formula f_s of a simple gravity pendulum is given by:

$$f_s = \frac{1}{2\pi}\left(\frac{g}{l}\right)^{1/2} \tag{8.1}$$

where l is the pendulum length. An impractically long pendulum length is required in this configuration to achieve a low frequency (e.g., 25 m for 0.1 Hz). In this regard, a traditional simple pendulum is not suitable for a low-frequency oscillator in WECs.

Figure 8.1 shows the conceptual design of the DMP, which is composed of two independent masses installed on a common vertical screw bar. An EMD is connected to the rotating shaft and converts vibration energy into electrical energy. Meanwhile, the EMD also exerts parasitic and EM damping forces on the shaft (Zhu et al., 2012). Despite their similar names, the DMP and the double pendulum consisting of two masses with a joint connection (Shinbrot et al., 1992) are different types of devices. The former, which is investigated in this thesis, is an SDOF electromechanical coupling structure, whereas the latter is a 2DOF nonlinear device.

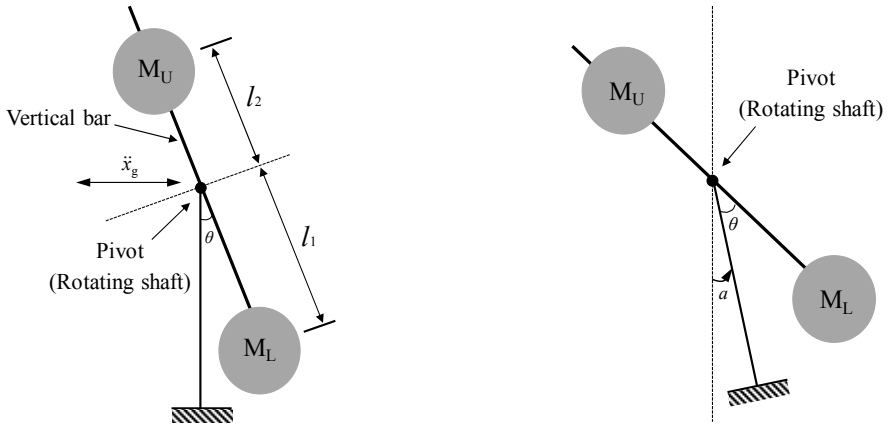

(a) Horizontal base motion (b) Tilt base motion

Note: θ is the relative degree of rotation; $\ddot{x}_g$ is the horizontal base acceleration; a is the tilt base motion; and l_1 and l_2 are the distances from the centroids of the lower and upper masses to the pivot, respectively.

Figure 8.1 Conceptual design of the DMP

8.2.2 Principle

8.2.2.1 Horizontal Base Motion

Considering two identical masses (i.e., $M_U = M_L = m_m$) and that the SDOF pendulum is subjected to horizontal base motion, the governing equation of the DMP-based energy harvester can be obtained using the Lagrange method as follows:

$$m_m\left(l_1^2+l_2^2\right)\ddot{\theta}+\frac{m_b l_3^2\ddot{\theta}}{2}+m_m g\left(l_1-l_2\right)\sin\theta+\left(c_{str}+c_p\right)\left(l_1^2+l_2^2\right)\dot{\theta}+K_{em}i=-m_m\ddot{x}_g\left(l_1-l_2\right)\cos\theta \tag{8.2}$$

where l_1 and l_2 are the absolute distances from the centroids of the lower and upper masses to the pivot, respectively; m_m is the mass of each block; m_b is half the mass of the vertical bar; c_{str} and c_p are the inherent and parasitic damping coefficients, respectively; K_{em} is the machine constant of the EMD, with the unit V·s/rad or N·m/A; $\ddot{x}_g$ is the base acceleration; and θ represents the rotation degree, which is the only DOF of the DMP-based energy harvester. In addition, l_3 is half the length of the vertical bar. Considering that l_1 is for the lower mass, we have $l_2 < l_1 < l_3$ in general. The detailed derivation of Equation (8.2) is

given in Appendix 8.5.1.

Defining the effective length l_e as:

$$l_e = \left(l_1^2 + l_2^2\right)^{1/2} \tag{8.3}$$

and assuming a small vibration amplitude (i.e., $\sin\theta \approx \theta$), Equation (8.2) can be linearized as:

$$m_s l_e \ddot{\theta} + c_t l_e \dot{\theta} + k_s l_e \theta = -\frac{m_m \ddot{x}_g \left(l_1 - l_2\right)}{l_e} \tag{8.4}$$

where

$$m_s = m_m + \frac{m_b l_3^2}{2 l_e^2} \tag{8.5a}$$

$$k_s = m_m g \frac{\left(l_1 - l_2\right)}{l_e^2} \tag{8.5b}$$

$$c_t = c_{str} + c_p + \frac{K_{eq}^2}{R_{coil} + R_{load}} \tag{8.5c}$$

$$K_{eq} = \frac{K_{em}}{l_e} \tag{8.5d}$$

where m_s, k_s, and c_t are the equivalent mass, stiffness, and damping of the SDOF structure, respectively; K_{eq} is the equivalent machine constant corresponding to the linear motion, with the unit V·s/m or N/A; R_{coil} is the coil resistance of the EMD; and R_{load} is the load resistance. Notably, the effect of L_{coil} is negligible, considering its small value and the ultra-low vibration frequencies of interest. The load connected to the EMD should be optimized to maximize the output power. According to the derivation in Chapter 7, the optimal load impedance under a resonant condition should be a pure resistance. Therefore, the load reactance is not considered in Equation (8.5c). Notably, in determining the optimal load impedance in a non-resonant state, the load reactance should be considered (see Equation (7.10)).

The frequency of the DMP-based energy harvester with the small-amplitude assumption can be expressed as follows:

$$f_s = \frac{1}{2\pi}\left(\frac{2m_m g\left(l_1 - l_2\right)}{2m_m l_e^2 + m_b l_3^2}\right)^{1/2} \tag{8.6}$$

If the vertical bar mass is negligible, Equation (8.6) can be approximated as:

$$f_s = \frac{1}{2\pi}\left(\frac{g\left(l_1 - l_2\right)}{l_e^2}\right)^{1/2} \tag{8.7}$$

Consequently, the frequency of the DMP can be easily tuned by adjusting the relative positions (i.e., l_1 and l_2) of the two masses. And two nearly symmetrical masses make the theoretical frequency approach zero. This design can realize ultra-low frequencies with a reasonable pendulum length and thus overcome the deficiencies of traditional pendulums.

The corresponding input power P_{in} and the output power P_{out} of the DMP device are:

$$P_{in} = \frac{1}{t_2 - t_1}\int_{t_1}^{t_2} c_t\left(l_1^2 + l_2^2\right)\dot{\theta}^2 dt = \frac{-1}{t_2 - t_1}\int_{t_1}^{t_2} m_m \ddot{x}_g\left(l_1 - l_2\right)\dot{\theta} dt \tag{8.8}$$

$$P_{out} = \frac{1}{t_2 - t_1}\int_{t_1}^{t_2} i^2 R_{load}\, dt \tag{8.9}$$

where i denotes the instantaneous current passing the coil and load resistance, and t_1 and t_2 are the start and end times of the measurement, respectively. The output power is used to evaluate the power extraction performance in this chapter and the next chapter.

8.2.2.2 Tilt Base Motion

Similarly, the governing equation of the DMP-based energy harvester subjected to tilt base motion can be obtained using the Lagrange method as follows:

$$\begin{aligned}&\left(m_m\left(l_1^2 + l_2^2\right) + \frac{m_b l_3^2}{2}\right)\ddot{\theta} + m_m g\left(l_1 - l_2\right)\sin\left(\theta + a\right) + \left(c_s + c_p\right)\left(l_1^2 + l_2^2\right)\dot{\theta} + K_{em} i \\ &= -\left(m_m\left(l_1^2 + l_2^2\right) + \frac{m_b l_3^2}{2}\right)\ddot{a}\end{aligned} \tag{8.10}$$

where a is the tilt degree of the base. The detailed derivation of Equation (8.10) is given in Appendix 8.5.2. Assuming a small tilt angle and vibration amplitude, i.e., $\sin(\theta + a) \approx (\theta + a)$, Equation (8.10) can be rewritten as follows:

$$m_s l_e \ddot{\theta} + k_s l_e \theta + c_{s+em} l_e \dot{\theta} = -m_m g l_e \left(\frac{l_1 - l_2}{l_1^2 + l_2^2} \right) a - m_s l_e \ddot{a} \tag{8.11}$$

The expressions of natural frequency and output power are the same as Equations (8.6) and (8.9), respectively, but the input power items are modified as follows:

$$P_{in} = \frac{1}{t_2 - t_1} \int_{t_1}^{t_2} c_{s+em} \left(l_1^2 + l_2^2 \right) \dot{\theta}^2 dt = \frac{-1}{t_2 - t_1} \int_{t_1}^{t_2} \left[m_m g \left(l_1 - l_2 \right) a + m_s \ddot{a} \left(l_1^2 + l_2^2 \right) \right] \dot{\theta} dt \tag{8.12}$$

8.2.2.3 Numerical Modeling

Based on the governing equations (i.e., Equations (8.2) and (8.10)), Figures 8.2 and 8.3 show the FRFs of the vertical bar rotation degree θ of the DMP-based harvester subjected to horizontal and tilt base motions, respectively, wherein the adopted modeling parameters were set to be the same as those of the prototype mentioned in the next subsection. An open circuit and constant parasitic damping coefficient of 1.1 N·s/m were assumed in the modeling. As shown in Figure 8.2, the DMP-based energy harvester exhibited rather softening nonlinearity in the case of relatively larger vibration amplitudes. Specifically, the frequency corresponding to the peak degree shifted from 1.00 to 0.91 Hz with increasing excitation amplitudes from 0.15 to 0.25 g. Notably, this nonlinear effect can be effectively reduced when the vibration amplitude is reduced by introducing EM damping.

In the case of tilt base motion, the FRFs of the rotation degree of the DMP-based energy harvester showed a totally different shape from those of the horizontal input. It showed a relatively larger response at low frequencies, whereas an extremely low response occurred near the resonant state. This phenomenon can be explained by Equation (8.11); that is, under a constant tilt acceleration amplitude input, the excitation item related to the tilt degree a corresponds to an extremely large value at a low frequency

and decreases with increasing frequency. Consequently, the response decreases with increasing frequency. Meanwhile, the excitation item related to the tilt acceleration $\ddot{a}$ results in a similar response, as represented by the shapes of the curves in Figure 8.2. Considering that the signs of the tilt degree a and acceleration $\ddot{a}$ are naturally opposite, the equivalent excitations corresponding to the two terms on the right side of Equation (8.11) essentially are mutually eliminated, leading to an extremely low response that occurs near the resonant frequency.

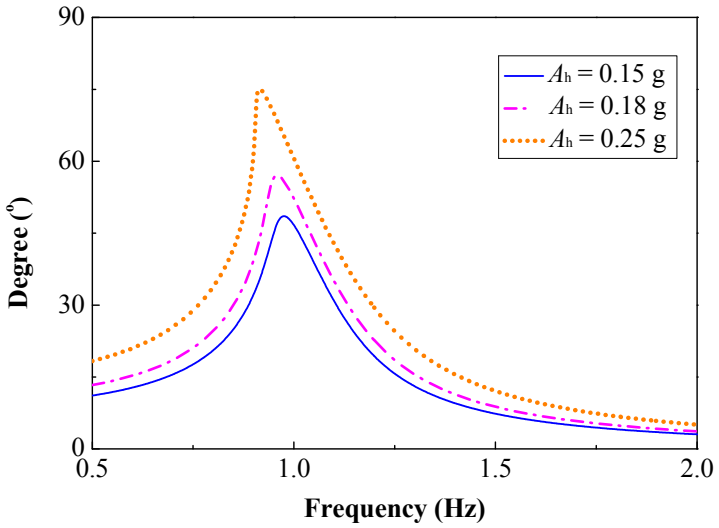

Note: A_h is the amplitude of horizontal base acceleration.

Figure 8.2 FRFs of a DMP-based harvester subjected to horizontal base motion

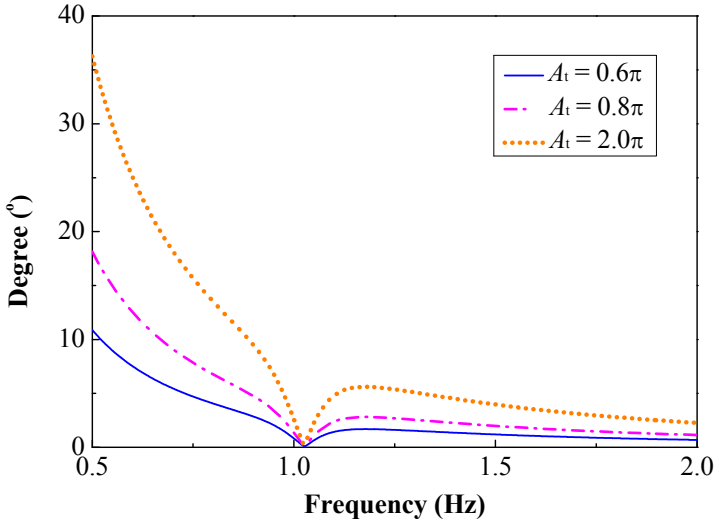

Note: A_t is the amplitude of tilt base degree.

Figure 8.3 FRFs of a DMP-based harvester subjected to tilt base motion

Notably, the effectiveness and accuracy of the numerical results of the DMP-based energy harvester subjected to tilt base motion still require further experimental validation on a 6DOF vibration platform. In the following sections, base motion refers to horizontal motion only, unless otherwise stated.

In Chapter 7, the analyzed EM energy harvester is limited to linear elastic structures, whereas the proposed DMP-based harvester is a softening nonlinear device. In this chapter, a small-amplitude assumption is adopted and its effect on the harvesting performance estimation is evaluated. Harmonic horizontal base motion with an amplitude of 0.18 g and constant parasitic damping of 1.1 N·s/m were applied in the following modeling process, regardless of resonant or non-resonant states.

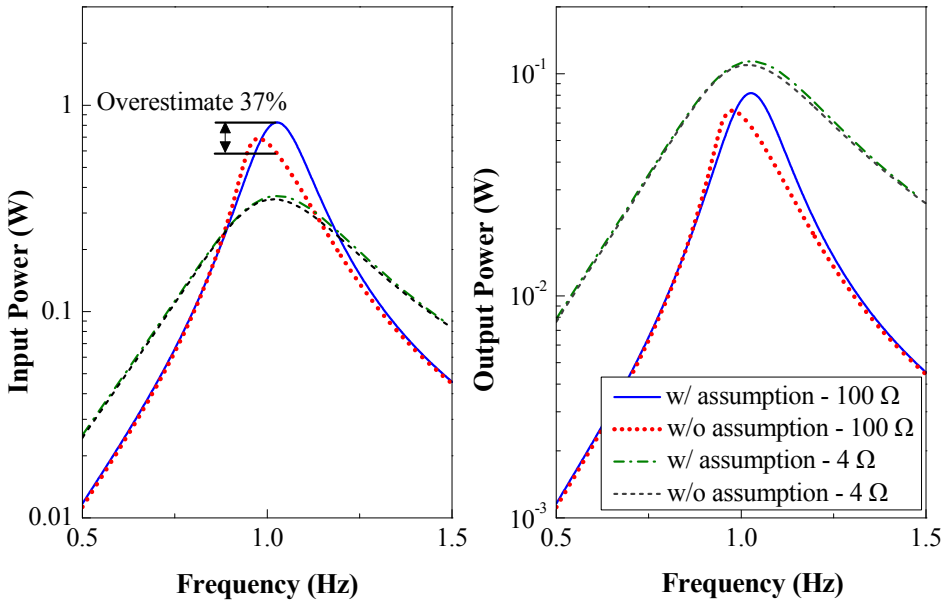

(a) Input power (b) Output power

Note: "w/o assumption" denotes that the nonlinear characteristic is considered.

Figure 8.4 Power FRF comparison of a DMP-based harvester with and without the small-amplitude assumption

Figure 8.4 compares the corresponding input and output power FRFs without and with the small-amplitude assumption, in which the term "w/o assumption" represents the practical device with nonlinear characteristics. Two different load resistances, 4 and

100 Ω, representing small and large load resistances, respectively, were considered in the modeling. It can be observed that such an assumption generally led to an overestimated input power and output power, particularly near the initial resonant state where the input power overestimation was as high as approximately 37% with a load resistance of 100 Ω. Nevertheless, when a smaller resistance corresponding to a larger EM damping was used, the power difference between the models with and without assumption was negligible. Furthermore, in both models, the curves of the input power FRFs connecting smaller resistances (corresponding to larger EM damping) were apparently much flatter, exhibiting much lower power amplitude near the initial resonant frequency than those with larger resistances. Conversely, the output power FRFs of both models with $R_{load} = 100\ \Omega$ were always below those of models with 4 Ω considering the power efficiency.

Figure 8.5 further illustrates the effect of load resistance in a nearly resonant state. Although the input powers of both models gradually became more stable at larger load resistances, the model with the small-amplitude assumption likely exhibited a sharper increasing trend. With such a trend, the relative error between both models became more evident with increasing load resistance. The reason for this difference is that a relatively larger vibration amplitude of the nonlinear DMP (connecting a larger load resistance) results in frequency detuning; consequently, the preset nearly resonant state cannot be guaranteed perfectly. As a result, the input power and output power decrease. These results demonstrate that the assumption of small-vibration amplitude for a DMP-based harvester introduces a relatively larger error into the energy harvesting estimation in the case of large load resistance.

The two key tunable parameters of the DMP-based energy harvesters, namely the natural frequency and the load resistance, were investigated in the following context. The frequency tuning function is validated in Subsection 8.2.3 through the free vibration tests of the DMP. Subsequently, the impedance optimization theory is validated in Section 8.3

through shake table tests of the DMP-based energy harvester connected to various load impedances. In the free vibration and shake table tests, the theoretical performance refers to the results obtained via modeling under the assumptions of small amplitude and constant parasitic damping. The power analyses in this subsection can also be regarded as error analyses.

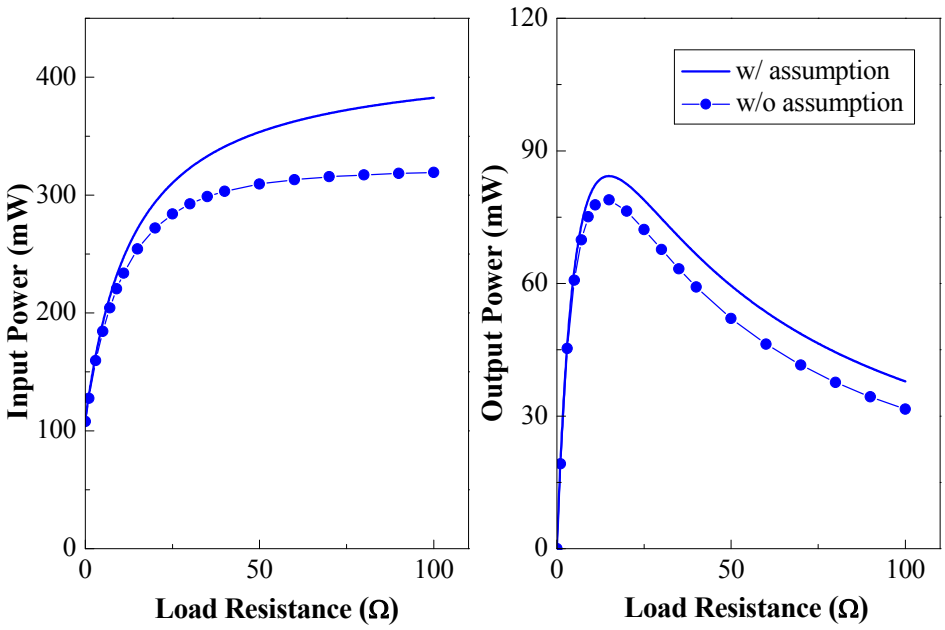

(a) Input Power (b) Output Power

Figure 8.5 Power performance comparison of a DMP-based harvester with and without the small-amplitude assumption: nearly resonant state

8.2.3 Parameters Characterization

Figure 8.6 shows the exploded view drawing of the fabricated DMP-based energy harvester, of which the main parameters are listed in Table 8.1. The coil resistance and inductance of the gearhead EMD (model No. Crouzet 8980A1-1) were identified as 3.74 Ω and 3 mH, respectively, using an LCR meter (model No. Hioki 3522-50). As aforementioned, the effect of coil inductance was neglected considering the relatively small value and low vibration frequencies in this study. A calibration test was conducted on a drilling machine to obtain the actual machine constant and parasitic damping of the EMD (Figure 8.7). Different rotational velocities were applied in this test, and the

corresponding measured reaction torque and open-circuit voltage are shown in Figure 8.8. The identified machine constant was approximately 0.48 V·s/rad, and the parasitic damping torque owned an initial value (0.035 N·m) and exhibited a nearly linear relationship with the rotational velocity. Although the parasitic damping coefficient strongly depended on the vibration amplitude, frequency, initial torque, and viscous damping coefficient (Zhu et al., 2012), it was estimated simply as a constant for each vibration scenario. For example, the parasitic damping coefficient was approximately 1.1 N·s/m in the 1 Hz resonant state.

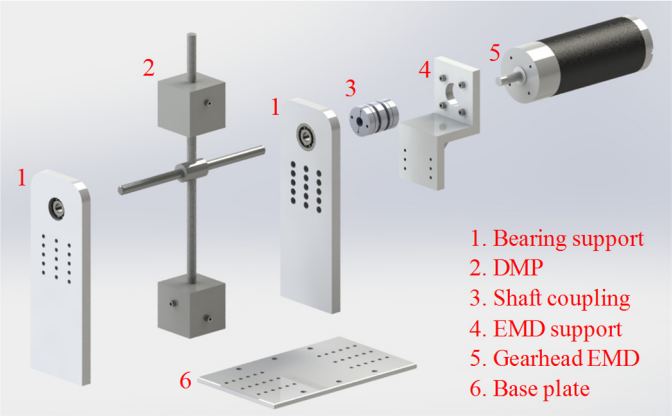

Figure 8.6 Exploded view drawing of the DMP-based harvester

Table 8.1 Main parameters of DMP-based energy harvester

Items	Value
Half the length of the vertical bar, l_3	150 mm
Half the mass of the vertical bar, m_b	0.1 kg
Individual mass, m_m	0.947 kg
Movement distance, l_1, l_2	35–125 mm
Inherent damping, c_{str}	ignored
Coil resistance, R_{coil}	3.74 Ω
Coil inductance, L_{coil}	3 mH
Machine constant, K_{em}	0.48 V·s/rad

Equation (8.6) reveals that the natural frequency of the DMP-based energy harvester can be tuned effectively by adjusting the lengths l_1 and l_2. Figure 8.9 shows the frequency

tuning results obtained in free vibration tests with an open circuit. During the tests, only the upper mass position l_2 was tuned, and the lower mass was fixed at one end of the vertical bar (l_1 = 0.125 m). The horizontal axis of Figure 8.9 represents the upper mass location l_2, in which the zero position corresponds to the pivot location, and the negative value denotes the scenarios where the upper mass is moved to the same side as the lower mass. Owing to the physical constraint that prevented the installation of the mass close to the pivot, the position range of −35 to 35 mm could not be tested. But it did not affect the illustration of the desirable frequency tuning function of the DMP. Two experimental curves in Figure 8.9 correspond to the DMP with the EMD disconnected and connected. The legend "w/EMD" means the case with an EM transducer in an open-circuit condition. Through the mass position tuning, the experimentally tested DMP achieved ultra-low frequencies down to 0.5 and 0.2 Hz, respectively, when the EMD was and was not connected. In general, the theoretical and experimental results agreed acceptably, regardless of whether the EMD was connected or not. The result demonstrates that the EMD installation did not significantly affect the concerned frequency performance. The free vibration test results demonstrate that the DMP-based energy harvester could realize the frequency tuning function and effectively cover the frequency range <1 Hz.

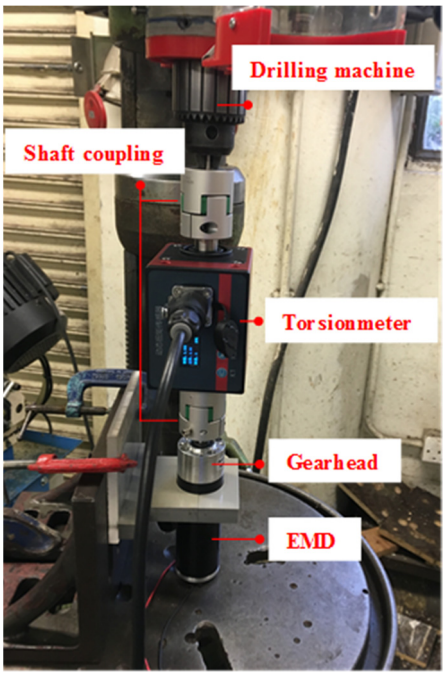

Figure 8.7 Parameter calibration of the gearhead EMD

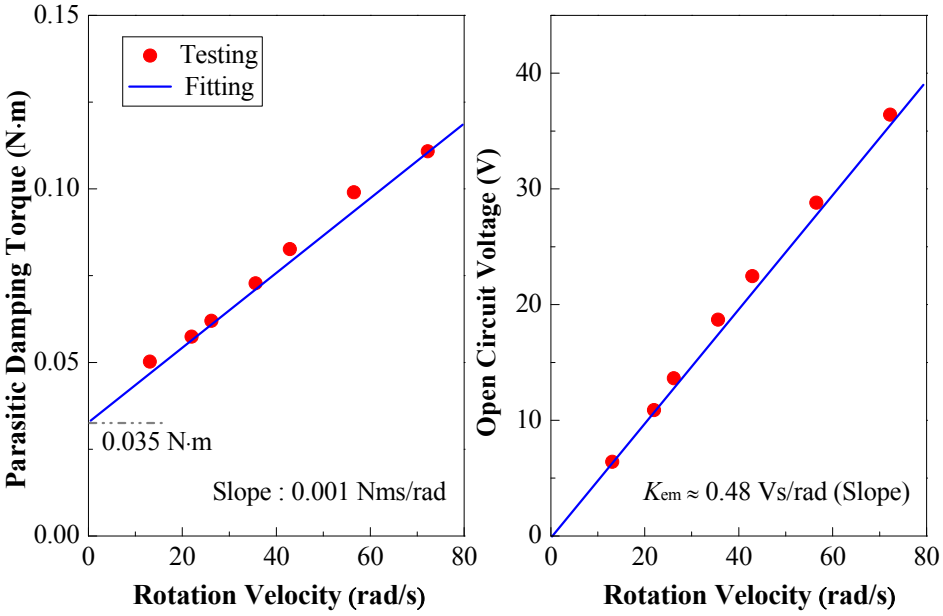

(a) Parasitic damping torque (b) Open-circuit voltage

Figure 8.8 Parasitic torque and open-circuit voltage vs. rotational velocities

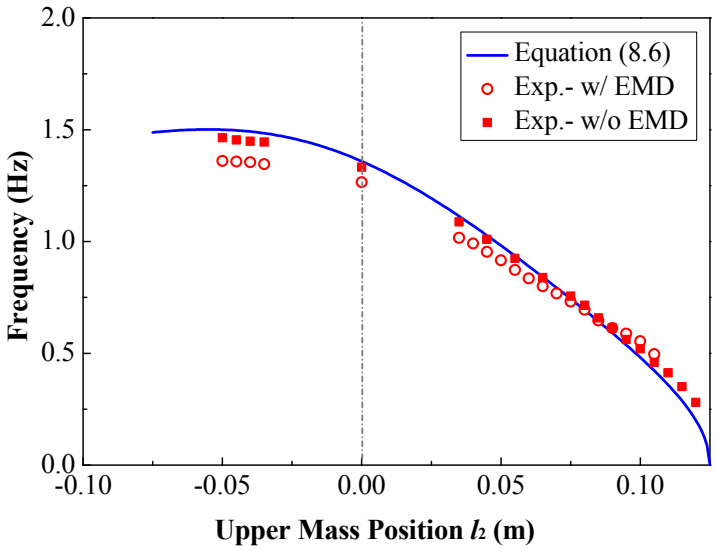

Figure 8.9 Frequency vs. location of the upper mass

Figure 8.10 shows a representative displacement time history of the lower mass under a free vibration test, in which l_1 and l_2 were set as 0.125 m and 0.045 m, respectively. The average frequency was estimated as 0.996 Hz based on the total duration of the first 20 cycles. More accurate transient frequency can be quantified from the backbone FRF obtained by using the Hilbert transform approach (Feldman, 2011), as shown in Figure 8.11. The DMP exhibited slight-softening nonlinear behavior with an increasing

vibration amplitude: the frequency changed from 1.02 to 0.98 Hz when the vibration amplitude increased to approximately 87 mm. This implies that the linearization in Equations (8.4) and (8.6) based on the small-amplitude assumption became slightly inaccurate with increasing amplitude. The slight-softening nonlinearity would not considerably affect the frequency tuning and optimal impedance determination. Furthermore, the addition of EM damping may weaken the nonlinearity. In general, the proposed DMP-based energy harvester is regarded to be suitable for WECs owing to its ultra-low-frequency tuning feature.

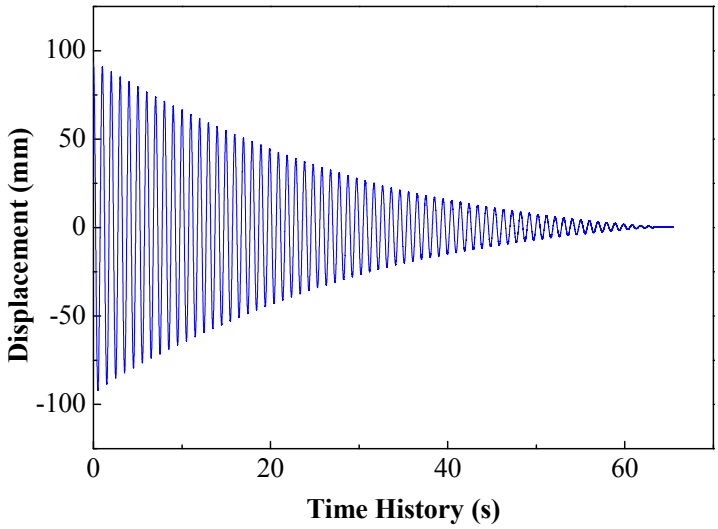

Figure 8.10 Time history of free vibration without connecting EMD

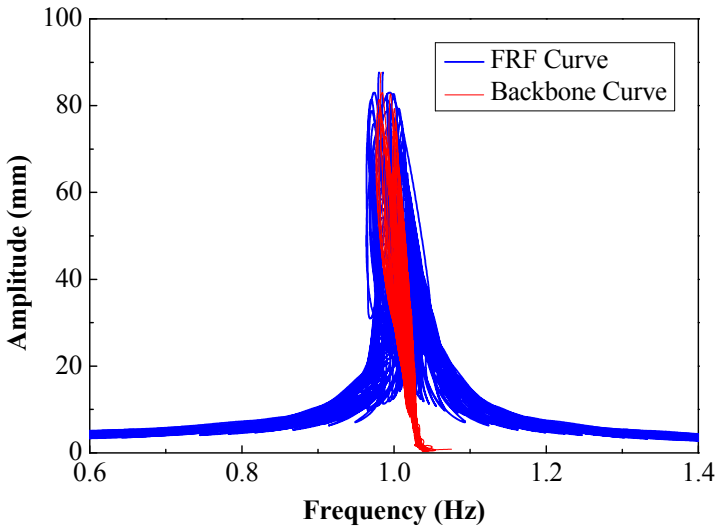

Figure 8.11 Backbone FRF corresponding to Figure 8.10

8.3 Shake Table Test

8.3.1 Experiment Setup

Shake table tests of the fabricated DMP-based energy harvester were performed to evaluate its power extraction performance. Figure 8.12 shows the experimental photo of the DMP-based energy harvester on the shake table test. The control signal generated by a digital signal generator (model No. SRS 35) was fed into a power amplifier (model no. APS 145) and then used to drive the shake table (model No. APS 420). Two uniaxial accelerometers (model No. KD1010) were attached to the lower mass and base to measure the accelerations of the mass and shake table, respectively. A resistance decade box (model No. DR04) was used to provide variable resistance. The acceleration responses were collected by a KYOWA data acquisition system (model No. EDX-100A) with a sampling frequency of 1000 Hz, whereas the voltage and current signals in the power extraction circuit were collected using an oscilloscope (model No. DPO 4104B-L) with a sampling frequency of 100 Hz. The current flowing through the load resistor was used to evaluate the output power performance. The shake table input was a base excitation with an acceleration amplitude of 0.18 g.

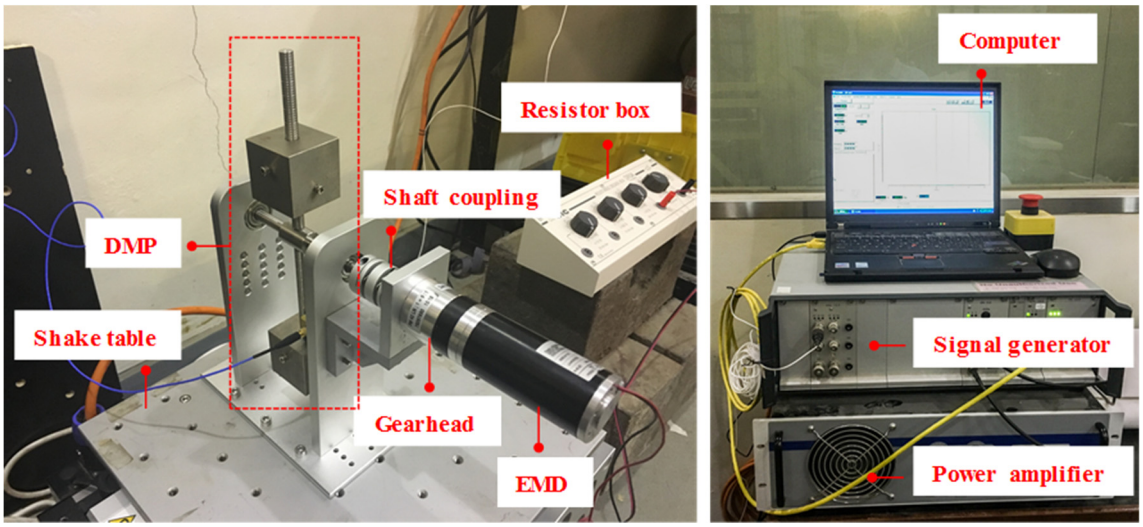

Figure 8.12 Shake table test setup

8.3.2 Optimal Impedance Validation

As aforementioned, the DMP-based energy harvester is regarded as an approximate

resonant-type harvester. The experimental search for the optimal impedance, i.e., the validation of Equation (7.10), was conducted in this subsection.

8.3.2.1 Harmonically Excited Harvester

Given a harmonic excitation of 1 Hz, the distances l_1 and l_2 were set as 125 mm and 45 mm, respectively, according to the previous free vibration tests (Figure 8.9), to realize a resonant state. Figure 8.13 shows the corresponding output power performance with varying load resistance. It can be seen that the classical IM, i.e., $R_{load} = R_{coil} = 4\ \Omega$, could not provide optimal output power owing to the electromechanical coupling effect. The actual optimal output power corresponded to $R_{load} \approx 15\ \Omega$, which agrees well with the theoretically predicted value of 16 Ω based on Equation (7.12). The maximum output power of nearly 78 mW was approximately 82% improvement in comparison with that of classical IM. The experimental results were generally lower than the analytical curve, as predicted in the last subsection (see Figure 8.5). This is because a linear elastic system (small-amplitude assumption) with constant parasitic damping c_p was assumed in the analytical prediction. In the shake table tests, the practical parasitic damping showed the dependence on the frequency and amplitude (Zhu et al., 2012). The complex parasitic damping and slightly softening nonlinearity resulted in the performance degradation. But corresponding to the peak point of the curve, the analytically predicted optimal load resistance and maximum output power still exhibited satisfactory accuracy. The difference in the maximum output power between the experimental and analytical results was only 7%. For comparison, the theoretical nonlinear result considering constant parasitic damping was also plotted in Figure 8.13, which was much closer to the experimental results than the linear prediction.

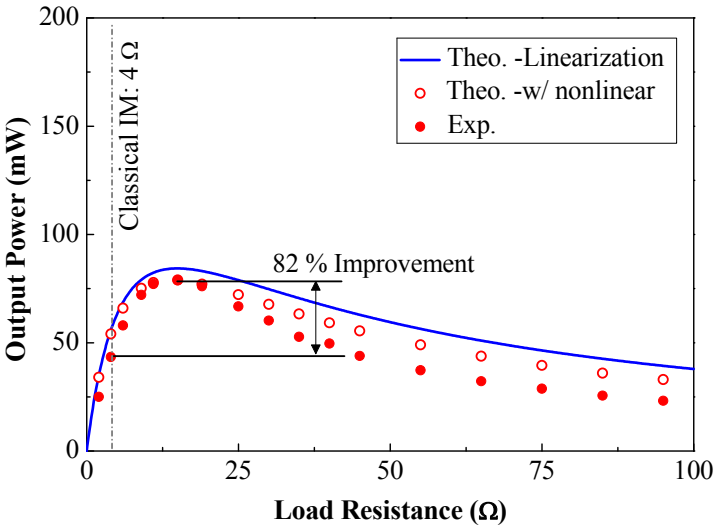

Figure 8.13 Output power vs. load resistance in nearly resonant state

At the non-resonance state with excitation frequency f_{ex} = 1.1 Hz, the parasitic damping increased to approximately 2.3 N·s/m owing to the reduction in vibration amplitude. Figure 8.14(a) shows the corresponding harvesting performance versus pure load resistance. The output power significantly varied with increasing load resistance, reaching a peak at 9 Ω, which agrees with the theoretical prediction (i.e., 9 Ω) and represents a 26% improvement compared with the output power corresponding to the classical IM. As for the connection to load inductance with R_{load} = 9 Ω (see Figure 8.14(b)), the theoretical maximum output power occurred at $L_{load} \approx 0.28$ H (see the theoretical line), although the improvement was negligible. In the experiment, owing to the influence of the ESR of the applied inductor, the output power in this scene continuously decreased, shifting away from the analytical line. Notably, the power can be enhanced if a small coil resistance and parasitic damping are adopted.

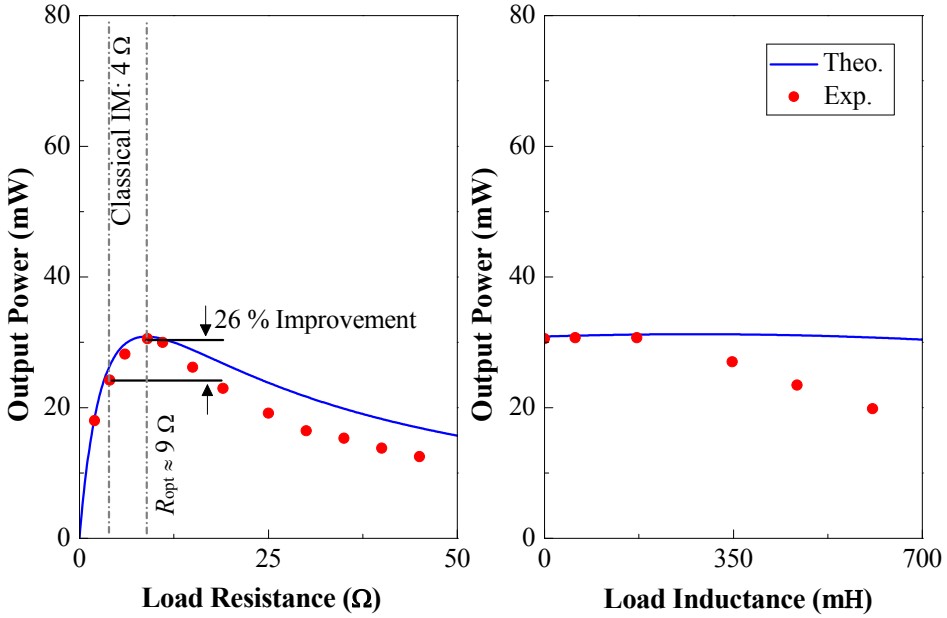

(a) Resistance (b) Inductance

Figure 8.14 Output power vs. load impedance in non-resonance state

8.3.2.2 Randomly Excited Harvester

Figure 8.15 shows the time history and PSD of the input random base excitation. This excitation bandwidth ranged from 0.7 to 3.5 Hz with a constant PSD value of approximately 0.35 $(m/s^2)^2/Hz$. Figure 8.16 illustrates the corresponding performance under random excitation. The optimal output power in this scene was merely 5 mW that corresponded to $R_{load} \approx 4$ Ω. It matched well with the classical IM because of the great parasitic damping (~8.5 N·s/m).

The shake table test results validate the efficacy of the impedance optimization theory in the DMP-based energy harvester. These results guide the optimal resistance selection in the following wave flume test in Chapter 9. The accuracy of numerical modeling can be further improved by considering the nonlinear vibrations and nonlinear parasitic-damping model.

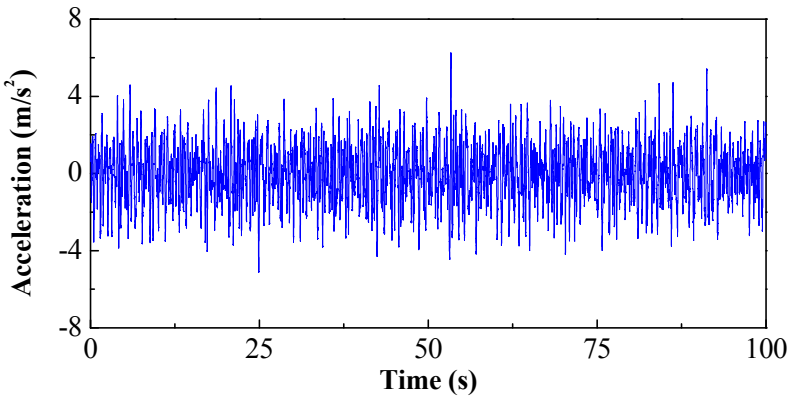

(a) Time history

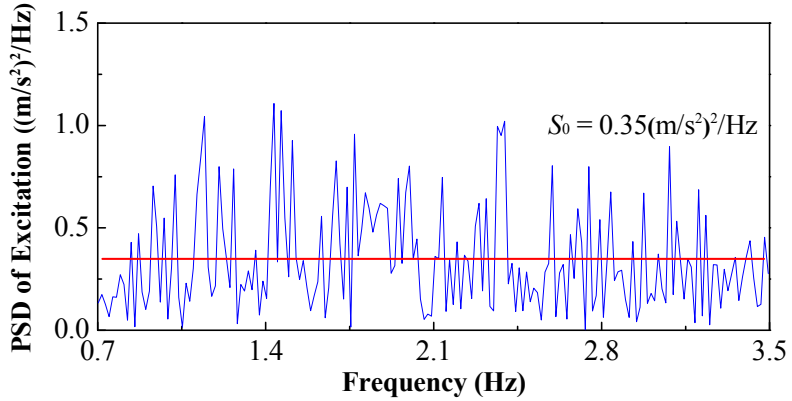

(b) PSD

Figure 8.15 Time history and PSD of input ground acceleration

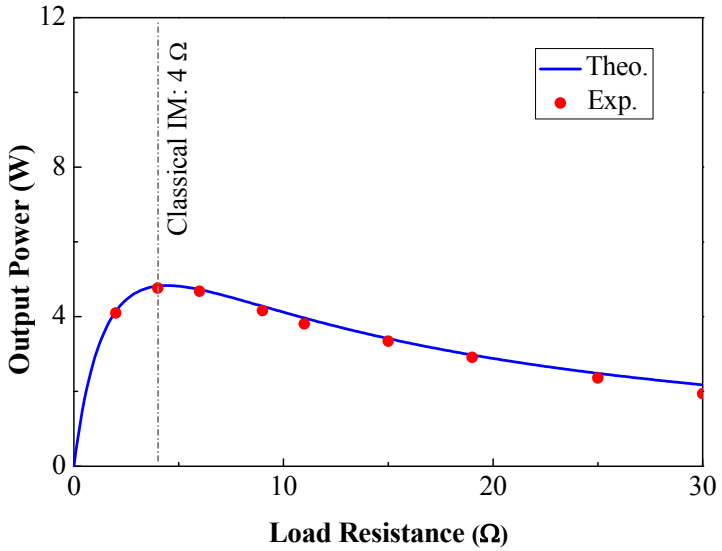

Figure 8.16 Output power vs. load resistance under random excitation

8.3.2.3 Buck–boost Converter

To examine the practical harvesting performance, the EHC introduced in Chapter 3 was utilized in this subsection. However, the major circuit parameters were redesigned. Considering the design resistance range, an inductance of 70 μH was applied. By setting a fixed duty cycle of 49%, the equivalent average resistance was set as approximately 15 Ω in DCM operation ($U_{\text{thres}} \approx 1.57$ V). In the DC input circuit test, Figure 8.17(a) shows the representative time history of the rectifier current in cases with a rectifier voltage of 1.46 V. The curve representing the rectifier current was likely a triangle instead of a trapezoid in each switching cycle, indicating that this converter operated in DCM. Correspondingly, Figure 8.17(b) presents the rectifier current in CCM in the case of a rectifier voltage of 5.4 V (much higher than the predicted voltages in the shake table tests). The current shapes resulting from these two scenarios were quite consistent with the introduction of DCM and CCM in Chapter 3.

Followed by the circuit test, the DMP-based energy harvester with the designed circuit was tested in the shake table. Figure 8.18 shows a typical time history (2 s) of the rectifier current and voltage in a resonance case. A larger rectifier current occurred when the rectifier voltage was relatively larger. The peak rectifier current was up to 0.26 A, and the average value was approximately 0.052 A. The equivalent resistance of the circuit behind the rectifier bridge was approximately 14.8 Ω. Notably, the switching frequency was much higher than that of the AC generated by the EMD; therefore, the instantaneous rectifier current can also be considered as DC during a switching period. The generated voltage before the rectifier was also plotted for comparison, and it was slightly larger than the rectifier voltage because of the voltage drop caused by the diodes.

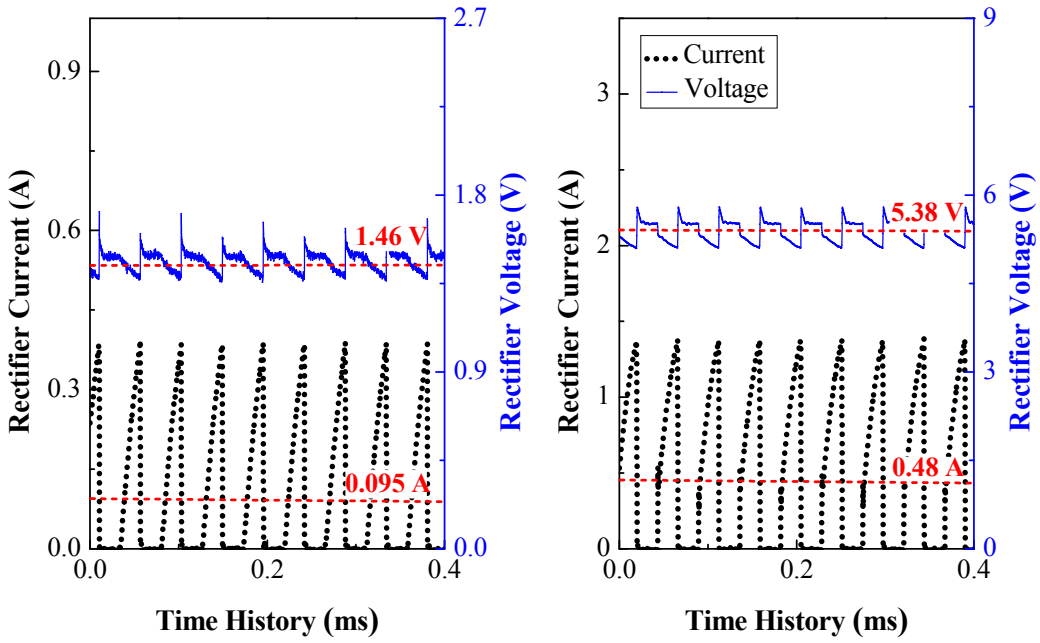

(a) DCM (b) CCM

Figure 8.17 Measured voltage and current under different operation modes

Table 8.2 Energy harvesting performance under the condition of EHC connection

	Duty cycle (%)	Resistance (Ω)	Output power (into battery) (mW)
Nearly resonant cases	48.9	14.8	21.7
Non-resonance cases	60.2	9.2	7.4
Random input cases	87.2	5.0	<1

In addition to the case of 15 Ω, other scenarios (i.e., 9 Ω for the non-resonance state and 4 Ω for the random case) were also considered in this experiment. Table 8.2 summarizes the energy harvesting performance and the average resistances in the shake table tests. With the optimal design, the average output powers (into the battery) in these three cases were 21.7, 7.4, and <1 mW, respectively. In almost all scenarios of the shake table tests, the EHC operated in DCM.

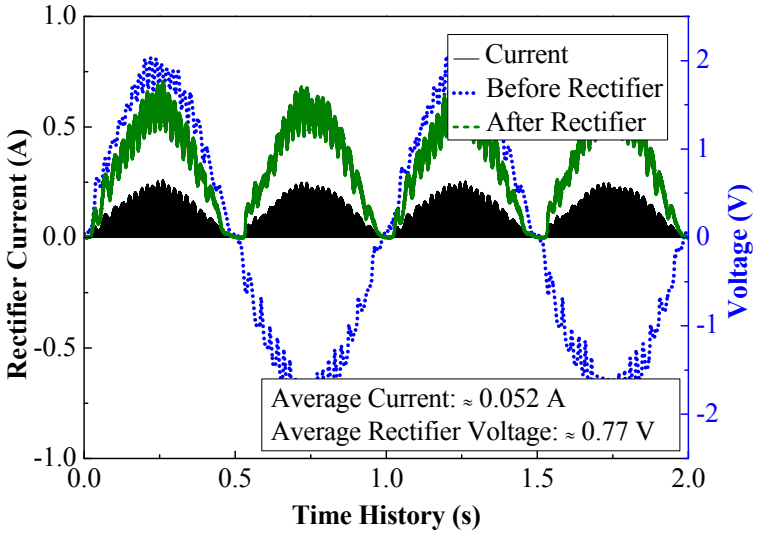

Figure 8.18 Typical time history of measured voltage and current in resonance state

8.4 Summary

This chapter presents a DMP-based energy harvester with tunable ultra-low frequencies that were realized by relocating the two independent masses in the DMP. The conceptual design and mechanism of the DMP-based energy harvester were introduced first. Then, the device was fabricated and tested successively through free vibration and shake table tests. The major conclusions are as follows:

1) The DMP-based energy harvester could realize the frequency tuning function in an ultra-low frequency range by adjusting the positions of the two independent masses. The tunable frequency range obtained in the free vibration tests was from 0.2 to 1.4 Hz, which is suitable for WECs.
2) The FRF of the DMP-based energy harvester subjected to tilt base motion showed an extremely large vibration amplitude at low frequencies but the lowest vibration amplitude in the nearly resonant state, which completely differs from the result of the harvester subjected to horizontal base motion. However, this result requires experimental validation.
3) The experimentally searched optimal impedance of the DMP-based energy harvester in the shake table tests showed satisfactory agreement with the theoretical prediction in Chapter 7, even though the assumptions of small amplitude and constant parasitic

damping introduced slight errors in power estimation. This finding also clarifies the impedance selection in the following wave flume tests in Chapter 9.

This device can also be employed as a low-frequency EHTMD for vibration control and energy harvesting simultaneously. In addition, the electrical tuning method cannot be successfully achieved in this chapter owing to the relatively large coil resistance and parasitic damping coefficient.

8.5 Appendix A: Derivation of Governing Equations for DMP

8.5.1 Horizontal Base Motion

Under horizontal base motions, the corresponding kinetic energy V, potential energy U, and dissipation energy D of the DMP-based energy harvester with an open circuit are given as:

$$V = \frac{1}{2}m_{\mathrm{m}}\left[\left(\dot{x}_{\mathrm{g}} + l_1\dot{\theta}\cos\theta\right)^2 + \left(l_1\dot{\theta}\sin\theta\right)^2\right] + \frac{1}{2}m_{\mathrm{m}}\left[\left(\dot{x}_{\mathrm{g}} - l_2\dot{\theta}\cos\theta\right)^2 + \left(l_2\dot{\theta}\sin\theta\right)^2\right] + \frac{1}{2}m_{\mathrm{b}}\left[\left(\dot{x}_{\mathrm{g}} + \frac{l_3}{2}\dot{\theta}\cos\theta\right)^2 + \left(\frac{l_3}{2}\dot{\theta}\sin\theta\right)^2\right] + \frac{1}{2}m_{\mathrm{b}}\left[\left(\dot{x}_{\mathrm{g}} - \frac{l_3}{2}\dot{\theta}\cos\theta\right)^2 + \left(\frac{l_3}{2}\dot{\theta}\sin\theta\right)^2\right] \tag{8.13}$$

$$U = -m_{\mathrm{m}}gl_1\cos\theta + m_{\mathrm{m}}gl_2\cos\theta \tag{8.14}$$

$$D = \frac{1}{2}\left(c_{\mathrm{str}} + c_{\mathrm{p}}\right)\left(l_1^2 + l_2^2\right)\dot{\theta}^2 + \left(c_{\mathrm{s}} + c_{\mathrm{p}}\right)\frac{l_3^2}{4}\dot{\theta}^2 \tag{8.15}$$

where θ represents the rotation degree; x_{g} is the base displacement; l_1 and l_2 are the absolute distances from the centroids of lower and upper masses to the pivot, respectively; l_3 and m_{b} are half the length and mass of the vertical bar, respectively; m_{m} is the mass of each block; and c_{str} and c_{p} are the inherent and parasitic damping coefficients, respectively. The specific values of these parameters of the DMP-based energy harvester are presented in Table 8.1. Assuming that the damping power of the two masses is dominant, the second term in Equation (8.15) is negligible. According to the Lagrange method, the corresponding governing equation is given as:

$$\frac{\partial}{\partial t}\left(\frac{\partial L}{\partial \dot{\theta}}\right)-\frac{\partial L}{\partial \theta}+\frac{\partial D}{\partial \dot{\theta}}=0 \tag{8.16}$$

where $L = V - U$. Then we have:

$$\left(m_{\mathrm{m}}\left(l_1^2+l_2^2\right)+\frac{m_b l_3^2}{2}\right)\ddot{\theta}+m_{\mathrm{m}} g\left(l_1-l_2\right)\sin\theta+\left(c_{\mathrm{str}}+c_{\mathrm{p}}\right)\left(l_1^2+l_2^2\right)\dot{\theta}=-m_{\mathrm{m}}\left(l_1-l_2\right)\ddot{x}_{\mathrm{g}}\cos\theta \tag{8.17}$$

If a power circuit with a load impedance of R_{oad} is connected, the EM torque should be considered:

$$\left(m_{\mathrm{m}}\left(l_1^2+l_2^2\right)+\frac{m_{\mathrm{b}} l_3^2}{2}\right)\ddot{\theta}+m_{\mathrm{m}} g\left(l_1-l_2\right)\sin\theta+\left(c_{\mathrm{s}}+c_{\mathrm{p}}\right)\left(l_1^2+l_2^2\right)\dot{\theta}+K_{\mathrm{em}} i=-m_{\mathrm{m}}\ddot{x}_{\mathrm{g}}\left(l_1-l_2\right)\cos\theta \tag{8.2}$$

By considering

$$K_{\mathrm{em}} i=\frac{K_{\mathrm{em}}^2}{Z_{\mathrm{coil}}+R_{\mathrm{load}}}\dot{\theta} \tag{8.18}$$

and assuming a small vibration amplitude (i.e., $\sin\theta \approx \theta$ and $\cos\theta \approx 1$), Equation (8.2) is simplified as:

$$m_{\mathrm{s}} l_{\mathrm{e}}\ddot{\theta}+c_{\mathrm{t}} l_{\mathrm{e}}\dot{\theta}+k_{\mathrm{s}} l_{\mathrm{e}}\theta=-\frac{m_{\mathrm{m}}\ddot{x}_{\mathrm{g}}\left(l_1-l_2\right)}{l_{\mathrm{e}}} \tag{8.4}$$

where

$$l_{\mathrm{e}}=\left(l_1^2+l_2^2\right)^{1/2} \tag{8.3}$$

$$m_{\mathrm{s}}=m_m+\frac{m_{\mathrm{b}} l_3^2}{2 l_{\mathrm{e}}^2} \tag{8.5a}$$

$$k_{\mathrm{s}}=m_m g\frac{\left(l_1-l_2\right)}{l_{\mathrm{e}}^2} \tag{8.5b}$$

$$c_{\mathrm{t}}=c_{\mathrm{str}}+c_{\mathrm{p}}+\frac{K_{\mathrm{eq}}^2}{R_{\mathrm{coil}}+R_{\mathrm{load}}} \tag{8.5c}$$

$$K_{\mathrm{eq}} = \frac{K_{\mathrm{em}}}{l_{\mathrm{e}}} \tag{8.5d}$$

8.5.2 Coupled Horizontal and Tilt Base Motion

In the case of coupled horizontal and tilt base motion, the corresponding energy items of the DMP-based harvester with an open circuit are, respectively:

$$\begin{aligned} Q = {} & m_{\mathrm{m}}\dot{x}_{\mathrm{g}}^2 + \frac{1}{2}m_{\mathrm{m}}\left(l_1^2 + l_2^2\right)\left(\dot{\theta}+\dot{a}\right)^2 + m_{\mathrm{m}}\dot{x}_{\mathrm{g}}\left(l_1 - l_2\right)\left(\dot{\theta}+\dot{a}\right)\cos\left(\theta + a\right) \\ & + m_{\mathrm{b}}\dot{x}_{\mathrm{g}}^2 + \frac{1}{4}m_{\mathrm{m}}l_3^2\left(\dot{\theta}+\dot{a}\right)^2 \end{aligned} \tag{8.19a}$$

$$E = -m_{\mathrm{m}}gl_1\cos\left(\theta + a\right) + m_{\mathrm{m}}gl_2\cos\left(\theta + a\right) \tag{8.19b}$$

$$D = \frac{1}{2}\left(c_{\mathrm{s}} + c_{\mathrm{p}}\right)\left(l_1^2 + l_2^2\right)\dot{\theta}^2 + \left(c_{\mathrm{s}} + c_{\mathrm{p}}\right)\frac{l_3^2}{4}\dot{\theta}^2 \tag{8.19c}$$

where a is the ground tilt. In a general situation considering a closed EHC, the governing equation is:

$$\begin{aligned} & \left(m_{\mathrm{m}}\left(l_1^2 + l_2^2\right) + \frac{m_b l_3^2}{2}\right)\ddot{\theta} + m_{\mathrm{m}}g\left(l_1 - l_2\right)\sin\left(\theta + a\right) + \left(c_{\mathrm{s}} + c_{\mathrm{p}}\right)\left(l_1^2 + l_2^2\right)\dot{\theta} + K_{\mathrm{em}}i \\ & = -m_{\mathrm{m}}\left(l_1 - l_2\right)\ddot{x}_{\mathrm{g}}\cos(\theta + a) - \left(m_{\mathrm{m}}\left(l_1^2 + l_2^2\right) + \frac{m_b l_3^2}{2}\right)\ddot{a} \end{aligned} \tag{8.20}$$

In the case of small tilt angle and vibration amplitude, i.e., $\sin(\theta + a) \approx (\theta + a)$ and $\cos(\theta + a) \approx 1 - (\theta + a)^2/2$, Equation (8.20) is rewritten as:

$$\begin{aligned} & \left(m_{\mathrm{m}}\left(l_1^2 + l_2^2\right) + \frac{m_b l_3^2}{2}\right)\ddot{\theta} + m_{\mathrm{m}}g\left(l_1 - l_2\right)\theta + \left(c_{\mathrm{s}} + c_{\mathrm{p}}\right)\left(l_1^2 + l_2^2\right)\theta + K_{\mathrm{em}}i \\ & = -m_{\mathrm{m}}\left(l_1 - l_2\right)\ddot{x}_{\mathrm{g}} - mg\left(l_1 - l_2\right)a - \left(m_{\mathrm{m}}\left(l_1^2 + l_2^2\right) + \frac{m_b l_3^2}{2}\right)\ddot{a} + m_{\mathrm{m}}\left(l_1 - l_2\right)\ddot{x}_{\mathrm{g}}\frac{\left(\theta + a\right)^2}{2} \end{aligned} \tag{8.21}$$

The four items on the right side of Equation (8.21) represent the equivalent excitation caused by horizontal acceleration, the additional tilt of the pendulum due to gravity, the angular acceleration of tilting, and the coupling effect, respectively. The high-order fourth item is negligible, considering the small tilt and vibration amplitude.

Note that if only tilt base motion exists, the governing equation can be obtained by setting $\ddot{x}_{\mathrm{g}} = 0$ in Equation (8.20):

$$\begin{aligned}&\left(m_{\mathrm{m}}\left(l_1^2+l_2^2\right)+\frac{m_b l_3^2}{2}\right)\ddot{\theta}+m_{\mathrm{m}} g\left(l_1-l_2\right)\sin\left(\theta+a\right)+\left(c_{\mathrm{s}}+c_{\mathrm{p}}\right)\left(l_1^2+l_2^2\right)\dot{\theta}+K_{\mathrm{em}} i\\&=-\left(m_{\mathrm{m}}\left(l_1^2+l_2^2\right)+\frac{m_b l_3^2}{2}\right)\ddot{a}\end{aligned} \tag{8.10}$$

Similarly, for a small tilt base motion and vibration amplitude, the equation is given as:

$$\begin{aligned}&\left(m_{\mathrm{m}}\left(l_1^2+l_2^2\right)+\frac{m_b l_3^2}{2}\right)\ddot{\theta}+m_{\mathrm{m}} g\left(l_1-l_2\right)\theta+\left(c_{\mathrm{s}}+c_{\mathrm{p}}+c_{\mathrm{em}}\right)\left(l_1^2+l_2^2\right)\theta\\&=-mg\left(l_1-l_2\right)a-\left(m_{\mathrm{m}}\left(l_1^2+l_2^2\right)+\frac{m_b l_3^2}{2}\right)\ddot{a}\end{aligned} \tag{8.22}$$

Note that the base motion is directly applied to the DMP pivot in the above derivation. If the base motion is applied to the base plate, the horizontal displacement of the DMP pivot is modified as:

$$x_{\mathrm{g}} \approx x_{\mathrm{gf}} + h_{\mathrm{s}} a \tag{8.23}$$

where x_{gf} is the absolute displacement of the base plate, and h_{s} is the distance from the floating hull base to the DMP pivot.

CHAPTER 9

WAVE FLUME TEST OF DMP-BASED POINT ABSORBER

9.1 Introduction

This chapter presents a promising application of the DMP oscillator developed in Chapter 8; thus, some of the observations are similar to those in the last chapter. This DMP oscillator is enclosed in a floating hull, which forms a novel floating-point absorber (one type of WEC). In addition to surge (horizontal) motion, the DMP-based point absorber subjected to a wave load exhibits more or less pitch (tilt) dynamics, which is relatively more complicated than the dynamics of the shake table tests.

The chapter first briefly introduces the design and mechanism of the DMP-based point absorber. Subsequently, the feasibility of this point absorber, which considers the frequency tuning function, was validated through a series of tests in a wave flume. The power extraction performance and vibration response of the point absorber are evaluated. Then, the power performance of a large-scale DMP-based point absorber is discussed briefly. Finally, the experimental results are summarized.

9.2 DMP-based Point Absorber

Figure 9.1(a) shows the conceptual design of the point absorber, in which the DMP oscillator is enclosed inside a hull without direct contact with seawater. It is essentially a small-sized two-body oscillating-type point absorber, but the second body is not submerged. The general 6DOF motions of the point absorber, namely surge, sway, heave, roll, pitch, and yaw, are illustrated in Figure 9.1(b). The point absorber was designed to

utilize the surge and pitch motions. Considering the water depth of 0.6 m, which was the same as that in the flume test, the hydrodynamic parameters of this point absorber corresponding to the surge and pitch motions are shown in Figure 9.2. Table 9.1 lists the main parameters of the fabricated floating hull, which was made of transparent acrylic material to allow the visualization of vibrations during the tests.

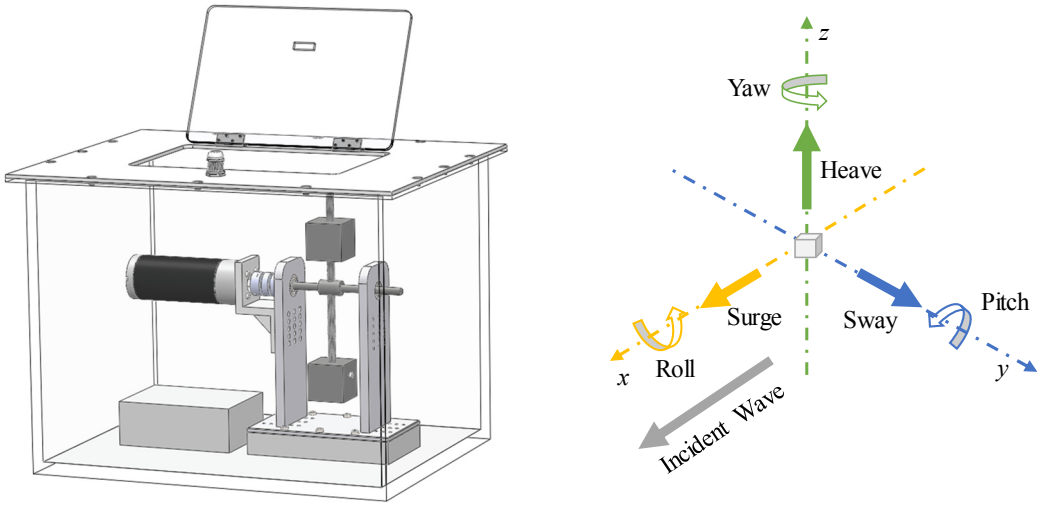

(a) DMP-based point absorber (b) 6DOF motions

Figure 9.1 Schematic of the DMP-based point absorber

Table 9.1 Parameters of the floating hull

Items	Parameters	Value
Floating hull	Mass	17.7 kg
	Dimensions	0.4 m × 0.5 m × 0.4 m
	Material	Acrylic
DMP oscillator	Mass	4.71 kg
Ballast	Mass	15.21 kg

Notably, the shape and geometry optimizations for point absorbers have been studied by different researchers to enhance power extraction (Pastor and Liu, 2014; Garcia-Teruel and Forehand, 2018; Vantorre et al., 2004; Shadman et al., 2018). The optimized shapes typically depend on the device oscillation modes and the objective function used (Garcia-

Teruel and Forehand, 2018). As this chapter is mainly focused on the functionality of the DMP oscillator inside the point absorber, a cuboid box was used as the buoy shape in this study for the sake of simplicity. The size of the buoy was determined based on the workspace constraints of the wave flume.

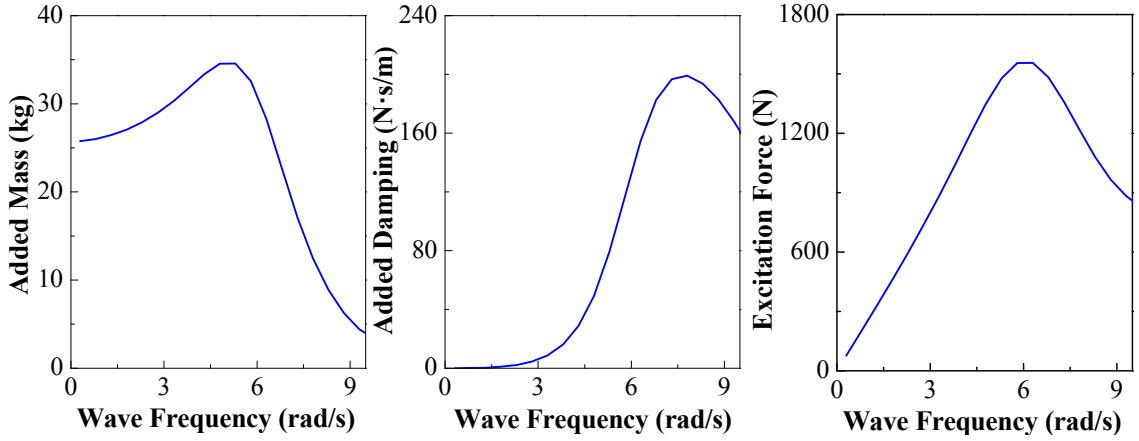

(a) Surge motion

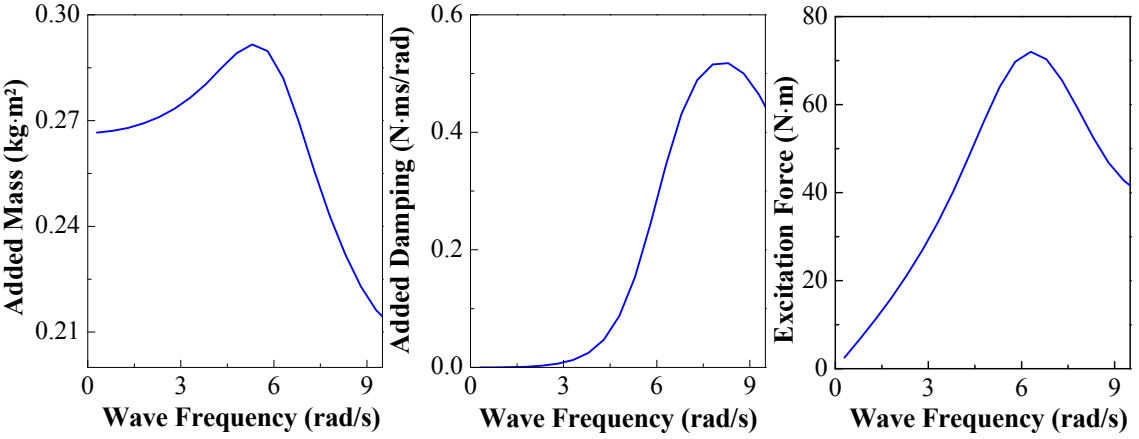

(b) Pitch motion

Figure 9.2 Hydrodynamic parameters of the DMP-based point absorber per unit wave height

Furthermore, this DMP-based WEC may operate in surge and pitch modes, both of which will induce the relative motion between the floating hull and DMP oscillator and enable energy extraction. However, the individual contributing factors from these two modes are not discussed in this study, as they are also related to the hull shape optimization. These factors need to be further investigated in the future.

Specifically, the general dynamics of the point absorber can be expressed by the following equations:

$$m_{\mathrm{f}}\mathbf{a}_{\mathrm{t}} = \mathbf{F}_{\mathrm{hd}} + \mathbf{F}_{\mathrm{res}} + \mathbf{F}_{\mathrm{PTO}} + \mathbf{F}_{\mathrm{ext}} \tag{9.1}$$

$$\mathbf{I}_{\mathrm{f}}\mathbf{a}_{\Phi} + \boldsymbol{\Phi} \times \mathbf{I}_{\mathrm{f}}\boldsymbol{\Phi} = \mathbf{M}_{\mathrm{hd}} + \mathbf{M}_{\mathrm{res}} + \mathbf{M}_{\mathrm{PTO}} + \mathbf{M}_{\mathrm{ext}} \tag{9.2}$$

where m_{f} is the mass of the floating hull; $\mathbf{I}_{\mathrm{f}}$ is the moment of inertia tensor at the center of gravity; $\mathbf{a}_{\mathrm{t}}$ and $\mathbf{a}_{\boldsymbol{\Phi}}$ are the translation and angular acceleration vectors, respectively; $\boldsymbol{\Phi}$ is the angular velocity vector; **M** and **F** are the force and moment acting on the floating hull, respectively; the subscript "hd" denotes the hydrodynamic excitation components in consideration of the added hydrodynamic mass (inertia) and damping; and the other subscripts, "res", "PTO", and "ext" denote the resorting components, PTO components, and external constraints (such as the mooring line), respectively. It needs to mention that the influence of the mooring line was not considered in this study.

Equations (9.1) and (9.2) reveal that the dynamics of a point absorber involve complex interactions among the waves, floating hull, and PTO system (including power circuit). The interaction between the waves and floating hull was not included in the scope of this study. Instead, the wave-induced vibration of the floating hull was directly measured and treated as the base motion input to the DMP oscillator. The relative motion between the floating hull and DMP oscillator drives the EM transducer to realize power extraction. If only the surge and pitch motions are considered, the corresponding PTO force and moment caused by the DMP oscillator can be expressed as:

$$\begin{aligned} F_{\mathrm{PTO}} = {} & 2\left(m_{\mathrm{m}} + m_{\mathrm{b}}\right)\left(\ddot{x}_{\mathrm{gf}} + h_{\mathrm{s}}\ddot{a}\right) + m_{\mathrm{m}}\left(l_1 - l_2\right)\left(\ddot{\theta} + \ddot{a}\right)\cos\left(\theta + a\right) \\ & - m_{\mathrm{m}}\left(l_1 - l_2\right)\left(\dot{\theta} + \dot{a}\right)^2 \sin\left(\theta + a\right) \end{aligned} \tag{9.3}$$

$$\begin{aligned} M_{\mathrm{PTO}} = {} & \left(m_{\mathrm{m}} l_{\mathrm{e}}^2 + \frac{m_b l_3^2}{2}\right)\left(\ddot{\theta} + \ddot{a}\right) + m_{\mathrm{m}} g\left(l_1 - l_2\right)\sin\left(\theta + a\right) \\ & + c_{\mathrm{t}} l_{\mathrm{e}}^2 \theta + m_{\mathrm{m}}\left(l_1 - l_2\right)\ddot{x}_{\mathrm{g}}\cos(\theta + a) \end{aligned} \tag{9.4}$$

where $\ddot{x}_{\mathrm{gf}}$ and $\ddot{a}$ are the surge (translational) and pitch (rotational) accelerations of the

floating hull base, respectively, and h_s is the distance from the base of the floating hull to the DMP pivot. The detailed derivation of Equations (9.3) and (9.4) is presented in Appendix 9.6. Equations (9.3) and (9.4) reveal that the DMP oscillator dynamic characteristics also affect the floating hull vibration. The interactions among the waves, floating hull, DMP oscillator, and power circuit may complicate the hull shape optimization, which need systematic studies in the future.

The corresponding power captured by the PTO system is equal to the input power to the DMP energy harvester:

$$P_{\mathrm{PTO}} = P_{\mathrm{in}} = \frac{1}{t_2 - t_1}\int_{t_1}^{t_2} c_{\mathrm{t}} \left(l_{\mathrm{e}}\dot{\theta}\right)^2 dt \tag{9.5}$$

9.3 Wave Flume Test

9.3.1 Experimental Introduction

The DMP-based point absorber was further tested in a wave flume, as shown in Figure 9.3. In addition to the sensors used in the shake table test (see Chapter 8), an iNEMO inertial module (model No. LSM9DS1) including a tri-axial accelerometer and a tri-axial gyroscope was connected to an Arduino Mega board and installed on the hull base to record the 6DOF motions of the floating hull. A series of regular wave tests considering different wave heights (0.08–0.15 m) and wave periods (0.6–1.8 s) were conducted in a 27 m long, 1.5 m wide, and 1.5 m deep Danish Hydraulic Institute wave flume. A piston-type wavemaker and wave absorber were placed at both ends of the wave flume. Three wave gauges were installed to measure the water surface elevation. The mean water depth in the whole test was set as 0.6 m; thus, the tested waves could be considered deep-water waves. To minimize the influence of the reflected waves from the flume end and prolong the measuring time, the point absorber was positioned approximately 4 m from the wavemaker (Figure 9.3). The corresponding photographs of the experimental setup are shown in Figure 9.4.

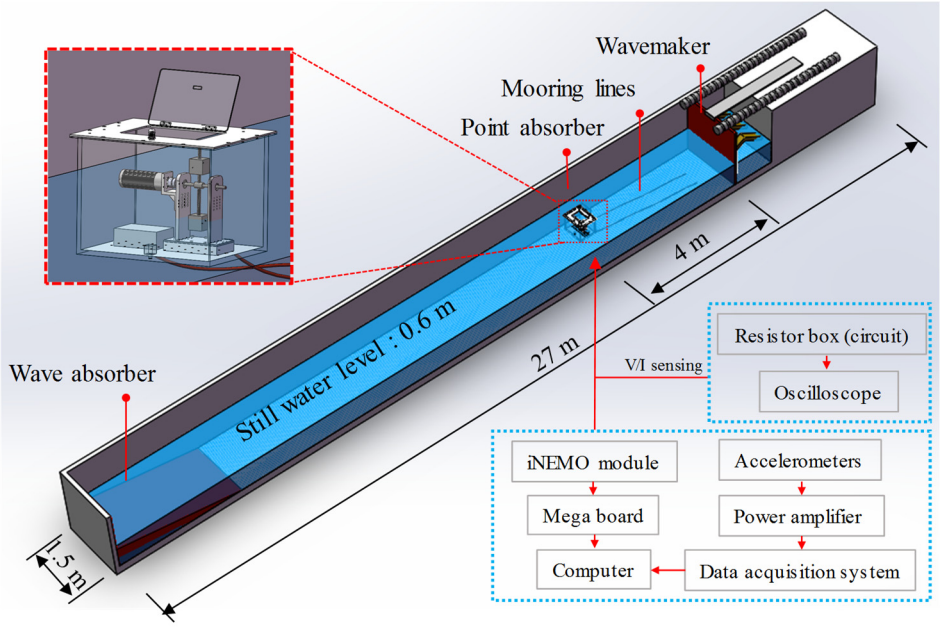

Figure 9.3 Schematic of the experimental layout in the wave flume

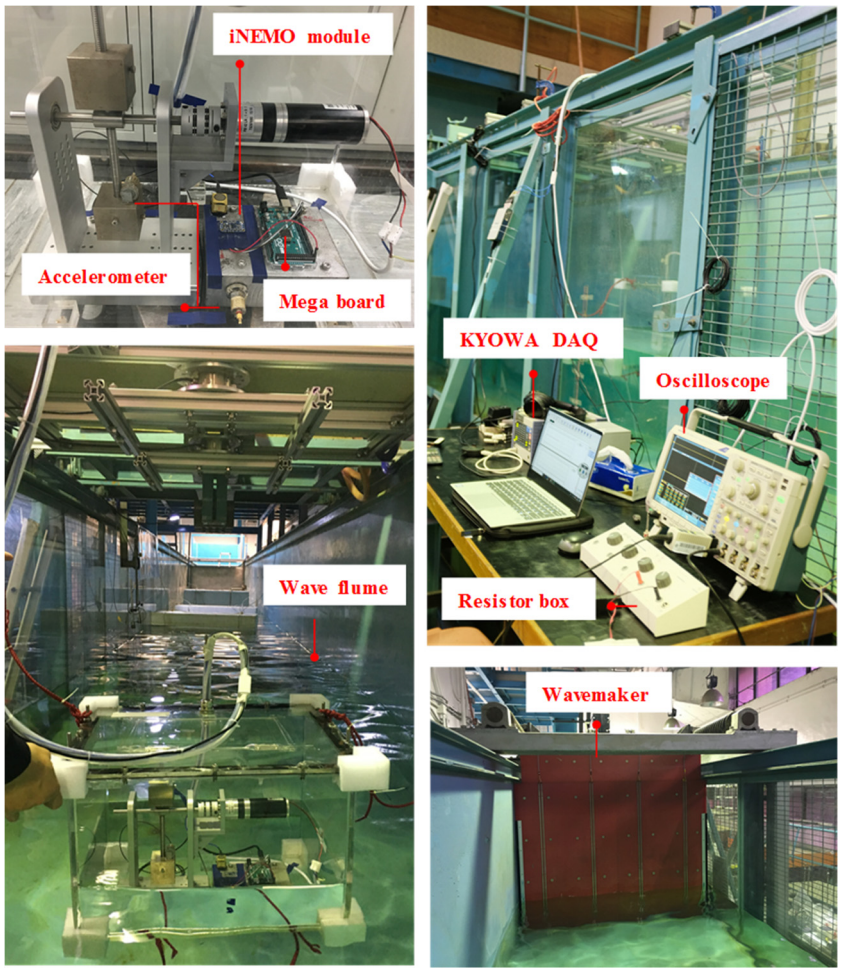

Figure 9.4 Wave flume test setup

9.3.2 Experimental Result

9.3.2.1 Energy Extraction Performance

Figure 9.5 illustrates the motions of the DMP oscillator enclosed inside the floating hull within several wave cycles (regular waves) with a wave frequency of f_w = 1 Hz, in which 0 s represents the start point of one cycle. In the first wave cycle, the pendulum bar was nearly perpendicular to the base support at 0.25 and 0.75 s, while the amplitude reached the maximum at 0.5 s and returned to the start point at 1 s. Given that the DMP oscillator was in a periodic oscillation, its vibrations in the period of 1–2.75 s were similar to those during 0–0.75 s.

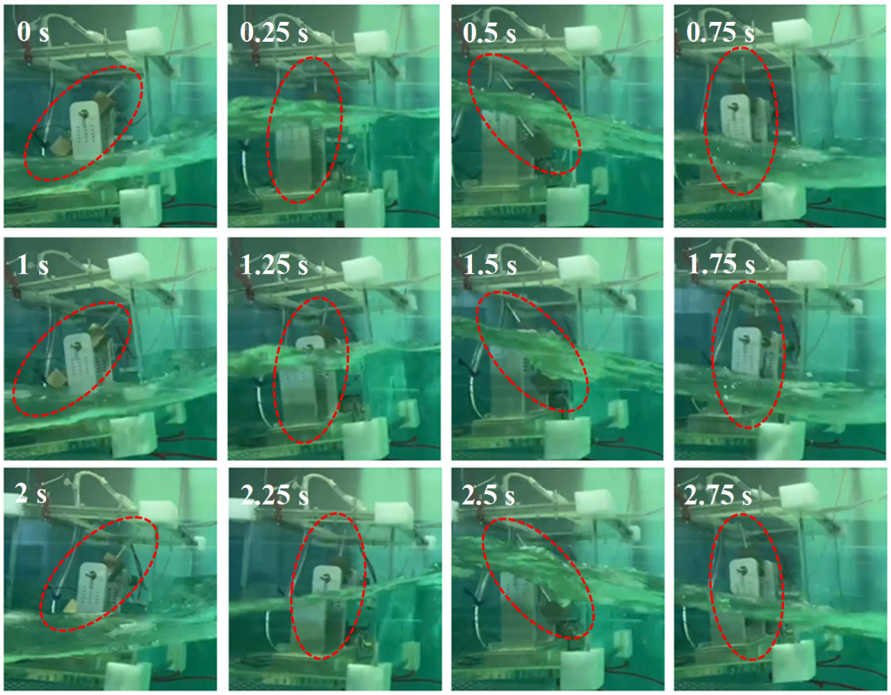

Figure 9.5 DMP oscillator at different time points during wave tests ($f_s \approx 1$ Hz, $f_w = 1$ Hz)

Figure 9.6 shows representative time histories of the measured output voltage and current on the connected load resistor, wherein the corresponding wave frequency and height were $f_w = 1$ Hz and $h = 0.1$ m, respectively, and the DMP oscillator was tuned to a nearly resonant condition, $f_s \approx 1$ Hz. Both the voltage and current curves were nearly harmonic. The partially enlarged plot depicts that the voltage and current were in phase.

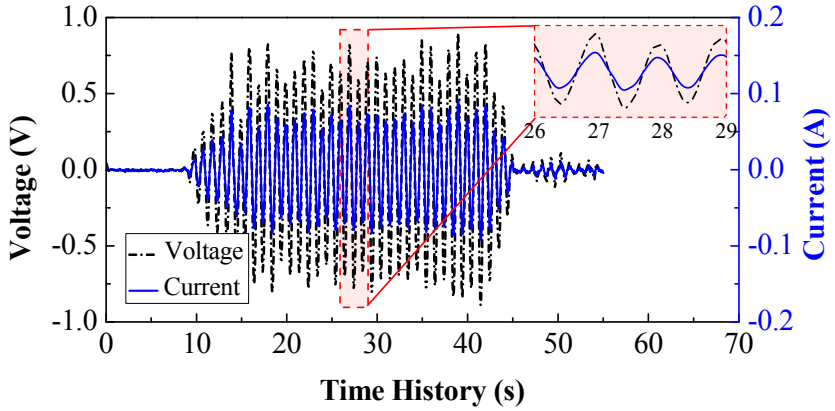

Figure 9.6 Representative time history of output voltage and current ($f_s \approx 1$ Hz, $f_w = 1$ Hz)

Corresponding to the wave frequency of $f_w = 1$ Hz, Figure 9.7(a) shows the variation of output power in a resonant condition with different pure load resistances R_{load} for different wave heights h. Different load resistances were provided using a resistance decade box that offered high accuracy, with 0.5% error. The resulting variation of the output power was similar to the observation in Figure 8.13. It can be observed that the maximum output power of 45 mW corresponded to $R_{load} \approx 20\ \Omega$. The optimal load resistance was slightly different from that in the shake table test (i.e., 15 Ω), because the resistance of the long conducting wire (approximately 4 Ω) was taken into account in the inherent resistance R_{coil} and thus the optimal load resistance slightly increased according to Equation (7.12). A long wire was selected to accommodate the quite long distance between the monitoring center and the tested WEC. Three curves in Figure 9.7(a) correspond to three wave heights from 0.08 to 0.12 m. It is apparent that a greater wave height resulted in larger output power. Another test with an extreme wave height of h = 0.15 m (nearly overtopping) was conducted, and the maximum output power increased to approximately 100 mW.

Corresponding to the DMP frequency of $f_s \approx 1$ Hz and wave height of $h = 0.1$ m, Figure 9.7(b) shows the variations of the output power with the wave period (0.8–1.2 s) at two load resistances (8 and 20 Ω); in the figure, 20 Ω represents the optimal load resistance case, and 8 Ω represents the resistance designed according to the classical IM. Compared with the classical IM, the optimal resistance case resulted in a remarkable

power improvement (approximately 70%) near the resonant range. The comparison again demonstrates the advantage of the adopted overall impedance optimization strategy over the classical IM. Furthermore, Figure 9.7(b) shows that the power performance degraded rapidly when the wave frequency shifted slightly, emphasizing the importance of frequency tuning in the resonant-type point absorber. All of the peak power occurred at the initial natural frequency of the DMP, $f_s \approx 1$ Hz, indicating that the effect of nonlinear characteristics was limited and the detuning due to large vibrations did not occur in the tests.

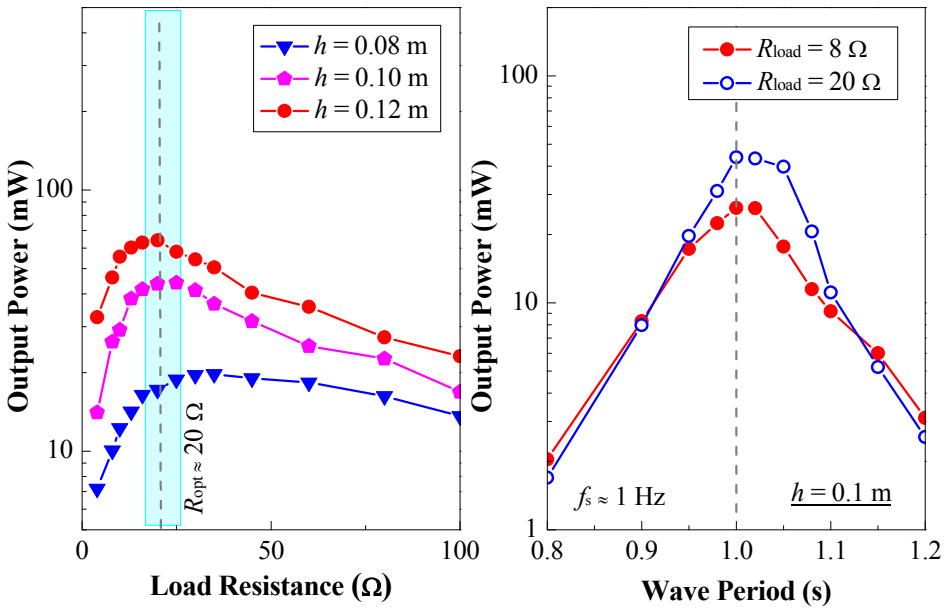

(a) Load resistance (f_w = 1 Hz) (b) Wave period

Figure 9.7 Power extraction performance of the point absorber under different conditions ($f_s \approx 1$ Hz)

Figure 9.8 presents the open-circuit voltage vs. wave periods in consideration of different wave heights. It can be inferred that different degrees of softening nonlinearity occurred under the varying incident wave heights; that is, the peak voltages under h = 0.08, 0.1, and 0.12 m occurred at wave periods of 1.05 s (0.95 Hz), 1.07 s (0.93 Hz), and 1.1 s (0.91 Hz), respectively. However, it needs to point out that a connecting load resistance always accompanies an additional damping effect, thereby reducing the vibration amplitude and weakening the nonlinearity in practice, as shown in Figure 9.7(b),

where $T \approx 1$ s ($f_s \approx 1$ Hz). Thus, it is reasonable to believe that this nonlinearity characteristic exerts a limited impact on the initial natural frequency when a small load resistance is connected.

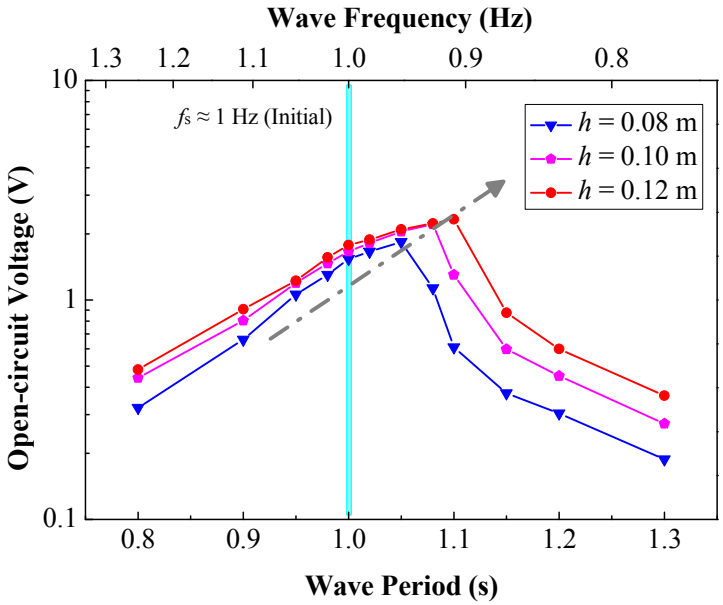

Figure 9.8 Open-circuit voltage vs. wave periods at different wave heights ($f_s \approx 1$ Hz)

Figure 9.9 illustrates the frequency tuning performance of interest, in which the open-circuit voltages corresponding to different upper mass positions are shown under different wave periods. Increasing the locations (l_2) of the upper mass from −75 to 85 mm can effectively increase the natural periods (i.e., reduce the natural frequencies) of the DMP oscillator. The wave heights in the cases of l_2 = 75 and 85 mm were set as 0.12 m and 0.15 m, respectively, while those in the other cases were 0.1 m. The case of l_2 = −75 mm represents the scenario where the upper mass is moved to the same side as the lower mass. Compared with the average frequencies shown in Figure 8.9, the nonlinearity slightly reduced the natural frequencies corresponding to the peak locations of each curve, but the impact was generally limited (less than 10% difference). The realized natural frequencies were as low as 0.67 Hz in the wave flume experiment, validating the ultra-low frequency characteristic. Furthermore, Figure 9.9 shows that the power extraction performance could be effectively enhanced with the appropriate frequency tuning. For example, when l_2 was fixed at 45 mm, the output voltage was merely 0.45 V,

corresponding to wave period T = 1.2 s, whereas the corresponding voltage was 1.2 V when l_2 was tuned to 65 mm, representing a significant improvement (170% increase). These results further validate the effectiveness and benefit of the frequency tuning function of the proposed DMP oscillator and demonstrate its promising prospects in WECs owing to its tunable ultra-low-frequency characteristics.

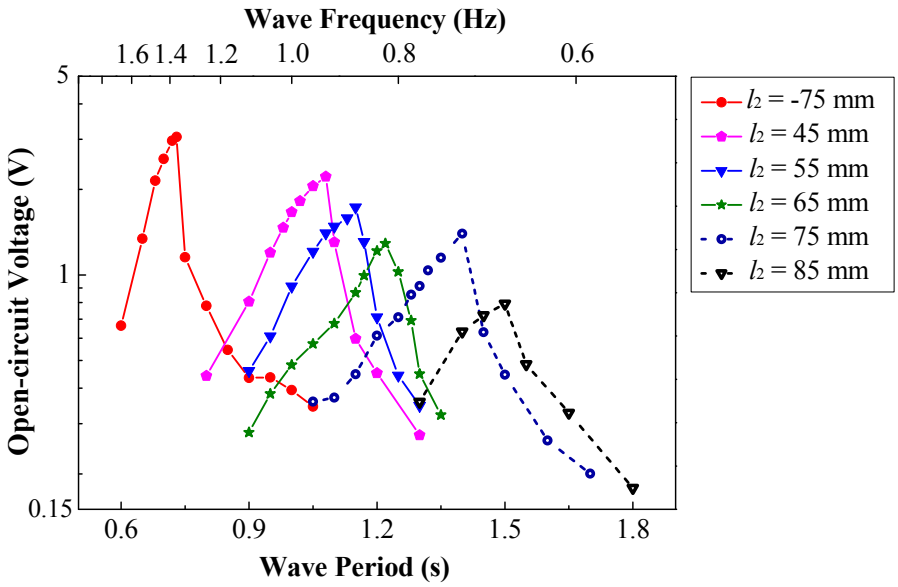

Figure 9.9 Performance of frequency tuning through the lower mass relocation

Note that the pure resistor, a power dissipative component, is only an oversimplified representation of the electric load connected to the EMD. To confirm the actual power extraction performance, the EHC mentioned in Chapter 3 was also connected in the test to realize the optimal synthetic resistance and store the output power in a rechargeable battery. The target resistance in this scene was designed as 20 Ω, corresponding to the optimal resistance for a near-resonance condition. Table 9.2 presents the power distribution in the EHC in different experimental cases with a wave period of f_w = 1 s, in which P_{pc} is the measured power transferred to the EHC, $P_{out\text{-}b}$ is the measured power transferred to the battery, and R_{eq} is the equivalent resistance of the buck–boost converter, ranging from 19 to 22 Ω in these four cases, which are very close to the design value. Note that the power loss inevitably occurred within the EHC owing to the bridge rectifier and the ESR of connected electrical components. For example, in the wave flume test

with wave height h = 0.15 m, although 94.9 mW was inputted into the circuit, only 31.6 mW could be charged into the battery. The average efficiency was approximately 33.3% (= 31.6/94.9), which indicates that the power prediction based on a simplified R_{load} will considerably overestimate the power extraction performance.

Table 9.2 Power distribution in buck–boost converter (f_w = 1 Hz)

Wave height (m)	P_{pc} (mW)	$P_{out\text{-}b}$ (mW)	R_{eq} (Ω)	Eff. (%)
0.08	19.7	6.0	18.98	30.4
0.1	37.7	11.7	22.41	31.0
0.12	66.0	20.5	21.02	31.1
0.15	94.9	31.6	19.76	33.3

9.3.2.2 Vibration Response Evaluation

This subsection presents the vibration responses based on the measurement by the iNEMO inertial module. Figure 9.10 presents representative 6DOF response time histories corresponding to wave periods T = 1 s, DMP frequency $f_s \approx$ 1 Hz, wave height h = 0.1 m, and open-circuit conditions. Notably, the following 6DOF responses were obtained based on the reference coordinate, with the origin coincident with the sensor location (at the hull base). The surge and pitch motions were dominant among the translational and rotational motions, respectively. Although the heave motion was relatively larger at the beginning and end of the test, it could not activate the lateral vibration of the proposed DMP oscillator. The wave-induced surge and pitch motions caused the relative vibrations between the DMP oscillator and the floating hull and enabled power extraction. The vibration responses of the DMP oscillator are discussed as follows.

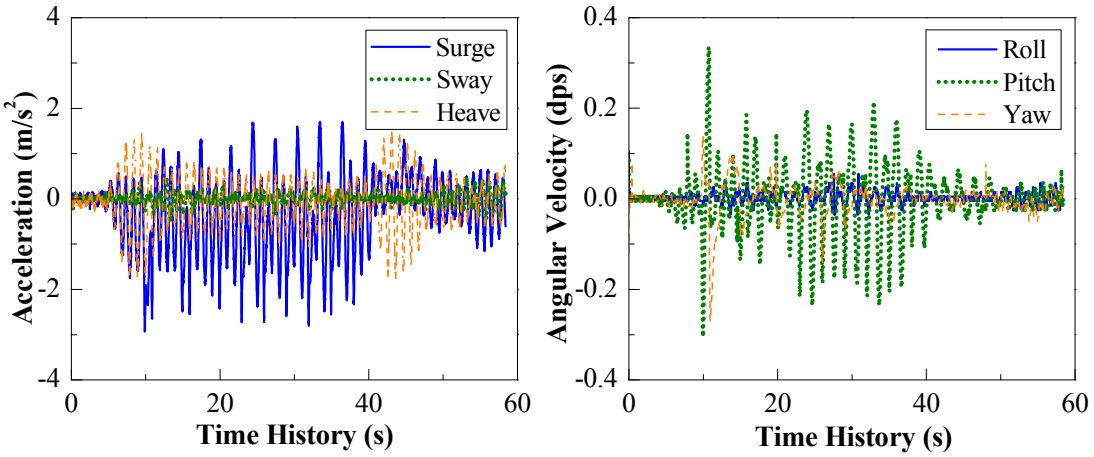

Note: dps denotes degree per second.

Figure 9.10 6DOF vibration responses measured by iNEMO sensors ($f_s \approx 1$ Hz, $f_w = 1$ Hz, $h = 0.1$ m)

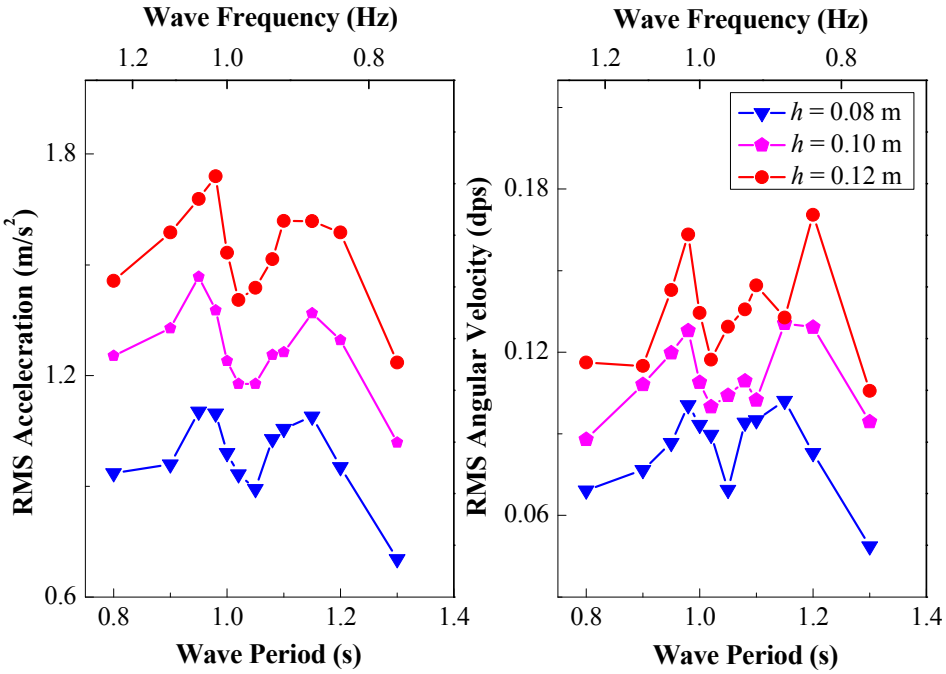

(a) Surge motion (b) Pitch motion

Figure 9.11 Vibration response vs. wave periods (frequencies) at different wave heights ($f_s \approx 1$ Hz)

Figure 9.11 presents the RMS accelerations of the measured surge and pitch motions of the hull of the point absorber when the natural frequency of the DMP oscillator with an open circuit was tuned as $f_s \approx 1$ Hz. The DMP oscillator functioned like a TMD, thereby

considerably mitigating the vibration responses (including surge and pitch motions) of the floating hull in the resonant range (near the natural frequency of the DMP $f_s \approx 1$ Hz). Both the RMS surge and pitch curves were nearly symmetric about the wave period of 1 s.

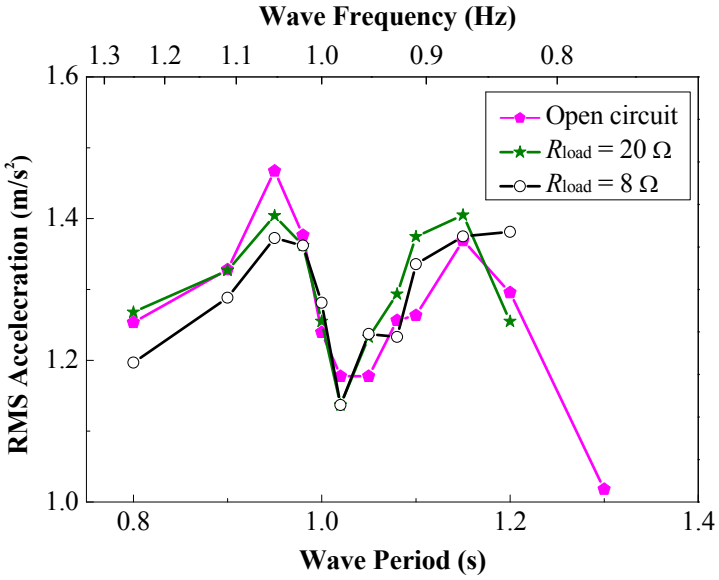

Figure 9.12 Surge response vs. wave periods (frequencies) considering different load resistance ($f_s \approx 1$ Hz, $h = 0.1$ m)

Furthermore, taking the surge response as an example, Figure 9.12 shows the cases with the connected load resistance R_{load} = 20 and 8 Ω under a wave height of 0.1 m. Compared with the open circuit case, the effect of load resistance was insignificant, because (1) the EM damping of the DMP oscillator was relatively small owing to the relative large coil and load resistances and (2) the acceleration responses of the hull were insensitive to slight damping variation in the DMP oscillator. These results indicate the great potential of energy regenerative TMD (Shen et al., 2012, 2018) in vibration response mitigation of floating structures. Moreover, it needs to mention that the decreasing vibration response of the floating hull near the resonant frequency did not lead to a reduced power extraction of the DMP oscillator, which is related to the specific power distribution of the wave power into the entire system.

Despite the limited effect of load resistance on the vibration response of the floating hull shown in Figure 9.12, the load resistance considerably influenced the responses of the internal DMP oscillator (Figure 9.13). With increasing load resistance, the RMS absolute acceleration of the lower mass and the output voltage on the load resistor increased accordingly, mainly because the EM damping was inversely proportional to the load resistance (Zhu et al., 2012). Consequently, small EM damping led to a large vibration of the DMP oscillator.

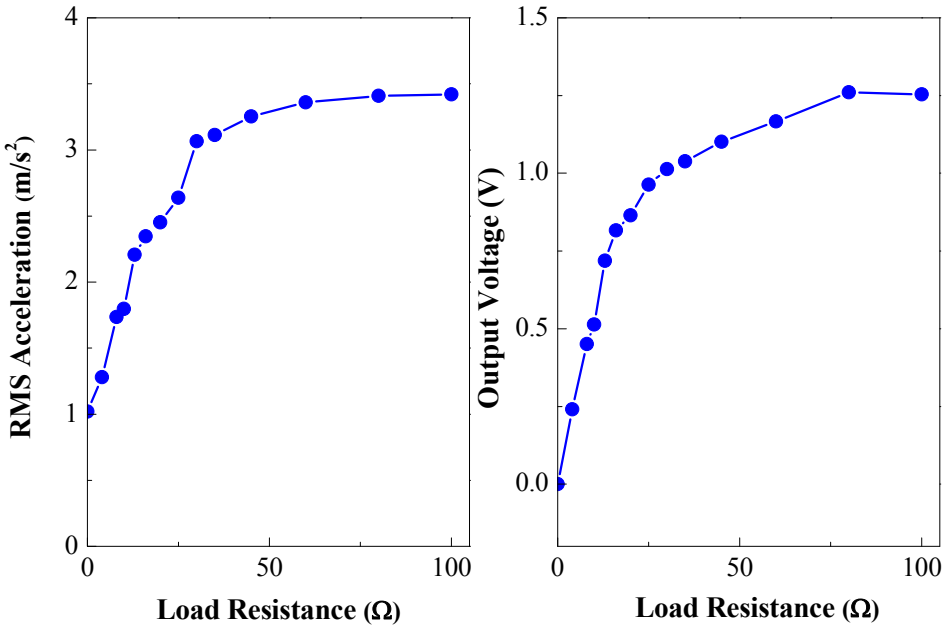

(a) Absolute acceleration (b) Output voltage

Figure 9.13 Responses of the DMP oscillator

Furthermore, Figure 9.14 shows the RMS absolute acceleration of the lower mass at different tuned frequencies. The overall trend is similar to that in Figure 9.9, which confirms the effectiveness of the frequency tuning function of the proposed DMP oscillator. Larger vibrations of the DMP occurred under resonant conditions; this occurrence corresponds to greater output power in Figure 9.9. Notably, given the same wave height, a shorter wave period corresponded to a larger vibration acceleration of the wave, inducing relatively larger absolute resonant accelerations of the DMP (Figure 9.14).

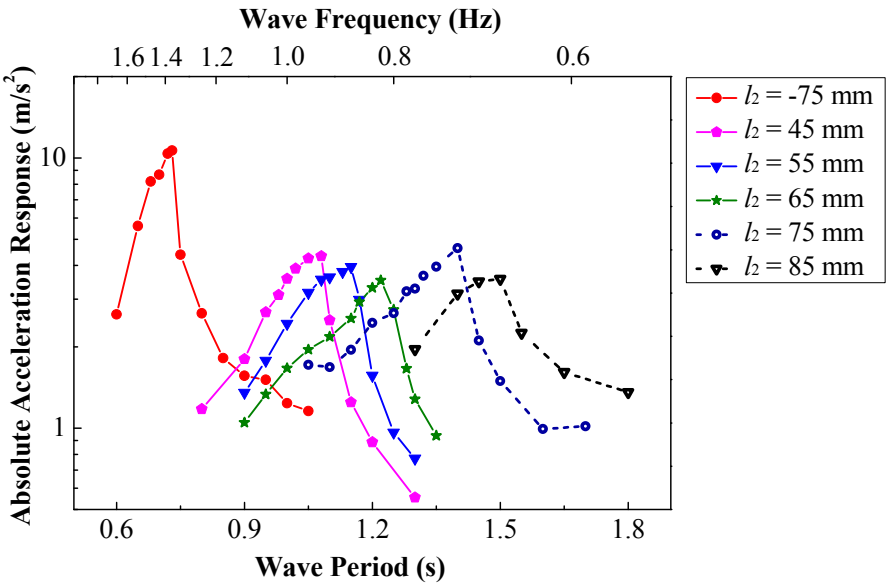

Figure 9.14 Absolute acceleration response of lower mass considering frequency tuning

9.4 Discussion on Full-scale Device

The tested point absorber represented only a preliminary small-scale prototype with a volume of 0.08 m^3. The Froude scaling law can be used to project the performance of a full-scale device (Payne, 2008). With a constant Froude number and gravitational acceleration, when the prototype is scaled up with a geometric ratio of s, the corresponding wave height and length, wave period, and power generation can be scaled up as s, $s^{0.5}$, and $s^{3.5}$, respectively. Consequently, Figure 9.15 shows the output power and natural period of the large-scale point absorbers predicted based on the recorded power in the wave flume tests, where the measured power was obtained under the conditions of wave height h = 0.1 m and R_{load} = 20 Ω, and the natural frequency of the DMP oscillator was tuned to agree with the wave frequency. The corresponding wave periods ranged from 0.7 to 1.35 s. It can be observed that the scaling-up of the DMP-based WECs will further lower the natural frequencies and enable considerable power extraction. Corresponding to the geometric scale s = 5, 10, and 20, the scaled wave heights were 0.5, 1, and 2 m, respectively; the tunable frequency ranges are predicted as 0.33–0.67, 0.23–0.45, and 0.17–0.32 Hz, respectively; and the predicted output power ranges are 0.8–27, 9–305, and 97–3456 W, respectively.

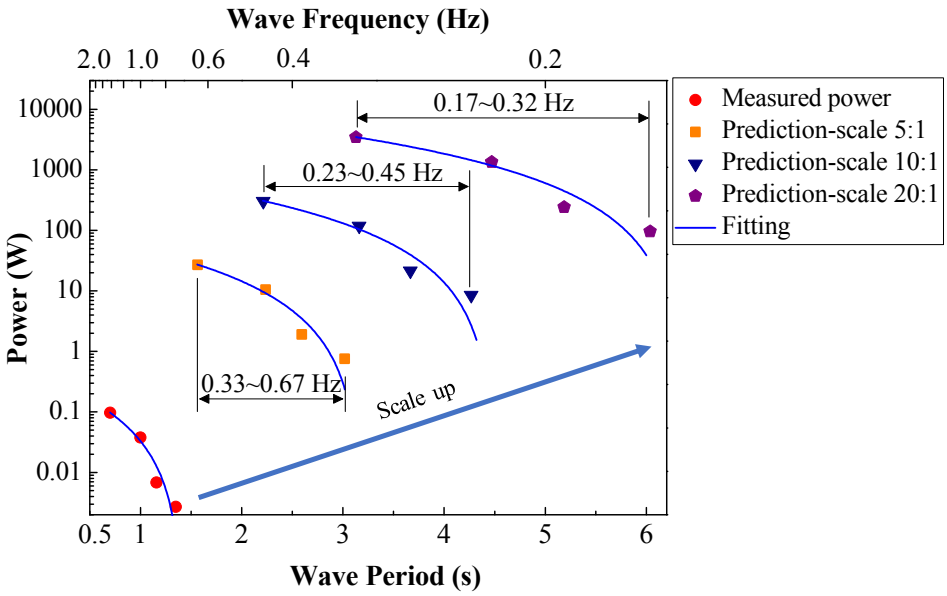

Figure 9.15 Power prediction with different geometric scales

Table 9.3 Parameters scaling using Froude scaling law

Geometric scale factor	Small-scale test			Full-scale		
	h (m)	T (s)	P_{out} (mW)	h (m)	T (s)	P_{out} (kW)
20	0.1	1	37.7	2	4.47	1.349
20	0.12	1	66	2.4	4.47	2.361
20	0.15	1	94.9	3	4.47	3.395
20	0.1	0.7	96.6	2	3.13	3.456
20	0.12	0.7	111	2.4	3.13	3.971

Note: The output power in the table is the dissipated power of a pure resistor.

Table 9.3 lists a few specific scaled results, with a geometric scale of s = 20. These specific cases were selected in consideration of the wave conditions of Shandong Peninsula, where the wave heights of 1.6–2.6 m account for approximately 74% of all waves during 1996–2011, and the wave period is mainly in the range of 2.5–7.0 s in all seasons, with a resultant average period of 3.23 s (Duan et al., 2020). The results in Table 9.3 and Figure 9.14 indicate that hundreds to thousands of watts of power can be potentially captured in a large-scale device, even though the shape of the floating hull has not been optimized. Moreover, an array configuration of several full-scale point absorbers will considerably enhance the power generation. Although low natural frequencies and

high output power are predicted in large-scale DMP-based WECs herein, in-situ tests of practical large-scale WECs are still needed to verify the corresponding predictions.

9.5 Summary

The DMP oscillator developed in Chapter 8 was enclosed in a buoy, which constituted a point absorber for converting wave energy. The power extraction and frequency tuning performance were validated through a series of wave flume tests under different wave heights and periods. The major conclusions of these investigations are as follows:

1) Although at a relatively high wave height, the open-circuit voltage of the point absorber exhibited an evident softening nonlinear characteristic, such nonlinearity in the output power became weak when the load resistor was connected in the circuit, and the vibration amplitude was reduced by the introduction of EM damping.
2) The frequency tuning characteristic enhanced the power extraction performance in the wave flume test. Its frequency was tuned from 0.65 to 1.4 Hz in a series of regular wave tests with wave heights from 0.1 to 0.15 m and wave periods from 0.6 to 1.8 Hz. With appropriate frequency tuning, the output voltage improvement could be 170% higher than that of the case with detuning.
3) The DMP oscillator inside the point absorber functioned like a regenerative TMD and thus mitigated the floating hull vibration. This result demonstrates the application potential of the DMP oscillator as a dual-function device for simultaneous vibration control and power extraction for floating structures, such as floating offshore wind turbines.
4) According to the scaling law, large-scale WECs based on the proposed technique were projected to generate power up to hundreds or thousands of watts. Specifically, with a geometric scale of 20, the large-scale WECs could realize frequency tuning in the range of 0.17 to 0.23 Hz with power extraction from 97 to 3456 W.

9.6 Appendix

9.6.1 Derivation of the PTO Force and Moment

If the DMP oscillator is installed on an additional mass subjected to pitch and surge motions, such as the floating hull in this study, the corresponding power items are derived as follows:

$$\begin{aligned} V = {} & m_{\mathrm{m}}\dot{x}_{\mathrm{g}}^2 + \frac{1}{2}m_{\mathrm{m}}\left(l_1^2 + l_2^2\right)\left(\dot{\theta}+\dot{a}\right)^2 + m_{\mathrm{m}}\dot{x}_{\mathrm{g}}\left(l_1 - l_2\right)\left(\dot{\theta}+\dot{a}\right)\cos\left(\theta + a\right) \\ & + m_{\mathrm{b}}\dot{x}_{\mathrm{g}}^2 + \frac{1}{4}m_{\mathrm{m}}l_3^2\left(\dot{\theta}+\dot{a}\right)^2 + \frac{1}{2}M\dot{x}_{\mathrm{gf}}^2 + \frac{1}{2}M\left(l_{\mathrm{f}}\dot{a}\right)^2 \end{aligned} \tag{9.6a}$$

$$U = -m_{\mathrm{m}}gl_1\cos\left(\theta + a\right) + m_{\mathrm{m}}gl_2\cos\left(\theta + a\right) + \frac{1}{2}K\left(x_{\mathrm{gf}} - d\right)^2 + \frac{1}{2}K_{\mathrm{t}}\left(a - \delta\right)^2 \tag{9.6b}$$

$$D = \frac{1}{2}c_{\mathrm{t}}\left(l_1^2 + l_2^2\right)\dot{\theta}^2 + \frac{1}{2}C\left(\dot{x}_{\mathrm{gf}} - \dot{d}\right)^2 + \frac{1}{2}C_{\mathrm{t}}\left(\dot{a} - \dot{\delta}\right)^2 \tag{9.6c}$$

where d and δ are the wave-induced equivalent horizontal and tilt base motion, respectively; a and x_{gf} are the wave-induced pitch and surge motions of the floating hull, respectively; l_{f} is the distance between the buoy base and the center of rotation of the floating hull; K_{t} and C_{t} are the rotational stiffness and damping of the floating hull, respectively; M is the mass of the floating hull; C and K are the horizontal stiffness and damping of the floating hull, respectively; and x_{g} is the equivalent surge motion of the DMP pivot.

The influence of the EM coupling effect is considered in Equation (9.6c). Then, the governing equations in this scene are given as follows:

$$\begin{aligned} & M\ddot{x}_{\mathrm{gf}} + C\left(\dot{x}_{\mathrm{gf}} - \dot{d}\right) + K\left(x_{\mathrm{gf}} - d\right) + 2\left(m_{\mathrm{m}} + m_{\mathrm{b}}\right)\left(\ddot{x}_{\mathrm{gf}} + h_{\mathrm{s}}\ddot{a}\right) \\ & + m_{\mathrm{m}}\left(l_1 - l_2\right)\left(\ddot{\theta}+\ddot{a}\right)\cos\left(\theta + a\right) - m_{\mathrm{m}}\left(l_1 - l_2\right)\left(\dot{\theta}+\dot{a}\right)^2\sin\left(\theta + a\right) = 0 \end{aligned} \tag{9.7}$$

$$\begin{aligned} & Ml_{\mathrm{f}}^2\ddot{a} + C_{\mathrm{t}}\left(\dot{a} - \dot{\delta}\right) + K_{\mathrm{t}}\left(a - \delta\right) + \left(m_{\mathrm{m}}l_{\mathrm{e}}^2 + \frac{m_b l_3^2}{2}\right)\ddot{\theta} + m_{\mathrm{m}}g\left(l_1 - l_2\right)\sin\left(\theta + a\right) \\ & + c_{\mathrm{t}}l_{\mathrm{e}}^2\theta = -m_{\mathrm{m}}\left(l_1 - l_2\right)\ddot{x}_{\mathrm{g}}\cos(\theta + a) - \left(m_{\mathrm{m}}l_{\mathrm{e}}^2 + \frac{m_b l_3^2}{2}\right)\ddot{a} \end{aligned} \tag{9.8}$$

The influences of the DMP oscillator on the floating hull are illustrated in

Equations (9.7) and (9.8), that is, Equations (9.3) and (9.4) in the study. They are regarded as the practical PTO force and moment, respectively.

9.6.2 Validation of the Derivation in Appendix 8.5.2

The measured vibration responses of the floating hull using the iNEMO inertial module can be regarded as the base motions inputted to the DMP oscillator. In this scene, the theoretical derivation in Appendix 8.5.2 can be adopted to predict the power and vibration response of the DMP oscillator.

Taking the responses presented in Figure 9.10 as an example, Figure 9.16(a) shows the corresponding open-circuit voltage time history calculated using the measured surge and pitch responses. For comparison, the experimental open-circuit voltage was also plotted. It can be observed that the simulated voltage matched fairly with the experimental one. The error was contributed by the constant-parasitic-damping assumption (i.e., 1.1 N·s/m) in the modeling. In addition to the resonant case (i.e., f_w = 1 s), the non-resonant case with f_w = 0.8 s was compared (Figure 9.16(b)). To some extent, these results demonstrate the accuracy of the derivation in Appendix 8.5.2. However, to better understand the DMP oscillator dynamics, a 6DOF vibration platform test needs to be conducted.

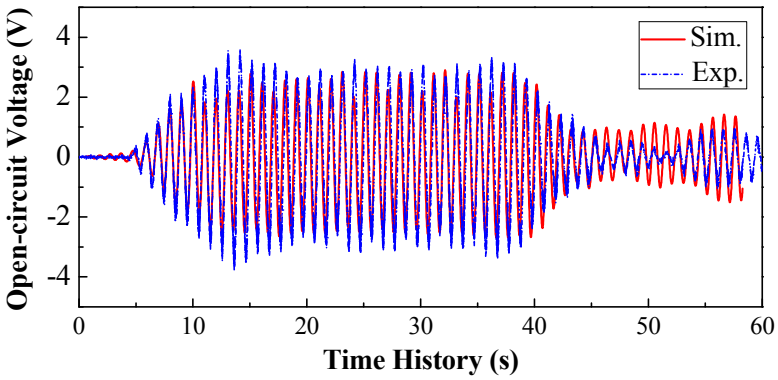

(a) T_w = 1 s

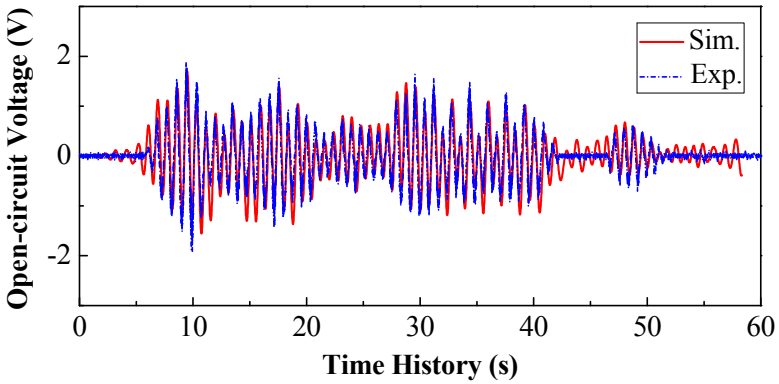

(b) T_w = 0.8 s

Figure 9.16 Open-circuit voltage time history calculated using the measured base responses (f_s ≈ 1 Hz, h = 0.1 m)

CHAPTER 10

CONCLUSIONS AND DISCUSSIONS

10.1 Summary

The typical output power levels of nano- or micro-scale vibration-based energy harvesters are limited and might not meet the power demands of wireless sensors or semi-active/active controls, which motivates to seek energy enhancement approaches for vibration-based energy harvesters. EMDs are selected as the energy transducers in this thesis, considering their compatibility with low-frequency vibrations and applications in large-scale structures. This study numerically and experimentally investigated two categories of vibration-based EM energy harvesters with functionality and performance enhancement. The study was completed by conducting the following tasks:

(1) An adaptive-duty-cycle EHC that can provide a stable controllable resistance characteristic with energy storage function was designed. The efficacy of the designed EHC was validated through circuit tests and MTS tests when it was connected to an EMD.

(2) An experiment of a 135 m–long bridge stay cable installed with an EHEMD (with the designed EHC) was conducted for the first time, demonstrating the EHEMD's functionality and practicability. The EHEMD in this situation can be regarded as a passive control device with energy harvesting function.

(3) An energy-harvesting adaptive vibration control strategy with EHEMDs was developed and applied to the lateral secondary suspension of an HST model.

(4) The relationship between the vibration control and energy harvesting objectives in dual-function devices (including EHEMD, EHTMD, and EHTID) was illustrated

analytically or numerically.

(5) A unified impedance optimization theory was proposed. This optimization theory was applicable to different structural complexities, coupling effect strengths, and excitation types. The electrical frequency tuning method was realized numerically using the impedance optimization theory.

(6) A novel structural configuration, i.e., DMP, with tunable ultra-low frequency, was designed. A prototype of the DMP-based energy harvester was tested through free vibration and shake table tests.

(7) A DMP-based WEC was tested in a wave flume to evaluate the energy enhancement of the DMP oscillator for wave energy conversion, with the focus on the benefits of the frequency tuning function.

The EHC in Task (1) was generally adopted in Tasks (2–7). Tasks (2–4), corresponding to Chapters 4–6, focus on dual-function devices simultaneously performing vibration control and energy harvesting; the devices were generally large-size, high-energy/damping-density systems and thus generated high output power. Tasks (5–7), corresponding to Chapter 7–9, focus on single-function devices (i.e., pure energy harvesters) with frequency tuning function, based on which the energy enhancement in terms of power peak or bandwidth could be realized.

10.2 Conclusions

Two categories of EM energy harvesters with enhanced functions and performances were investigated in this study. The first category, known as dual-function dampers, simultaneously performs vibration control and energy harvesting by leveraging the coupled dynamics with the vibration sources. The second category realizes energy harvesting only but possesses a frequency tuning function. A series of numerical and experimental studies were conducted to study the feasibility, optimization, and implementation of the two types of EM energy harvesters.

The EMD and EHC are key components in both categories of energy harvesters. In the first step, the basic mechanism of the EMD and EHC (buck–boost converter with bridge rectifier) was studied. Given the limitations (i.e., equivalent resistance and power efficiency degradation in CCM) of the conventional fixed-duty-cycle buck–boost converter in the previous studies, an MCU was introduced to adaptively regulate the duty cycle according to the sensing rectifier voltage. The adaptive-duty-cycle buck–boost converter was utilized as the main part of the EHC. As a result, the equivalent characteristics of the EHC could be maintained as designed. Notably, the EMD plus EHC system is likely the simplest form of a dual-function damper, and it can provide equivalent EM damping depending on the machine constant, coil resistance, and equivalent impedance of the EHC.

In the circuit test of the EHC, the empirical relationship between the duty cycle and designed resistance of the EHC was determined. In CCM, the adaptive-duty-cycle EHC could effectively maintain a constant equivalent resistance as designed and a relatively higher output power/efficiency when compared with the fixed-duty-cycle EHC, which exhibited decreased resistance and power efficiency. When the presented EHC was connected to the EMD, the EMD-EHC system exhibited a stable damping coefficient in a wide range of vibration levels in the cyclic test. Additionally, the overall power efficiency of the system in the cyclic test was as high as 18%, which was approximately 2.5 times that of the fixed-duty-cycle one.

A dual-function damper with a large damping density, termed EHEMD, was fabricated. The EHEMD comprised an EMD connected to an adaptive-duty-cycle EHC. The fabricated prototype of the EHEMD was applied to a 135 m–long bridge cable as a passive control device. A constant equivalent resistance characteristic of the EHC was observed in the test. The experimental result demonstrates the capability of the EHEMD to simultaneously fulfill vibration control and energy harvesting functions, with approximately 67% further response reduction compared with that connected an open

circuit and 200 mW of output power. This is a strong proof-of-concept test to highlight the promising prospect of the EHEMD in a large-scale structure, although the overall power efficiency was merely 3% owing to the relatively large parasitic damping and relatively small design resistance.

The numerical study of an HST equipped with the EHEMD(s) demonstrates the potential to realize the adaptive damping control of the secondary suspension with an energy harvesting function. Given that the optimal damping requirements for different train speeds are different, the sensing information of the train speed was sent to the MCU for duty-cycle adjustment. The duty cycle was adjusted adaptively with the different train speeds. The numerical results demonstrate that the EHAC outperformed the EHPC in terms of vibration control; under a relatively high train speed, the EHAC could further reduce the vibration by ~40% compared with the reduction achieved by the EHPC. With the increase in the train speed from 100 to 340 km/h, the output power by one single EHEMD increased from 10.56 to 125.26 W, which is probably sufficient for a number of wireless sensors in train monitoring or semi-active/active vibration control. Meanwhile, it needs to mention that the optimizations of the two objectives of EHEMD in the train system were conflicting.

A fundamental question in dual-function dampers is whether the optimizations of the two objectives, i.e., vibration control and energy harvesting, are consistent or conflicting. In this study, the two objectives were set as the minimization of the structural kinetic energy and maximization of the input power. Different representative scenarios, including an SDOF structure coupled with an EHEMD, EHTMD, and EHTID individually, were analytically studied. The corresponding results conditionally and systematically clarify the ambiguity in dual-function dampers.

The closed-form solution for the optimal damping ratio and frequency tuning ratio of an EHTMD installed in a damped structure subjected to random excitation was derived.

The consistency between the vibration control and energy harvesting for EHTMD in this scene was analytically validated. Moreover, a larger mass ratio resulted in a large power distribution into the EHTMD, benefiting both vibration control and energy harvesting. Ten inerter-based networks, covering all possible networks containing two or three components (stiffness, damping, and inerter), were considered. Analytical and numerical results demonstrate that the introduction of a grounded inerter reduced the input excitation power and the gross output power when the system was subjected to random excitation. Further numerical optimal power distribution analysis indicated that for networks without a grounded inerter, the vibration control and energy harvesting were consistent, even under various inertances. For a given inerter ratio, the optimization of the two objectives in EHTID was always consistent, regardless of which network was applied.

EM energy harvesters in the second category typically contain an oscillating structure with a small mass and a limited effect on the vibration source.

An overall impedance optimization theory is proposed considering different excitation types, coupling effect strengths, and oscillator complexities. By considering the electromechanical dynamic analogy, the entire EM harvester, regardless of SDOF or MDOF oscillator, is presented by an equivalent circuit model. Based on this circuit model, the corresponding optimal impedance for the maximum output power and power efficiency is theoretically derived. The numerical results demonstrate that the classical IM, which ignores the oscillator and EMD characteristics cannot guarantee the maximum output power, whereas the overall IM can achieve the maximum output power under harmonic excitation. Furthermore, the numerical results under harmonic excitation indicate that the impedance for the maximum output power does not correspond to the maximum power efficiency. Given a relatively low oscillator damping, the maximum output power and power efficiency can be achieved simultaneously in the case of random excitation. By applying the overall IM strategy to each frequency of harmonic excitations, the electrical frequency tuning can improve the power performance in terms of energy

harvesting peak and bandwidth.

A DMP comprising two independent masses installed on a common vertical bar is proposed. It can provide a frequency tuning function by resetting the locations of the two individual masses, realizing novel mechanical frequency tuning. Its natural frequency can approach nearly zero, and the measured frequency was as low as 0.2 Hz in the free vibration tests of a small prototype. The dynamics of this DMP-based harvester subjected to horizontal or tilt base motions are discussed. In the shake table test, the power performance of this DMP-based energy harvester subjected to horizontal harmonic and random excitation validates the overall impedance optimization theory, although the constant-parasitic-damping and small-amplitude assumptions introduce certain errors into the analysis.

The DMP-based energy harvester was enclosed in a floating hull, thereby forming a novel floating-point absorber for wave energy conversion. A series of tests in a wave flume demonstrated the frequency tuning performance of this device, which ranged from 0.65 to 1.4 Hz. The output voltage under appropriate frequency tuning was 170% higher than that in the case without tuning. For the specific EHC mentioned above, only 31 mW output power was charged into the battery, but approximately 100 mW occurred at a wave height of 0.15 m when a pure load resistor was used. Additionally, the DMP-based harvester functions as an EHTMD for the floating hull to reduce the vibration responses under concerned wave periods. This finding demonstrates the potential of using this DMP-based harvester as a dual-function device for floating structures, such as the base of a floating wind turbine.

In conclusion, two configurations of vibration-based EM energy harvesters were investigated in this study. The scaled-up EM energy harvesters increase the machine constant (K_{eq}). As a result, the first configuration, comprising EMD and EHC, can simultaneously provide vibration control and energy harvesting functions owing to the

relatively larger coupling effect with the vibration sources. The feasibility and optimization of the dual-function devices were numerically and experimentally validated. The second configuration is EM energy harvesters with frequency tuning function. The power performance enhancements of this configuration by electrical and mechanical frequency tuning were demonstrated numerically and experimentally.

10.3 Discussions

Issues related to the presented work in this thesis, including the limitations and future work, are discussed in this section.

The energy-harvesting adaptive vibration control using the EHEMD, described in in Chapter 5, is still considered adaptive passive control. It may not be the optimal strategy for vibration suppression compared with semi-active control. Self-powered semi-active control based on the EHEMD is a more attractive solution. Noted that the EM damping force adjustment of the presented EHEMD has been proved. The potential solution is to integrate the information sensing, control algorithm operation, and PWM with duty cycle generation into the MCU.

The optimization of dual-function dampers was based on a strong assumption that the excitation is white noise random excitation with a constant PSD. However, the PSDs of some specific practical excitations (such as harmonic, waves, wind, earthquakes, etc.) cannot meet this condition. Hence, the trade-off between vibration control and energy harvesting objectives needs to be addressed under practical excitation other than white-noise random excitation. Moreover, a consistency analysis of the MDOF structure needs to be conducted for the sake of completeness.

In the overall impedance optimization theory, the conclusion that the optimal impedance under random excitation is a resistor is conditional. Notably, the connecting capacitor and inductor can be analogous to the inerter and stiffness, respectively.

According to the analysis of the inerter-based networks in Chapter 6, the input excitation power should decrease if the capacitor has a ground connection and the coil resistance is zero. Under random excitation, the optimizations of the power distribution in the inerter-based networks and the impedance optimization in EM harvesters were essentially consistent. Hence, a more accurate discussion on impedance optimization under random excitation considering the capacitor/inductor is needed. Furthermore, a corresponding theory for a nonlinear vibration-based energy harvester needs to be developed.

Although the feasibility of the frequency tuning function of the DMP-based energy harvester and point absorber has been proved in the experiment, the tuning is realized by manual adjustment. An approach involving automatic adjustment by sensing the vibration response/voltage is needed. One potential solution is to use the MCU in the EHC to sense the generated voltage of the EMD and then calculate the excitation frequency based on the voltage. With this excitation frequency and preprogrammed control algorithm, the MCU can send control signals to the stepper motors installed inside the moving masses to reach the target locations.

Furthermore, the wave flume tests only validate the potential energy harvesting performance of the DMP-based point absorber under regular wave scenarios. Tests under irregular wave scenarios should be conducted in future work. Meanwhile, the DMP-based energy harvester can be treated as an EHTMD. The results of the wave flume tests preliminarily demonstrate the feasibility of using this EHTMD for the vibration control of floating structures subjected to 6DOF motions. More systematic analyses and experiments on a 6DOF vibration platform should be performed to validate the complex behavior of the DMP.

REFERENCES

Abdelkareem, M. A., Xu, L., Ali, M. K. A., Elagouz, A., Mi, J., Guo, S., Liu, Y. and Zuo, L. (2018a). "Vibration energy harvesting in automotive suspension system: A detailed review." *Applied Energy*. 229: 672–699.

Abdelkareem, M. A., Xu, L., Zou, J., Ali, M. K. A., Essa, F. A., Elagouz, A., and Hassan, M. A. (2018b). "Energy-harvesting potential and vehicle dynamics conflict analysis under harmonic and random road excitations." *SAE Technical Paper*. No. 2018-01-0568.

Abdulkarem, M., Samsudin, K., Rokhani, F. Z., and A Rasid, M. F. (2020). "Wireless sensor network for structural health monitoring: A contemporary review of technologies, challenges, and future direction." *Structural Health Monitoring*. 19(3): 693–735.

Aboulfotoh, N. A., Arafa, M. H., and Megahed, S. M. (2013). "A self-tuning resonator for vibration energy harvesting." *Sensors and Actuators A: Physical*. 201: 328–334.

Ahamed, R., McKee, K., and Howard, I. (2020). "Advancements of wave energy converters based on power take off (PTO) systems: A review." *Ocean Engineering*. 204: 107248.

Akkaya, S. (2020). "A piezoelectric energy harvesting from the vibration of the airflow around a moving vehicle." *International Transactions on Electrical Energy Systems*. 30(12): e12655.

Anton, S. R., and Sodano, H. A. (2007). "A review of power harvesting using piezoelectric materials (2003–2006)." *Smart Materials and Structures*. 16(3): R1.

Arms, S. W., Townsend, C. P., Churchill, D. L., Galbreath, J. H., and Mundell, S. W. (2005, May). "Power management for energy harvesting wireless sensors." In *Smart Structures and Materials 2005: Smart Electronics, MEMS, BioMEMS, and Nanotechnology, International Society for Optics and Photonics*, San Diego, California, USA. Vol. 5763, pp. 267–275.

Arsem, H. B. (1971). "Electric shock absorber." *U.S. Patent No. 3,559,027*.

Asai, T., Araki, Y., and Ikago, K. (2018). "Structural control with tuned inertial mass

electromagnetic transducers." *Structural Control and Health Monitoring*. 25(2): e2059.

Augé, L. J. (2003). *Structural magnetic induction dampers in buildings*. M. Eng. thesis. Massachusetts Institute of Technology. USA.

Babarit, A. L., Clément, A. H., and Gilloteaux, J. C. (2005, January). "Optimization and time-domain simulation of the SEAREV wave energy converter." In *ASME 24th International Conference on Offshore Mechanics and Arctic Engineering*, Halkidiki, Greece. Vol. 2, pp. 703–712.

Ballo, I. G. O. R. (2007). "Comparison of the properties of active and semiactive suspension." *Vehicle System Dynamics*. 45(11): 1065–1073.

Bayik, B., Aghakhani, A., Aridogan, U., and Basdogan, I. (2014, September). "Piezoelectric patch-based energy harvesting on a heavy duty vehicle panel." In *Smart Materials, Adaptive Structures and Intelligent Systems, American Society of Mechanical Engineers*, Newport, Rhode Island, USA. Vol. 46155, p. V002T07A015.

Beeby, S. P., Tudor, M. J., and White, N. M. (2006). "Energy harvesting vibration sources for microsystems applications." *Measurement Science and Technology*. 17(12): R175.

Beeby, S. P., Tudor, M. J., Torah, R. N., Roberts, S., O'Donnell, T., and Roy, S. (2007). "Experimental comparison of macro and micro scale electromagnetic vibration powered generators." *Microsystem Technologies*. 13(11–12): 1647–1653.

Bowden, J. A., Burrow, S. G., Cammarano, A., Clare, L. R., and Mitcheson, P. D. (2014). "Switched-mode load impedance synthesis to parametrically tune electromagnetic vibration energy harvesters." *IEEE/ASME Transactions on Mechatronics*. 20(2): 603–610.

Brennan, M. J., Tang, B., Melo, G. P., and Lopes Jr, V. (2014). "An investigation into the simultaneous use of a resonator as an energy harvester and a vibration absorber." *Journal of Sound and Vibration*. 333(5): 1331–1343.

Bukhari, M., Malla, A., Kim, H., Barry, O., and Zuo, L. (2020). "On a self-tuning sliding-

mass electromagnetic energy harvester." *AIP Advances*. 10(9): 095227.

Burns, J. R. (1987). "Ocean wave energy conversion using piezoelectric material members." *U.S. Patent No. 4,685,296*.

Cahill, P., Nuallain, N. A. N., Jackson, N., Mathewson, A., Karoumi, R., and Pakrashi, V. (2014). "Energy harvesting from train-induced response in bridges." *Journal of Bridge Engineering*. 19(9): 04014034.

Cahill, P., Hazra, B., Karoumi, R., Mathewson, A., and Pakrashi, V. (2018). "Vibration energy harvesting based monitoring of an operational bridge undergoing forced vibration and train passage." *Mechanical Systems and Signal Processing*. 106: 265–283.

Cai, M., Yang, Z., Cao, J., and Liao, W. H. (2020). "Recent advances in human motion excited energy harvesting systems for wearables." *Energy Technology*. 8(10): 2000533.

Cammarano, A., Burrow, S. G., Barton, D. A. W., Carrella, A., and Clare, L. R. (2010). "Tuning a resonant energy harvester using a generalized electrical load." *Smart Materials and Structures*. 19(5): 055003.

Cammarano, A., Neild, S. A., Burrow, S. G., Wagg, D. J., and Inman, D. J. (2014). "Optimum resistive loads for vibration-based electromagnetic energy harvesters with a stiffening nonlinearity." *Journal of Intelligent Material Systems and Structures*. 25(14): 1757–1770.

Caruso, G., Chirianni, G., and Vairo, G. (2016). "Energy harvesting from wind-induced bridge vibrations via electromagnetic transduction." *Engineering Structures*. 115: 118–128.

Casciati, F., and Rossi, R. (2007). "A power harvester for wireless sensing applications." *Structural Control and Health Monitoring*. 14(4): 649–659.

Cassidy, I. L., Scruggs, J. T., Behrens, S., and Gavin, H. P. (2011). "Design and experimental characterization of an electromagnetic transducer for large-scale vibratory energy harvesting applications." *Journal of Intelligent Material Systems and Structures*. 22(17): 2009–2024.

Chalasani, S., and Conrad, J. M. (2008, April). “A survey of energy harvesting sources for embedded systems.” In *IEEE Southeastcon 2008*, Huntsville, Alabama, USA. pp. 442–447.

Challa, V. R., Prasad, M. G., Shi, Y., and Fisher, F. T. (2008). “A vibration energy harvesting device with bidirectional resonance frequency tunability.” *Smart Materials and Structures*. 17(1): 015035.

Chaplin, R. V., and Aggidis, G. A. (2007, May). “An investigation into power from pitch-surge point-absorber wave energy converters.” In *IEEE 2007 International Conference on Clean Electrical Power*, Capri, Italy. pp. 520–525.

Charnegie, D. (2007). *Frequency tuning concepts for piezoelectric cantilever beams and plates for energy harvesting*. Ph.D. thesis, University of Pittsburgh, USA.

Chen, C., and Liao, W. H. (2012). “A self-sensing magnetorheological damper with power generation.” *Smart Materials and Structures*. 21(2): 025014.

Chen, C., Zou, L., and Liao, W. H. (2015, April). “Regenerative magnetorheological dampers for vehicle suspensions.” In *Sensors and Smart Structures Technologies for Civil, Mechanical, and Aerospace Systems 2015, International Society for Optics and Photonics*, San Diego, California, USA. Vol. 9435, p. 94353K.

Chen, C., Chan, Y. S., Zou, L., and Liao, W. H. (2018). “Self-powered magnetorheological dampers for motorcycle suspensions.” *Proceedings of the Institution of Mechanical Engineers, Part D: Journal of Automobile Engineering*. 232(7): 921–935.

Chen, J., Qiu, Q., Han, Y., and Lau, D. (2019). “Piezoelectric materials for sustainable building structures: Fundamentals and applications.” *Renewable and Sustainable Energy Reviews*. 101: 14–25.

Cheng, S., Wang, N., and Arnold, D. P. (2007). “Modeling of magnetic vibrational energy harvesters using equivalent circuit representations.” *Journal of Micromechanics and Microengineering*. 17(11): 2328.

Chiu, Y., and Lee, Y. C. (2012). “Flat and robust out-of-plane vibrational electret energy harvester.” *Journal of Micromechanics and Microengineering*. 23(1): 015012.

Cho, S. W., Jung, H. J., and Lee, I. W. (2005). “Smart passive system based on magnetorheological damper.” *Smart Materials and Structures*. 14(4): 707.

Choi, Y. T., and Wereley, N. M. (2009). “Self-powered magnetorheological dampers.” *Journal of Vibration and Acoustics*. 131(4): 044501.

Claus, H., and Schiehlen, W. (1998). “Modeling and simulation of railway bogie structural vibrations.” *Vehicle System Dynamics*. 29(S1): 538–552.

Clough, R. W., and Penzien, J. (2003) *Dynamics of structures*. 3rd Edition, Berkeley: Computers and Structures, Inc.

Dell'Anna, F., Dong, T., Li, P., Wen, Y., Yang, Z., Casu, M. R., Azadmehr, M., and Berg, Y. (2018). “State-of-the-art power management circuits for piezoelectric energy harvesters.” *IEEE Circuits and Systems Magazine*. 18(3): 27–48.

Duan, D., Chen, F., Zhang, H., Yang, X., and Zhao F. (2020). “Study on capture power of the sealed-buoy wave energy converter in low energy flow density area.” *Renewable Energy*. 152, 1024–1034.

Eichhorn, C., Goldschmidtboeing, F., and Woias, P. (2008, November). “A frequency tunable piezoelectric energy converter based on a cantilever beam.” In *Proceedings of the International Workshops on Micro and Nanotechnology for Power Generation and Energy Conversion Applications - PowerMEMS*, Sendai, Japan. pp. 309–312.

Elliott, S. J., and Zilletti, M. (2014). “Scaling of electromagnetic transducers for shunt damping and energy harvesting.” *Journal of Sound and Vibration*. 333(8): 2185–2195.

Falcão, A. F. (2010). “Wave energy utilization: A review of the technologies.” *Renewable and Sustainable Energy Reviews*. 14(3): 899–918.

Falnes, J. (2007). “A review of wave-energy extraction.” *Marine Structures*. 20(4): 185–201.

Fan, K., Cai, M., Wang, F., Tang, L., Liang, J., Wu, Y., Qu, H., and Tan, Q. (2019). “A string-suspended and driven rotor for efficient ultra-low frequency mechanical energy harvesting.” *Energy Conversion and Management*. 198: 111820.

Fang, Z., Guo, X., Xu, L., and Zhang, H. (2013). “An optimal algorithm for energy recovery of hydraulic electromagnetic energy-regenerative shock absorber.” *Applied Mathematics and Information Sciences*. 7(6): 2207.

Feenstra, J., Granstrom, J., and Sodano, H. (2008). “Energy harvesting through a backpack employing a mechanically amplified piezoelectric stack.” *Mechanical Systems and Signal Processing*. 22(3): 721–734.

Feldman, M. (2011). “Hilbert transform in vibration analysis.” *Mechanical Systems and Signal Processing*. 25(3): 735–802.

Firestone, F. A. (1933). “A new analogy between mechanical and electrical systems.” *The Journal of the Acoustical Society of America*. 4(3): 249–267.

Garcia-Teruel, A., and Forehand, D. I. M. (2018, October). “Optimal wave energy converter geometry for different modes of motion.” In *Advances in Renewable Energies Offshore: Proceedings of the 3rd International Conference on Renewable Energies Offshore (RENEW 2018),* Lisbon, Portugal. pp. 299–305.

Gatti, G., Brennan, M. J., Tehrani, M. G., and Thompson, D. J. (2016). “Harvesting energy from the vibration of a passing train using a single-degree-of-freedom oscillator.” *Mechanical Systems and Signal Processing*. 66: 785–792.

Gonzalez-Buelga, A., Clare, L. R., Cammarano, A., Neild, S. A., Burrow, S. G., and Inman, D. J. (2014). “An optimised tuned mass damper/harvester device.” *Structural Control and Health Monitoring*. 21(8): 1154–1169.

Guo, X., Zhang, Y., Fan, K., Lee, C., and Wang, F. (2020). “A comprehensive study of non-linear air damping and “pull-in” effects on the electrostatic energy harvesters.” *Energy Conversion and Management.* 203: 112264.

Halim, M. A., Rantz, R., Zhang, Q., Gu, L., Yang, K., and Roundy, S. (2018). “An electromagnetic rotational energy harvester using sprung eccentric rotor, driven by pseudo-walking motion.” *Applied Energy*. 217: 66–74.

Hambley, A. R., Kumar, N., and Kulkarni, A. R. (2013). *Electrical engineering: principles and applications*. 6th Edition, Upper Saddle River, NJ: Pearson Prentice Hall.

Harne, R. L. (2013). “Development and testing of a dynamic absorber with corrugated piezoelectric spring for vibration control and energy harvesting applications.” *Mechanical Systems and Signal Processing*. 36(2): 604–617.

Harne, R. L. (2013). “Modeling and analysis of distributed electromagnetic oscillators for broadband vibration attenuation and concurrent energy harvesting.” *Applied Mathematical Modelling*. 37(6): 4360–4370.

Harne, R. L., and Wang, K. W. (2013). “A review of the recent research on vibration energy harvesting via bistable systems.” *Smart Materials and Structures*. 22(2): 023001.

Hansen, S. E., Pourghodrat, A., Nelson, C. A., and Fateh, M. (2010, April). “On-track testing of a power harvesting device for railroad track health monitoring.” In *Health Monitoring of Structural and Biological Systems 2010, International Society for Optics and Photonics*, San Diego, California, USA. Vol. 7650, p. 76500Y.

Hu, G., Tang, L., Das, R., and Marzocca, P. (2018). “A two-degree-of-freedom piezoelectric energy harvester with stoppers for achieving enhanced performance.” *International Journal of Mechanical Sciences*. 149: 500–507.

Hu, X., Wang, B., and Ji, H. (2013). “A wireless sensor network-based structural health monitoring system for highway bridges.” *Computer-Aided Civil and Infrastructure Engineering*. 28(3): 193–209.

Iqbal, M., Nauman, M. M., Khan, F. U., Abas, P. E., Cheok, Q., Iqbal, A., and Aissa, B. (2021). “Vibration-based piezoelectric, electromagnetic, and hybrid energy harvesters for microsystems applications: A contributed review.” *International Journal of Energy Research*. 45: 65–102.

Jahangiri, V., and Sun, C. (2019). “Integrated bi-directional vibration control and energy harvesting of monopile offshore wind turbines.” *Ocean Engineering*. 178: 260–269.

Jamshidi, M., Chang, C. C., and Bakhshi, A. (2017). “Self-powered hybrid electromagnetic damper for cable vibration mitigation.” *Smart Structures and Systems*. 20(3): 285–301.

Jamshidi, M., Chang, C. C., and Bakhshi, A. (2018). “Design and control of a self-

powered hybrid electromagnetic damper." *Journal of Sound and Vibration*. 428: 147–167.

Johnson, E. A., Baker, G. A., Spencer Jr, B. F., and Fujino, Y. (2007). "Semiactive damping of stay cables." *Journal of Engineering Mechanics*. 133(1): 1–11.

Jung, H. J., Kim, I. H., and Jang, S. J. (2011a). "An energy harvesting system using the wind-induced vibration of a stay cable for powering a wireless sensor node." *Smart Materials and Structures*. 20(7): 075001.

Jung, H. J., Kim, I. H., and Koo, J. H. (2011b). "A multi-functional cable-damper system for vibration mitigation, tension estimation and energy harvesting." *Smart Structures and Systems*. 7(5): 379–392.

Jung, H. J., Park, J., and Kim, I. H. (2012). "Investigation of applicability of electromagnetic energy harvesting system to inclined stay cable under wind load." *IEEE Transactions on Magnetics*. 48(11): 3478–3481.

Karnopp, D. (1989). "Permanent magnet linear motors used as variable mechanical dampers for vehicle suspensions." *Vehicle System Dynamics*. 18(4): 187–200.

Kecik, K., and Mitura, A. (2020). "Energy recovery from a pendulum tuned mass damper with two independent harvesting sources." *International Journal of Mechanical Sciences*. 105568.

Khan, F. U., and Ali, T. (2019). "A piezoelectric based energy harvester for simultaneous energy generation and vibration isolation." *International Journal of Energy Research*. 43(11): 5922–5931.

Kim, I. H., Jang, S. J., and Jung, H. J. (2013). "Performance enhancement of a rotational energy harvester utilizing wind-induced vibration of an inclined stay cable." *Smart Materials and Structures*. 22(7): 075004.

Kopylov, S., Chen, Z., and Abdelkareem, M. A. (2020). "Implementation of an electromagnetic regenerative tuned mass damper in a vehicle suspension system." *IEEE Access*. 8: 110153–110163.

Kovacs I. (1982) "Zurfrage der seilschwingungen und der seildämpfung." *Bautechnik*. 59(10).

Krack, M., Aboulfotoh, N., Twiefel, J., Wallaschek, J., Bergman, L. A., and Vakakis, A. F. (2017). “Toward understanding the self-adaptive dynamics of a harmonically forced beam with a sliding mass.” *Archive of Applied Mechanics*. 87(4): 699–720.

Kremer, D., and Liu, K. (2017). “A nonlinear energy sink with an energy harvester: harmonically forced responses.” *Journal of Sound and Vibration*. 410: 287–302.

Kye, S., Jung, H. J., and Jung, H. Y. (2019). “Experimental investigation on a cable structure equipped with an electrodynamic damper and its monitoring strategy through energy harvesting.” *Sensors*. 19(11): 2631.

Lafarge, B., Grondel, S., Delebarre, C., and Cattan, E. (2018). “A validated simulation of energy harvesting with piezoelectric cantilever beams on a vehicle suspension using Bond Graph approach.” *Mechatronics*. 53: 202–214.

Lai, S. K., Wang, C., and Zhang, L. H. (2019). “A nonlinear multi-stable piezomagnetoelastic harvester array for low-intensity, low-frequency, and broadband vibrations.” *Mechanical Systems and Signal Processing*. 122: 87–102.

Leadenham, S., and Erturk, A. (2014). “M-shaped asymmetric nonlinear oscillator for broadband vibration energy harvesting: harmonic balance analysis and experimental validation.” *Journal of Sound and Vibration*. 333(23): 6209–6223.

Lee, J., and Choi, B. (2014). “Development of a piezoelectric energy harvesting system for implementing wireless sensors on the tires.” *Energy Conversion and Management*. 78: 32–38.

Lefeuvre, E., Audigier, D., Richard, C., and Guyomar, D. (2007). “Buck–boost converter for sensorless power optimization of piezoelectric energy harvester.” *IEEE Transactions on Power Electronics*. 22(5): 2018–2025.

Lei, X. (2017). *High speed railway track dynamics: models, algorithms and applications.* Berlin: Springer.

Li, C., and Tse, W. (2013). “Fabrication and testing of an energy-harvesting hydraulic damper.” *Smart Materials and Structures*. 22(6): 065024.

Li, C., Zhu, R., Liang, M., and Yang, S. (2014). “Integration of shock absorption and energy harvesting using a hydraulic rectifier.” *Journal of Sound and Vibration*.

333(17): 3904–3916.

Li, J. Y., and Zhu, S. (2021) “Self-powered active vibration control: Concept, modeling and testing.” *Engineering*. Accepted.

Li, J. Y., Zhu, S., Shi, X., and Shen, W. (2020). “Electromagnetic shunt damper for bridge cable vibration mitigation: Full-scale experimental study.” *Journal of Structural Engineering*. 146(1): 04019175.

Li, M., and Jing, X. (2019). “Novel tunable broadband piezoelectric harvesters for ultralow-frequency bridge vibration energy harvesting.” *Applied Energy*. 255: 113829.

Li, P., and Zuo, L. (2013, August). “Equivalent circuit modeling of vehicle dynamics with regenerative shock absorbers.” In *International Design Engineering Technical Conferences and Computers and Information in Engineering Conference, American Society of Mechanical Engineers*, Portland, Oregon, USA. Vol. 55843, p. V001T01A011.

Li, S., Xu, J., Pu, X., Tao, T., and Mei, X. (2019). “A novel design of a damping failure free energy-harvesting shock absorber system.” *Mechanical Systems and Signal Processing*. 132: 640–653.

Li, X., Martin, D., Liang, C., Chen, C., Parker, R. G., and Zuo, L. (2020). “Characterization and verification of a two-body wave energy converter with a novel power take-off.” *Renewable Energy*. 163: 910–920.

Li, Z., Zuo, L., Luhrs, G., Lin, L., and Qin, Y. X. (2012). “Electromagnetic energy-harvesting shock absorbers: Design, modeling, and road tests.” *IEEE Transactions on Vehicular Technology*. 62(3): 1065–1074.

Liang, C., Ai, J., and Zuo, L. (2017). “Design, fabrication, simulation and testing of an ocean wave energy converter with mechanical motion rectifier.” *Ocean Engineering*. 136: 190–200.

Liang, J., and Liao, W. H. (2011). “Impedance modeling and analysis for piezoelectric energy harvesting systems.” *IEEE/ASME Transactions on Mechatronics*. 17(6): 1145–1157.

Liao, Y., and Sodano, H. (2009). “Optimal power, power limit and damping of vibration based piezoelectric power harvesters.” *Smart Materials and Structures*. 27(7): 075057.

Liao, Y., and Sodano, H. (2018). “Optimal power, power limit and damping of vibration based piezoelectric power harvesters.” *Smart Materials and Structures*. 27(7): 075057.

Liao, Y., and Liang, J. (2018). “Maximum power, optimal load, and impedance analysis of piezoelectric vibration energy harvesters.” *Smart Materials and Structures*. 27(7): 075053.

Lin, T., Pan, Y., Chen, S., and Zuo, L. (2018). “Modeling and field testing of an electromagnetic energy harvester for rail tracks with anchorless mounting.” *Applied Energy*. 213: 219–226.

Liu, C., Zhang, N., Li, J., Dong, L., Wang, T., Wang, Z., Wang, G., Zhou, X., and Zhang, J. (2019). “Harvesting ultralow frequency (<1 Hz) mechanical energy using triboelectric nanogenerator.” *Nano Energy*. 65: 104011.

Liu, J., Li, X., Wang, Z., and Zhang, Y. (2016). “Modelling and experimental study on active energy-regenerative suspension structure with variable universe fuzzy PD control.” *Shock and Vibration*. 2016: 6170275.

Liu, Y. (2016). *Design, modeling and control of vibration systems with electromagnetic energy harvesters and their application to vehicle suspensions*. Ph.D. thesis, Virginia Polytechnic Institute and State University, USA.

Liu, Y., Lin, C. C., Parker, J., and Zuo, L. (2016). “Exact H_2 optimal tuning and experimental verification of energy-harvesting series electromagnetic tuned-mass dampers.” *Journal of Vibration and Acoustics*. 138(6): 061003.

Loong, C.N. (2020). *Vibration mitigation and energy scavenging of a nonlinear electromagnetic energy harvester - structure system*. Ph.D. thesis, The Hong Kong University of Science and Technology, Hong Kong.

Loong, C. N., and Chang, C. C. (2020). “Performance of a nonlinear electromagnetic energy harvester–structure system under random excitation.” *Journal of*

Engineering Mechanics. 146(9): 04020098.

Lu, Q., Loong, C., Chang, C. C., and Dimitrakopoulos, E. G. (2014, April). "Scavenging vibration energy from seismically isolated bridges using an electromagnetic harvester." In *Sensors and Smart Structures Technologies for Civil, Mechanical, and Aerospace Systems 2014, International Society for Optics and Photonics*, San Diego, California, USA. Vol. 9061, p. 90610I.

Luo, Y., Sun, H., Wang, X., Zuo, L., and Chen, N. (2017). "Wind induced vibration control and energy harvesting of electromagnetic resonant shunt tuned mass-damper-inerter for building structures." *Shock and Vibration*. 2017: 4180134.

Lynch, J. P., and Loh, K. J. (2006). "A summary review of wireless sensors and sensor networks for structural health monitoring." *Shock and Vibration Digest*. 38(2): 91–130.

Maamer, B., Boughamoura, A., El-Bab, A. M. F., Francis, L. A., and Tounsi, F. (2019). "A review on design improvements and techniques for mechanical energy harvesting using piezoelectric and electromagnetic schemes." *Energy Conversion and Management*. 199: 111973.

Mallick, D., and Roy, S. (2015). "Bidirectional electrical tuning of FR4 based electromagnetic energy harvesters." *Sensors and Actuators A: Physical*. 226: 154–162.

Mann, B. P., and Owens, B. A. (2010). "Investigations of a nonlinear energy harvester with a bistable potential well." *Journal of Sound and Vibration*. 329(9): 1215–1226.

Marian, L., and Giaralis, A. (2017). "The tuned mass-damper-inerter for harmonic vibrations suppression, attached mass reduction, and energy harvesting." *Smart Structures and Systems*. 19(6): 665–678.

McDaid, A. J., and Mace, B. R. (2013). "A self-tuning electromagnetic vibration absorber with adaptive shunt electronics." *Smart Materials and Structures*. 22(10): 105013.

Mi, J., Xu, L., Guo, S., Abdelkareem, M. A., and Meng, L. (2017). "Suspension performance and energy harvesting property study of a novel railway vehicle bogie with the hydraulic-electromagnetic energy-regenerative shock absorber." *SAE*

Technical Paper. No. 2017-01-1483.

Miller, L. M., Pillatsch, P., Halvorsen, E., Wright, P. K., Yeatman, E. M., and Holmes, A. S. (2013). "Experimental passive self-tuning behavior of a beam resonator with sliding proof mass." *Journal of Sound and Vibration*. 332(26): 7142–7152.

Miller, T. I., Spencer, B. F. Jr., Li, J. and Jo, H. (2010). "Solar energy harvesting and software enhancements for autonomous wireless smart sensor network." *NSEL Report No. NSEL-022.* University of Illinois at Urbana-Champaign, Illinois, USA.

Mitcheson, P. D. (2005). *Analysis and optimisation of energy-harvesting micro-generator systems*. Ph.D. thesis, Imperial College London, United Kingdom.

Mitcheson, P. D., Toh, T. T., Wong, K. H., Burrow, S. G., and Holmes, A. S. (2011). "Tuning the resonant frequency and damping of an electromagnetic energy harvester using power electronics." *IEEE Transactions on Circuits and Systems II: Express Briefs*. 58(12): 792–796.

Mofidian, S. M., and Bardaweel, H. (2019). "A dual-purpose vibration isolator energy harvester: experiment and model." *Mechanical Systems and Signal Processing*. 118: 360–376.

Mossberg, J., Anderson, Z., Tucker, C., and Schneider, J. (2012). "Recovering energy from shock absorber motion on heavy duty commercial vehicles." *SAE Technical Paper*. No. 2012-01-0814.

Murray, R., and Rastegar, J. (2009, April). "Novel two-stage piezoelectric-based ocean wave energy harvesters for moored or unmoored buoys." In *Active and Passive Smart Structures and Integrated Systems 2009, International Society for Optics and Photonics*, San Diego, California, USA. Vol. 7288, p. 72880E.

Nakano, K., Suda, Y., and Nakadai, S. (1999, September). "Self-powered active vibration control with continuous control input (application to a cab suspension of a heavy duty truck)." In *1999 ASME Design Engineering Technical Conferences*, Las Vegas, Nevada, USA. pp. 181–188.

Nakano, K., Suda, Y., and Nakadai, S. (2003). "Self-powered active vibration control using a single electric actuator." *Journal of Sound and Vibration*. 260(2): 213–235.

Nelson, C. A., Platt, S. R., Albrecht, D., Kamarajugadda, V., and Fateh, M. (2008, April). "Power harvesting for railroad track health monitoring using piezoelectric and inductive devices." In *Active and Passive Smart Structures and Integrated Systems 2008, International Society for Optics and Photonics*, San Diego, California, USA. Vol. 6928, p. 69280R.

Nelson, C. A., Platt, S. R., Hansen, S. E., and Fateh, M. (2009, April). "Power harvesting for railroad track safety enhancement using vertical track displacement." In *Active and Passive Smart Structures and Integrated Systems 2009, International Society for Optics and Photonics*, San Diego, California, USA. Vol. 7288, p. 728811.

Newell, D., and Duffy, M. (2019). "Review of power conversion and energy management for low-power, low-voltage energy harvesting powered wireless sensors." *IEEE Transactions on Power Electronics*. 34(10): 9794–9805.

Ni, T., Zuo, L., and Kareem, A. (2011, January). "Assessment of energy potential and vibration mitigation of regenerative tuned mass dampers on wind excited tall buildings." In *2011 ASME International Design Engineering Technical Conferences and Computers and Information in Engineering Conference*, Washington DC, USA. Vol. 54785, pp. 333–342.

Ning, D., Sun, S., Du, H., Li, W., and Zhang, N. (2018a). "Vibration control of an energy regenerative seat suspension with variable external resistance." *Mechanical Systems and Signal Processing*. 106: 94–113.

Ning, D., Du, H., Sun, S., Li, W., and Li, W. (2018b). "An energy saving variable damping seat suspension system with regeneration capability." *IEEE Transactions on Industrial Electronics*. 65(10): 8080–8091.

Ning, D., Du, H., Sun, S., Zheng, M., Li, W., Zhang, N., and Jia, Z. (2019). "An electromagnetic variable stiffness device for semiactive seat suspension vibration control." *IEEE Transactions on Industrial Electronics*. 67(8): 6773–6784.

Ormondroyd, J., and Den Hartog, J. P. (1928). "The theory of the dynamic vibration absorber." *Transactions of the ASME, Journal of Applied Mechanics*. 50: 9–22.

OVM Co. Ltd. 2014. "OVM GJ prefabricated strand cable system with integral swaging

anchorage." Accessed December 2020. http://kwansooweb.cafe24.com/wp-content/uploads/2016/02/Prefabricated-Strand-Cable.pdf

Palomera-Arias, R. (2005). *Passive electromagnetic damping device for motion control of building structures*. Ph.D. thesis, Massachusetts Institute of Technology. USA.

Palomera-Arias, R., Connor, J. J., and Ochsendorf, J. A. (2008). "Feasibility study of passive electromagnetic damping systems." *Journal of Structural Engineering*. 134(1): 164–170.

Pan, P., Zhang, D., Nie, X., and Chen, H. (2017). "Development of piezoelectric energy-harvesting tuned mass damper." *Science China Technological Sciences*. 60(3): 467–478.

Park, G., Rosing, T., Todd, M. D., Farrar, C. R., and Hodgkiss, W. (2008). "Energy harvesting for structural health monitoring sensor networks." *Journal of Infrastructure Systems*. 14(1): 64–79.

Park, J. Y., Salauddin, M., and Rasel, M. S. (2019). "Nanogenerator for scavenging low frequency vibrations." *Journal of Micromechanics and Microengineering*. 29(5): 053001.

Pastor, J., and Liu, Y. (2014). "Power absorption modeling and optimization of a point absorbing wave energy converter using numerical method." *Journal of Energy Resources Technology*. 136(2): 021207.

Payne, G. (2008). "Guidance for the experimental tank testing of wave energy converters." *SuperGen Marine*. 254.

Peigney, M., and Siegert, D. (2013). "Piezoelectric energy harvesting from traffic-induced bridge vibrations." *Smart Materials and Structures*. 22(9): 095019.

Pecher, A., and Peter, Kofoed, J. (2017). *Handbook of ocean wave energy*. Springer Nature.

Peters, C., Maurath, D., Schock, W., Mezger, F., and Manoli, Y. (2009). "A closed-loop wide-range tunable mechanical resonator for energy harvesting systems." *Journal of Micromechanics and Microengineering*. 19(9): 094004.

Pillatsch, P., Miller, L. M., Halvorsen, E., Wright, P. K., Yeatman, E. M., and Holmes, A.

S. (2013, December). “Self-tuning behavior of a clamped-clamped beam with sliding proof mass for broadband energy harvesting.” In *Journal of Physics: Conference Series*, Vol. 476, No. 1, p. 012068.

Platt, S. R., Farritor, S., and Haider, H. (2005). “On low-frequency electric power generation with PZT ceramics.” *IEEE/ASME Transactions on Mechatronics*. 10(2): 240–252.

Pourghodrat, A. (2011). *Energy harvesting systems design for railroad safety*. M.Sc. thesis, University of Nebraska-Lincoln, USA.

Pozzi, N. (2018). *Numerical modeling and experimental testing of a pendulum wave energy converter (PeWEC)*. Ph.D. thesis, Politecnico di Torino, Torino, Italy.

Priya, S. (2005). “Modeling of electric energy harvesting using piezoelectric windmill.” *Applied Physics Letters*. 87(18): 184101.

Qian, F., Luo, Y., Sun, H., Tai, W. C., and Zuo, L. (2019). “Optimal tuned inerter dampers for performance enhancement of vibration isolation.” *Engineering Structures*. 198: 109464.

Renno, J. M., Daqaq, M. F., and Inman, D. J. (2009). “On the optimal energy harvesting from a vibration source.” *Journal of Sound and Vibration*. 320(1–2): 386–405.

Resen Waves. Accessed December 2020. http://www.resenwaves.com/

Rome, L. C., Flynn, L., Goldman, E. M., and Yoo, T. D. (2005). “Generating electricity while walking with loads.” *Science*. 309(5741): 1725–1728.

Roundy, S., and Wright, P. K. (2004). “A piezoelectric vibration based generator for wireless electronics.” *Smart Materials and Structures*. 13(5): 1131.

Safaei, M., Sodano, H. A., and Anton, S. R. (2019). “A review of energy harvesting using piezoelectric materials: state-of-the-art a decade later (2008–2018).” *Smart Materials and Structures*. 28(11): 113001.

Saha, C. R., O’Donnell, T., Wang, N., and McCloskey, P. (2008). “Electromagnetic generator for harvesting energy from human motion.” *Sensors and Actuators A: Physical*. 147(1): 248–253.

Samad, F. A., Karim, M. F., Paulose, V., and Ong, L. C. (2015). “A curved electromagnetic

energy harvesting system for wearable electronics." *IEEE Sensors Journal*. 16(7): 1969–1974.

Sarmento, A. J. N. A., Neumann, F., and Brito-Melo, A. (2004, June). "Non-technical barriers to large-scale wave energy utilisation." In *2004 New and renewable energy technologies for sustainable development,* Evora, Portugal. pp. 225–233.

Sazonov, E., Li, H., Curry, D., and Pillay, P. (2009). "Self-powered sensors for monitoring of highway bridges." *IEEE Sensors Journal*. 9(11): 1422–1429.

Shadman, M., Estefen, S. F., Rodriguez, C. A., and Nogueira, I. C. (2018). "A geometrical optimization method applied to a heaving point absorber wave energy converter." *Renewable Energy*. 115: 533–546.

Shahruz, S. M. (2006). "Design of mechanical band-pass filters for energy scavenging." *Journal of Sound and Vibration*. 292(3–5): 987–998.

Shaikh, F. K., and Zeadally, S. (2016). "Energy harvesting in wireless sensor networks: A comprehensive review." *Renewable and Sustainable Energy Reviews*. 55: 1041–1054.

Shen, W. (2014). *Electromagnetic damping and energy harvesting devices in civil structures*. Ph.D. thesis, The Hong Kong Polytechnic University, Hong Kong.

Shen, W. A., Zhu, S., and Xu, Y. L. (2012). "An experimental study on self-powered vibration control and monitoring system using electromagnetic TMD and wireless sensors." *Sensors and Actuators A: Physical*. 180: 166–176.

Shen, W., and Zhu, S. (2015). "Harvesting energy via electromagnetic damper: Application to bridge stay cables." *Journal of Intelligent Material Systems and Structures*. 26(1): 3–19.

Shen, W., Zhu, S., and Zhu, H. (2016a). "Experimental study on using electromagnetic devices on bridge stay cables for simultaneous energy harvesting and vibration damping." *Smart Materials and Structures*. 25(6): 065011.

Shen, W., Zhu, S., Zhu, H., and Xu, Y. L. (2016b). "Electromagnetic energy harvesting from structural vibrations during earthquakes." *Smart Structures and Systems*. 18(3): 449–470.

Shen, W., Zhu, S., Xu, Y. L., and Zhu, H. P. (2018). "Energy regenerative tuned mass dampers in high-rise buildings." *Structural Control and Health Monitoring*. 25(2): e2072.

Shen, W., Zhu, S., and Zhu, H. (2019). "Unify energy harvesting and vibration control functions in randomly excited structures with electromagnetic devices." *Journal of Engineering Mechanics*. 145(1): 04018115.

Shen, W., Long, Z., Wang, H., and Zhu, H. (2021). "Power analysis of SDOF structures with tuned inerter dampers subjected to earthquake ground motions." *ASCE-ASME Journal of Risk and Uncertainty in Engineering Systems, Part B: Mechanical Engineering*. 7(1): 010907.

Shenck, N. S., and Paradiso, J. A. (2001). "Energy scavenging with shoe-mounted piezoelectrics." *IEEE Micro*. 21(3): 30–42.

Shi, D., Chen, L., Wang, R., Jiang, H., and Shen, Y. (2014). "Design and experiment study of a semi-active energy-regenerative suspension system." *Smart Materials and Structures*. 24(1): 015001.

Shi, M. (2013). *Energy harvesting from wind-induced vibration of suspension bridges*. M. Eng. thesis, Massachusetts Institute of Technology, USA.

Shi, X., Zhu, S., Ni, Y. Q., and Li, J. (2018). "Vibration suppression in high-speed trains with negative stiffness dampers." *Smart Structures and Systems*. 21(5): 653–668.

Shinbrot, T., Grebogi, C., Wisdom, J., and Yorke, J. A. (1992). "Chaos in a double pendulum." *American Journal of Physics*. 60(6): 491–499.

Siddique, A. R. M., Mahmud, S., and Van Heyst, B. (2015). "A comprehensive review on vibration based micro power generators using electromagnetic and piezoelectric transducer mechanisms." *Energy Conversion and Management*. 106: 728–747.

Singh, S., and Satpute, N. V. (2015). "Design and analysis of energy-harvesting shock absorber with electromagnetic and fluid damping." *Journal of Mechanical Science and Technology*. 29(4): 1591-1605.

Smith, M. C. (2002). "Synthesis of mechanical networks: the inerter." *IEEE Transactions on Automatic Control*. 47(10): 1648–1662.

Sodano, H. A., Inman, D. J., and Park, G. (2004). “A review of power harvesting from vibration using piezoelectric materials.” *Shock and Vibration Digest*. 36(3): 197–206.

Soliman, M. S. M., Abdel-Rahman, E. M., El-Saadany, E. F., and Mansour, R. R. (2008). “A wideband vibration-based energy harvester.” *Journal of Micromechanics and Microengineering*. 18(11): 115021.

Spencer Jr, B. F., Ruiz-Sandoval, M. E., and Kurata, N. (2004). “Smart sensing technology: Opportunities and challenges.” *Structural Control and Health Monitoring*. 11(4): 349–368.

Staaf, L. G. H., Smith, A. D., Köhler, E., Lundgren, P., Folkow, P. D., and Enoksson, P. (2018). “Achieving increased bandwidth for 4 degree of freedom self-tuning energy harvester.” *Journal of Sound and Vibration*. 420: 165–173.

Staaf, L. G. H., Smith, A. D., Lundgren, P., Folkow, P. D., and Enoksson, P. (2019). “Effective piezoelectric energy harvesting with bandwidth enhancement by assymetry augmented self-tuning of conjoined cantilevers.” *International Journal of Mechanical Sciences*. 150: 1–11.

Starner, T., and Paradiso, J. A. (2004). “Human generated power for mobile electronics.” *Low-power Electronics Design*. 45: 1–35.

Stephen, N. G. (2006). “On energy harvesting from ambient vibration.” *Journal of Sound and Vibration*. 293(1–2): 409–425.

Suda, Y., and Shiiba, T. (1996). “A new hybrid suspension system with active control and energy regeneration.” *Vehicle System Dynamics*. 25(S1): 641–654.

Suda, Y., Nakadai, S., and Nakano, K. (1998a). “Study on the self-powered active vibration control.” *Ratio*. 10: 9.

Suda, Y., Nakadai, S., and Nakano, K. (1998b). “Hybrid suspension system with skyhook control and energy regeneration (development of self-powered active suspension).” *Vehicle System Dynamics*. 29(S1): 619–634.

Sugiura, K., Watanabe, Y., Asai, T., Araki, Y., and Ikago, K. (2020). “Experimental characterization and performance improvement evaluation of an electromagnetic

transducer utilizing a tuned inerter." *Journal of Vibration and Control*. 26(1–2): 56–72.

Suzuki, Y., Miki, D., Edamoto, M., and Honzumi, M. (2010). "A MEMS electret generator with electrostatic levitation for vibration-driven energy-harvesting applications." *Journal of Micromechanics and Microengineering*. 20(10): 104002.

Symans, M. D., and Constantinou, M. C. (1999). "Semi-active control systems for seismic protection of structures: a state-of-the-art review." *Engineering Structures*. 21(6): 469–487.

Szarka, G. D., Stark, B. H., and Burrow, S. G. (2011). "Review of power conditioning for kinetic energy harvesting systems." *IEEE Transactions on Power Electronics*. 27(2): 803–815.

Tang, L., and Yang, Y. (2012). "A multiple-degree-of-freedom piezoelectric energy harvesting model." *Journal of Intelligent Material Systems and Structures*. 23(14): 1631–1647.

Tang, L., Yang, Y., and Soh, C. K. (2010). "Toward broadband vibration-based energy harvesting." *Journal of Intelligent Material Systems and Structures*. 21(18): 1867–1897.

Tang, X. (2013). *Simultaneous energy harvesting and vibration control of tall buildings using electricity-generating tuned mass dampers*. Ph.D. thesis, Stony Brook University, New York, USA.

Tang, X., and Zuo, L. (2010, June). "Regenerative semi-active control of tall building vibration with series TMDs." In *Proceedings of the 2010 American Control Conference. IEEE*, Baltimore, Maryland, USA. pp. 5094–5099.

Tang, X., and Zuo, L. (2011). "Enhanced vibration energy harvesting using dual-mass systems." *Journal of Sound and Vibration*. 330(21): 5199–5209.

Tang, X., and Zuo, L. (2012). "Simultaneous energy harvesting and vibration control of structures with tuned mass dampers." *Journal of Intelligent Material Systems and Structures*. 23(18): 2117–2127.

Tavares, R., and Ruderman, M. (2020). "Energy harvesting using piezoelectric

transducers for suspension systems." *Mechatronics*. 65: 102294.

Toffoli, A., and Bitner-Gregersen, E. M. (2017). "Types of ocean surface waves, wave classification." *Encyclopedia of Maritime and Offshore Engineering*. 1–8.

Toh, T. T., Mitcheson, P. D., Dussud, L., Wright, S. W., and Holmes, A. S. (2011, November). "Electronic resonant frequency tuning of a marine energy harvester." In *Proceedings of the International Workshops on Micro and Nanotechnology for Power Generation and Energy Conversion Applications - PowerMEMS*, Seoul, Korea, pp. 383–386.

Tollefson, J. (2014). "Blue energy: After years in the doldrums, the quest to harvest energy from the oceans is gathering speed." *Nature*. 508(7496): 302–305.

Vantorre, M., Banasiak, R., and Verhoeven, R. (2004). "Modelling of hydraulic performance and wave energy extraction by a point absorber in heave." A*pplied Ocean Research*. 26(1–2): 61–72.

Viet, N. V., Xie, X. D., Liew, K. M., Banthia, N., and Wang, Q. (2016). "Energy harvesting from ocean waves by a floating energy harvester." *Energy*. 112: 1219–1226.

Viet, N. V., and Wang, Q. (2018). "Ocean wave energy pitching harvester with a frequency tuning capability." *Energy*. 162: 603–617.

Wang, F., and Hansen, O. (2014). "Electrostatic energy harvesting device with out-of-the-plane gap closing scheme." *Sensors and Actuators A: Physical*. 211: 131–137.

Wang, J., Lin, T., and Zuo, L. (2013, August). "High efficiency electromagnetic energy harvester for railroad application." In *ASME 18th International Design Engineering Technical Conferences and Computers and Information in Engineering Conference*, Portland, Oregon, USA. Vol. 4.

Wang, J., Shi, Z., Xiang, H., and Song, G. (2015). "Modeling on energy harvesting from a railway system using piezoelectric transducers." *Smart Materials and Structures*. 24(10): 105017.

Wang, L., Engström, J., Göteman, M., and Isberg, J. (2015). "Constrained optimal control of a point absorber wave energy converter with linear generator." *Journal of Renewable and Sustainable Energy*. 7(4): 043127.

Wang, M., Yin, P., Li, Z., Sun, Y., Ding, J., Luo, J., Xie, X., Peng, Y., and Pu, H. (2020). "Harnessing energy from spring suspension systems with a compressive-mode high-power-density piezoelectric transducer." *Energy Conversion and Management*. 220: 113050.

Wang, P., Mei, T. X., Zhang, J., and Li, H. (2015). "Self-powered active lateral secondary suspension for railway vehicles." *IEEE Transactions on Vehicular Technology*. 65(3): 1121–1129.

Wang, Y., and Inman, D. J. (2012). "A survey of control strategies for simultaneous vibration suppression and energy harvesting via piezoceramics." *Journal of Intelligent Material Systems and Structures*. 23(18): 2021–2037.

Wang, Y., and Inman, D. J. (2013). "Simultaneous energy harvesting and gust alleviation for a multifunctional composite wing spar using reduced energy control via piezoceramics." *Journal of Composite Materials*. 47(1): 125–146.

Wang, Z., Chen, Z., and Spencer Jr, B. F. (2009, March). "Self-powered and sensing control system based on MR damper: presentation and application." In *Sensors and Smart Structures Technologies for Civil, Mechanical, and Aerospace Systems 2009, International Society for Optics and Photonics*, San Diego, California, USA. Vol. 7292, p. 729240.

Wang, Z. L. (2017). "On Maxwell's displacement current for energy and sensors: The origin of nanogenerators." *Materials Today*. 20(2): 74–82.

Warburton, G. B. (1982). "Optimum absorber parameters for various combinations of response and excitation parameters." *Earthquake Engineering and Structural Dynamics*. 10(3): 381–401.

Wei, C., and Jing, X. (2017). "A comprehensive review on vibration energy harvesting: Modelling and realization." *Renewable and Sustainable Energy Reviews*. 74: 1–18.

Wei, C., and Taghavifar, H. (2017). "A novel approach to energy harvesting from vehicle suspension system: half-vehicle model." *Energy*. 134: 279-288.

Williams, C. B., and Yates, R. B. (1996). "Analysis of a micro-electric generator for microsystems." *Sensors and Actuators A: Physical*. 52(1–3): 8–11.

Williams, C. B., Shearwood, C., Harradine, M. A., Mellor, P. H., Birch, T. S., and Yates, R. B. (2001). "Development of an electromagnetic micro-generator." *IEE Proceedings-Circuits, Devices and Systems*. 148(6): 337–342.

Wischke, M., Masur, M., Kröner, M., and Woias, P. (2011). "Vibration harvesting in traffic tunnels to power wireless sensor nodes." *Smart Materials and Structures*. 20(8): 085014.

Wu, N., Wang, Q., and Xie, X. (2015). "Ocean wave energy harvesting with a piezoelectric coupled buoy structure." *Applied Ocean Research*. 50: 110–118.

Wu, W. J., Chen, Y. Y., Lee, B. S., He, J. J., and Peng, Y. T. (2006, March). "Tunable resonant frequency power harvesting devices. In *Smart Structures and Materials 2006: Damping and Isolation, International Society for Optics and Photonics*, San Diego, California, USA. Vol. 6169, p. 61690A.

Wu, Y., Qiu, J., Zhou, S., Ji, H., Chen, Y., and Li, S. (2018). "A piezoelectric spring pendulum oscillator used for multi-directional and ultra-low frequency vibration energy harvesting." *Applied Energy*. 231: 600–614.

Xiao, H., Wang, X., and John, S. (2016). "A multi-degree of freedom piezoelectric vibration energy harvester with piezoelectric elements inserted between two nearby oscillators." *Mechanical Systems and Signal Processing*. 68: 138–154.

Xie, L., and Cai, M. (2015). "Increased energy harvesting and reduced accelerative load for backpacks via frequency tuning." *Mechanical Systems and Signal Processing*. 58: 399–415.

Xie, L., Cai, S., Huang, G., Huang, L., Li, J., and Li, X. (2019). "On energy harvesting from a vehicle damper." *IEEE/ASME Transactions on Mechatronics*. 25(1): 108–117.

Xie, L., Li, J., Cai, S., and Li, X. (2017). "Electromagnetic energy-harvesting damper with multiple independently controlled transducers: on-demand damping and optimal energy regeneration." *IEEE/ASME Transactions on Mechatronics*. 22(6): 2705–2713.

Xie, L., Li, J., Li, X., Huang, L., and Cai, S. (2018). "Damping-tunable energy-harvesting

vehicle damper with multiple controlled generators: Design, modeling and experiments." *Mechanical Systems and Signal Processing*. 99: 859–872.

Xie, X. D., and Wang, Q. (2015a). "A mathematical model for piezoelectric ring energy harvesting technology from vehicle tires." *International Journal of Engineering Science*. 94: 113–127.

Xie, X. D., and Wang, Q. (2015b). "Energy harvesting from a vehicle suspension system." *Energy*. 86: 385–392.

Xie, X. D., and Wang, Q. (2016). "Design of a piezoelectric harvester fixed under the roof of a high-rise building." *Engineering Structures*. 117: 1–9.

Xie, X. D., Wang, Q., and Wu, N. (2014a). "Potential of a piezoelectric energy harvester from sea waves." *Journal of Sound and Vibration*. 333(5): 1421–1429.

Xie, X. D., Wang, Q., and Wu, N. (2014b). "A ring piezoelectric energy harvester excited by magnetic forces." *International Journal of Engineering Science*. 77: 71–78.

Xie, X. D., Wu, N., Yuen, K. V., and Wang, Q. (2013). "Energy harvesting from high-rise buildings by a piezoelectric coupled cantilever with a proof mass." *International Journal of Engineering Science*. 72: 98–106.

Xu, Y. L., and Yu, Z. (1998). "Vibration of inclined sag cables with oil dampers in cable-stayed bridges." *Journal of Bridge Engineering*. 3(4): 194–203.

Yamaguchi, H. (1998). "Stayed cable dynamics and its vibration control." *Bridge aerodynamics*. 235–253.

Yan, B., Wang, K., Kang, C. X., Zhang, X. N., and Wu, C. Y. (2017). "Self-sensing electromagnetic transducer for vibration control of space antenna reflector." *IEEE/ASME Transactions on Mechatronics*. 22(5): 1944–1951.

Yan, B., Zhou, S., Zhao, C., Wang, K., and Wu, C. (2019). "Electromagnetic energy harvester for vibration control of space rack: modeling, optimization, and analysis." *Journal of Aerospace Engineering*. 32(1): 04018126.

Yang, J., Christie, M. D., Sun, S., Ning, D., Nakano, M., Li, Z., Du, H., and Li, W. H. (2020). "Integration of an omnidirectional self-powering component to an MRE isolator towards a smart passive isolation system." *Mechanical Systems and Signal*

Processing. 144: 106853.

Yang, Z., and Yang, J. (2009). "Connected vibrating piezoelectric bimorph beams as a wide-band piezoelectric power harvester." *Journal of Intelligent Material Systems and Structures*. 20(5): 569–574.

Ye, J., Lu, Z., Chen, C., and Wang, M. (2017, June). "Power analysis of a single degree of freedom (DOF) vibration energy harvesting system considering controlled linear electric machines." In *2017 IEEE Transportation Electrification Conference and Expo (ITEC)*, Chicago, USA. pp. 158–163.

Yildiz, F. (2009). "Potential ambient energy-harvesting sources and techniques." *Journal of Technology Studies*. 35(1): 40–48.

Yu, L., Tang, L., and Yang, T. (2019). "Experimental investigation of a passive self-tuning resonator based on a beam-slider structure." *Acta Mechanica Sinica*. 35(5): 1079–1092.

Yu, L., Tang, L., and Yang, T. (2020). "Piezoelectric passive self-tuning energy harvester based on a beam-slider structure." *Journal of Sound and Vibration*. 115689.

Yuan, M., and Liu, K. (2018). "Vibration suppression and energy harvesting with a non-traditional vibration absorber: transient responses." *Vibration*. 1(1): 105–122.

Yuan, M., Liu, K., and Sadhu, A. (2018). "Simultaneous vibration suppression and energy harvesting with a non-traditional vibration absorber." *Journal of Intelligent Material Systems and Structures*. 29(8): 1748–1763.

Yuan, T. C., Yang, J., Song, R. G., and Liu, X. W. (2014). "Vibration energy harvesting system for railroad safety based on running vehicles." *Smart Materials and Structures*. 23(12): 125046.

Zhang, X., Pan, H., Qi, L., Zhang, Z., Yuan, Y., and Liu, Y. (2017). "A renewable energy harvesting system using a mechanical vibration rectifier (MVR) for railroads." *Applied Energy*. 204: 1535–1543.

Zhang, X., Zhang, Z., Pan, H., Salman, W., Yuan, Y., and Liu, Y. (2016). "A portable high-efficiency electromagnetic energy harvesting system using supercapacitors for renewable energy applications in railroads." *Energy Conversion and Management*.

118: 287–294.

Zhang, Y., Guo, K., Wang, D., Chen, C., and Li, X. (2017). “Energy conversion mechanism and regenerative potential of vehicle suspensions.” *Energy*. 119: 961-970.

Zhang, Z., Zhang, X., Chen, W., Rasim, Y., Salman, W., Pan, H., Yuan, Y., and Wang, C. (2016). “A high-efficiency energy regenerative shock absorber using supercapacitors for renewable energy applications in range extended electric vehicle.” *Applied Energy*. 178: 177–188.

Zhao, Z., Chen, Q., Zhang, R., Pan, C., and Jiang, Y. (2020). “Input energy reduction and energy dissipation enhancement mechanism of inerter systems.” *International Journal of Mechanical Sciences*. 105845.

Zhou, M., Al-Furjan, M. S. H., Zou, J., and Liu, W. (2018). “A review on heat and mechanical energy harvesting from human–principles, prototypes and perspectives.” *Renewable and Sustainable Energy Reviews*. 82: 3582–3609.

Zhu, D., Roberts, S., Mouille, T., Tudor, M. J., and Beeby, S. P. (2012). “General model with experimental validation of electrical resonant frequency tuning of electromagnetic vibration energy harvesters.” *Smart Materials and Structures*. 21(10): 105039.

Zhu, D., Tudor, J., and Beeby, S. (2011, November). “Frequency tuning of vibration energy harvesters using compressive and tensile axial loads.” In *Proceedings of the International Workshops on Micro and Nanotechnology for Power Generation and Energy Conversion Applications - PowerMEMS*, Seoul, Korea, pp. 290–293.

Zhu, H., Li, Y., Shen, W., and Zhu, S. (2019). “Mechanical and energy-harvesting model for electromagnetic inertial mass dampers.” *Mechanical Systems and Signal Processing*. 120: 203–220.

Zhu, S., Shen, W. A., and Xu, Y. L. (2011). “Regenerative electromagnetic TMD-a novel integration of energy harvesting and vibration control.” In *the 6th International Workshop on Advanced Smart Materials and Smart Structures Technology, ANCRiSST2011*. Dalian, China.

Zhu, S., Shen, W. A., and Xu, Y. L. (2012). “Linear electromagnetic devices for vibration damping and energy harvesting: Modeling and testing.” *Engineering Structures*. 34: 198–212.

Zhu, S., Shen, W., and Qian, X. (2013). “Dynamic analogy between an electromagnetic shunt damper and a tuned mass damper.” *Smart Materials and Structures*. 22(11): 115018.

Zilletti, M., Elliott, S. J., and Rustighi, E. (2012). “Optimisation of dynamic vibration absorbers to minimise kinetic energy and maximise internal power dissipation.” *Journal of Sound and Vibration*. 331(18): 4093–4100.

Zong, L. H., Gong, X. L., Xuan, S. H., and Guo, C. Y. (2013). “Semi-active H∞ control of high-speed railway vehicle suspension with magnetorheological dampers.” *Vehicle System Dynamics*. 51(5): 600–626.

Zou, J., Guo, X., Abdelkareem, M. A., Xu, L., and Zhang, J. (2019). “Modelling and ride analysis of a hydraulic interconnected suspension based on the hydraulic energy regenerative shock absorbers.” *Mechanical Systems and Signal Processing*. 127: 345–369.

Zuo, L., and Cui, W. (2013). “Dual-functional energy-harvesting and vibration control: electromagnetic resonant shunt series tuned mass dampers.” *Journal of Vibration and Acoustics*. 135(5): 051018.

Zuo, L., and Tang, X. (2013). “Large-scale vibration energy harvesting.” *Journal of Intelligent Material Systems and Structures*. 24(11): 1405–1430.

Zuo, L., and Zhang, P. S. (2013). “Energy harvesting, ride comfort, and road handling of regenerative vehicle suspensions.” *Journal of Vibration and Acoustics*. 135(1): 011002.